

MOLECULAR BEAM INVESTIGATIONS
OF SURFACE CHEMICAL REACTIONS AND DYNAMICS

Thesis by
Charles Buddie Mullins

In Partial Fulfillment of the Requirements
for the Degree of
Doctor of Philosophy

California Institute of Technology
Pasadena, California

1990
(Submitted September 29, 1989)

ACKNOWLEDGEMENTS

I am sincerely grateful to the organizations which helped fund my graduate education. IBM generously provided me with a fellowship for two years. The Link Foundation awarded me a fellowship for one year and the Grace Chemical Company provided funds to support me during one summer. The Caltech Chemical Engineering Department arranged a fellowship for me during my initial year. The National Science Foundation has provided the bulk of the funding for the research reported in this thesis.

During my tenure at Caltech I have had the great fortune of making many friends, some of which helped in this work a great deal. I hope all of you know how grateful I am for your assistance and most of all for your friendship.

My advisor, Henry Weinberg, has allowed me considerable freedom throughout the course of my research coupled with very strong support, even when he disagreed with the approach I pursued. Henry was especially supportive during the "lean years" when I had considerable trouble making the apparatus operable. We have become very good friends over the past six years and it is this aspect of our relationship that I appreciate the most. Thanks so very much Henry!

Without the support of the excellent staff at Caltech this work would have been impossible. I owe special thanks to Kathy, Floyd, Chic, John and Helen in Chemical Engineering and Tony, Guy, Ray and Tom of the Division Electrical and Mechanical Shops.

The Weinberg group has had several members that have devoted significant amounts of effort to this work and I thank all of them, especially Malina Hills, Jenna Zinck, Jim Engstrom, Brad Anton, Eric Hood, Steve George, Chuan Kang and Randy Verhoef. John Parmeter, Yong-Kui Sun and Udo Schwalke have been good friends as well as research colleagues and I appreciate all their help and friendship over the years. I owe a particularly large debt of gratitude to Youqi Wang. Youqi has been an inspiration with his boundless energy, enthusiasm and integrity. It is truly a pleasure and honor to be his friend.

The Caltech environment is such that it is virtually impossible to study and work without also making friends outside of your research area. Howard Stone has been a close friend and sounding board for several years. It has always been fun and educational to interact with Howard. Greg Voth has shared significant amounts of his time, energy and advice with me over the past 5 years. In addition to being my regular tennis practice and doubles partner Greg has been a friendly and enthusiastic tutor regarding theoretical chemistry and other esoteric topics. I miss the "good old days" when I could talk with Greg and Howard virtually everyday.

I spent 5 months at the IBM Almaden Research Center in San Jose in 1988 working with Charlie Rettner on a project included in this thesis. This experience was everything I had hoped it would be and more thanks to Charlie's support and enthusiasm. Charlie is one of a kind and I am extremely grateful to have had the chance to work with him and to be his friend. During my stay at Almaden I found many helpful and friendly people and I thank them all. However, Joe Schlaegel, Erhard Schweizer and Dan Auerbach deserve special thanks for all their efforts.

Finally, words cannot express the gratitude and overwhelming feeling of warmth and closeness I have toward my family for their undying support over the past six years. My mom and dad helped me maintain my sanity and enthusiasm during those previously mentioned "lean years" and shared in my excitement when "good things" started to happen. Thanks mom and dad for all your love. My wife Melissa should be given the Nobel Prize in patience. She has put up with more baloney during this period than any one person deserves in a lifetime. I will try very hard to make it up to her. She gives my life meaning and purpose and I love her very much.

ABSTRACT

Experimental results from molecular beam investigations of trapping and dissociative chemisorption phenomena for several gas-surface systems are presented. The dissociative chemisorption of oxygen on Ir(110)-(1x2) in the limit of zero coverage S_0 was studied as a function of incident kinetic energy E_i , incident angle θ_i and surface temperature T_s . Results from this investigation indicate that two mechanisms account for the initial chemisorption. At low incident kinetic energy (less than 4 kcal/mol) chemisorption mediated by trapping is primarily responsible for the dissociative adsorption while at high energies a direct mechanism can account for the results. In both energy ranges the initial dissociative chemisorption probability is insensitive to incident angle.

The trapping of molecular ethane as well as the dissociative chemisorption of ethane on the clean Ir(110)-(1x2) surface has also been investigated. The initial trapping probability ζ_0 is found to decrease with incident kinetic energy from a value of ~ 0.98 at 1 kcal/mol to ~ 0.1 at 16 kcal/mol. These data scale with $E_i \cos^{0.5} \theta_i$. The initial dissociative chemisorption of ethane on Ir(110)-(1x2) occurs via a trapping-mediated mechanism at low E_i and a direct mechanism at high kinetic energies. In the trapping-mediated regime S_0 decreases rapidly with increasing T_s . These data

quantitatively support a kinetic model consistent with a trapping-mediated chemisorption mechanism. The difference in the activation energies for desorption and chemisorption from the physically adsorbed, trapped state $E_d - E_c$ is 2.2 ± 0.2 kcal/mol. Chemisorption at high kinetic energies, in the direct regime, is independent of surface temperature.

Additionally, the trapping probability of Ar on Pt(111) has been measured as a function of incident kinetic energy, and angle for $T_s = 80, 190$ and 273 K. The trapping probability decreases with increasing E_i in a manner that depends on both θ_i and T_s . The angular scaling law governing the trapping is a function of T_s such that ζ_0 scales with $E_i \cos^{1.5} \theta_i$ at 80 K, $E_i \cos^{1.0} \theta_i$ at 190 K and $E_i \cos^{0.5} \theta_i$ at 273 K. These results suggest that parallel momentum dissipation becomes increasingly more important to the trapping dynamics as the surface temperature is increased.

TABLE OF CONTENTS

ACKNOWLEDGEMENTS	ii
ABSTRACT	v
I. INTRODUCTION	I-1
II. DYNAMICS OF THE DISSOCIATIVE CHEMISORPTION OF OXYGEN ON AN Ir(110)-(1x2) SURFACE	II-1
III. A MOLECULAR BEAM STUDY OF THE DISSOCIATIVE CHEMISORPTION OF O ₂ ON Ir(110)-(1x2)	III-1
IV. TRAPPING OF MOLECULAR ETHANE ON THE Ir(110)-(1x2) SURFACE	IV-1
V. TRAPPING-MEDIATED DISSOCIATIVE CHEMISORPTION OF ETHANE ON Ir(110)-(1x2)	V-1
VI. VARIATION OF THE TRAPPING PROBABILITY OF Ar ON Pt(111) WITH KINETIC ENERGY AND ANGLE OF INCIDENCE: THE CHANGING ROLE OF PARALLEL MOMENTUM WITH SURFACE TEMPERATURE	VI-1

- A. MOLECULAR ADSORPTION OF ETHANE ON THE
Ir(110)-(1x2) SURFACE: MONTE-CARLO SIMULATIONS
AND MOLECULAR BEAM REFLECTIVITY MEASUREMENTS A-1

- B. DESORPTION AND TRAPPING OF ARGON AT A 2H-W(100)
SURFACE AND A TEST OF THE APPLICABILITY OF
DETAILED BALANCE TO A NONEQUILIBRIUM SYSTEM B-1

- C. ELECTRON ENERGY LOSS SPECTROSCOPY OF AMMONIA
ON Ru(001) C-1

- D. INTERACTION OF ETHYLENE WITH THE Ru(001) SURFACE D-1

CHAPTER I

INTRODUCTION

The study of gas-surface dynamics and reactions is important for both fundamental and practical reasons. At a basic level, the chemical and physical processes that occur when a particle collides with a surface are only poorly understood. For example, the energy transfer mechanisms that account for the physical adsorption of a rare gas atom at a solid surface are just beginning to be recognized. The dynamics and energetics of the dissociative chemisorption of gas phase molecules at solid surfaces are even more complicated. Thus, this type of phenomena provides many intellectually challenging problems. The results of such studies are frequently useful in understanding and enhancing industrial processes also. For example, quantifying and understanding dissociative chemisorption is useful in improving the performance of heterogeneously catalyzed commercial reactors.

Fundamental studies over the past 30 years have carried surface science and in particular the dynamics of gas-surface interactions to a new level of maturity¹. Increasingly more detailed questions are being asked and answered. The past five years have witnessed a virtual explosion in activity with regard to studies of the dynamics and reactions of gas-surface systems by molecular beam techniques²⁻¹⁴. Much of the recent progress in surface science

is due to these studies. Thus, this thesis reports findings from several investigations of gas-surface dynamics employing the molecular beam technique.

Chapters II and III contain the results of research concerning the chemisorption dynamics of the interaction of oxygen with the Ir(110)-(1x2) surface. Experimental results of the dissociative adsorption as a function of incident kinetic energy, incident angle and surface temperature are reported. Chapter II also contains a detailed description of the apparatus used in obtaining the experimental data reported in Chapters II-V and Appendix A.

Chapters IV and V and Appendix A report results from an investigation of the interaction of ethane with the Ir(110)-(1x2) surface. In particular, Chapter IV is an account of the initial probability of physical adsorption on the surface at 77 K. The incident kinetic energy and angle dependence of the trapping probability are reported and discussed. Chapter V describes the results of experiments concerning the initial dissociative chemisorption of ethane as a function of incident kinetic energy, incident angle and surface temperature. Appendix A reports findings from a comparison of Monte-Carlo simulations and molecular beam reflectivity measurements of the physical adsorption probability of ethane on Ir(110)-(1x2) as a function of time.

Chapter VI and Appendix B contain descriptions of results from experiments probing the interaction of argon at relatively low

kinetic energy with the Pt(111) surface and the 2H-W(100) surface. These studies were motivated by a desire to better understand the trapping step in trapping-mediated chemisorption. Chapter VI reports studies of the trapping probability as a function of incident energy and angle as does Appendix B. In addition, Chapter VI reports the surface temperature dependence of the trapping probability.

Appendices C and D display and discuss experimental results from electron energy loss measurements of ammonia and ethylene on Ru(001).

REFERENCES

1. A. Zangwill, *Physics at Surfaces*, Cambridge University Press, Cambridge 1988.
2. D.J. Auerbach, H.E. Pfnur, C.T. Rettner, J.E. Schlaegel, J. Lee and R.J. Madix, *J. Chem. Phys.* **81**, 2515 (1984); H.E. Pfnur, C.T. Rettner, D.J. Auerbach, R.J. Madix and J. Lee, *ibid.* **85**, 7452 (1986).
3. C.T. Rettner, H.E. Pfnur and D.J. Auerbach, *Phys. Rev. Lett.* **54**, 2716 (1985).
4. S.T. Ceyer, *Ann. Rev. Phys. Chem.* **39**, 479 (1988); and references therein.
5. M.B. Lee, Q.Y. Yang and S.T. Ceyer, *J. Chem. Phys.* **87**, 2724 (1987).
6. M.P. D'Evelyn, A.V. Hamza, G.E. Gdowski and R.J. Madix, *Surf. Sci.* **167**, 451 (1986).
7. A.C. Luntz and D.S. Bethune, *J. Chem. Phys.* **90**, 1274 (1989).
8. C.T. Rettner and H. Stein, *Phys. Rev. Lett.* **59**, 2768 (1987); *J. Chem. Phys.* **87**, 770 (1987).
9. G.R. Schoofs, C.R. Arumainayagam, M.C. McMaster and R.J. Madix, *Surf. Sci.* **215**, 1 (1989).
10. C.B. Mullins and W.H. Weinberg, *J. Chem. Phys.* (submitted).
11. A.V. Hamza, H.-P. Steinruck and R.J. Madix, *J. Chem. Phys.* **85**, 7494 (1986).
12. A.C. Luntz, M.D. Williams and D.S. Bethune, *J. Chem. Phys.* **89**, 4381 (1988).
13. C.T. Rettner, L.A. DeLouise and D.J. Auerbach, *J. Vac. Sci. Technol. A* **4**, 1491 (1986); *J. Chem. Phys.* **85**, 1131 (1986).

14. C.T. Rettner, H. Stein and E.K. Schweizer, *J. Chem. Phys.* **89**, 3337 (1988).

II-1

CHAPTER II

DYNAMICS OF THE DISSOCIATIVE CHEMISORPTION OF
OXYGEN ON AN Ir(110)-(1x2) SURFACE

[The text of Chapter II consists of an article coauthored with W.H. Weinberg, to be submitted.]

ABSTRACT

The dissociative chemisorption of oxygen on Ir(110)-(1x2) has been investigated employing molecular beam techniques. The probability of dissociative chemisorption as a function of incident kinetic energy between 1 and 23 kcal/mol, incident angle between 0 and 45°, and surface temperature between 150 and 600 K is reported in the limit of zero-coverage. For kinetic energies less than approximately 4 kcal/mol the initial probability of dissociative chemisorption data are explained via a trapping-mediated mechanism. For kinetic energies greater than 4 kcal/mol a direct mechanism is primarily responsible for dissociative chemisorption. The data are insensitive to surface temperature except at greater than 500 K in the trapping-mediated chemisorption regime where the temperature effect is manifested in a decrease in the trapping probability. The height of the activation barriers for desorption and chemisorption from the trapped state are equivalent to within 100 cal/mol. Both the direct and trapping-mediated chemisorption regimes are very insensitive to incident angle scaling with total energy.

I. INTRODUCTION

Quantifying and understanding the dynamics and energetics of the dissociative chemisorption of a gas-phase diatomic molecule on a transition metal surface is a problem attracting a great deal of interest currently. Indeed, the problem is multifaceted and complex. Comparatively little is known, for example, regarding the mechanism with which the impinging molecule transfers its kinetic energy to substrate and internal molecular excitations. The surface site at which dissociation occurs for a given incident kinetic energy remains a pertinent question. The role of electrons in the dissociation mechanism is only beginning to be understood. There are far more questions than answers concerning this class of chemical reactions. It is clear this problem is important for fundamental reasons but answers to the above questions are also of practical significance. Heterogeneously catalyzed chemical reactions are an important part of industrial chemical processing and the dissociation of a diatomic at a surface is among the simplest of the profusion of reactions occurring in an industrial reactor. Obviously the dissociation of a diatomic molecule at a surface will have to be understood before significant progress on other more complex reactions can be made. Perhaps more relevant to this discussion, the dissociative chemisorption of oxygen is an important step in the epoxidation of ethylene and the oxidation of carbon monoxide.

Recently several groups¹⁻¹⁴ have investigated the dynamics of dissociative chemisorption utilizing molecular beam techniques. These studies have greatly enhanced our understanding of the gross features of the molecule-surface interaction potential. Thus we employ a molecular beam apparatus in this investigation of the dissociative chemisorption of oxygen on Ir(110)-(1x2) to probe and determine the general features of the potential hypersurface for this system.

The results from a large body of work including the previously mentioned molecular beam investigations indicate that there are two basic mechanisms that account for most dissociative surface reactions in the limit of zero surface coverage. There is a direct mechanism whereby the molecule dissociates upon impact with the surface at relatively high incident kinetic energy and with little or no surface temperature dependence. There is also a trapping-mediated mechanism in which the molecule transfers sufficient translational energy to substrate and internal excitations during the collision to trap in a molecularly adsorbed state. The probability of trapping at the surface increases with decreasing incident kinetic energy. Once it is trapped the molecule equilibrates with the surface and either desorbs or reorientates such that dissociation can occur. Thus, trapping-mediated chemisorption rates are typically strong functions of temperature. However, this is not always true and the system discussed in this paper (O_2 /Ir(110)-(1x2)) is one of the exceptions. Indeed, increasing surface temperature T_s can serve to both decrease and increase reaction

rates or have no effect at all¹⁵. The chemisorption rate decreases with increasing T_s if the activation barrier to dissociation is less than the barrier to desorb from the molecularly adsorbed (trapped) state. On the other hand, the chemisorption rate increases with increasing T_s if the reverse is true. Systems with the former characteristics are relatively facile so that chemisorption probabilities can be quite high while the latter characteristics are relevant to activated chemisorption systems since the barrier to dissociation is higher than the vacuum zero energy level. It is our belief that both channels exist for most molecule/surface systems. However the probability of dissociative chemisorption can be quite low in the activated systems. Obviously if the probability of dissociation in a trapping-mediated chemisorption mechanism is surface temperature independent the barrier to desorb is the same height as the barrier to dissociate.

Some of the earlier molecular beam studies of chemisorption dynamics focussed on the direct mechanism of dissociation for activated systems¹⁻⁹. These studies revealed that translational energy can be very effective in surmounting the barrier to dissociative chemisorption and that this barrier is often very nearly one-dimensional. However, this work generally has not revealed any details regarding the trapping-mediated mechanism for activated systems. That this channel exists for these activated systems has been demonstrated with experiments at relatively high pressure in batch reactors^{16,17} where the available kinetic energies are limited to low values according to a Maxwell-Boltzmann distribution. Thus

indicating the importance of this channel in industrial heterogeneously catalyzed chemical reactions.

Some of the more recent accounts of molecular beam studies of surface chemical reaction dynamics have described relatively facile chemisorption systems which have been particularly useful in uncovering the relevant dynamics in a trapping-mediated mechanism¹⁰⁻¹⁴. In a study of N₂ on W(100) Rettner, et al.¹⁴ convincingly demonstrated the existence of a trapping-mediated channel at low incident kinetic energies. In a separate paper on the same system Rettner, et al.¹⁸ also showed that the trapping probability was only weakly influenced by surface temperature, a critical assumption in several analyses prior to these measurements.

Rettner and coworkers have also investigated the initial and coverage-dependent dissociative chemisorption of oxygen on W(110). This study has not supported assignment of a trapping-mediated mechanism for dissociative chemisorption for T_s between 280 and 800 K. In fact, the initial probability of dissociative chemisorption S₀ increases rapidly with increasing E_i from 2.3 to 11.5 kcal/mol which fits better with a direct dissociation mechanism. Only weak indirect evidence for trapping-mediated dissociative chemisorption was found for incident kinetic energies of less than 1.1 kcal/mol. However a study of O₂ chemisorption on W(110) using an effusive beam source by Wang and Gomer¹⁹ indicates that a trapping-

mediated chemisorption channel may be significant for surface temperatures less than 200 K.

Luntz and coworkers have investigated the dissociative chemisorption of oxygen on Pt(111) recently using molecular beam techniques¹². This study unambiguously shows both trapping-mediated and direct channels to dissociative chemisorption. The high incident kinetic energy direct channel for this system also showed a weak but surprising temperature dependence. In a separate paper Luntz, et al. have also demonstrated the existence of a physically adsorbed state of O₂ on Pt(111) which is believed to be the precursor to the molecular chemisorbed state²⁰.

Of particular interest with regard to the present study is the work of Taylor, et al.²¹ on the dissociative chemisorption of O₂ on Ir(110)-(1x2). Indeed this work provided some motivation for this study. In their investigation Taylor, et al. employed thermal desorption mass spectrometry, low-energy electron diffraction and work function measurements to determine initial and coverage-dependent chemisorption probabilities. Their results indicate that the initial probability of chemisorption is independent of surface temperature. They also concluded for T_s between 300 and 700 K that the adsorption kinetics could be described by a second-order precursor model.

This paper is a presentation and discussion of experimental data concerning the interaction of O₂ with the Ir(110)-(1x2) surface

employing a molecular beam apparatus. In particular, measurements of the initial probability of dissociative chemisorption as a function of incident kinetic energy, incident angle and surface temperature are presented and discussed in light of the mechanisms described above. We find evidence at low kinetic energies for a trapping-mediated chemisorption channel and a direct channel at high E_i . We also find that the initial probability of chemisorption is relatively insensitive to incident angle and surface temperature. A detailed description of the apparatus and procedures used to obtain the data is presented next. A brief, preliminary account of this work has appeared previously²².

II. EXPERIMENTAL

The experimental apparatus is shown schematically in an overhead view in Fig. 1 and consists of an ultra-high vacuum (UHV) scattering chamber and a thrice differentially pumped molecular beam source. The apparatus is particularly well suited for studies of the dynamics of adsorption because of its relatively small volume and high pumping speed. These attributes simplify and increase the accuracy of the analysis that is necessary to determine probabilities of adsorption from uptake measurements. Determination of the probability of adsorption by coverage versus exposure measurements either by thermal desorption mass spectrometry or Auger analysis can also easily be performed. Ease of operation and maintenance are also a consideration in the design of a molecular beam apparatus. The machine has a particularly

simple yet effective sample manipulator which allows extremely rapid cooling via liquid nitrogen. The nozzle, nozzle heater and nozzle temperature controller were also very easy to construct and have provided simple operation and stable performance. Experiments are typically conducted by directing a supersonic beam of oxygen at an Ir single crystalline sample and measuring the scattered flux. Details of the experimental procedure and the relevant portions of the apparatus are provided below.

The scattering chamber is the largest vacuum chamber in the system and is also the focus of the apparatus since it houses the crystal sample and all the spectroscopic instrumentation. The scattering chamber has a volume of ~100 liters and is pumped by a turbo-molecular pump (Balzers TPU2000) with an effective pumping speed of approximately 1000 liters/s. A typical base pressure of $\sim 1 \times 10^{-10}$ Torr is achieved within a few days of a 36 hour bakeout at 150°C. The third beam-source chamber (C3 in Fig. 1) is also pumped by a turbo-molecular pump (Balzers TPU270) and after bakeout has a pressure of $\sim 1 \times 10^{-9}$ Torr. The other beam-source chambers (C1 and C2) are pumped by diffusion pumps and do not need to be baked to attain adequate vacuum. The function and contents of the beam-source chambers is explained below.

The iridium crystal was cut from a boule that was oriented with a Laue diffractometer and then polished using standard techniques. The surface was cleaned routinely by argon ion sputtering and annealing the surface in an oxygen background. This

treatment reduced impurity levels on the surface (mainly carbon) to below the detection level of our Auger spectrometer (Physical Electronics Industries, 15-255G). The clean surface exhibited a sharp (1x2) low-energy electron diffraction (LEED) pattern indicative of the reconstructed Ir(110) surface. LEED measurements are made using a 4-grid screen (Varian) which can be viewed and photographed through a standard 6 in. flanged window. The azimuthal orientation of the sample as determined by LEED is such that an [001] vector lying in the plane of the sample surface is approximately 15° from the axis of rotation of the manipulator (i.e., the polar angle).

The single crystalline sample is mounted on a manipulator which can be rotated to vary the angle of incidence of the molecular beam on the surface. The crystal is mounted on the manipulator by small copper blocks that clamp on two short Ta wires spot welded to the backside of the sample. The crystal is heated by passing a current through the Ta supports and the sample itself. With liquid nitrogen flowing through the manipulator the sample can be cooled from 1600 K to 80 K in less than 90 seconds. The sample temperature is determined by a 0.003 in. W-5%Re/W-26%/Re thermocouple spot-welded to the backside of the crystal. The copper mounting blocks are attached to the copper rods from a miniconflat combination power and thermocouple feedthrough. The upper end of the feedthrough copper rods, located inside the stainless steel manipulator shaft, are immersed in liquid nitrogen when cooling is desired. The liquid nitrogen flows down a tube

inside and coaxial to the manipulator shaft directly to the attached feedthrough whereupon the fluid turns 180° and flows back over the inner tube to exit the manipulator shaft. This aspect of the design together with the small thermal resistance from the copper rod to the crystal is largely responsible for the rapid cooling of the crystal. The molecular beam is horizontal and therefore the surface normal of the crystal is aligned in a horizontal plane during mounting using a HeNe laser beam. The angle of incidence of the molecular beam can be read and repositioned to $\sim 0.1^\circ$ and its absolute value has been determined to $\sim 1^\circ$ using a HeNe laser beam coaxial with the molecular beam apertures.

A supersonic beam of molecular oxygen is generated using a heatable nozzle source with a 100 μm diameter orifice and a total of three differential pumping stages. The vacuum chamber housing the nozzle is shown in Fig. 1 and denoted C1. A 0.48 mm skimmer (Beam Dynamics, Model 1) is mounted in this chamber and the nozzle is positioned from 2-8 mm from the knife-edge orifice of this skimmer, depending on the gas, nozzle temperature and pressure. The second beam chamber, C2, has a 0.98 mm skimmer (Beam Dynamics, Model 1) mounted inside, as well as a beam stopping flag (Newport). The flag has a response time of ~ 0.001 seconds and can be used to accurately dose the crystal with the molecular beam (as short as 0.01 seconds). The flag is also used in making reflectivity or uptake measurements, as is discussed later. Finally, the third beam chamber, C3, has a 2.0mm plate aperture which is the last the beam must pass through before entering the scattering chamber. The

third beam chamber also contains a chopper so that modulation of the beam is possible. The two skimming apertures and the final plate aperture were aligned concentrically visually with a telescope and also by diffraction of light from the HeNe laser. The laser has an optical fiber attached which directs light coaxial with the molecular beam to aid in aligning the crystal in the beam. The nozzle has a window at the end outside the vacuum chamber which can also be used with the laser for alignment of the nozzle with the apertures.

As mentioned above the third beam chamber contains a high speed chopper which allows beam energies to be determined via time-of-flight measurements using a quadrupole mass spectrometer (ExtraNuclear) as a detector. This operation is conducted in pulse counting mode using a multichannel scaler board (Ortek, ACE-MCS) inside a personal computer. The chopper is composed of an aluminum disc with 2 narrow slits machined into it radially 180° apart, near the disc edge. The disc is mounted on and driven by a synchronous motor (Globe-TRW, 75A6000). As the disc rotates and the upper slit passes through the molecular beam, light from an incandescent bulb passes through the lower slit illuminating a photodiode. This creates a voltage pulse which is used as a trigger signal for the multichannel scaler. In practice there is a small lag (or lead) time due to misalignment of the diode and light bulb with respect to the molecular beam. Thus the real zero time is established by running the chopper both clockwise and counter-clockwise and averaging the

results of the time-of-flight measurement to cancel the lead and lag effects.

To accurately determine beam kinetic energies it is also necessary to measure the ion flight time to the electron multiplier following ionization. Ion flight times have been calibrated using a molecular beam of SF₆ and comparing the time-of-flight measurements of the various mass fragments from the cracking pattern. These data are then fit to an equation of the form $t_{ion} \sim (C_{ion} \times M_{ion})^{0.5}$ where M_{ion} is the ion mass and C_{ion} is a constant determined by the fit. Ion flight times are between 5 and 10% of the total flight time.

Beam kinetic energies between approximately 1 and 23 kcal/mol can be generated by controlling the nozzle temperature and seeding in Ar and He. Nozzle heating is accomplished by passing an AC current through a ceramic insulated inconel clad nichrome wire which is tightly wrapped around the final 9 inches of length of the nozzle. Even with this long heated length there is a maximum 15% discrepancy between the measured nozzle temperature and time-of-flight determined gas temperature (for rare gases) for nozzle temperatures above 300 K. The nozzle temperature is measured with a Chromel-Alumel thermocouple spot welded to the end of the nozzle and the temperature is controlled and stabilized with the aid of a temperature controller (Omega). The energy spread of the beam is typical of most supersonically generated beams with $\Delta E_{FWHM}/E_{Peak} \sim 0.15$.

Dissociative chemisorption probabilities are measured primarily using an uptake method commonly known as the beam reflectivity method of King and Wells²³. In this transient measurement the surface acts as a getter and the experimentally determined partial pressure of oxygen is used as a measure of the molecules that reflect from the surface without adsorbing. In principle this technique can yield the value of the chemisorption probability as a function of surface coverage in a single measurement. For a system with negligible vacuum time constant (e.g., Fig. 2) the initial probability of chemisorption would be determined by a comparison of the initial oxygen partial pressure, following the opening of the high speed shutter (at t_1), to the oxygen partial pressure from the beam scattering from the saturated surface (at t_3). In this case the initial probability of dissociative chemisorption is simply $P_1/(P_1+P_2)$.

Data is acquired during a reflectivity measurement in the pulse counting mode using the same multichannel scaler and quadrupole mass spectrometer mentioned earlier. The data can be analyzed using the same personal computer that is used for acquisition. This analysis is relatively straightforward for an ideal system as demonstrated above. However, for a real system with finite vacuum time constant and increases in the observed partial pressure which are not totally due to the supersonic beam impinging on the surface, extra measures must be taken. Fortunately another complicating factor, unstable pumping speed, has a negligible effect

on our measurements. The high pumping speed of the turbomolecular pump (effectively 1000 l/s) and the small chamber decreases the effect of pumping by chamber walls to an immeasurable effect.

In cases with reactive gases where the chemisorption probability is near unity such as the present study, oxygen dissociation on Ir(110)-(1x2), the initial rate of change of the surface coverage is too rapid to neglect the vacuum time constant. We have accounted for this complication with two measures. Firstly, we dilutely seed all beams to reduce the flux of reactive gases to the surface. Secondly, we directly measure the vacuum time constant, ignore the initial transient and linearly extrapolate back to the beginning of the transient using data that is at least 5 time constants ($< 0.1\text{s}$) removed from the time zero.

As pointed out by Rettner et al.¹³ there is a component in the partial pressure rise in the scattering chamber in addition to the component due to the supersonic beam impinging on the crystal surface. This additional nonnegligible partial pressure rise is due to an effusive beam of gas emanating from the final differentially pumped chamber, C3. This gas scatters out of the supersonic beam and eventually effuses into the main chamber contributing to the oxygen flux. To measure this component we note the pressure rise in the third beam chamber with the beam on and the flag open and then measure the partial pressure of oxygen increase in the scattering chamber. Then, with the flag shut a leak valve mounted on the third chamber is opened and adjusted to give the same pressure rise in

this chamber as with the beam on and flag open. The partial pressure of oxygen in the scattering chamber is then measured once again and attributed entirely to the effusive beam component. The effusive beam component has been measured for several gas mixtures (oxygen and carrier gas) and in all cases yields a value that is 1.75% of the supersonic component. Since the effusive component radiates into a half space with a cosine distribution that is azimuthally symmetric the number of particles that interact with the crystal surface is negligible. This means that the entire effusive component adds to the partial pressure recorded during a reflectivity measurement at each instant in time after the initial 0.5 seconds, where time constant effects are present. Hence, the effusive component is subtracted from the reflectivity measurement from $t_1+0.5$ s through t_3 .

The initial probability of dissociative chemisorption is computed as follows. The values of the partial pressures from t_0 to t_1 are averaged and this average is labeled $P_{t_0-t_1}$ and an uncertainty σ_{0-1} is computed for this average. A similar computation is performed for partial pressures from t_2 to t_3 and the average is labeled $P_{t_2-t_3}$. The uncertainty in $P_{t_2-t_3}$ is labeled σ_{2-3} . Finally, as mentioned earlier a linear least squares fit is performed on the initial transient partial pressure data suitably removed from t_1 (>5 vacuum time constants) and the line generated by this fit is extrapolated to t_2 . This value is labeled P_i and the associated uncertainty is labelled σ_i . The initial probability of dissociative chemisorption is then computed as:

$$S_o = (P_{t_2-t_3} - P_i) / \{(P_{t_2-t_3} - P_{t_0-t_1}) 0.9825\}.$$

The factor of 0.9825 in the equation accounts for the effusive component in the partial pressure.

Uncertainties for each measurement are estimated from the individual uncertainties that make up the computation of the initial dissociative chemisorption probability. The uncertainty in the effusive component is not included in the propagation of uncertainty since the contribution to the total uncertainty is much less than that of the other components (always < 5% of the total uncertainty). The propagation of uncertainties is straightforward and leads to the following simple formula for computation:

$$(\sigma_{S_o})^2 [P_{t_2-t_3} - P_{t_0-t_1}]^2 = [1 - S_o]^2 (\sigma_{2-3})^2 + S_o^2 (\sigma_{0-1})^2 + (\sigma_i)^2.$$

Uncertainties in S_o are always less than 0.05 and typically ~ 0.025 .

Finally, the surface coverage during a reflectivity measurement is represented by the cross-hatched area in Fig. 2 so that probabilities of chemisorption versus coverage can be obtained. However in practice this tends to be quite difficult since the beam reflectivity technique is not accurate for values of $S_o < 0.05$ thus making the area representing coverage ill-defined.

III. RESULTS AND DISCUSSION

Figure 3 shows the initial probability of dissociative chemisorption of oxygen on the Ir(110)-(1x2) surface as a function of incident kinetic energy for $T_s=150$ and 300 K at normal incidence. At low incident kinetic energies (< 4 kcal/mol) the initial probability of chemisorption decreases with increasing E_i . This behavior is characteristic of a trapping-mediated mechanism for chemisorption and is completely different from that which is expected for direct chemisorption. As previously mentioned, the trapping probability is expected to decrease with increasing E_i since the fraction of kinetic energy dissipation that is required in order to trap will increase. Simply put, trapping will occur when the fraction of incident kinetic energy that is dissipated upon impingement is greater than $E_i/(E_i+\epsilon)$, where ϵ is an effective attractive well depth²⁴. This qualitative feature has also been demonstrated with simple hard-cube models²⁵ and classical trajectory techniques²⁶. Additionally, recent experiments investigating trapping of rare gases²⁷⁻²⁹ and molecules³⁰⁻³² exhibit similar trends.

As mentioned earlier, a trapping-mediated dissociative chemisorption mechanism has previously been identified for O_2 on Pt(111)¹². The falloff in S_0 with increasing E_i for oxygen on Pt(111) in the trapping regime occurs over nearly the same energy range as that shown in Fig. 3. This falloff in S_0 with E_i is quite rapid compared to other systems. The kinetic energy range over which

trapping-mediated chemisorption occurs is smaller for oxygen on Ir(110)-(1x2) and Pt(111) than for N₂ on W(100)¹⁴ or C₂H₆ on Ir(110)-(1x2)¹⁰. This is probably due to the depth of the well in which trapping occurs being smaller for the oxygen on Ir(110)-(1x2) and Pt(111) cases than the latter cases. Indeed for trapping-mediated chemisorption of O₂ on Pt(111) the well into which the particle traps appears to be the well for physical adsorption²⁰ which is approximately 3 kcal/mol deep. Alternatively, the well depth for the physical adsorption of C₂H₆ on Ir(110)-(1x2) is approximately 9 kcal/mol¹⁰. However, this explanation is by no means definitive. Prior to their identification of a physically adsorbed state of oxygen on Pt(111) Luntz, et al. favored trapping into the molecularly chemisorbed state²⁰. The reconstructed (110) surface of iridium is expected to be more reactive than either the (110) or (111) surfaces of Pt however the two metals show similar behavior in their reactions with hydrogen³³ and hydrocarbons³⁴. Indeed Taylor, et al.²¹ mention a stable molecularly chemisorbed state of oxygen on Ir(110)-(1x2) for T_s less than 100 K. The similarities between the two surfaces leads us to believe that the oxygen molecule is probably trapping into the physically adsorbed well on the Ir(110)-(1x2) surface also. Until additional surface spectroscopic work is performed with O₂ on Ir(110)-(1x2), particularly vibrational spectroscopy at low T_s, comparisons with Pt are the only alternative.

Also shown in Fig. 3 is a rapid increase in S₀ with increasing incident kinetic energy for E_i greater than approximately 4 kcal/mol.

This behavior is typical of that expected for dissociative chemisorption via a direct mechanism. A direct chemisorption mechanism has also been identified for oxygen chemisorption on Pt(111)¹² and on W(110)¹³.

The data shown in Fig. 3 are for two surface temperatures (150 and 300 K) and have virtually the same value of S_0 as a function of E_i indicating a lack of dependence on T_s . Such behavior is expected for dissociative chemisorption via a direct mechanism but it is somewhat atypical of chemisorption in the trapping-mediated regime. Figure 4 shows the initial probability of dissociative chemisorption as a function of surface temperature for two incident conditions. The upper data represented by a Δ are in the direct regime with $E_i=9.1\text{kcal/mol}$ and $\theta_i=15^\circ$ whereas the lower data are in the trapping-mediated regime with $E_i=980\text{cal/mol}$ and $\theta_i=45^\circ$. This figure is further evidence of a lack of surface temperature dependence on the initial probability of chemisorption. The decrease in S_0 for T_s greater than 500 K for the data in the trapping-mediated regime (lower data in Fig. 4) is most likely due to a decrease in the trapping probability as will be discussed shortly.

As mentioned previously the probability of trapping-mediated dissociative chemisorption can increase with T_s , decrease with T_s or be independent of surface temperature, depending on the details of the potential energy surface. Once the molecule is trapped it loses all memory of its prior gas-phase conditions and accommodates fully to the surface temperature. Thus the surface temperature

dependence of S_0 in the trapping-mediated regime arises from a kinetic competition between the dissociative chemisorption and desorption of the molecule from the trapped state. A simple kinetic model has been constructed that can account for this kinetic behavior for the relatively facile reactions of N_2 on $W(100)$ ^{14,23}, O_2 on $Pt(111)$ ¹² and C_2H_6 on $Ir(110)-(1 \times 2)$ ¹⁰ and the activated reactions of alkanes on $Pt(110)-(1 \times 2)$ ¹⁶ and Ni ¹⁷. However for systems where the activation barrier to desorption from the trapped state is equivalent to the activation barrier to dissociation from the trapped state there is no surface temperature dependence. Using the kinetic model mentioned above^{10,14,16,23} we estimate that the difference in the heights of the barriers to dissociate and desorb from the trapped state is approximately 100 cal/mol.

As mentioned previously the decrease in the initial probability of dissociative chemisorption for surface temperatures greater than 500 K as shown in Fig. 4 is probably due to a decrease in the trapping probability. Recently Rettner, et al.¹⁸ have made detailed measurements of the trapping of N_2 on $W(100)$ for T_s from 300 to 1000 K. These studies indicate that the trapping probability does decrease slightly ($\leq 20\%$) over this temperature range. Intuitively we would expect that the amount of decrease in the trapping probability for a given system would depend on the trapping well depth and the vibrational structure of the substrate. Additional work regarding the trapping of Ar on $Pt(111)$ as a function of surface temperature²⁹ support the weak but measurable dependence of the trapping probability on T_s .

Figure 5 shows S_0 as a function of incident angle for measurements in the trapping-mediated and direct regime. As clearly shown in Fig. 5 the value of the initial probability of dissociative chemisorption is independent of the incident angle for both the direct and the trapping-mediated regime. Also shown in Fig. 5 are predicted curves of the value of S_0 assuming normal energy scaling of the data. It is clear that normal energy scaling does not hold and that the system scales with total energy. The nature of the angular dependence on dissociative chemisorption as well as on trapping is poorly understood at the moment. Total energy scaling was found for N_2 activated dissociative chemisorption on $W(110)$ ¹ and explained by invoking a model³⁵ which scrambles the parallel and perpendicular components of momentum via relatively small corrugations in the molecule-surface interaction potential. However the activated dissociative chemisorption of H_2 on various Cu surfaces⁴ has been found to scale with normal energy. Trapping-mediated chemisorption of ethane on $Ir(110)-(1 \times 2)$ is found to nearly scale with total energy while the direct channel scales with normal energy¹⁰. Oxygen chemisorption on $W(110)$ ¹³ scales with normal energy but O_2 dissociative chemisorption on $Pt(111)$ ¹² scales between normal and total energy scaling. Clearly much more experimental and theoretical work is required to understand the nature of the angular dependence on dissociative chemisorption.

IV. SUMMARY

The results of a molecular beam investigation of the dynamics of the dissociative chemisorption of oxygen on Ir(110)-(1x2) in the limit of zero-coverage have been presented. We find that the initial dissociative chemisorption probability can be described by a trapping-mediated mechanism at low kinetic energies and by a direct mechanism at high kinetic energies. The value of S_0 is independent of the surface temperature except in the trapping-mediated regime for T_s greater than 500 K. Here the value of the initial probability of chemisorption decreases most likely due to a decrease in the trapping probability. We also find that the value of S_0 is insensitive to incident angle in both the trapping-mediated and the direct chemisorption regimes scaling with total energy.

This work was supported by the National Science Foundation under grant number CHE-8617826. Acknowledgment is also made to the Donors of the Petroleum Research Fund of the American Chemical Society for partial support of this research under grant number PRF 19819-AC5-C.

REFERENCES

1. D.J. Auerbach, H.E. Pfnur, C.T. Rettner, J.E. Schlaegel, J. Lee and R.J. Madix, *J. Chem. Phys.* **81**, 2515 (1984); H.E. Pfnur, C.T. Rettner, D.J. Auerbach, R.J. Madix and J. Lee, *ibid.* **85**, 7452 (1986).
2. C.T. Rettner, H.E. Pfnur and D.J. Auerbach, *Phys. Rev. Lett.* **54**, 2716 (1985).
3. S.T. Ceyer, *Ann. Rev. Phys. Chem.* **39**, 479 (1988).
4. M. Balooch, M.J. Cardillo, D.R. Miller and R.E. Stickney, *Surf. Sci.* **46**, 358 (1974).
5. M.B. Lee, Q.Y. Yang and S.T. Ceyer, *J. Chem. Phys.* **87**, 2724 (1987).
6. M.P. D'Evelyn, A.V. Hamza, G.E. Gdowski and R.J. Madix, *Surf. Sci.* **167**, 451 (1986).
7. A.C. Luntz and D.S. Bethune, *J. Chem. Phys.* **90**, 1274 (1989).
8. C.T. Rettner and H. Stein, *Phys. Rev. Lett.* **59**, 2768 (1987); *J. Chem. Phys.* **87**, 770 (1987).
9. G.R. Schoofs, C.R. Arumainayagam, M.C. McMaster and R.J. Madix, *Surf. Sci.* **215**, 1 (1989).
10. C.B. Mullins and W.H. Weinberg, *J. Chem. Phys.* (submitted).
11. A.V. Hamza, H.-P. Steinruck and R.J. Madix, *J. Chem. Phys.* **85**, 7494 (1986).
12. A.C. Luntz, M.D. Williams and D.S. Bethune, *J. Chem. Phys.* **89**, 4381 (1988).
13. C.T. Rettner, L.A. DeLouise and D.J. Auerbach, *J. Vac. Sci. Technol. A* **4**, 1491 (1986); *J. Chem. Phys.* **85**, 1131 (1986).
14. C.T. Rettner, H. Stein and E.K. Schweizer, *J. Chem. Phys.* **89**, 3337 (1988).

15. W.H. Weinberg, in Kinetics of Interface Reactions, edited by M. Grunze and H.J. Kreuzer, Springer Series in Surface Science, Vol. 8 (Springer-Verlag, Berlin, 1987), p. 94.
16. Y.-K. Sun and W.H. Weinberg, to be published.
17. A.G. Sault and D.W. Goodman, J. Chem. Phys. **88**, 7232 (1988).
18. C.T. Rettner, E.K. Schweizer, H. Stein and D.J. Auerbach, Phys. Rev. Lett. **61**, 986 (1988).
19. C. Wang and R. Gomer, Surf. Sci. **84**, 329 (1979).
20. A.C. Luntz, J. Grimblot and D.E. Fowler, Phys. Rev. B **39**, 12903 (1989).
21. J.L. Taylor, D.E. Ibbotson and W.H. Weinberg, Surf. Sci. **79**, 349 (1979).
22. C.B. Mullins, Y. Wang and W.H. Weinberg, J. Vac. Sci. Tech. A **7**, 2125 (1989).
23. D.A. King and M.G. Wells, Proc. R. Soc. London Ser. A **339**, 245 (1974).
24. W.H. Weinberg and R.P. Merrill, J. Vac. Sci. Technol. **8**, 718 (1971).
25. R.M. Logan and R.E. Stickney, J. Chem. Phys. **44**, 195 (1966).
26. J.C. Tully, Surf. Sci. **111**, 461 (1981).
27. C.T. Rettner, E.K. Schweizer and C.B. Mullins, J. Chem. Phys. **90**, 3800 (1989).
28. C.T. Rettner, D.S. Bethune and D.J. Auerbach, J. Chem. Phys. **91**, 1942 (1989).
29. C.B. Mullins, C.T. Rettner, D.J. Auerbach and W.H. Weinberg, to be published.

30. E.W. Kuipers, M.G. Tenner, M.E.M. Spruit and A.W. Kleyn, Surf. Sci. **205**, 241 (1988).
31. S. Andersson, L. Wilzen and J. Harris, Phys. Rev. Lett. **55**, 2591 (1985).
32. C.B. Mullins and W.H. Weinberg, to be published.
33. J.R. Engstrom, W. Tsai and W.H. Weinberg, J. Chem. Phys. **87**, 3104 (1987).
34. P.D. Szuromi, Ph.D. Thesis California Institute of Technology, 1985.
35. J.W. Gadzuk and S. Holloway, Chem. Phys. Lett. **114**, 314 (1985); S. Holloway and J.W. Gadzuk, J. Chem. Phys. **82**, 5203 (1985).

FIGURE CAPTIONS

Figure 1. Schematic of molecular beam apparatus for determining the probability of dissociative chemisorption. Key: C1-C3, differential pumping chambers for nozzle source (ns), GM, gas manifold, VG, valve for gas flow, VP, view port, sa, skimmer aperture, F, flag, a, aperture, BC, beam chopper, UHV, ultra-high vacuum scattering chamber, Ar⁺, argon ion gun, QMS, quadrupole mass spectrometer, AES, Auger electron spectrometer, LEED, low-energy electron diffraction optics. The single crystalline sample is held on a manipulator which can cool or heat the sample and rotates on an axis perpendicular to the molecular beam.

Figure 2. Schematic of the partial pressure of oxygen in the scattering chamber as a function of time during a beam reflectivity measurement. At t_0 the nozzle is filled with gas and at t_1 the flag is opened so that the beam impinges on the crystal surface. The partial pressure at t_1 is P_2 greater than the baseline partial pressure. As time proceeds the partial pressure approaches a value P_1+P_2 greater than the baseline and is steady after t_2 . This is because the surface is saturated with oxygen at this point and thus all oxygen molecules in the beam are reflected from the surface. Finally, at t_3 the flag is shut again.

Figure 3. The initial probability of dissociative chemisorption of O₂ on Ir(110)-(1x2) as a function of incident kinetic energy for $T_s=150$ K (\square) and for $T_s=300$ K (X) at normal incidence.

Figure 4. The initial probability of dissociative chemisorption of O_2 on Ir(110)-(1x2) as a function of surface temperature for $E_i=980$ cal/mol and $\theta_i=45^\circ$ (\square) and for $E_i=9.1$ kcal/mol and $\theta_i=15^\circ$ (Δ).

Figure 5. The initial probability of dissociative chemisorption of O_2 on Ir(110)-(1x2) as a function of incident angle for $E_i=9.1$ kcal/mol and $T_s=300$ K (\square) and $E_i=2.6$ kcal/mol and $T_s=225$ K (\circ). The X symbol and Δ symbol represent the values of S_0 at $E_i=9.1$ kcal/mol and $E_i=2.6$ kcal/mol, respectively, if normal energy scaling held. These values are obtained by interpolating between points on Fig. 3.

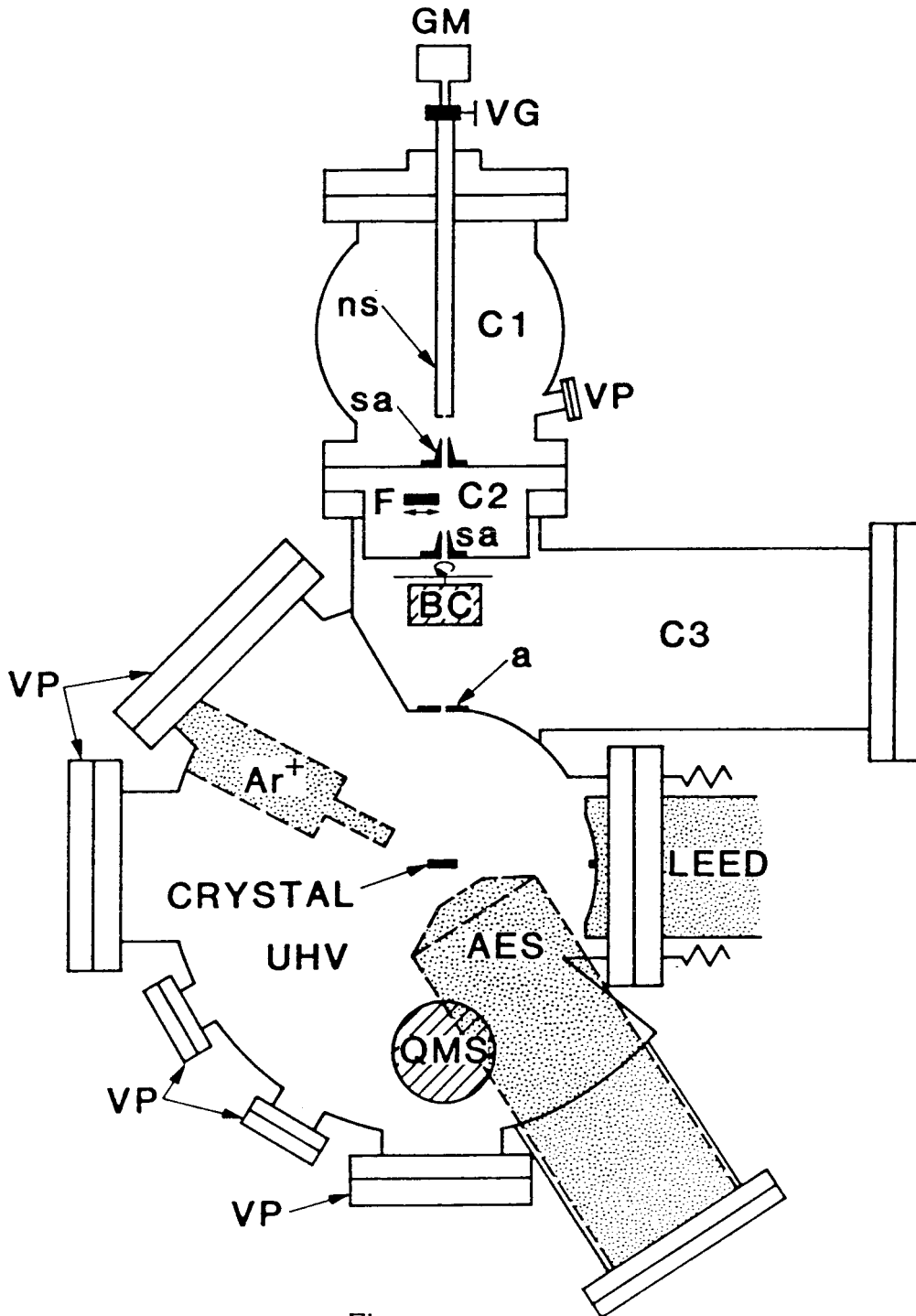


Figure 1

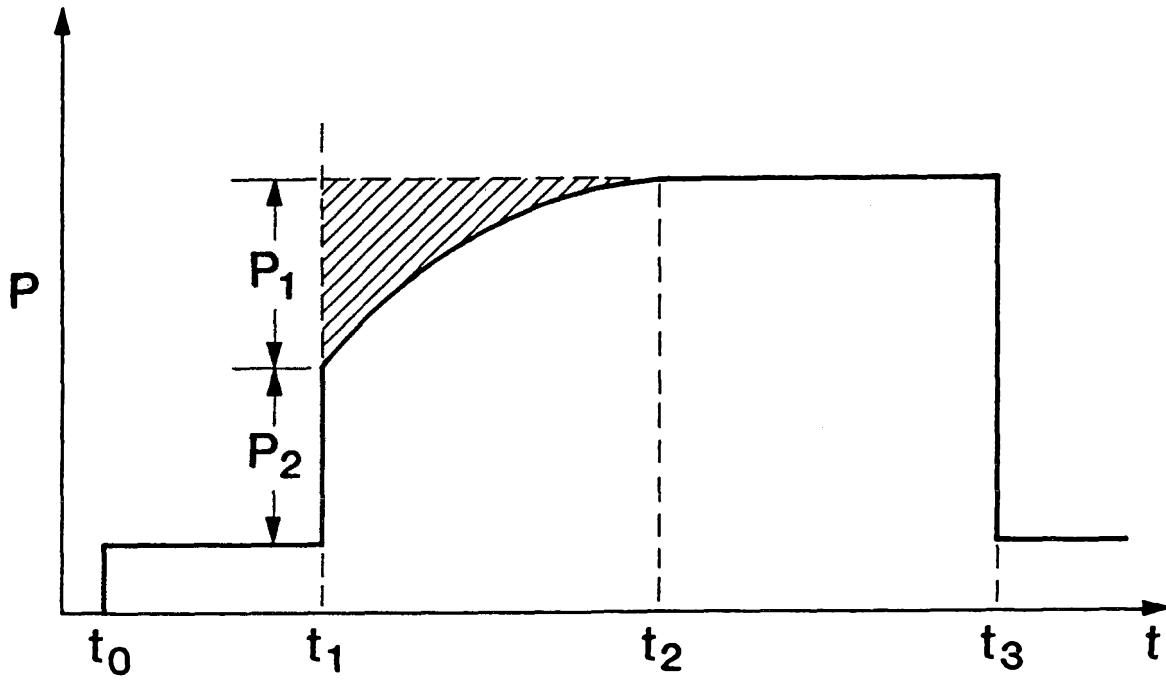


Figure 2

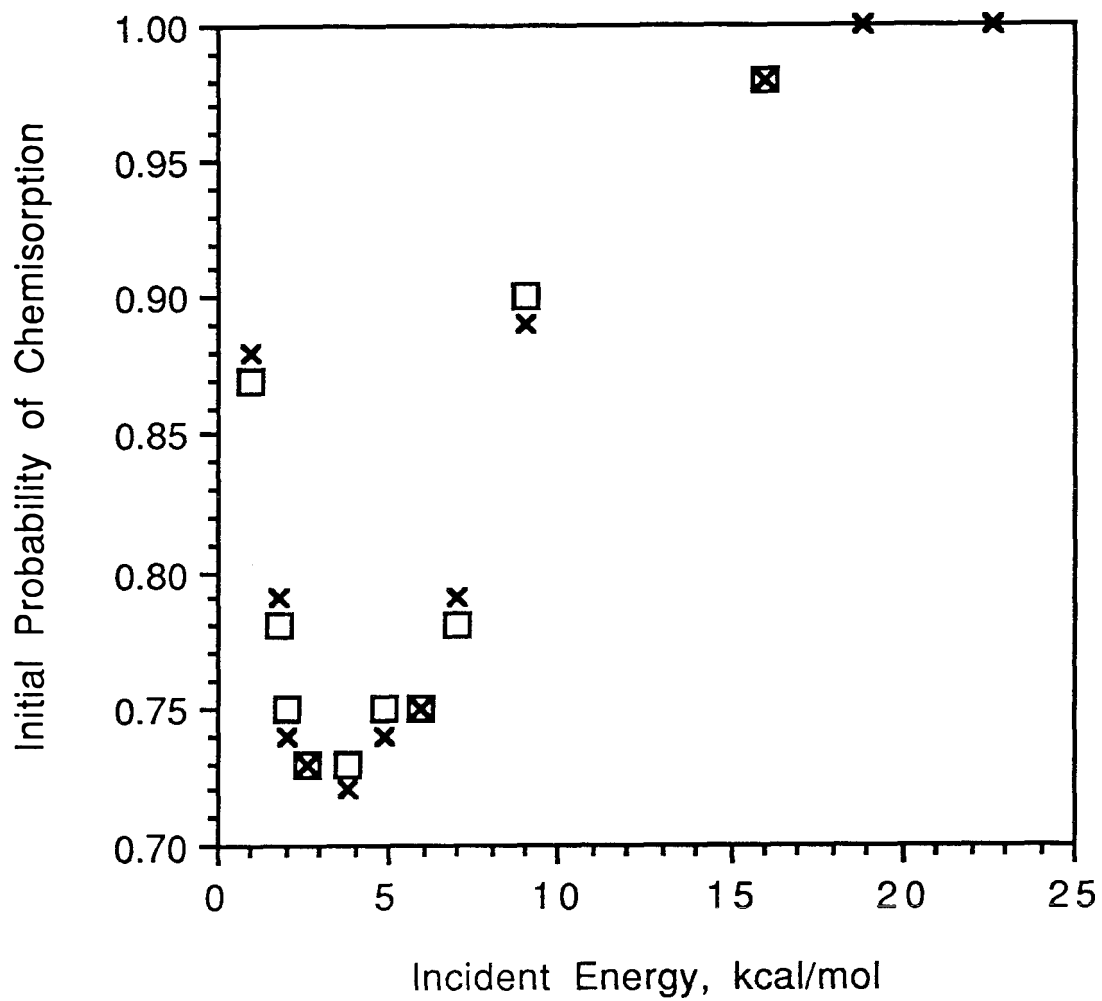


Figure 3

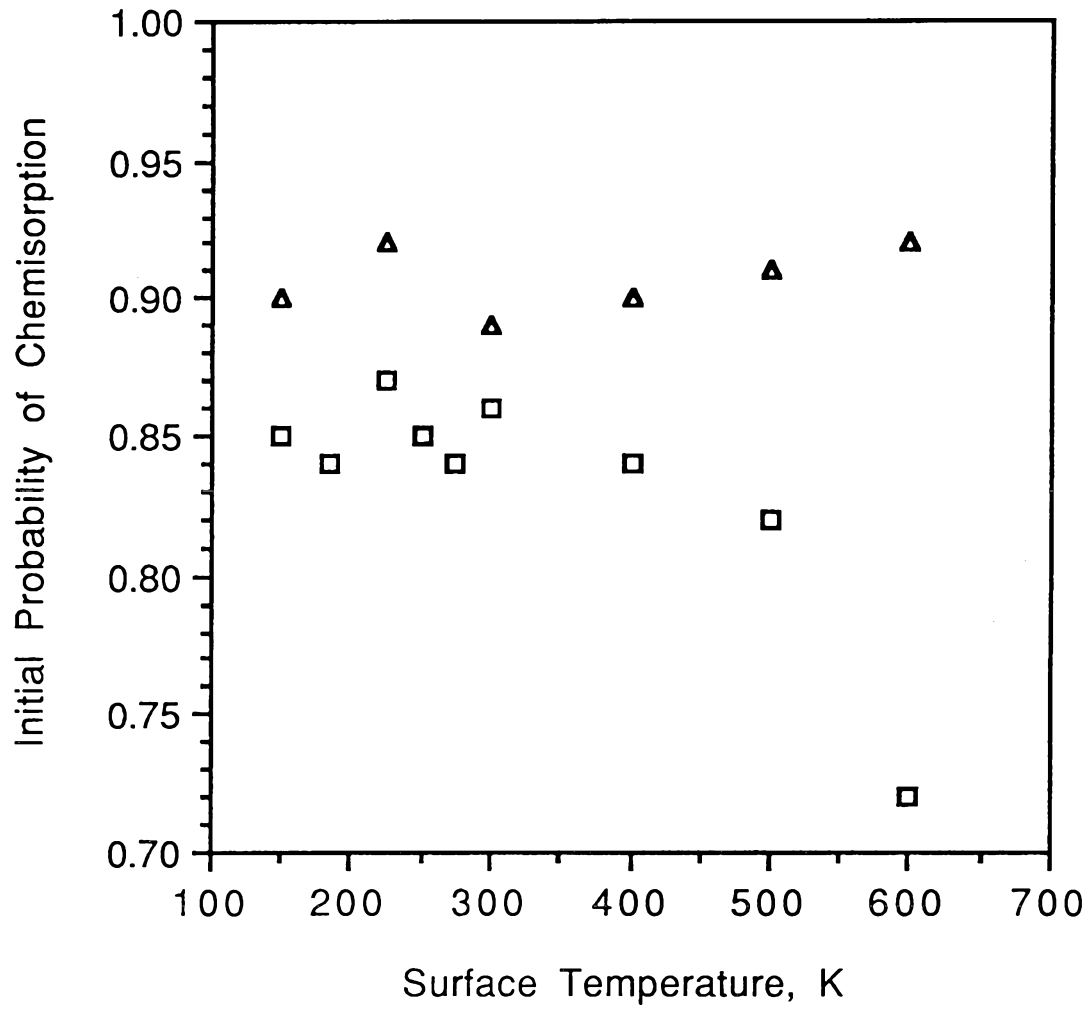


Figure 4

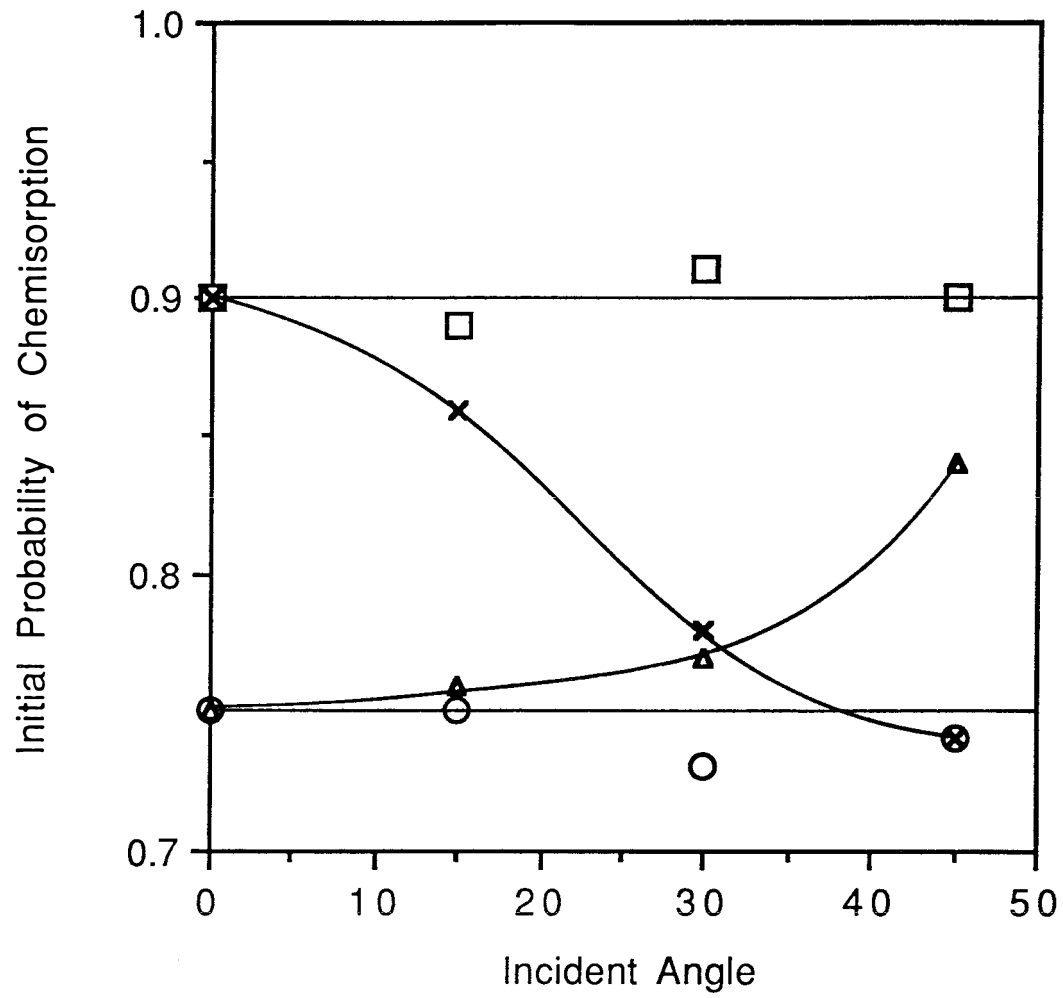


Figure 5

CHAPTER III

A MOLECULAR-BEAM STUDY OF THE DISSOCIATIVE CHEMISORPTION
OF O₂ ON Ir(110)-(1x2)

[The text of Chapter III consists of an article coauthored with Y. Wang and W.H. Weinberg, which has appeared in *J. Vac. Sci. Technol. A* 7, 2125 (1989).]

A molecular-beam study of the dissociative chemisorption of O₂ on Ir(110)-(1×2)

C. B. Mullins,^{a)} Y. Wang, and W. H. Weinberg
 Division of Chemistry and Chemical Engineering, California Institute of Technology,
 Pasadena, California 91125

(Received 14 October 1988; accepted 31 October 1988)

The zero-coverage probability of dissociative chemisorption of O₂ on Ir(110)-(1×2) has been measured using molecular-beam techniques for a wide range of incident kinetic energies, incident angles, and surface temperatures. The data indicate that a trapping-mediated mechanism is responsible for dissociative chemisorption at low energies, whereas at high energies a direct mechanism accounts for dissociative adsorption. Total energy scaling approximately describes the dissociative dynamics on the very corrugated Ir(110)-(1×2) surface.

Dissociative chemisorption on transition-metal surfaces is a key step in many industrially important heterogeneous catalytic reactions. The dynamics of dissociative chemisorption are currently poorly understood and an active area of research. In an effort to contribute further to an understanding of dissociative chemisorption, we have conducted a series of experiments to probe the interaction of molecular oxygen with the Ir(110)-(1×2) surface.

Two studies of oxygen chemisorption dynamics employing molecular beams have appeared recently. Rettner *et al.*¹ have studied the interaction of oxygen with a W(110) surface and concluded that the initial probability of adsorption depends strongly on the incident kinetic energy E_i , scaling with the normal energy $E_n = E_i \cos^2 \theta_i$, where θ_i is the angle of incidence. They also found some evidence for the existence of a weakly bound precursor to dissociative chemisorption at low incident kinetic energies. Williams *et al.*² have investigated the dynamics of dissociative adsorption of oxygen on Pt(111). They concluded that trapping-mediated chemisorption occurred for low incident energies and low surface temperatures, whereas at high incident kinetic energies a direct mechanism was likely the mechanism for chemisorption of oxygen. Taylor *et al.*³ have investigated the interaction of oxygen with Ir(110)-(1×2) previously, and their work provided motivation for this study. They used thermal desorption mass spectrometry, low-energy electron diffraction, and work function measurements, and concluded that the initial probability of chemisorption was independent of surface temperature T_s . They also concluded for T_s between 300 and 700 K that the adsorption kinetics could be described by a second-order precursor model.

Zero-coverage dissociative chemisorption measurements have been made using the reflectivity method (of King and Wells⁴) employing an apparatus that will be described in detail elsewhere.⁵ Briefly, the apparatus consists of a thrice differentially pumped supersonic molecular-beam source and ultrahigh vacuum scattering chamber. Low-energy electron diffraction optics, Auger electron spectroscopy, and an ion gun are mounted on the scattering chamber for obtaining and checking surface cleanliness and order. A quadrupole mass spectrometer is also mounted on the scattering chamber for thermal desorption mass spectrometry, reflectivity measurements, and beam time-of-flight measure-

ments. The source chambers contain the nozzle, a high-speed shutter, and a chopper for beam modulation as well as apertures for beam collimation. Both the scattering chamber and the third-beam chamber are pumped by turbomolecular pumps. The other two beam chambers are pumped by diffusion pumps. The Ir(110)-(1×2) sample is mounted on a manipulator in the scattering chamber which provides precise alignment of the sample in the beam. The manipulator is liquid nitrogen cooled, providing rapid cooling of the sample to 80 K. The sample temperature is determined from a 0.003-in. W/5% Re-W/26% Re thermocouple spotwelded to the back of the crystal. As mentioned above, the initial probability of adsorption data reported here have been determined by a beam reflectivity method similar to that of King and Wells.⁴ The partial pressure of oxygen in the scattering chamber is used as a measure of the flux of O₂ molecules that do not chemisorb. Initial chemisorption probabilities S_0 (corresponding to chemisorption at zero coverage) are thus determined by a comparison of the initial oxygen partial pressure, following the opening of the high-speed shutter, to the oxygen partial pressure from the beam scattering from the saturated surface. Beam energies are varied by a combination of seeding and variation of nozzle temperature, and are measured by time-of-flight techniques.

Figure 1 shows S_0 as a function of incident kinetic energy for an angle of incidence of 15° with respect to the surface normal and surface temperatures of 150 and 300 K. As E_i is increased from its lowest values, S_0 decreases from a relatively high value to a minimum at ~4 kcal/mol. Note that this occurs for the measurements at 150 K as well as those at 300 K. The data displayed in Fig. 2 support the insensitivity of S_0 to T_s . This figure shows S_0 vs T_s for an incident angle of 45° and total incident energy of 980 cal/mol, and an incident angle of 15° and E_i of 9.1 kcal/mol. A decrease in S_0 with increasing kinetic energy in the low-energy range is associated with a trapping- or precursor-mediated chemisorption mechanism, cf. Fig. 1. A similar decrease in S_0 with E_i in the low E_i regime for O₂/W(110),¹ O₂/Pt(111),² N₂/W(100),⁷ C₃H₈/Ir(110)-(1×2),⁸ and C₄H₁₀/Ir(110)-(1×2)⁸ has been observed before. However these systems displayed a strong sensitivity to surface temperature, with S_0 decreasing with increasing surface temperature. This type of behavior can be interpreted as follows: the trapping proba-

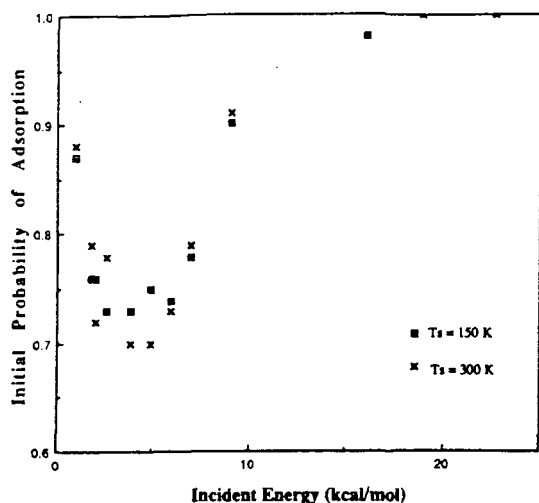


FIG. 1. The initial probability of dissociative chemisorption S_0 as a function of incident kinetic energy for $T_s = 150$ and 300 K, and incident angle of 15° .

bility into the precursor state is a strong function of E_i , decreasing with increasing E_i , but weakly influenced by T_s .⁹ Once a particle is in the precursor state it either desorbs or chemisorbs dissociatively, the temperature dependence of which depends on the kinetic parameters for desorption and dissociation.¹⁰ For the system under discussion, O₂/Ir(110)-(1×2), the relative insensitivity of S_0 to T_s at low E_i suggests that the activation energy for dissociation is nearly equal to the activation energy for desorption from the precursor or trapped state. The slight decrease in S_0 observed from 400 to 600 K is probably due to a decrease in the trapping probability.⁹ The insensitivity of S_0 to T_s at high E_i supports the assignment of a direct mechanism to dissociative chemisorption in this regime. Behavior of this type has been observed previously,^{1,7,8} but one should note that in the study by Williams *et al.*² S_0 was found to have a surface temperature dependence even at high E_i . The previous study of O₂/Ir(110)-(1×2) by Taylor *et al.*³ supports these conclusions in that S_0 was determined to be insensitive to T_s from 300 to 700 K. The fact that S_0 for the O₂/Ir(110)-(1×2) system is nearly insensitive to incident angle suggests near total energy scaling for the chemisorption dynamics of this system. This is not too surprising considering that the surface reconstructs into a very corrugated geometrical structure, providing a corrugated potential energy surface. Total energy scaling in dissociative chemisorption of a diatomic has been reported previously for the N₂/W(110) system⁶ and the N₂/W(100) system.⁷ Chemisorption probabi-

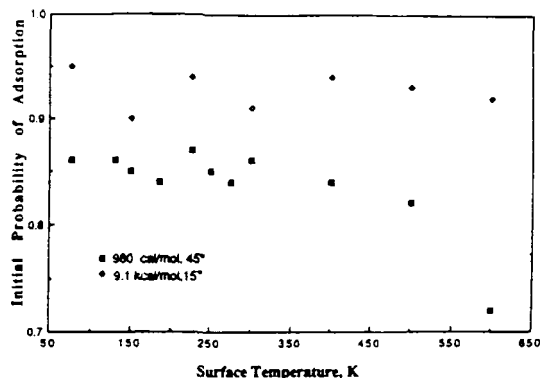


FIG. 2. The initial probability of dissociative chemisorption S_0 as a function of surface temperature for $E_i = 980$ cal/mol and $\theta = 45^\circ$, and for $E_i = 9.1$ kcal/mol and $\theta = 15^\circ$.

lities S' have also been determined as a function of coverage over a wide range of conditions. At low incident kinetic energies and low surface temperatures, S remains constant or decreases slowly for low coverages. This provides further supporting evidence for our assignment of a trapping-mediated chemisorption mechanism for the low E_i regime. A more complete description of the coverage dependence of the probability of dissociative chemisorption, as well as other details, will appear in a future publication.⁵

Acknowledgment: This work was supported by the National Science Foundation under Grant No. CHE-8617826.

¹ IBM Predoctoral Fellow.

² C. T. Rettner, L. A. DeLouise, and D. J. Auerbach, *J. Chem. Phys.* **85**, 1131 (1986); *J. Vac. Sci. Technol. A* **4**, 1491 (1986).

³ M. D. Williams, D. S. Bethune, and A. C. Luntz, *J. Chem. Phys.* **88**, 2843 (1988); *J. Vac. Sci. Technol. A* **6**, 788 (1988).

⁴ J. L. Taylor, D. E. Ibbotson, and W. H. Weinberg, *Surf. Sci.* **79**, 349 (1979).

⁵ D. A. King and M. G. Wells, *Surf. Sci.* **29**, 454 (1971).

⁶ C. B. Mullins, Y. Wang, and W. H. Weinberg (to be published).

⁷ D. J. Auerbach, H. E. Pfnür, C. T. Rettner, J. E. Schlaegel, J. Lee, and R. J. Madix, *J. Chem. Phys.* **81**, 2515 (1984).

⁸ C. T. Rettner, H. Stein, and E. K. Schweizer, *J. Chem. Phys.* **89**, 3337 (1988).

⁹ A. V. Hamza, H.-P. Steinrück, and R. J. Madix, *J. Chem. Phys.* **85**, 7494 (1986).

¹⁰ C. T. Rettner, E. K. Schweizer, H. Stein, and D. J. Auerbach, *Phys. Rev. Lett.* **61**, 986 (1988).

¹¹ W. H. Weinberg, in *Kinetics of Interface Reactions*, edited by M. Grunze and H. J. Kreuzer, Vol. 8 in Springer Series in Surface Science (Springer, Berlin, 1987), p. 94.

CHAPTER IV

TRAPPING OF MOLECULAR ETHANE ON THE Ir(110)-(1x2) SURFACE

[The text of Chapter IV consists of an article coauthored with W.H. Weinberg, which has been submitted to *The Journal of Chemical Physics*.]

Trapping of a gas-phase particle at a surface is fundamentally important and an elementary step in many physical and chemical processes. Yet there is a paucity of data available concerning the kinetic energy and angular dependence of trapping. Moreover, most of the extant data are from measurements of rare gas scattering¹⁻⁶ and extraction of thermally averaged trapping probabilities from accommodation coefficients⁷. The relevant dynamics regarding atomic versus molecular trapping are somewhat different. In both cases the particle must transfer sufficient normal kinetic energy to other degrees of freedom to remain bound. For a molecule-surface collision, transfer of kinetic energy to internal rotational and vibrational degrees of freedom is possible, as well as substrate excitations. Parallel momentum must ultimately be dissipated also to insure complete translational accommodation, and this is usually much slower than loss of normal momentum⁸. Although simple to discuss qualitatively, an accurate quantitative description of molecular trapping dynamics is very complicated to construct. Dynamical measurements of molecular trapping will increase our understanding of the role played by the excitation of various degrees of freedom and provide a benchmark for predictive schemes.

Our particular interest in studying the trapping of molecular ethane on Ir(110)-(1x2) was motivated by studies of trapping-mediated dissociative chemisorption in this same gas-surface system⁹. We present here the results of such a study employing a molecular beam apparatus. In particular, measurements of the trapping probability as a function of E_i , the incident kinetic energy

(1.2 - 17.3 kcal/mol), and θ_i , the incident angle (0° - 45°), at a surface temperature T_s of 77 K are presented and discussed.

Measurements of the trapping probability in the limit of zero surface coverage, ζ_0 , have been made using the reflectivity method of King and Wells¹¹ employing an apparatus that will be described in detail elsewhere⁹. Briefly, the apparatus consists of a thrice differentially pumped, supersonic molecular beam source and ultra-high vacuum scattering chamber. Low-energy electron diffraction optics, Auger electron spectroscopy and an ion gun are mounted on the scattering chamber for obtaining and checking surface cleanliness and order. A quadrupole mass spectrometer is also mounted on the scattering chamber for thermal desorption mass spectrometry, reflectivity measurements and beam time-of-flight measurements. The source chambers contain the nozzle, a high-speed shutter and a chopper for beam modulation, as well as apertures for beam collimation. Beam energies are varied by a combination of seeding and variation of the nozzle temperature (300-750 K), and are measured by time-of-flight techniques. With the beam-reflectivity method¹¹, the partial pressure of ethane in the scattering chamber is used as a measure of the flux of C_2H_6 that *does not adsorb*. Initial trapping probabilities are thus determined by a comparison of the initial ethane partial pressure following the opening of the high-speed shutter, to the ethane partial pressure from the beam scattered from a saturated surface.

At $T_s=77$ K all molecules that trap on the clean surface will remain physically adsorbed since the desorption temperature at low coverages of ethane on Ir(110)-(1x2) is approximately 150 K¹². This fact has been verified by also measuring ζ_0 at $T_s=90$ K and 110 K. There is no change in ζ_0 for $77 \text{ K} \leq T_s \leq 110 \text{ K}$, although there is a reduction in the saturation coverage with increasing T_s . Previous studies of the trapping of Ar on Pt(111)⁵ have shown ζ_0 to be sensitive to background contamination on the surface. Indeed, in the measurements reported here, ζ was observed to increase with coverage until near saturation¹³. The effect of background contaminants on the ζ_0 measurements reported here are insignificant since the base pressure in our scattering chamber is $\sim 1 \times 10^{-10}$ Torr, and the sample can be cooled from ~ 1620 K to 77 K in < 90 seconds. For normal kinetic energies ($E_i \cos^2 \theta_i$) ≥ 8 kcal/mol, there is a significant component of direct dissociative chemisorption. The measured values of the direct chemisorption component^{9,10} have been subtracted from the initial adsorption probabilities for the relevant measurements to obtain values for ζ_0 .

Figure 1 shows ζ_0 for ethane at three different incident angles as a function of $E_i \cos^{0.5} \theta_i$. The initial trapping probability decreases with increasing E_i since the molecule must dissipate a larger fraction of the normal component of its linear momentum. We find empirically that the data scale very well with $E_i \cos^{0.5} \theta_i$, as is apparent in Fig. 1. This suggests a rather corrugated interaction potential which is consistent with the corrugated geometrical structure of this reconstructed surface^{14,15}.

It is possible that the internal degrees of freedom of the molecule play a significant role in the dissipation of kinetic energy. The trapping probability of Xe interacting with Pt(111)⁶ for $\theta_i=0^\circ$ and $E_i=10$ kcal/mol ($\zeta_{o,Xe}\sim 0.1$) is lower than the trapping probability for ethane on Ir(110)-(1x2) for the same conditions ($\zeta_{o,C_2H_6}\sim 0.35$), even though Xe is much more massive than C_2H_6 and the well depths for physical adsorption of the two particles are nearly equal. However, at low E_i (~ 1 kcal/mol) ζ_o for both systems is nearly unity. Trajectory calculations for NO and N_2 scattering from Ag(111) performed by Tully and coworkers¹⁶⁻¹⁸ demonstrate that conversion of translational to rotational energy during impact makes a very important contribution to trapping for these systems. Additionally, Tully and Cardillo¹⁸ suggest that molecules with low-frequency vibrations can be expected to transfer vibrational energy easily to and from rotational, translational and surface vibrational motion. Intuitively, it is easy to visualize conversion of translational energy to rotational and vibrational energy, but the *relative* roles of the internal degrees of freedom of the impinging molecule and the substrate surface excitations are difficult to quantify. However, recent experimental and theoretical work regarding NO impinging on Ag(111)¹⁹ suggests that increasing rotational excitation is accompanied by decreasing energy transfer to phonons.

Further experimental and theoretical work is required in order to assess the significance of the observed scaling of ζ_o with

$E_i \cos^{0.5} \theta_i$ on Ir(110)-(1x2) and the role of internal degrees of freedom.

This work was supported by the National Science Foundation under grant number CHE-8617826. Acknowledgment is also made to the Donors of the Petroleum Research Fund of the American Chemical Society for partial support of this research under grant number PRF 19819-AC5-C.

REFERENCES

1. C.T. Rettner, E.K. Schweizer and C.B. Mullins, *J. Chem. Phys.* **90**, 3800 (1989).
2. J.E. Hurst, L. Wharton, K.C. Janda and D.J. Auerbach, *J. Chem. Phys.* **83**, 1376 (1985).
3. H.P. Steinruck and R.J. Madix, *Surf. Sci.* **185**, 36 (1987).
4. H. Schlichting, D. Menzel, T. Brunner, W. Brenig and J.C. Tully, *Phys. Rev. Lett.* **60**, 2515 (1988).
5. C.B. Mullins, C.T. Rettner, D.J. Auerbach and W.H. Weinberg, to be published.
6. C.T. Rettner and D.S. Bethune, to be published.
7. W.H. Weinberg and R.P. Merrill, *J. Vac. Sci. Tech.* **8**, 718 (1971).
8. J.C. Tully, *Faraday Discuss. Chem. Soc.* **80**, 291 (1985).
9. The direct chemisorption component is taken as the value of the (temperature independent) probability of dissociative chemisorption at $T_s=550$ K where trapping-mediated chemisorption is negligible, as discussed in C.B. Mullins and W.H. Weinberg, to be published.
10. Probabilities of direct chemisorption as a function of kinetic energy for ethane interacting with Ir(110)-(1x2) are also presented in A.V. Hamza, H.-P. Steinruck and R.J. Madix, *J. Chem. Phys.* **86**, 6506 (1987); and H.-P. Steinruck, A.V. Hamza and R.J. Madix, *Surf. Sci.* **173**, L571 (1986).
11. D.A. King and M.G. Wells, *Proc. Royal Soc. London A* **339**, 245 (1974).

12. T.S. Wittrig, P.D. Szuromi and W.H. Weinberg, *J. Chem. Phys.* **76**, 3305 (1982).
13. H.C. Kang, C.B. Mullins and W.H. Weinberg, *J. Chem. Phys.* (submitted).
14. C.-M. Chan, M.A. Van Hove, W.H. Weinberg and E.D. Williams, *Surf. Sci.* **91**, 440 (1980).
15. M.A. Van Hove, W.H. Weinberg and C.-M. Chan, *Low-Energy Electron Diffraction*, Springer-Verlag, Berlin, 1986.
16. C.W. Muhlhausen, L.R. Williams and J.C. Tully, *J. Chem. Phys.* **83**, 2594 (1985).
17. J.C. Tully, C.W. Muhlhausen and L.R. Ruby, *Ber. Bunsenges. Phys. Chem.* **86**, 433 (1982).
18. J.C. Tully and M.J. Cardillo, *Science* **223**, 445 (1984).
19. J. Kimman, C.T. Rettner, D.J. Auerbach, J.A. Barker and J.C. Tully, *Phys. Rev. Lett.* **57**, 2053 (1986).

FIGURE CAPTION

Figure 1. Trapping probability as a function of $E_i \cos^{0.5} \theta_i$ (kcal/mol) for ethane on Ir(110)-(1x2) at $T_s=77$ K for θ_i of 0° (\square), 22.5° ($+$) and 45° (Δ). Experimental uncertainties⁹ in ζ_0 range from ± 0.020 to ± 0.040 with an average uncertainty for all 23 measurements of ± 0.029 . The azimuthal orientation of the sample is such that an [001] vector lying in the plane of the sample surface is $\sim 15^\circ$ from the axis of rotation of the manipulator (i.e., the polar axis). The inset shows the same data plotted versus the total incident kinetic energy E_i .

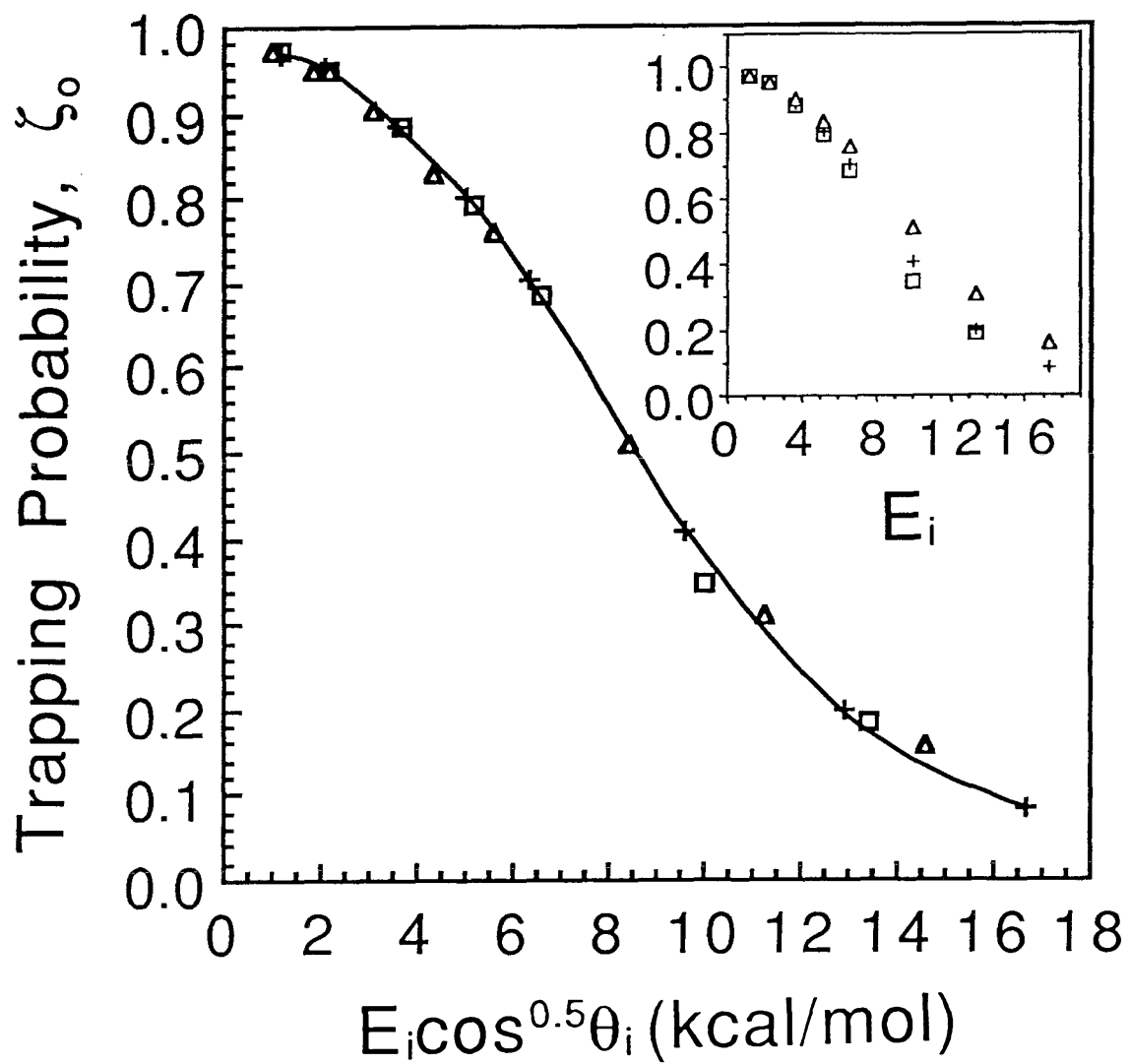


Figure 1

V - 1

CHAPTER V

TRAPPING-MEDIATED DISSOCIATIVE CHEMISORPTION OF ETHANE
ON Ir(110)-(1x2)

[The text of Chapter V consists of an article coauthored with W.H. Weinberg, which has been submitted to *The Journal of Chemical Physics*.]

ABSTRACT

Evidence is presented to support a trapping-mediated dissociative chemisorption mechanism for ethane interacting with an Ir(110)-(1x2) surface. The data were obtained from supersonic molecular beam measurements with an incident kinetic energy E_i ranging between 1.2 and 24.1 kcal/mol, a surface temperature T_s between 154 and 500K, and an incident angle θ_i between 0° and 45° . For E_i less than approximately 13 kcal/mol, the probability of dissociative chemisorption S_0 decreases rapidly with increasing T_s . For a surface temperature of 154 K, S_0 decreases with increasing E_i for $1.2 \leq E_i \leq 13.4$ kcal/mol, consistent with a trapping-mediated chemisorption mechanism. Indeed, the data support quantitatively a kinetic model consistent with a trapping-mediated chemisorption mechanism. The difference in the activation energies for desorption and chemisorption from the physically adsorbed, trapped state $E_d - E_c$ is 2.2 ± 0.2 kcal/mol. In the trapping-mediated regime, S_0 is found to be rather insensitive to incident angle, scaling with $E_i \cos^{0.5} \theta_i$.

I. INTRODUCTION

Although dissociative chemisorption of a gas-phase molecule on a metal surface is one of the "simpler" surface chemical processes and an important step in many industrial catalytic reactions, the dynamics and energetics of this class of chemical reactions are currently only poorly understood. This is due in part to the inherent theoretical difficulties in describing molecule-surface interactions accurately, and also because there have been relatively few fundamental studies of the dynamics of dissociative chemisorption. Current understanding of dissociative chemisorption on a bare metal surface involves two distinct mechanisms: a direct mechanism¹⁻⁴ and a mechanism mediated by trapping of the incident particle in a molecularly adsorbed state^{1,5-9}. In the trapping-mediated case, the molecule must lose sufficient energy to become trapped in a molecularly bound, adsorbed state after a collision with the surface. The molecule remains in this molecularly bound state until it either desorbs from the surface or reorientates into an appropriate configuration for dissociation to occur. Trapping-mediated chemisorption is thought to be an important mechanism in industrial catalytic processes, which are often activated, because of the relatively low kinetic energies of the gaseous reactants. In the case of the direct mechanism, dissociation occurs upon impact with the surface if the molecule has sufficient energy to surmount any activation barriers extant.

Heretofore, most molecular beam studies of chemisorption dynamics have focused on dissociative chemisorption by the direct mechanism. The primary thrust of this earlier work has been to study the effect of incident kinetic energy and angle on the initial probability of dissociative chemisorption for systems with an activation barrier^{1-4,10-13}. These studies have contributed significantly to a clearer understanding of the nature of the barrier to chemisorption for the systems studied. For these systems the probability of dissociative chemisorption increases with increasing kinetic energy. Variation of the incident angle also provides information regarding the potential energy surface of interaction by providing, for example, a systemization of the scaling relationship that exists between the probability of dissociation and the incident kinetic energy. These studies demonstrated also that the probability of direct dissociative chemisorption is typically a weak function of surface temperature.

The microscopic phenomena that are expected to be relevant for trapping-mediated dissociative chemisorption are rather different, and variations in the incident kinetic energy and angle will provide quantitative information reflecting these differences. In particular, a variation of these two parameters will probe the dynamics and energy transfer processes by which the molecule traps, permitting it to enter and remain in a weakly bound potential well. Intuitively, one would expect that the trapping probability ζ_0 of a particle impinging on a bare surface would decrease with increasing kinetic energy E_i , since a greater fraction of the incident

energy must be dissipated. Indeed, several experimental studies of the trapping dynamics of rare gases and molecules have shown this to be the case¹⁴⁻¹⁷. A molecule would be expected to trap more readily than a rare gas atom with the same heat of physical adsorption, since translational energy can be converted to rotational and vibrational energy in the molecular case, in addition to substrate excitations^{14,18-20}. Additionally, there is frequently a strong dependence on surface temperature T_s in trapping-mediated chemisorption due to the kinetic competition between desorption and dissociative chemisorption from the trapped state. How the trapping probability scales with incident angle is less intuitive, although several experimental studies with both rare gases and molecules have shown it to be between normal ($E_i \cos^2 \theta_i$) and total energy scaling¹⁴⁻¹⁷. Although experimental studies of these phenomena are of great practical and fundamental interest, only recently have relevant dynamical data appeared in the literature²¹⁻²⁸. Traditionally, the evidence for *precursor-mediated* chemisorption has been the insensitivity of the probability of chemisorption to adsorbate coverage⁹. This experimental observation is explained by assuming that an impinging molecule can trap efficiently on an *occupied* site with subsequent migration to an empty site^{9,29}. In this work we distinguish between on the one hand phenomena occurring within the traditional framework of precursor-mediated chemisorption and on the other hand dissociative chemisorption in the limit of zero-coverage, mediated by trapping of the molecule in a molecularly adsorbed state with subsequent molecular desorption or reorientation into a configuration more

favorable for chemisorption (i.e., trapping-mediated chemisorption). Indeed, we concentrate here on the latter point of view.

In a study of the dissociative chemisorption of O_2 on W(110) employing an effusive molecular beam source with T_s ranging from 20 to 1000K, Wang and Gomer⁷ demonstrated that the probability of chemisorption was insensitive to the adsorbate coverage at low surface temperatures. A molecular beam study by Rettner et al.²⁵ of both the initial and the coverage-dependent dissociative adsorption for this system has not supported assignment of either a trapping-mediated or a precursor-mediated mechanism of chemisorption for T_s between 280 and 800K. In fact, the initial probability of dissociative chemisorption S_0 increases rapidly with increasing E_i from 2.3 to 11.5 kcal/mol and was explained to be due to a direct dissociation mechanism. Only weak indirect evidence for *trapping-mediated* dissociative chemisorption was found for kinetic energies less than 1.1 kcal/mol.

The $N_2/W(100)$ system is recognized^{8,30-32} as a system exhibiting *precursor-mediated* chemisorption. In a well-documented dynamical study, Rettner et al.²⁶ found strong supporting evidence for both trapping-mediated and precursor-mediated chemisorption of N_2 on W(100). Finally and particularly relevant to our work are the molecular beam results of Hamza et al.²¹ regarding propane and butane dissociation on Ir(110)-(1x2). Evidence for trapping-mediated chemisorption at low values of E_i and a direct mechanism

at high E_i was presented, similar to the results reported here for ethane.

This paper is a presentation and discussion of data concerning the interaction of ethane with the Ir(110)-(1x2) surface employing a molecular beam apparatus. In an earlier thermal desorption study³³, evidence was presented for molecular adsorption of ethane on Ir(110)-(1x2) at 100K. Subsequent heating caused C-H bond cleavage at approximately 130K in some of the adsorbed ethane with the remainder desorbing. The activation energy for C-H bond cleavage was estimated to be approximately 6-7 kcal/mol with respect to the bottom of the well for physical adsorption, the depth of which is approximately 8-9 kcal/mol. In a recent molecular beam study of ethane activation on Ir(110)-(1x2) using a beam reflectivity technique, Steinruck et al.³⁴ concluded that there was no evidence for trapping-mediated dissociative chemisorption for surface temperatures between 300 and 1400K. In the work we report here, we find strong evidence indicating that a trapping-mediated mechanism dominates the dissociative chemisorption of ethane on Ir(110)-(1x2) for surface temperatures between 154 and 250K and for E_i between 1.2 and 13.4 kcal/mol. As expected for a trapping mediated reaction, S_0 decreases with increasing E_i (up to approximately 13 kcal/mol). We also find for trapping-mediated chemisorption that S_0 is relatively insensitive to incident angle, nearly scaling with total energy; whereas the direct chemisorption channel scales with normal energy^{34,35}.

II. EXPERIMENTAL METHODS

Measurements of the probability of dissociative chemisorption in the limit of zero surface coverage have been made using the reflectivity method of King and Wells³⁶, employing an apparatus that will be described in detail elsewhere²⁸. Briefly, the apparatus consists of a thrice differentially pumped, supersonic molecular beam source and ultrahigh vacuum scattering chamber. Low-energy electron diffraction optics, Auger electron spectroscopy and an ion gun are mounted on the scattering chamber for obtaining and verifying surface cleanliness and order. A quadrupole mass spectrometer is also mounted on the scattering chamber for thermal desorption mass spectrometry, reflectivity measurements and beam time-of-flight measurements. The source chambers contain the nozzle, a high-speed shutter, a chopper for beam modulation, and apertures for beam collimation. Both the scattering chamber and the third beam chamber are pumped by turbomolecular pumps; the other two beam chambers are pumped by diffusion pumps. The single crystalline sample was cut from a boule that was oriented with a Laue diffractometer and then polished using standard techniques. The Ir(110)-(1x2) sample is mounted on a manipulator in the scattering chamber, which provides precise alignment of the crystal in the beam. The azimuthal orientation of the sample is such that an [001] vector lying in the plane of the sample surface is approximately 15° from the axis of rotation of the manipulator (i.e. the polar angle). The crystal is cleaned in vacuum by occasional argon ion bombardment and routine annealing in oxygen. Sharp LEED

patterns and negligible contamination as judged by Auger spectroscopy are obtained easily with this procedure. The manipulator is liquid nitrogen cooled, providing rapid cooling of the sample to below 80K. The sample temperature is determined by a 0.003 in. W/5%Re-W/26%Re thermocouple that is spot welded to the back of the crystal.

As mentioned above, the data reported here for the initial probability of adsorption were determined by a beam reflectivity method similar to that of King and Wells³⁶. With this method the partial pressure of ethane in the scattering chamber is used as a measure of the flux of C₂H₆ molecules that do not chemisorb. There is no significant steady-state accumulation of physically adsorbed ethane for any of the experimental conditions reported here. Initial probabilities of chemisorption are determined by a comparison of the initial ethane partial pressure, following the opening of the high-speed shutter, to the ethane partial pressure from the beam scattering from the saturated surface. The kinetic energies of the beam are varied by a combination of seeding and variation of nozzle temperature, and are measured by time-of-flight techniques.

III. RESULTS AND DISCUSSION

Figure 1 shows the initial probability of dissociative chemisorption of ethane on the Ir(110)-(1x2) surface as a function of incident kinetic energy, parametric in surface temperature. For a given surface temperature ($T_s \leq 250\text{K}$), S_0 decreases as E_i increases,

which is consistent with trapping-mediated chemisorption and completely different from that which is expected for direct chemisorption. As mentioned earlier, the trapping probability should decrease with increasing E_i since the fraction of kinetic energy dissipation that is required to trap will increase. A simple model illustrates the idea: trapping will occur when the fraction of incident kinetic energy that is dissipated upon impingement is greater than $E_i/(E_i+\epsilon)$, where ϵ is an effective attractive well depth³⁷. The shape of the $S_0(E_i)$ curve for $T_s=154\text{K}$ and $E_i\leq 10$ kcal/mol is very similar to that for the trapping of molecular ethane on Ir(110)-(1x2) at 77K¹⁴. Also apparent in Fig. 1 is the strong dependence of S_0 on T_s , especially at relatively low incident kinetic energies. For E_i greater than approximately 13 kcal/mol, S_0 increases with increasing E_i , and there is a significantly weaker dependence on surface temperature. In this higher energy regime, the primary (but not exclusive) mechanism for dissociative chemisorption is the direct mechanism^{34,35}.

As may be seen in Fig. 1, the value of S_0 is a function of T_s at each value of the impact energy. The functional dependence is stronger at lower kinetic energies, since this is the regime in which the trapping-mediated channel of chemisorption is dominant. The probability of trapping-mediated dissociative chemisorption can either be independent of temperature, increase with T_s or decrease with T_s , depending on the details of the potential energy surface. A simple model serves to explain the temperature dependence of the trapping-mediated chemisorption of ethane on Ir(110)-(1x2). A gas-

phase molecule which impinges on the clean surface traps with a probability of ζ_0 . Once the ethane molecule is trapped in the physically adsorbed state, it loses all "memory" of its prior gas-phase conditions and accommodates fully to the surface temperature. A particle in this weakly bound, trapped state will eventually either desorb or chemisorb. Here we are concerned with chemisorption in the zero coverage limit, and there is negligible accumulation of physically adsorbed ethane at the surface temperatures at which measurements were carried out. Thus, the rates of chemisorption and desorption from the trapped molecular state are extremely rapid compared to the ethane impingement rate. In this case the probability of dissociative chemisorption for the trapping-mediated component in the zero-coverage limit can be written as

$$S_0 = \zeta_0 k_c / (k_c + k_d), \quad (1)$$

where k_d is the rate coefficient of desorption, and k_c is the rate coefficient of dissociative chemisorption from the physically adsorbed state. Equation (1) can be rewritten as

$$S_0 = \zeta_0(E_i, \theta_i, T_s) / [1 + (k_d^{\circ} / k_c^{\circ}) \exp\{(E_c - E_d) / k_B T_s\}], \quad (2)$$

where k_d° and k_c° are the preexponential factors of the two rate coefficients, and E_d and E_c are the corresponding activation energies. In Eq. (2) the trapping probability is written explicitly as a function of E_i , θ_i and T_s . However, we assume surface-temperature

independence here since a recent study by Rettner et al.³⁸ of N₂ trapping on W(100) indicates that varying T_s from 300 to 1000K decreases ζ₀ by less than 20 %.

A verification of this kinetic model would be provided if a plot of $\ln[(\zeta_0/S_0) - 1]$ as a function of $1/T_s$ were linear. For such a case the slope of the line would be equal to $(E_c - E_d)/k_B$, the difference in the activation energies for dissociative chemisorption and desorption from the physically adsorbed well divided by the Boltzmann constant. Figure 2 is such a plot of data for several values of E_i and θ_i , for which the measured values of ζ_0 ¹⁴ are used in evaluating the ordinate. It is clear that a straight line provides a good fit to all of the data over an extremely wide range of measurements (the ordinate spans a factor of more than two orders of magnitude and the abscissa a ΔT_s of 350K), providing strong support for the proposed trapping-mediated chemisorption model. The slope of this line corresponds to a value for $E_d - E_c$ of 2.2 ± 0.2 kcal/mol³⁹. Since the depth of the physical adsorption well for ethane is approximately 8.0 to 9.0 kcal/mol, the activation barrier to reaction from the physically adsorbed state is approximately 5.8 to 6.8 kcal/mol, in excellent agreement with the earlier study by Wittrig et al.³³ The value of the ratio of preexponential factors is equal to $k_d^{\ddagger}/k_c^{\ddagger} \approx 390 \pm 100$.³⁹ A ratio of $k_d^{\ddagger}/k_c^{\ddagger}$ that is greater than unity is expected since, entropically, desorption is favored over dissociation due to the limited phase space in which dissociation can occur compared to desorption.

Figure 3 shows S_0 as a function of incident angle θ_i , measured with respect to the surface normal, for two combinations of kinetic energy and surface temperature. For trapping-mediated dissociative chemisorption, the scaling is $E_i \cos^{0.5} \theta_i$; whereas the direct channel of dissociative chemisorption scales with normal energy. For $E_i=10.0$ kcal/mol and $T_s=154$ K, Fig. 3 shows the trapping-mediated component of S_0 to increase slightly with increasing incident angle⁴⁰. As clearly shown by the upper curve in Fig. 3 (labeled " $E_i \cos^2 \theta_i$ Scaling"), normal-energy scaling does not hold; whereas $E_i \cos^{0.5} \theta_i$ scaling describes the measured data very well. The increase in S_0 with increasing θ_i is due to an enhancement in the trapping probability, which also scales as $E_i \cos^{0.5} \theta_i$.¹⁴ Indeed, the trapping-mediated component of dissociative chemisorption scales as $E_i \cos^{0.5} \theta_i$ *because* the trapping probability scales in this manner. This conclusion is verified by the excellent fit of the model embodied by Eqs. (1) and (2) to the experimental data, as shown in Fig. 2. In these equations the "dynamics" are contained in the $\zeta_0(E_i, \theta_i, T_s)$ term and the "kinetics" in the $k_c/(k_c + k_d)$ term. Thus we would expect the scaling law to be contained in the trapping probability. This relative insensitivity to incident angle is consistent with other recent studies of trapping. In trapping studies of argon conducted on hydrogen precovered W(100)¹⁵ and clean Pt(111)¹⁶ surfaces, it was also found that the trapping probability did not scale with normal energy. Indeed, the trapping of N_2 on W(100) has been found to scale with total energy²⁶.

Also shown in Fig. 3 are data for purely direct dissociative chemisorption ($E_i=20.9$ kcal/mol and $T_s=500$ K). which support a normal-energy scaling assignment^{34,35}. The predicted values of S_0 shown in Fig. 3 for both normal energy scaling (the lower + symbol) and $E_i \cos^{0.5} \theta_i$ scaling (the lower x symbol) at $E_i=20.9$ kcal/mol and $T_s=500$ K are based solely on data displayed in Fig. 1. At this kinetic energy and surface temperature, the trapping-mediated component is negligible. It is clear from Fig. 3 that normal-energy scaling accurately describes the direct chemisorption channel. Normal energy scaling is very common for direct, dissociative chemisorption in activated systems^{3,4}; although the direct dissociative chemisorption of N_2 on both $W(110)^2$ and $W(100)^{26}$ scales with total energy.

IV. SYNOPSIS

Evidence, obtained from an experimental study employing a molecular beam apparatus, has been presented which supports a trapping-mediated mechanism of chemisorption for ethane interacting with an $Ir(110)-(1 \times 2)$ surface. At low incident kinetic energies, the probability of dissociative chemisorption decreases with increasing E_i , as would be expected for a trapping-mediated mechanism. Moreover, the form of $S_0(E_i)$ for $T_s=154$ K and $E_i \leq 10$ kcal/mol, is very similar to that for the trapping of molecular ethane on $Ir(110)-(1 \times 2)$ at 77K¹⁴. The value of the probability of dissociative chemisorption depends on the surface temperature at all measured values of incident kinetic energy. However, the

functional dependence is stronger at lower impact energies, since this is the regime in which trapping-mediated chemisorption is dominant.

The data support quantitatively a kinetic model that embodies a trapping-mediated mechanism of chemisorption. The measurements indicate that the activation barrier to dissociation from the trapped (physically adsorbed) state E_c is approximately 5.8 to 6.8 kcal/mol, whereas the depth of the physical adsorption well E_d is approximately 8.0 to 9.0 kcal/mol. The difference between these two energies, $E_d - E_c$, was measured accurately and found to be 2.2 ± 0.2 kcal/mol.

The trapping-mediated component of dissociative chemisorption increases with increasing incident angle and scales as $E_i \cos^{0.5} \theta_i$. The increase in S_o with increasing θ_i is due to an enhancement in the trapping probability, which also scales as $E_i \cos^{0.5} \theta_i$.¹⁴ Indeed, the trapping-mediated component of S_o scales as $E_i \cos^{0.5} \theta_i$ because the trapping probability scales in this manner. At higher kinetic energies direct dissociative chemisorption was observed, the probability of which scales with the normal component of the kinetic energy.

ACKNOWLEDGMENTS

This work was supported by the Office of Basic Energy Sciences of the Department of Energy under grant number DE-FG03-

89ER14048. Acknowledgment is also made to the Donors of the Petroleum Research Fund of the American Chemical Society for partial support of this research under grant number PRF 19819-AC5-C. We wish to thank Mr. Y.-Q. Wang for experimental assistance and Dr. J. R. Engstrom for many useful discussions.

REFERENCES

1. J.A. Barker and D.J. Auerbach, Surf. Sci. Rep. **4**, 1 (1984).
2. D.J. Auerbach, H.E. Pfnur, C.T. Rettner, J.E. Schlaegel, J. Lee and R.J. Madix, J. Chem. Phys. **81**, 2515 (1984); H.E. Pfnur, C.T. Rettner, D.J. Auerbach, R.J. Madix and J. Lee, *ibid.* **85**, 7452 (1986).
3. C.T. Rettner, H.E. Pfnur and D.J. Auerbach, Phys. Rev. Lett. **54**, 2716 (1985).
4. S.T. Ceyer, Ann. Rev. Phys. Chem. **39**, 479 (1988).
5. I. Langmuir, Chem. Rev. **6**, 451 (1929); J.B. Taylor and I. Langmuir, Phys. Rev. **44**, 23 (1933).
6. G. Ehrlich, J. Phys. Chem. Solids **1**, 3 (1956).
7. C. Wang and R. Gomer, Surf. Sci. **84**, 329 (1979).
8. D.A. King and M.G. Wells, Proc. Royal Soc. London, Ser. A **339**, 245 (1974).
9. W.H. Weinberg, in Kinetics of Interface Reactions, Eds., M. Grunze and H.J. Kreuzer, Springer Series in Surface Science, Vol. 8 (Springer-Verlag, Berlin, 1987), p. 94.
10. M. Balooch, M.J. Cardillo, D.R. Miller and R.E. Stickney, Surf. Sci. **46**, 358 (1974).
11. M.B. Lee, Q.Y. Yang and S.T. Ceyer, J. Chem. Phys. **87**, 2724 (1987).
12. M.P. D'Evelyn, A.V. Hamza, G.E. Gdowski and R.J. Madix, Surf. Sci. **167**, 451 (1986).
13. A.C. Luntz and D.S. Bethune, J. Chem. Phys. **90**, 1274 (1989).
14. C.B. Mullins and W.H. Weinberg, J. Chem. Phys. (submitted).

15. C.T. Rettner, E.K. Schweizer and C.B. Mullins, *J. Chem. Phys.* **90**, 3800 (1989).
16. C.B. Mullins, C.T. Rettner, D.J. Auerbach and W.H. Weinberg, to be published.
17. C.T. Rettner and D.S. Bethune, *J. Chem. Phys.* (in press).
18. J.C. Tully and M.J. Cardillo, *Science* **223**, 445 (1984).
19. J.C. Tully, C.W. Muhlhausen and L.R. Ruby, *Ber. Bunsenges. Phys. Chem.* **86**, 433 (1982).
20. C.W. Muhlhausen, L.R. Ruby and J.C. Tully, *J. Chem. Phys.* **83**, 2594 (1985).
21. A.V. Hamza, H.-P. Steinruck and R.J. Madix, *J. Chem. Phys.* **85**, 7494 (1986).
22. M.D. Williams, D.S. Bethune and A.C. Luntz, *J. Chem. Phys.* **88**, 2843 (1988).
23. D.A. King, *CRC Crit. Rev. Solid State Mater. Sci.* **167**, 451 (1978).
24. K.C. Janda, J.E. Hurst, C.A. Becker, J.P. Cowin, L. Wharton and D.J. Auerbach, *Surf. Sci.* **93**, 270 (1980).
25. C.T. Rettner, L.A. DeLouise and D.J. Auerbach, *J. Vac. Sci. Technol. A* **4**, 1491 (1986); *J. Chem. Phys.* **85**, 1131 (1986).
26. C.T. Rettner, H. Stein and E.K. Schweizer, *J. Chem. Phys.* **89**, 3337 (1988).
27. C.B. Mullins, Y. Wang and W.H. Weinberg, *J. Vac. Sci. Tech. A* **7**, 2125 (1989).
28. C.B. Mullins and W.H. Weinberg, to be published.
29. E.S. Hood, B.H. Toby and W.H. Weinberg, *Phys. Rev. Lett.* **55**, 2437 (1985).
30. R. Clavenna and L.D. Schmidt, *Surf. Sci.* **22**, 365 (1970).

31. S.P. Singh-Boparai, M. Bowker and D.A. King, Surf. Sci. **53**, 55 (1975).
32. P. Alnot and D.A. King, Surf. Sci. **126**, 359 (1983).
33. T.S. Wittrig, P.D. Szuromi, W.H. Weinberg, J. Chem. Phys. **76**, 3305 (1982).
34. H.-P. Steinruck, A.V. Hamza and R.J. Madix, Surf. Sci. **173**, L571 (1986).
35. C.B. Mullins and W.H. Weinberg, to be published.
36. D.A. King and M.G. Wells, Surf. Sci. **29**, 454 (1971).
37. W.H. Weinberg and R.P. Merrill, J. Vac. Sci. Technol. **8**, 718 (1971).
38. C.T. Rettner, E.K. Schweizer, H. Stein and D.J. Auerbach, Phys. Rev. Lett. **61**, 986 (1988).
39. The experimental uncertainties correspond to one standard deviation.
40. For $\theta_i=0^\circ$ and 22.5° , components of direct chemisorption (0.05 and 0.035, respectively) were subtracted from the total value of S_o to obtain the trapping-mediated component of chemisorption.

FIGURE CAPTIONS

Figure 1. The initial probability of dissociative chemisorption of ethane on Ir(110)-(1x2) as a function of incident kinetic energy for $T_s=154, 182, 250$ and 500K . All measurements were made at normal incidence.

Figure 2. A plot of $\ln[(\zeta_o/S_o)-1]$ as a function of $1/T_s$ for numerous different incident kinetic energies and angles. Only the trapping-mediated component of S_o is used for the ordinate (i.e., the measured direct component of dissociative chemisorption is subtracted from the measured value of S_o).

Figure 3. The initial probability of dissociative chemisorption of ethane on Ir(110)-(1x2) for $E_i=20.9$ kcal/mol and $T_s=500\text{K}$ (O symbol) and the trapping-mediated component of dissociative chemisorption for $E_i=10.0$ kcal/mol and $T_s=154\text{K}$ (Δ symbol) as a function of incident angle. Also shown, for both cases, are the predicted values of dissociative chemisorption for normal energy scaling ($E_i\cos^2\theta_i$, + symbol) and $E_i\cos^{0.5}\theta_i$ scaling (x symbol). The experimentally measured values are represented by the Δ and O symbols, and the calculated values are represented by the + and x symbols.

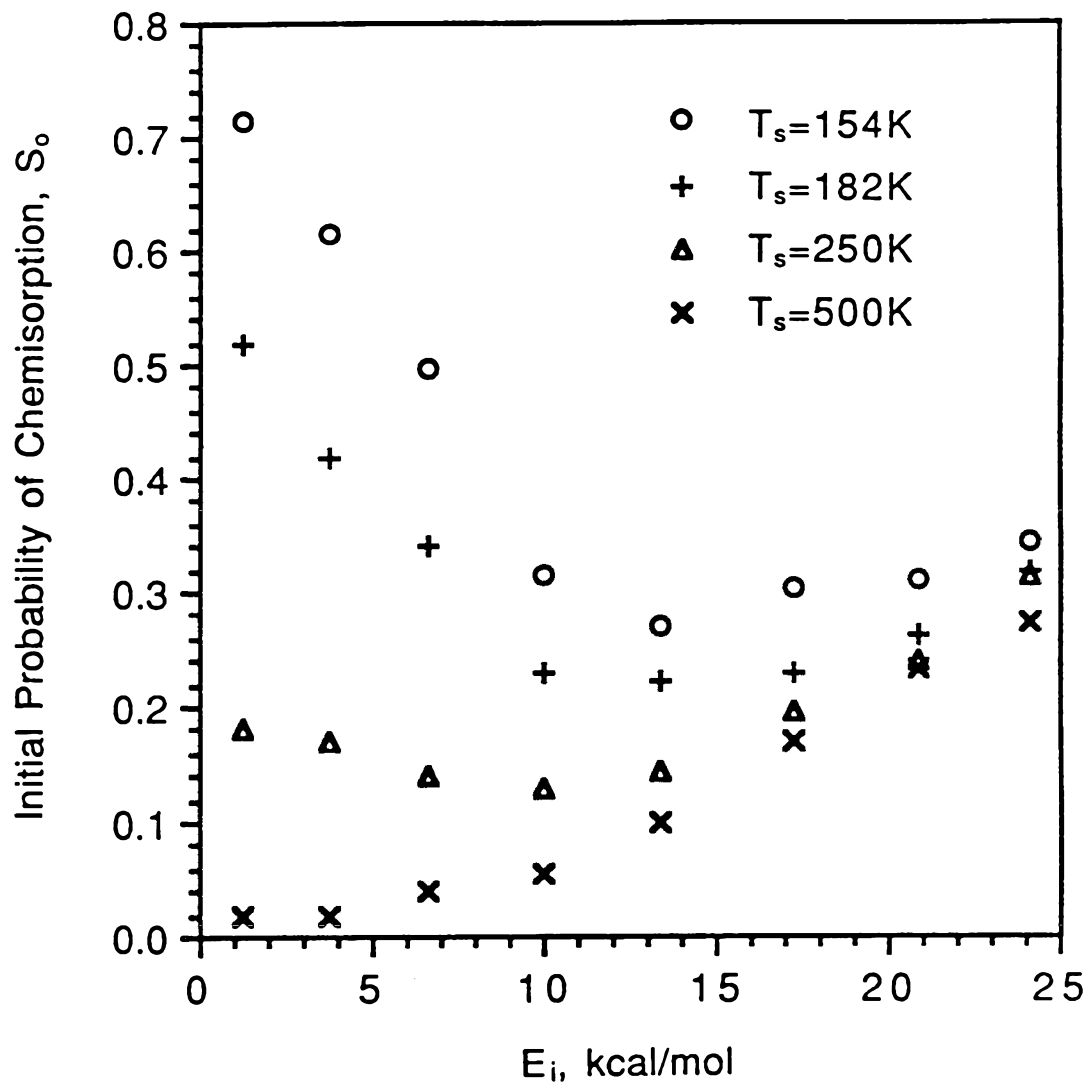


Figure 1

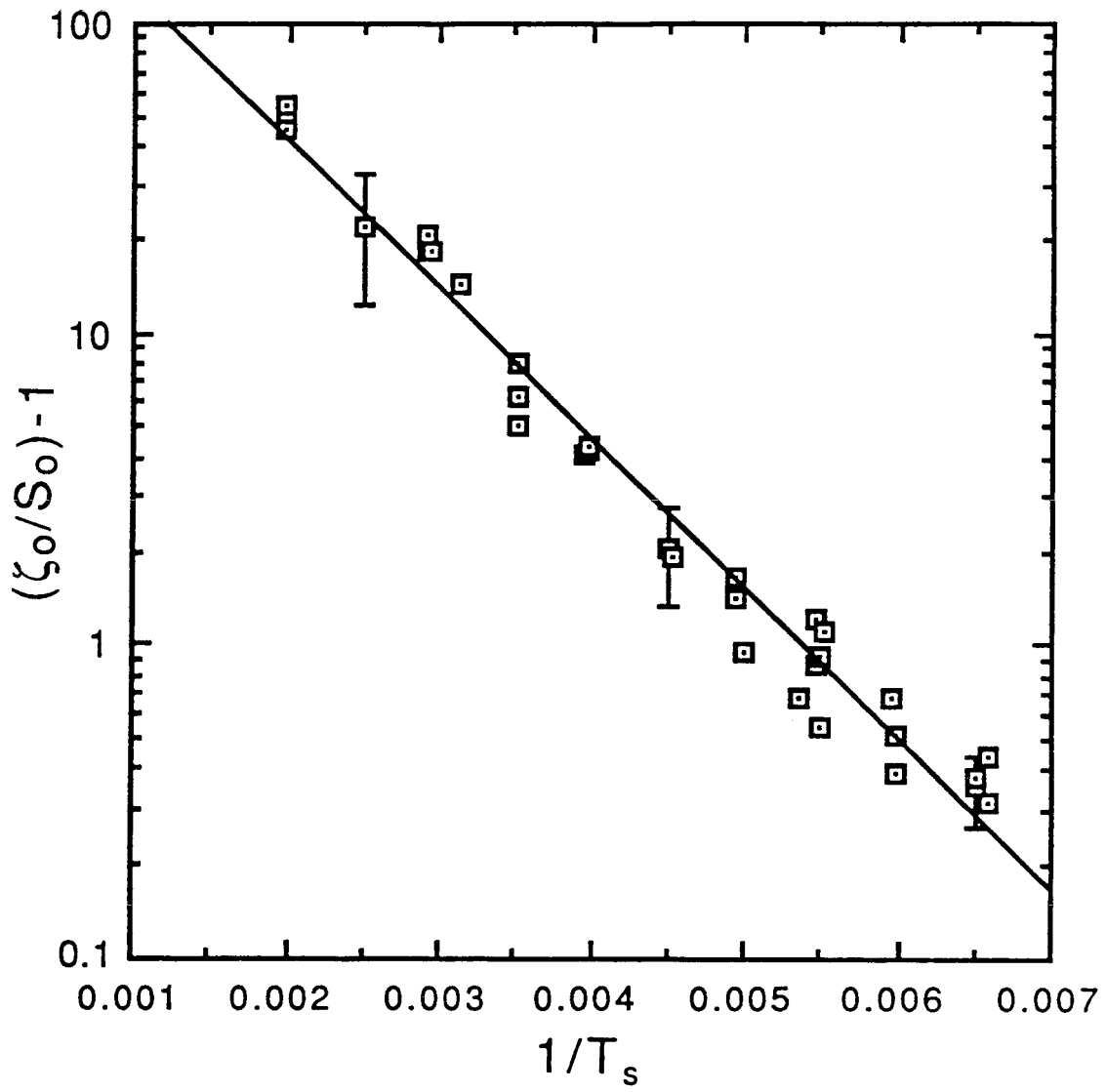


Figure 2

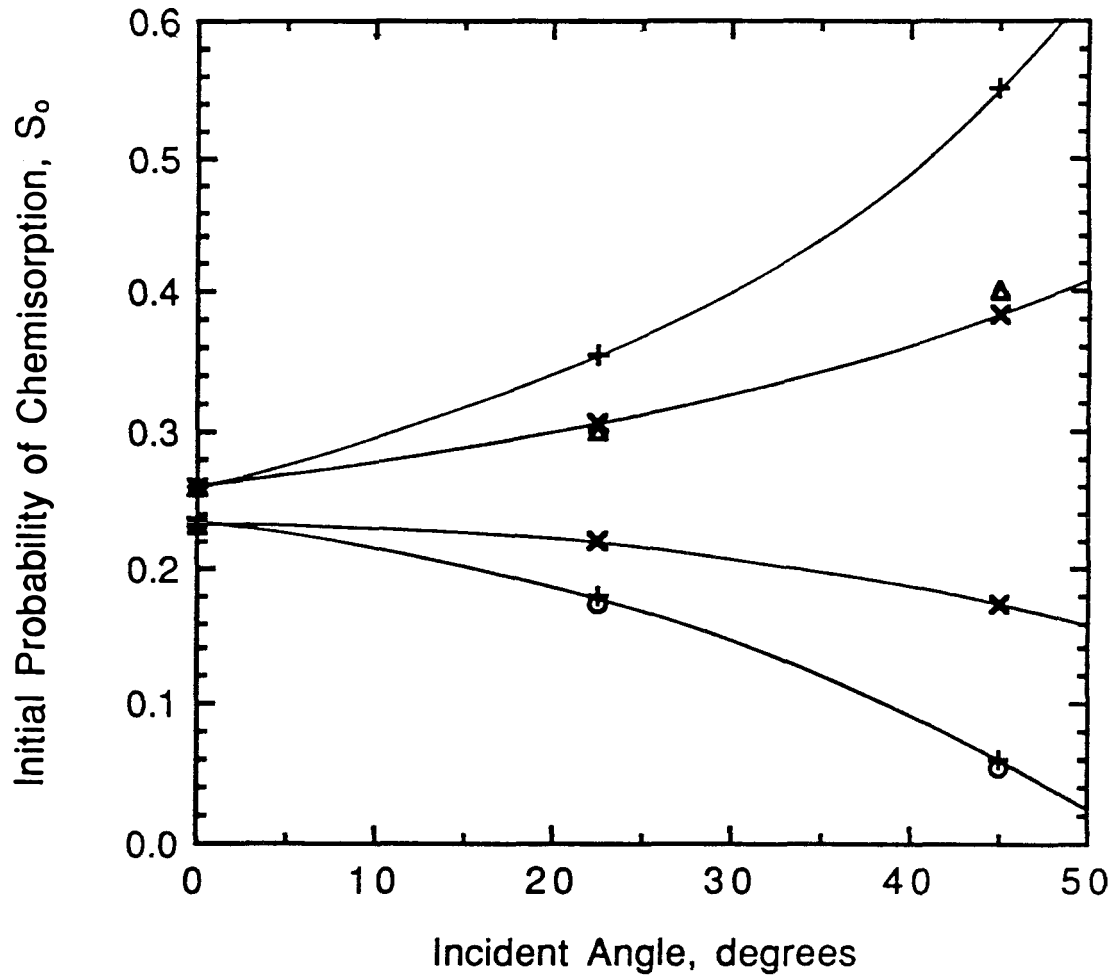


Figure 3

VI-1

CHAPTER VI

VARIATION OF THE TRAPPING PROBABILITY OF Ar ON Pt(111) WITH
KINETIC ENERGY AND ANGLE OF INCIDENCE: THE CHANGING ROLE
OF PARALLEL MOMENTUM WITH SURFACE TEMPERATURE

[The text of Chapter VI consists of an article coauthored with C.T. Rettner, D.J. Auerbach and W.H. Weinberg, which will be submitted to *Chemical Physics Letters*.]

VI-2
ABSTRACT

The trapping probability of Ar on Pt(111) has been measured as a function of incident kinetic energy E_i and angle θ_i for surface temperatures T_s of 80, 190 and 273 K. This probability decreases with increasing E_i in a manner that depends on both θ_i and T_s . For each surface temperature the measured trapping probability at different angles can be reduced to a common curve if it is plotted as a function of the variable $E_i \cos^n \theta_i$. For $T_s=80, 190$ and 273 K we find optimal values of n of approximately 1.5, 1.0 and 0.5, respectively. These results indicate that parallel momentum dissipation becomes increasingly more important to the trapping dynamics as T_s increases.

Understanding the dynamics of energy exchange and the equilibration of gases impinging on solid surfaces is of both fundamental and practical importance. These phenomena are key steps in the physical adsorption of gases at surfaces, chemisorption in heterogeneous catalytic chemistry, crystal growth, and other industrially important processes. Although there is a large body of data concerning the inelastic scattering of rare gases from metal surfaces¹, only recently have the dynamics of the trapping process been studied specifically²⁻⁸. Hurst, et al.⁹ have demonstrated that the flux of Xe atoms leaving a Pt(111) surface can be resolved into both direct and trapping-desorption components. A later study by the same group focused on Ar scattering from Pt(111)¹⁰, and it was shown that the value of the trapping probability ζ_0 was less than for Xe on Pt(111) for similar incident beam conditions. These studies enhanced the available data base considerably, but they did not provide comprehensive answers to questions regarding the detailed dynamics of trapping. Lately, these questions have been addressed more fully for both rare gas atoms²⁻⁵ and molecules⁶⁻⁸ interacting with well-characterized metal surfaces. An important goal of these studies has been to assess the relative role of parallel and perpendicular momentum transfer in the trapping process through measurements of the effect of angle of incidence on the rate at which trapping decreases with increasing energy.

A considerable amount of data concerning inelastic scattering of rare gases from metal surfaces indicates that momentum

exchange is much more efficient in the normal than in the tangential direction¹. Hence, we might expect the trapping probability to be primarily a function of normal momentum, or the so-called "normal-energy" $E_i \cos^2 \theta_i$. Two groups have recently measured the trapping probability of Xe on Pt(111) at surface temperatures of 85 K³ and 95 K⁴ as a function of incident kinetic energy and angle to examine this issue. Both groups observed a decrease in ζ_0 with E_i but found significant deviations from the simple normal-energy scaling. In one case³ results obtained at different angles scaled as $E_i \cos^{1.6} \theta_i$ while in the other⁴ $E_i \cos^{1.0} \theta_i$ scaling was reported, the same as that found in an earlier investigation of Ar trapping on W(100)-2H². These studies suggest that parallel momentum is more important in trapping than previously thought. While these measurements have begun to elucidate the physics of the microscopic energy transfer, much remains to be understood. In particular, the effect of surface temperature on the detailed trapping dynamics has yet to be examined. This is partly due to the difficulties inherent in making such measurements. Most previous studies have been carried out at temperatures at which the residence time of the trapped species is sufficiently long to permit the trapping to be inferred from the surface coverage or the adsorption of incidence flux. However, at temperatures that are sufficiently high to alter the trapping probability significantly, residence times will usually be much too small for such methods. In these cases the trapping probability can be deduced instead from the intensity of the trapping-desorption component of the "scattered" flux. This approach was used in the previously mentioned study of Ar trapping on W(100)-2H at a surface

temperature of 85 K². Here we report an extension of this work to the case of Ar trapping on Pt(111), where we have been able to determine the probability of trapping as a function of incident energy and angle for different surface temperatures. The results reveal that the energy-scaling relation is not constant with surface temperature thus indicating the varying role of parallel momentum transfer in the trapping process as a function of surface temperature.

A detailed description of the apparatus has been presented previously^{2,11}, and thus we present only a brief account here. Generally, beams of Ar generated by a supersonic nozzle are directed at a single crystal of platinum and the scattered flux is detected. The platinum sample is contained in an ultrahigh vacuum (UHV) scattering chamber and is mounted on a manipulator which provides accurate control of the incident angle and the surface temperature between approximately 80 and 1500 K. Particular care was taken in the preparation of the sample. Alignment and polishing were accomplished on a carefully machined sample mount that allowed both orientation adjustment from Laue photographs and polishing. The surface is within $\pm 0.2^\circ$ of the (111) plane. The crystal has been mounted on the manipulator such that the [121] vector lies in the scattering plane. The sample was cleaned routinely using standard oxygen cleaning and Ar ion sputtering techniques. Sharp LEED patterns are obtained and contamination levels (mainly carbon) are below 1%, as determined by Auger electron spectroscopy. In addition, the scattering of a 30 mev beam of He from the cooled

surface ($T_s=80$ K) gives a specular peak with a width indistinguishable from the instrumental resolution of 1.6° and which contains greater than 80% of the incident flux.

Beam energies are varied by changing the nozzle temperature T_{noz} of a $75 \mu\text{m}$ nozzle and by seeding in He. For the lowest energies, the nozzle is cooled to approximately 100 K, and the pressure of Ar in the nozzle is held at about 500 Torr, in order to avoid condensation. For T_{noz} above 250 K, Ar pressures of up to 1500 Torr are used. The insensitivity of the results to the beam conditions suggests that clustering in these beams is negligible. The beam energies are determined from flight times between a high-speed chopper and a differentially pumped rotatable mass spectrometer. This device is also used to measure the time-of-flight and angular distributions of the scattered and desorbing Ar. Angular distributions have been obtained using two schemes. The distributions of the total scattered and desorbing flux can be recorded using phase sensitive detection, referenced to the chopper and processed with a lock-in amplifier. Alternatively, distributions can be constructed by analyzing time-of-flight spectra for specific scattering angles so that flux distributions can be obtained, rather than the density distributions that result from the lock-in method. Details of the time-of-flight analysis are given in Ref. 2.

Time-of-flight distributions have been recorded over a wide range of conditions and show bimodality in many cases. Although bimodal distributions have not been reported previously for the

Ar/Pt(111) system, qualitatively similar distributions have been obtained for the Ar/W(100)-2H² and Xe/Pt(111)⁹ systems, which can be separated into direct-inelastic component and trapping-desorption components. Thus, we use the flux-weighted signal of the trapping-desorption component as a measure of the *relative* trapping probabilities for differing incident beam conditions. A separate mass spectrometer is used to measure the Ar partial pressure rise in the scattering chamber in order to account for differences in incident beam intensity. We have assumed that, for a given T_s, all Ar atoms that trap and thus accommodate to the surface desorb with energy and angular distributions that are a function of surface temperature only, i.e., the particles have no "memory" of their incident conditions. Hence, for all the measurements of the *relative* trapping probabilities, the differentially pumped quadrupole mass spectrometer was positioned 5° from the surface normal in order to measure the appropriate desorbing flux consistently for all incident beam conditions and to minimize the direct-inelastic component. The technique described above for measuring relative trapping probabilities has the advantage of allowing trapping to be studied as a function of surface temperature. However, if the surface temperature is too high (for this study \simeq 300 K), two effects combine to eliminate the separability of the direct-inelastic and trapping-desorption components. The direct-inelastic lobe broadens and the trapping-desorption component is faster.

Absolute trapping probabilities can be estimated from angular distributions, where this probability is taken to be the fraction of

scattered species *not* contained in the direct-inelastic lobe¹². Here it is necessary to estimate the form of the out-of-plane distribution for the direct-inelastic lobe. We have not measured out-of-plane angular distributions, but experiments on Ar scattering from Pt(111) by Hurst et al.¹³ suggest that the out-of-plane angular width is between 0.5 and 1 times the in-plane width. The accuracy of this method increases rapidly as the trapping probability approaches unity, where the flux contained in the direct-inelastic lobe becomes negligible. As a result of the uncertainty in the out-of-plane angular width, the absolute values of the trapping probability reported here should be considered accurate to only $\pm 10\%$. The relative values of ζ_0 are accurate to $\pm 5\%$. The results reported here also agree with an estimation of the absolute trapping probability that is based on comparing the absolute intensities in the desorption component with the diffuse scattering from a nominally flat part of the sample holder that is aligned at the crystal position. In this case we observe only a single scattering component that peaks at the surface normal, which we take to represent 100% trapping¹².

We find that the trapping probability has a strong dependence on both incident kinetic energy and angle, increasing with angle of incidence for a given kinetic energy. For $T_s=80$ K, the angular dependence is in qualitative agreement with normal-energy scaling, as can be seen in Fig 1 where ζ_0 is plotted as a function of $E_i \cos^2 \theta_i$. However, it is apparent that this scaling law is far from being satisfactory. To describe these results more accurately, we have considered a scaling variable of the form $E_i \cos^n \theta_i$, which allows for a

continuous variation between normal energy scaling ($n=2$) and total energy scaling ($n=0$). Figure 2 shows the trapping probability plotted as a function of $E_i \cos^{1.5} \theta_i$ which is much closer to an ideal scaling function. This value of n is actually noticeably better than $n=1.6$ or 1.4 , but considering systematic errors this and other values quoted below should be taken as accurate to only ± 0.2 . The chosen value of $n=1.5$ is remarkably similar to that obtained recently for trapping of Xe on Pt(111) at nearly the same surface temperature ($T_s=85$ K)³, where a value of $n=1.6$ was estimated based on data obtained using a different technique. We also note that there is no obvious physical basis for this form, but contend that such a scaling law may be generally applicable to trapping.

The decrease of ζ_0 with E_i is expected, since the fraction of this energy that must be lost increases rapidly as it is raised. The qualitative form of this curve has been reproduced using hard-cube¹⁴, "washboard"¹⁵ and full classical trajectory methods¹⁶, the details of which will be reported elsewhere. Similarly, this form is in good basic agreement with previous calculations for this system by Tully¹⁶ and Leuthausser¹⁷, and with an experimental curve obtained by Hurst, et al.¹⁰ who used detailed balance arguments to estimate its form from time-of-flight measurements of Ar scattering from Pt(111) at $T_s=100$ K. Furthermore, a similar detailed balance analysis^{2,10}, applied to the present time-of-flight spectra gives values of the trapping probability in good agreement with the directly measured values for all three temperatures. Additionally, a detailed balance analysis of the directly measured

trapping probabilities predicts the correct degree of translational cooling in the desorbing flux. For example, at $\theta_i=5^\circ$, we estimate effective temperatures for the desorbing Ar of approximately 70, 145 and 196 K for $T_s=80,190$ and 273 K, respectively, which are within 10% of the fitted temperatures in almost all cases. Again, details are deferred to a future publication.

Figures 3 and 4 show experimentally determined trapping probabilities for Ar interacting with Pt(111) with surface temperatures of 190 K and 273 K, respectively. In these cases we find that rather different scaling laws apply, corresponding to $n=1.0$ and 0.5. Fig. 3 shows the trapping probability as a function of $E_i \cos^{1.0} \theta_i$ at $T_s=190$ K. Similarly, in Fig. 4 the trapping data at $T_s=273$ K are shown with $n=0.5$. As mentioned earlier, these scaling laws are merely for convenience. However, the changes in the scaling relationships with T_s can be used to gain further insight into the relative role parallel momentum transfer plays in trapping as a function of surface temperature and will be discussed later. The value of ζ_0 at the two higher surface temperatures also decreases with increasing E_i . However, a closer inspection of the low E_i data for Figs. 2-4 also reveals a decrease in ζ_0 with increasing T_s , while at higher energies the reverse is true. This behavior reflects the fact that surface atoms that are moving towards the incoming Ar atoms will reduce the trapping probability of slow incident species, while at high energies, where trapping is low, collisions with surface atoms that are moving away from the incident species have a net effect of increasing the number that trap. This effect is

readily seen in simple hard-cube models^{14,18}, and has been discussed, for example, for the NO/Ag(111) system¹⁹.

It is apparent that the optimum value of the exponent n systematically decreases with increasing T_s as can be seen in Fig. 4, which summarizes this behavior. This plot further suggests that normal-energy scaling ($n=2$) may be applicable as T_s approaches zero, while trapping at 500 K or so may be expected to be largely independent of angle of incidence.

The dynamical origin of this effect is by no means obvious. Clearly parallel momentum becomes increasingly more important in the trapping process as the surface temperature is increased, suggesting a corresponding increase in the effective corrugation of the interaction potential. However, the actual surface roughness due to the thermal displacement of surface atoms is almost certainly too small for this behavior to be accounted for by simple single-collision models. Specifically, we estimate that the local normal at the point of impact deviates from the true normal by less than 3° at 273 K. Calculations based on a "washboard" model¹⁵, which is similar to a hard-cube model but incorporating surface corrugation, reveal this to have only a weak effect on the dependence on angle of incidence. Thus, we believe that a multiple collision picture is most likely required. A key issue here is the fate of atoms that are initially trapped by virtue of loss of normal momentum, but which retain sufficient total energy to escape. Calculations based on a semi-classical treatment of the forced oscillator model have shown

that the effect of angle of incidence on the trapping of Ne on Cu(100) depends sensitively on the fate of these atoms, and even decreases with increasing angle of incidence ($n < 0$) if it is assumed that the initial collision must leave the atom with a net negative total energy for trapping to occur²⁰. Classical trajectory calculations for Ar and Xe trapping on Pt(111)¹⁶ suggest that parallel momentum accommodation is relatively slow and that a significant fraction of species that lose their normal energy in the first collision escape before their parallel momentum is fully accommodated. It may be that as T_s is increased, thermal roughness serves to couple parallel and perpendicular momenta at a rate that can compete with the rate at which these are dissipated. Detailed calculations are required to further address this question.

Finally we note that the value of ζ_0 for $T_s = 80$ K appears to extrapolate to near unity as E_i approaches zero as seen in Fig. 1. This is in contrast to recent results for Ne and Ar adsorption on Ru(001)^{5,21}. The physical adsorption probability tends to values far less than one with decreasing E_i for both Ne and Ar indicating the importance of quantum effects for these rare gas atoms interacting with Ru(001). These quantum effects appear to be completely accounted for when the solid is treated quantum mechanically and the gas atom classically. The apparent absence of quantum effects for Ar trapping on Pt(111) appears to be due to the differences in vibrational structure for the Pt(111) and Ru(001) surfaces.

In summary we have presented measured values, obtained using a novel molecular beam technique, of the trapping probability of Ar on Pt(111) as a function of incident energy and angle and surface temperature. The experimental results demonstrate an increasingly more important role for parallel momentum in the trapping process with increasing surface temperature, which is manifested by a decrease in the exponent n in the scaling relation $E_i \cos^n \theta_i$ with increasing T_s . Thus, as the surface temperature rises there appears to be a shift in the relative rate of dissipation of parallel momentum versus scattering from the surface via a coupling of parallel momentum to normal momentum. Additionally, our results do not show any significant quantum effects with regard to the trapping process. The trapping probability of Ar on Pt(111) increases both with decreasing surface temperature and with decreasing Ar kinetic energy.

We are indebted to J.E. Schlaegel for assistance in the maintenance and upkeep of the apparatus, and to D.S. Bethune for helpful discussions. One of us (W.H.W.) thanks the National Science Foundation for partial support of this research under grant number CHE-8617826, and the Donors of the Petroleum Research Fund of the American Chemical Society for partial support under grant number PRF 19819-AC5-C.

REFERENCES

1. J.A. Barker and D.J. Auerbach, Surf. Sci. Rep. **4**, 1 (1984).
2. C.T. Rettner, E.K. Schweizer and C.B. Mullins, J. Chem. Phys. **90**, 3800 (1989).
3. C.T. Rettner, D.S. Bethune and D.J. Auerbach, J. Chem. Phys. **91**, 1942 (1989).
4. C.R. Arumainayagam, R.J. Madix, M.C. McMaster, V.M. Suzawa and J.C. Tully, to be published.
5. H. Schlichting, D. Menzel, T. Brunner, W. Brenig and J.C. Tully, Phys. Rev. Lett. **60**, 2515 (1988).
6. C.B. Mullins and W.H. Weinberg, to be published.
7. E.W. Kuipers, M.G. Tenner, M.E.M. Spruit and A.W. Kleyn, Surf. Sci. **205**, 241 (1988).
8. S. Andersson, L. Wilzen and J. Harris, Phys. Rev. Lett. **55**, 2591 (1985).
9. J.E. Hurst, C.A. Becker, J.P. Cowin, K.C. Janda, L. Wharton and D.J. Auerbach, Phys. Rev. Lett. **43**, 1175 (1979).
10. J.E. Hurst, L. Wharton, K.C. Janda and D.J. Auerbach, J. Chem. Phys. **83**, 1376 (1985).
11. C.T. Rettner, L.A. DeLouise and D.J. Auerbach, J. Chem. Phys. **95**, 1131 (1986).
12. C.T. Rettner, E.K. Schweizer, H. Stein and D.J. Auerbach, Phys. Rev. Lett. **61**, 986 (1988).
13. J.E. Hurst, L. Wharton, K.C. Janda and D.J. Auerbach, J. Chem. Phys. **78**, 1559 (1983).
14. R.M. Logan and R.E. Stickney, J. Chem. Phys. **44**, 195 (1966).

15. J.C. Tully, to be published.
16. J.C. Tully, Surf. Sci. **111**, 461 (1981).
17. U. Leuthausser, Z. Phys. B **50**, 65 (1983).
18. W.H. Weinberg, Adv. Coll. Inter. Sci. **4**, 301 (1975).
19. G.D. Kubiak, J.E. Hurst, H.G. Rennagel, G.M. McClelland and R.N. Zare, J. Chem. Phys. **79**, 5163 (1983).
20. M. Persson and J. Harris, Surf. Sci. **187**, 67 (1987).
21. D. Menzel, private communication.

FIGURE CAPTIONS

Figure 1. The experimentally determined trapping probability of argon on Pt(111) as a function of $E_i \cos^2 \theta_i$ at $T_s=80$ K.

Figure 2. The same data as in Fig. 1 showing the experimentally determined trapping probability of argon on Pt(111) at $T_s=80$ K plotted as a function of $E_i \cos^{1.5} \theta_i$ rather than the normal-energy.

Figure 3. The experimentally determined trapping probability of argon on Pt(111) as a function of $E_i \cos^{1.0} \theta_i$ at $T_s=190$ K.

Figure 4. The experimentally determined trapping probability of argon on Pt(111) as a function of $E_i \cos^{0.5} \theta_i$ at $T_s=273$ K.

Figure 5. The exponent n in the scaling relation $E_i \cos^n \theta_i$ as a function of surface temperature.

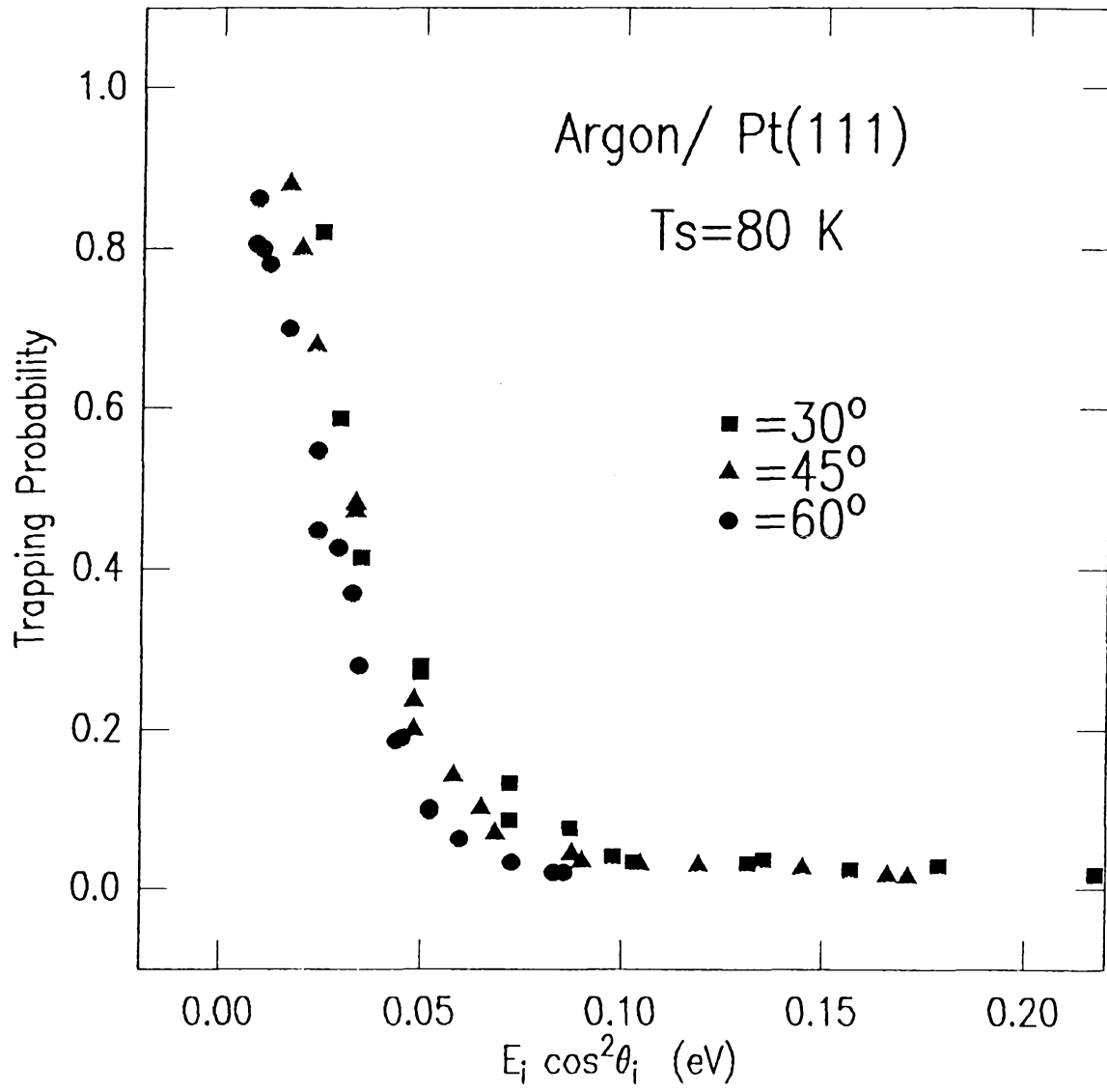


Figure 1

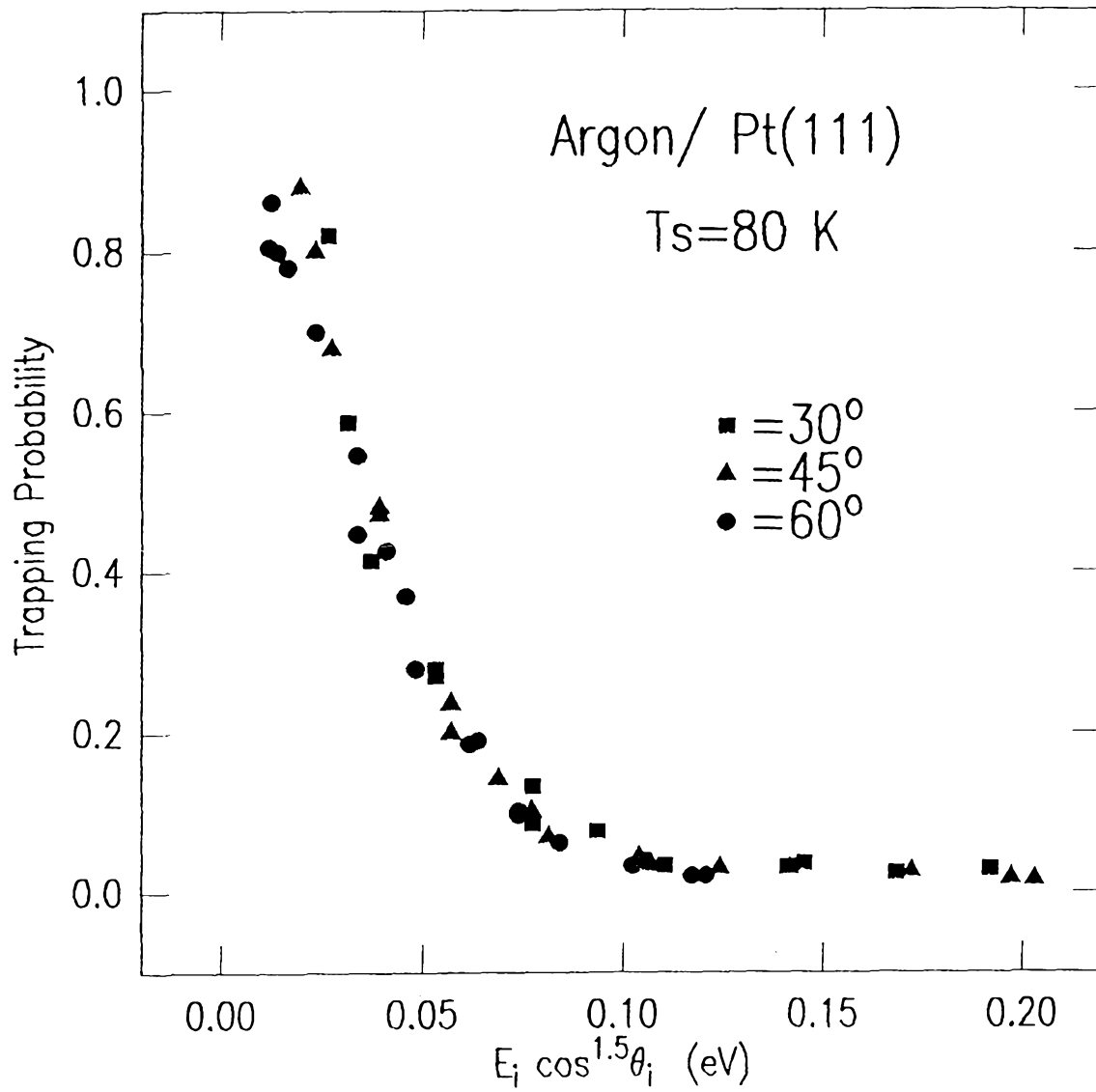


Figure 2

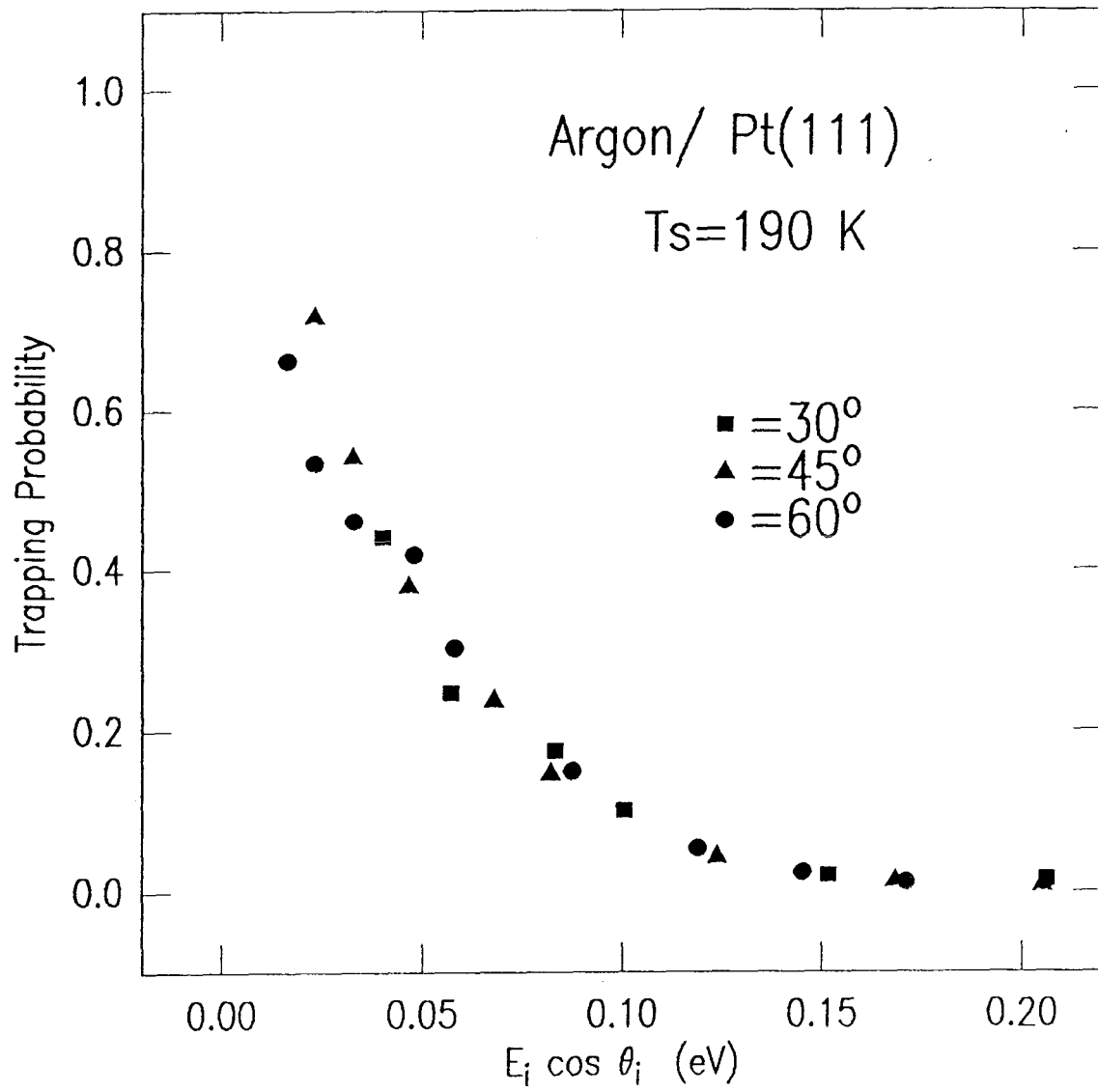


Figure 3

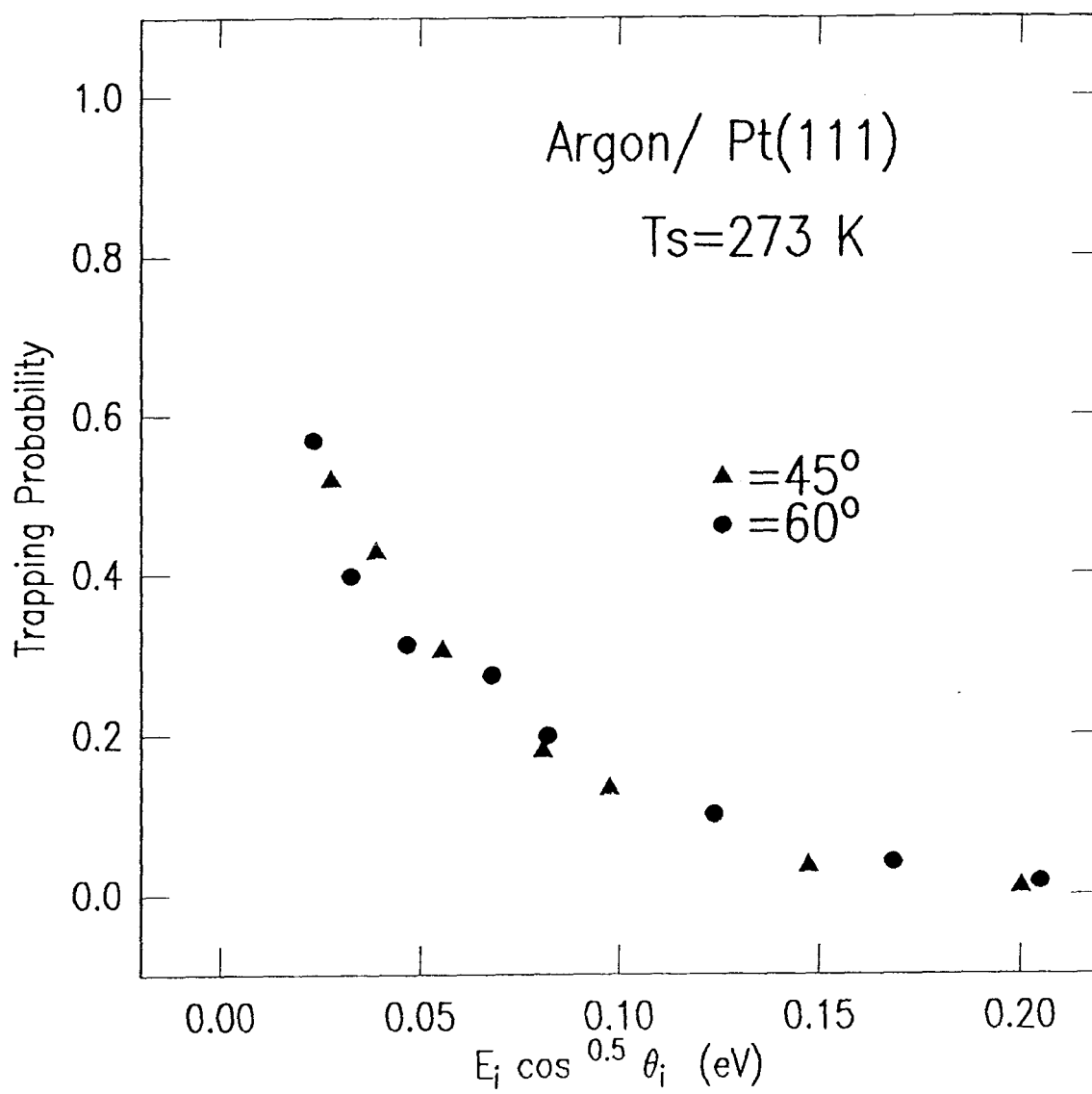


Figure 4

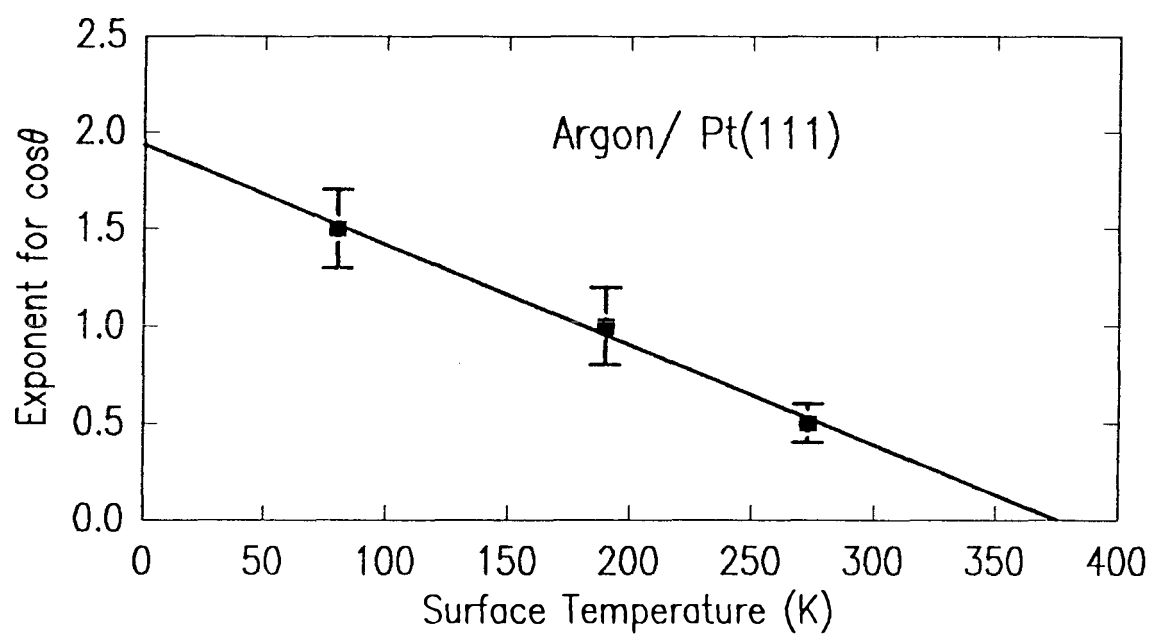


Figure 5

A - 1

APPENDIX A

MOLECULAR ADSORPTION OF ETHANE ON THE Ir(110)-(1X2) SURFACE:
MONTE-CARLO SIMULATIONS AND MOLECULAR BEAM REFLECTIVITY
MEASUREMENTS

[The text of Appendix A consists of an article coauthored with H. C. Kang and W. H. Weinberg, which has been submitted to *The Journal of Chemical Physics*.]

ABSTRACT

Experimental results, obtained using a molecular beam reflectivity method, for the probability of molecular physical adsorption of ethane on the Ir(110)-(1x2) surface are presented. We analyze these results using Monte-Carlo simulations and show that molecular adsorption can occur either "directly" or through a precursor state in which an ethane molecule is trapped in a second layer of molecularly adsorbed ethane with subsequent migration to a vacant site. From the Monte-Carlo simulations, we are able to establish that the energy barrier for the desorption of an ethane molecule from the precursor state is approximately 4.5 kcal/mol. We also find that the energy barrier for diffusion of an ethane molecule on top of a monolayer of ethane molecularly adsorbed on the Ir(110)-(1x2) surface is approximately 3.7 kcal/mol.

1. Introduction

The adsorption of a molecule from the gas phase onto a solid surface does not necessarily occur in one direct step. The impinging molecule may be trapped temporarily in a weakly bound precursor well before it reaches the adsorption well. For example, a physically adsorbed molecule could be a precursor to either molecular or dissociative chemisorption (1). Likewise, condensed molecules in a second layer could be precursors to adsorption on the surface, depending on the relative rates of migration in the second layer and desorption from the second layer (1). The concept of such precursor states, first proposed by Langmuir (2,3), is rather important in understanding the kinetics of a variety of surface phenomena. If, for instance, chemisorption is mediated by a precursor state in which the adsorbing molecule accommodates thermally to the surface, then the probability of chemisorption would be strongly affected by the surface temperature. This would not be true if chemisorption occurs directly, i.e., without passing through a precursor state. Descriptions of the kinetics of precursor-mediated adsorption have been presented by Becker (4,5), Ehrlich (6) and Kisliuk (7); and they have been reviewed by Weinberg (1). There have been important refinements of these macroscopic approaches by treating the microscopic configurations of the adsorbed layer in a statistical manner (8-14). Monte-Carlo modeling, taking into account the microscopic configuration of the adsorbed layer around each adsorbed molecule, and hence the lateral interactions by which each molecule is influenced, has also been formulated (13). In this paper we present evidence demonstrating that the molecular physical adsorption of ethane on the Ir(110)-(1x2) surface can be understood by drawing upon the concept of a precursor to molecular adsorption. We show that molecular adsorption can occur directly when an ethane molecule impinges upon the bare iridium surface or indirectly when an ethane molecule impinges upon already molecularly adsorbed ethane. The "extrinsic" precursor in this case is the mobile ethane molecule trapped on

top of a layer of molecularly adsorbed ethane (15). The experimental results, which are obtained from reflectivity measurements performed using a molecular beam apparatus, are shown to be well described by Monte-Carlo simulations of a model which takes into account the two pathways delineated above.

2. Experimental and Algorithmic Details

Measurements of the probability of molecular adsorption of ethane on the Ir(110)-(1x2) surface have been made using the reflectivity method of King and Wells (12), employing a molecular beam apparatus that will be described in detail elsewhere (16). Briefly, the apparatus consists of a thrice differentially pumped, supersonic nozzle molecular beam source and an ultrahigh vacuum scattering chamber. Low-energy electron diffraction optics, Auger electron spectroscopy and an ion gun are mounted on the scattering chamber for obtaining and checking surface cleanliness and order. A quadrupole mass spectrometer is also mounted on the scattering chamber for thermal desorption mass spectrometry, reflectivity measurements and beam time-of-flight measurements. The source chambers contain the nozzle, a high-speed shutter and a chopper for beam modulation, as well as apertures for beam collimation. Beam energies are varied by a combination of seeding and variation of nozzle temperature, and are measured by time-of-flight techniques. Both the scattering chamber and the third-beam chamber are pumped by turbomolecular pumps; the other two beam chambers are pumped by diffusion pumps. The iridium crystal is mounted on a manipulator which provides precise alignment. The manipulator is liquid nitrogen cooled, providing rapid cooling of the sample to below 80 K. The sample temperature is determined by a 0.003 in. W/5%Re-W/26%Re thermocouple spot welded to the back of the crystal.

The partial pressure P_E of ethane, at time t , in the scattering chamber is used as a measure of the flux of ethane molecules that do not adsorb. Hence,

the probability of adsorption at time t is $(P_S - P_E)/P_S$, where P_S is the partial pressure of ethane in the chamber due to scattering from a saturated surface. Both P_E and P_S are corrected for a small effusive component of the flux (16). This technique is particularly useful in measuring the adsorption probability as a function of time or coverage. The surface temperature T_s was maintained constant at approximately 77 K for all the measurements reported here. The experiments were performed with beam energies E_i ranging from approximately 2.2 kcal/mol to 10 kcal/mol, and with incident angles θ_i ranging from 0° to 45° . The incident energy and angle for each experiment are summarized in Table 1. For normal kinetic energies $E_i \cos^2 \theta_i$ greater than approximately 8 kcal/mol, there is a non-zero component of direct dissociative chemisorption in the adsorption at 77 K (16). As shown in Table 1, experiment f has a normal kinetic energy of approximately 8.5 kcal/mol and hence has a small component of direct dissociative chemisorption. The initial probability of dissociative chemisorption under these conditions is approximately 0.03, and this has been ignored. We can also ignore desorption of the molecularly adsorbed ethane, which only occurs at temperatures above 100 K (17).

The Monte-Carlo simulations are carried out as follows. The surface is modelled by a square lattice of size 400x400. Each site is allowed to be in one of three possible states: the site can be vacant; the site can be occupied by a molecularly adsorbed particle; or the site can be occupied by a molecularly adsorbed particle and a particle trapped in the precursor state. A site on the lattice is selected at random. If it is occupied by a trapped particle, then the particle is allowed either to hop to a nearest-neighbor site or to desorb. The choice is determined as follows. The trapped particle has a probability of 1/5 of attempting to move in each of five directions: the four lattice directions in the plane of the surface and the direction into the gas phase. If one of the lattice directions is chosen, the particle successfully moves to the nearest-neighbor site

in that direction with a probability of p_m . If the direction into the gas phase is chosen, the particle successfully desorbs with a probability of p_d . If the site chosen is vacant, or is occupied by only a molecularly adsorbed particle, then a particle from the gas phase impinges upon it with a probability of p_f . If the site chosen is vacant, then the impinging particle molecularly adsorbs with a probability p_0 . If the site chosen is occupied by a molecularly adsorbed particle, then the impinging particle is trapped with a probability p_1 . Upon completion of this procedure, the time is increased by one Monte-Carlo step, another site is selected at random, and the procedure is repeated. The quantity measured in the reflectivity experiments is the partial pressure of ethane as a function of time. From the Monte-Carlo simulations, we obtain the values of n_i , the number of particles impinging upon the lattice, and n_r , the number of particles "reflecting" from the lattice in each Monte-Carlo step/site. The quantity n_r includes both the particles that impinge upon and fail to be adsorbed molecularly or trapped, and the previously trapped particles that desorb from the lattice. The quantity that is obtained from the reflectivity experiments is $(n_i - n_r)/n_i$. It should be noted that this is equal to the quantity n_a/n_i , where n_a is the number of particles molecularly adsorbing per Monte-Carlo step/site, only when the number of trapped ethane molecules in the second layer at any instant of time is vanishingly small.

There are five parameters in the simulations, namely p_0 , p_1 , p_m , p_d and p_f . The value of p_0 used in the simulations is obtained from the zero-coverage limit of the *experimentally measured* probability of molecular adsorption (16). This is the probability with which an ethane molecule accommodates and adsorbs molecularly on the bare Ir(110)-(1x2) surface. At a particular surface temperature, it is strongly dependent on the energy of the incident beam of ethane. For the results that are presented here, the beam energy varies from ~ 2.2 kcal/mol to ~ 10 kcal/mol, and the corresponding values of p_0 vary from ~ 0.95 to ~ 0.45

at a surface temperature of 77 K. The value of p_1 , the probability of accommodation of an ethane molecule on top of a physically adsorbed layer of ethane, is clearly larger than p_0 due to a better match of masses, facilitating momentum transfer, and the existence of a softer potential than in the case of a collision with the bare iridium surface (18-20). In principle, both p_0 and p_1 are dependent on the beam energy. On the other hand, in our model p_m and p_d must not be dependent on the beam energy because the trapped particle is assumed to be completely accommodated thermally to the surface. In the experiments the surface temperature is kept constant at approximately 77 K. Hence, for the simulations to be consistent physically, it is necessary that the same values of p_m and p_d successfully describe the experimental results at all beam energies. We choose p_m to be unity, and vary the ratio of p_d/p_m . As a result, we have set the time-scale of the simulation to be the time-scale for a trapped ethane molecule to hop from one site to the next. The parameter p_f is the probability, in each Monte-Carlo step, that a gas-phase molecule impinges upon each site. This parameter can, in principle, be determined from an accurate measurement of the flux of ethane in the molecular beam used in the experiments. If each Monte-Carlo step corresponds to a real time of τ_r , then the incident flux would be p_f/τ_r site⁻¹s⁻¹. A crude estimate of this flux in the experimental measurements is $0.1 \sigma^{-1} \text{s}^{-1}$, where σ is the area occupied by one adsorbed ethane molecule when the surface is covered by one monolayer of ethane at 77 K. This is because the experiments take approximately 10 s, and, as shown below, the final fractional coverages are only slightly greater than one monolayer. In the simulations, however, we used a range of values of p_f , and chose the value that best fits the experimental results, cf. Table 1.

3. Results and Discussion

Before we compare the simulations with the experimental results, we discuss the simulation in the limiting case where p_f is set equal to zero, i.e. the limit of infinitesimally small flux. In this case the simulation cannot be done as we have discussed above. This is because with $p_f = 0$, the procedure discussed above will not allow the number of particles on the surface to increase. When the flux is infinitesimally small then any particle that impinges on the surface will have already adsorbed molecularly or desorbed before the next particle impinges on the surface. Hence, particles will have to be introduced one at a time onto the surface. Then the time in the simulations is not measured as before. In this case, the time is linearly proportional to the number of particles that are introduced onto the surface, regardless of the number of hops that each trapped particle takes before it desorbs or adsorbs. This is in contrast to the simulation procedure for the case in which p_f is not zero, where the time is increased by one Monte-Carlo step each time an attempt is made to hop, desorb or trap a particle. The simulations for $p_f = 0$ are done as follows. First, we determine the probability of molecular adsorption for a fixed coverage on the surface, and then we increase the coverage on the surface. The probability of molecular adsorption is determined by introducing test particles one at a time, and counting the fraction that adsorbs molecularly. If a test particle impinges on a vacant site, then molecular adsorption occurs with a probability of p_0 . If the test particle impinges on a site which already has a molecularly adsorbed particle, then it traps with a probability of p_1 . A trapped particle is allowed to attempt a move in one of the four lattice directions or in the direction into the gas phase. Each of these directions is picked with a probability of $1/5$. An attempted hop to a nearest-neighbor site is successful with a probability of p_m . If the test particle attempts to move into the gas phase, it desorbs with a probability of p_d . A test particle is allowed to migrate on the lattice by nearest-neighbor hops until it

either desorbs or reaches a vacant lattice site whereupon it immediately adsorbs molecularly. Then the next test particle is introduced. In order to obtain the probability of molecular adsorption at a constant coverage the configuration on the lattice is not updated even if a test particle molecularly adsorbs. For each datum point we introduce 2000 test particles. The configuration on the lattice is updated as follows. A certain number of test particles are introduced, again one at a time. However, now the positions of the test particles which adsorb molecularly are recorded. A test particle which adsorbs molecularly into a site at which an earlier test particle had adsorbed is not counted. After N particles have been introduced, the configuration is updated by using the recorded positions of the molecularly adsorbed test particles. Time is increased by N/FL^2 , where F is the flux from the gas phase in units of $\text{site}^{-1}\text{s}^{-1}$ and L^2 is the number of sites on the lattice. For our simulations, we used $N = 1600$, so that we obtain the adsorption probabilities for every fractional surface coverage increment of 0.01. The procedure is then repeated with the new configuration. It should be noted that the time increment is not dependent upon the actual number of migration steps that are taken by the test particles, since the time for each migration step is infinitesimally small compared to that between subsequent particle impingements on the surface when $p_f = 0$.

The physical situation to which simulations with $p_f = 0$ can be applied is when the rate at which particles from the gas phase impinge upon the surface is much smaller than $1/\tau$, where τ is the lifetime of a trapped particle. When the fractional coverage of molecularly adsorbed particles is not high, a trapped particle can find a vacant site in a time interval τ such that $1/\tau$ is much smaller than the rate at which particles impinge on the surface. In this case the quantity $(n_i - n_r)/n_i$ obtained from the simulations in which p_f is not zero would be equal to the fraction of molecularly adsorbed test particles in the simulations in which $p_f = 0$. In the simulations using $p_f = 0$, the lifetime of the trapped particles is

infinitesimally small compared to the time between which particles impinge on the surface from the gas phase. Therefore, there is no accumulation of trapped particles. This means that the simulations in which $p_f = 0$ model the situation when a second adsorbed layer is not allowed. As a result, by comparing such simulations with experimental results it is possible to infer the accumulation of a second adsorbed layer. Since both desorption and migration occur infinitely fast on the timescale of the particle flux onto the surface, it is not possible to establish, via comparison with experimental results, the absolute rates of desorption and migration. This, however, can be done with the simulations in which p_f is not zero.

The results of the reflectivity measurements are plotted as crosses in Figs. 1 and 2. The ordinate has been labelled as the probability of adsorption although for the experimental data it really corresponds to the quantity $(n_i - n_r)/n_i$. As mentioned earlier, this is equal to n_a/n_i only when the incident flux is extremely low. The abscissa is the time in units of 0.1 s. The experiments were not all performed with the same value of the incident angle θ_i . Thus, even though the beam intensities are the same for all the experiments, the incident fluxes are not. In order to correct for this we have scaled the time by $\cos \theta_i$. Although it would be interesting to perform the experiment at lower surface temperatures (this would give us an independent estimate of the difference between the desorption and migration barriers discussed below), we were not able to cool below the temperature of liquid nitrogen. However, it should be noted that for this particular system, the temperature of ~ 77 K is optimal. At higher temperatures the fractional coverage of the second layer and hence the 'tail' in the experimental data would not be so large, and at lower temperatures it might become necessary to consider the accumulation of more than two layers of ethane on the surface. A smaller 'tail' would lower the accuracy of the Monte-Carlo analysis, and the accumulation of multilayers would render it necessary to introduce ad-

ditional parameters to describe the third or fourth layers and hence complicate the simulations.

The parameters that were fitted to the data are p_1 , p_d/p_m and p_f/p_m . As explained earlier, p_0 is obtained directly from the experimentally measured adsorption probability at zero coverage. The parameters which best fit the experimental data are summarized in Table 1, where each row refers to the correspondingly labelled curves in Figs. 1 and 2. The results of simulations in which $p_f = 0$ are shown by the lines in Fig. 1, while the results of simulations in which p_f is not zero are shown by the circles in Fig. 2. Since the second layer does not accumulate until the first layer is close to saturation, the optimal values of p_1 and p_d/p_m can be determined from simulations in which p_f is zero. The values of p_1 used for each beam energy are shown in Table 1. It should be noted that these values are all rather close to unity, although there is a dependence on the beam energy as would be expected. Having determined the values for p_1 and p_d/p_m that best fit the experimental data except for values of the coverage close to saturation of the first layer, the same values of p_1 and p_d/p_m are used in simulations in which p_f is varied. In this systematic way, we have determined that the value of p_d/p_m is ~ 0.005 and the value of p_f is $\sim 6 \times 10^{-5}$. Note that the relationship between the incident flux and p_f is given by $F = p_f/\tau_r$. Thus, the simulations in which $p_f = 0$ are simulations of experiments in which the incident flux is infinitesimally small on the time scale for migration or desorption. These simulations are sufficiently sensitive that significant deviations between the experimental data and the simulation results are observed if p_d/p_m is set less than 0.001 or greater than 0.01. Similarly, deviations between the experimental 'tail' and the simulation results are apparent if p_f is set greater than $\sim 1 \times 10^{-4}$ or less than 1×10^{-5} . From Fig. 1 it can be inferred that at 77 K a second layer of ethane accumulates on the surface (at least at coverages where the first layer is nearly saturated). This is indicated by the 'tail' in the

experimental data which is not seen in the simulation results in which $p_f = 0$. It is possible that such a 'tail' can result from an equilibrium between the first monolayer of ethane and the gas phase rather than the second layer with the gas phase. However, the desorption barrier for a molecularly adsorbed ethane molecule from the Ir(110)-(1x2) surface is approximately 7.5 kcal/mol (17). As will be seen below, this 'tail' indicates equilibration between the gas phase and a layer of adsorbed ethane with a desorption barrier of 4.5 kcal/mol. Hence, the 'tail' in the experimental data is much too long to be accounted for by desorption from the first monolayer. From Fig. 2, it can be seen that by simply allowing p_f to be non-zero, the simulations can produce the 'tail' observed in the reflectivity experiments. The accompanying accumulation of particles in the second layer in these simulations is shown in Fig. 3. The equilibrium second-layer coverage for the simulation parameters used is approximately 0.057.

By comparing the experimental data with the simulations in which p_f is not zero, it is possible to determine the real time τ_r that corresponds to each Monte-Carlo step/site. In many simulations, it is convenient to use ν^{-1} , the reciprocal of the frequency of the frustrated translational degree of freedom parallel to the surface, as the time scale so that each Monte-Carlo step corresponds to an attempted hop. However, we have set p_m to be unity so that the time scale in these simulations is not the time scale of the frustrated translational motion. Rather, it is the time scale at which successful hops occur. Therefore, τ_r can be much larger than ν^{-1} of which the latter has a typical value of approximately 10^{-13} s. The rate of desorption of a trapped particle is $p_d/5$ per Monte-Carlo step. The factor of 1/5 arises from allowing a trapped particle to attempt to move with equal probability in each of five directions, as discussed above; and desorption is allowed in only one of these directions. Hence, the rate of desorption from the second layer of ethane is given by $R_d = p_d/5\tau_r$. Similarly, as mentioned earlier, the flux incident upon the surface is given by p_f/τ_r . For each

value of the beam energy, the values of the incident flux and the values of the energy barrier for desorption from the second layer E_d are summarized in Table 1 (21). The simulation results presented in Fig. 2 are from simulations in which $p_f = 6 \times 10^{-5}$. As mentioned earlier deviations between the experimental 'tail' and the Monte-Carlo 'tail' begin to be apparent for p_f greater than 1×10^{-4} , the simulation results showing a longer 'tail' than is observed experimentally. This analysis indicates that the fluxes used in the reflectivity measurements are constant to approximately 20 percent, which is physically reasonable. This uncertainty in the value of flux is from the uncertainty in the value of τ_r . This same 20 percent uncertainty in τ_r implies an uncertainty of approximately 50 cal/mol in the value of E_d but, as noted earlier, there is a much greater uncertainty due to the lack of information concerning the preexponential factor for desorption (21). For the simulation results shown in both Figs. 1 and 2, the value of p_d/p_m is 0.005. This is the ratio of the probability of success of desorption to the probability of success of migration. Hence the difference between the respective energy barriers $\delta E = E_d - E_m$ is approximately 800 cal/mol, assuming that the preexponential factors for these two processes are equal. If the preexponential factor for desorption is larger than that for migration, as might be expected, then δE would be somewhat larger than 800 cal/mol (22). Simulations were also performed for $p_d/p_m = 0.01$ and $p_d/p_m = 0.001$ to estimate the sensitivity of the fit. These runs allow us to conclude that the uncertainty in δE is approximately 200 cal/mol.

4. Conclusions

We have analyzed molecular beam reflectivity measurements by Monte-Carlo simulations of a model in which ethane adsorption can occur through two routes: a direct molecular adsorption pathway, and a precursor-mediated adsorption pathway in which the precursor is an ethane molecule trapped above

a previously adsorbed ethane molecule. We have performed simulations for the limiting case in which the flux incident upon the surface is infinitesimally small, and also for cases in which this flux is not zero. It is possible to infer from the discrepancy between the 'tail' of the experimental data and the simulations with infinitesimally small flux that some accumulation of a second layer of ethane occurs. The simulations with non-zero flux allow us to determine the real time corresponding to each Monte-Carlo step in these simulations. Thus, it is possible to determine the rate of desorption of ethane from the second layer and hence the energy barrier for this process. This is approximately 4.5 ± 0.3 kcal/mol, and the barrier to migration of trapped ethane molecules is approximately 3.7 ± 0.2 kcal/mol. The saturation coverage for the second layer is approximately 0.06 relative to the saturation coverage of the first monolayer at 77 K.

It is difficult to imagine a simpler and yet more intuitively reasonable model that would give rise to the experimentally observed maximum in the probability of adsorption. The essential ingredient in the model is the physically reasonable assumption that an incident ethane molecule accommodates better if it impinges on a previously adsorbed ethane molecule than if it impinges on the bare iridium surface. It should be noted that the use of a square lattice to simulate the Ir(110)-(1x2) surface, which is a rectangular lattice, is acceptable. The probable anisotropy of the Ir(110)-(1x2) surface to diffusion need not be considered because the hopping of trapped ethane molecules occurs on top of a layer of molecularly adsorbed ethane, which probably presents an isotropic surface to a trapped ethane molecule. The validity of using a square lattice is also indicated by the good agreement obtained. It is gratifying that using values of p_0 obtained from experiments, values of p_f that are consistent with the beam flux, and assuming (reasonably) that $p_1 \sim 1$, it is possible to describe the probability of adsorption for the entire range of surface coverage from zero coverage to saturation using only a single value of p_d/p_m . This single value of p_d/p_m also describes the data

obtained using beams of different incident energies, and is physically consistent with the idea that the trapped ethane molecules are completely accommodated thermally to the surface.

Acknowledgment: This research was supported by the National Science Foundation under Grant No. CHE-8617826. Acknowledgment is also made to the donors of the Petroleum Research Fund for partial support of this research under Grant No. PRF 19819-AC5-C.

References

1. W.H. Weinberg, in **Kinetics of Interface Reactions**, Eds., H.J. Kreuzer and M. Grunze, Springer-Verlag, Heidelberg, 1987, p. 94.
2. I. Langmuir, *Chem. Rev.* **6**, 451 (1929).
3. J.B. Taylor and I. Langmuir, *Phys. Rev.* **44**, 423 (1933).
4. J.A. Becker, in **Structure and Properties of Solid Surfaces**, Eds., R. Gomer and C.S. Smith (Univ. of Chicago Press 1953) p. 459.
5. J.A. Becker and C.D. Hartman, *J. Phys. Chem.* **57**, 157 (1953).
6. G. Ehrlich, *J. Phys. Chem.* **59**, 473 (1955).
7. P. Kisliuk, *J. Phys. Chem. Solids* **3**, 95 (1957); **5**, 78 (1958).
8. P.W. Tamm and L.D. Schmidt, *J. Chem. Phys.* **52**, 1150 (1970); **55**, 4253 (1971).
9. L.R. Clavenna and L.D. Schmidt, *Surf. Sci.* **22**, 365 (1970).
10. C. Kohrt and R. Gomer, *J. Chem. Phys.* **52**, 3283 (1970).
11. D.A. King and M.G. Wells, *Surf. Sci.* **23**, 120 (1971).
12. D.A. King and M.G. Wells, *Proc. Roy. Soc. (Lond.)* **A339**, 245 (1974).
13. E.S. Hood, B.H. Toby and W.H. Weinberg, *Phys. Rev. Lett.* **55**, 2437 (1985).
14. O.M. Becker and A. Ben-Shaul, *Phys. Rev. Lett.* **61**, 2859 (1988).
15. Since the product of the adsorption reaction is physically adsorbed ethane, there can be no "intrinsic" precursor to adsorption in the usual sense on the bare surface (1).
16. C.B. Mullins and W.H. Weinberg, *J. Chem. Phys.* (submitted).
17. T.S. Wittrig, P.D. Szuromi and W.H. Weinberg, *J. Chem. Phys.* **76**, 3305 (1982).

18. C.B. Mullins, C.T. Rettner, D.J. Auerbach and W.H. Weinberg, to be published.
19. R.J. Hamers, P.L. Houston and R.P. Merrill, *J. Chem. Phys.* **88**, 6548 (1988).
20. L. Wilzen, S. Andersson and J. Harris, *Surf. Sci.* **205**, 387 (1988).
21. The values of E_d are calculated from $R_d = k_d^{(0)} \exp(-E_d/k_B T)$, where $k_d^{(0)}$ is assumed to be 10^{13} s^{-1} . If $k_d^{(0)}$ is assumed to be 10^{14} s^{-1} , the corresponding values of E_d would be about 0.4 kcal/mol greater than the values indicated in Table 1.
22. For example, if the ratio of the preexponential factors $k_d^{(0)}/k_m^{(0)}$ were equal to 100, then δE would be equal to 1500 cal/mol, and E_m would be 3.0 ± 0.2 kcal/mol.

Table 1

<u>Set</u>	<u>E_i</u>	<u>θ_i</u>	<u>p₀</u>	<u>p₁</u>	<u>E_d</u>	<u>Flux</u>
a	2.2	0	0.95	1.00	4.55	0.087
b	3.7	45	0.90	1.00	4.57	0.077
c	5.2	45	0.83	0.97	4.53	0.102
d	6.6	0	0.68	0.96	4.52	0.107
e	10.0	45	0.50	0.95	4.53	0.104
f	10.0	22.5	0.45	0.95	4.55	0.085

Values of parameters used in simulations and experiments. The energy of the beam E_i is in units of kcal/mol and the incident angle θ_i is in degrees. The energy barrier for desorption is in units of kcal/mol and the fluxes in units of $s^{-1} \sigma^{-1}$ for each beam energy, where σ is the area occupied by a molecularly adsorbed ethane molecule in a saturated first layer on the Ir (110)-(1x2) surface at 77 K. The probability of adsorption on the clean surface (in the limit of zero coverage) is p_0 , and the probability of trapping on top of an adsorbed ethane molecule is p_1 . The value of p_d/p_m , where p_d is the probability of success of an attempted desorption event and p_m is the probability of success of an attempted hop by a trapped particle, is 0.005 for all the simulation results shown here.

Figure Captions

Figure 1. The crosses indicate experimental data, and the lines indicate results from simulations in the zero-flux limit. The abscissa is time in units of 0.1 s. For each experiment, the time has been multiplied by $\cos \theta_i$, where θ_i is the angle of incidence in order to normalize the area of the surface upon which ethane molecules are incident. The parameters for each figure can be found in the corresponding rows of Table 1.

Figure 2. The crosses indicate experimental data as in Fig. 1. The circles indicate results from simulations in which the value of p_f , and thus the flux which is equal to p_f/τ_r , is not zero. The abscissa for the Monte-Carlo data has been converted from Monte-Carlo steps/site to real time. The conversion factor τ_r gives the number of seconds in real time to which each Monte-Carlo step/site corresponds. This, as explained in the text, enables an absolute determination of the desorption rate from the second layer. The units for the abscissa are 0.1 s.

Figure 3. Simulations in which p_f is not zero enable a second layer of particles to accumulate. The fractional coverage of this second layer is shown here as a function of time which, as in Fig. 2, has been converted from Monte-Carlo steps/site to real time.

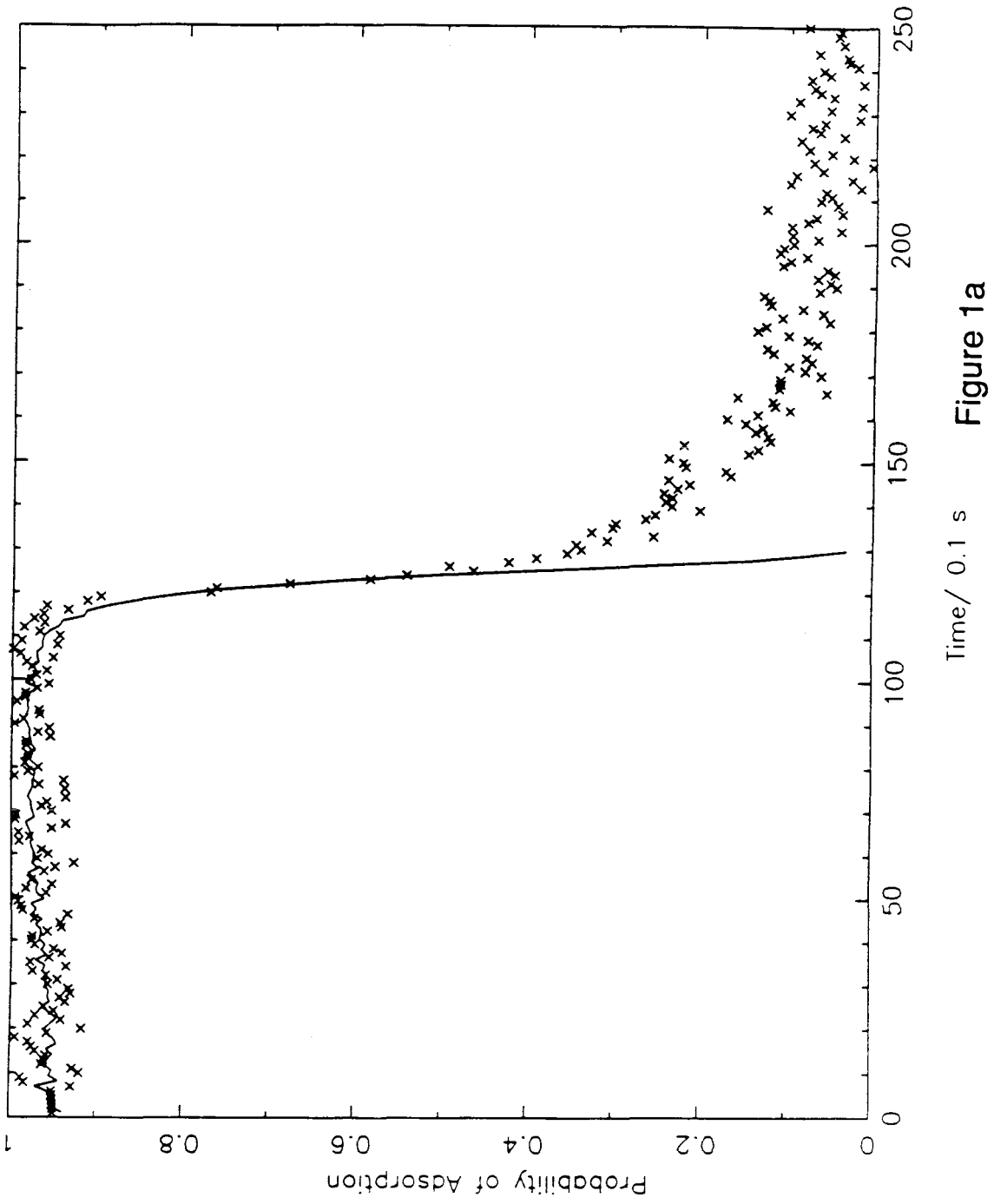


Figure 1a

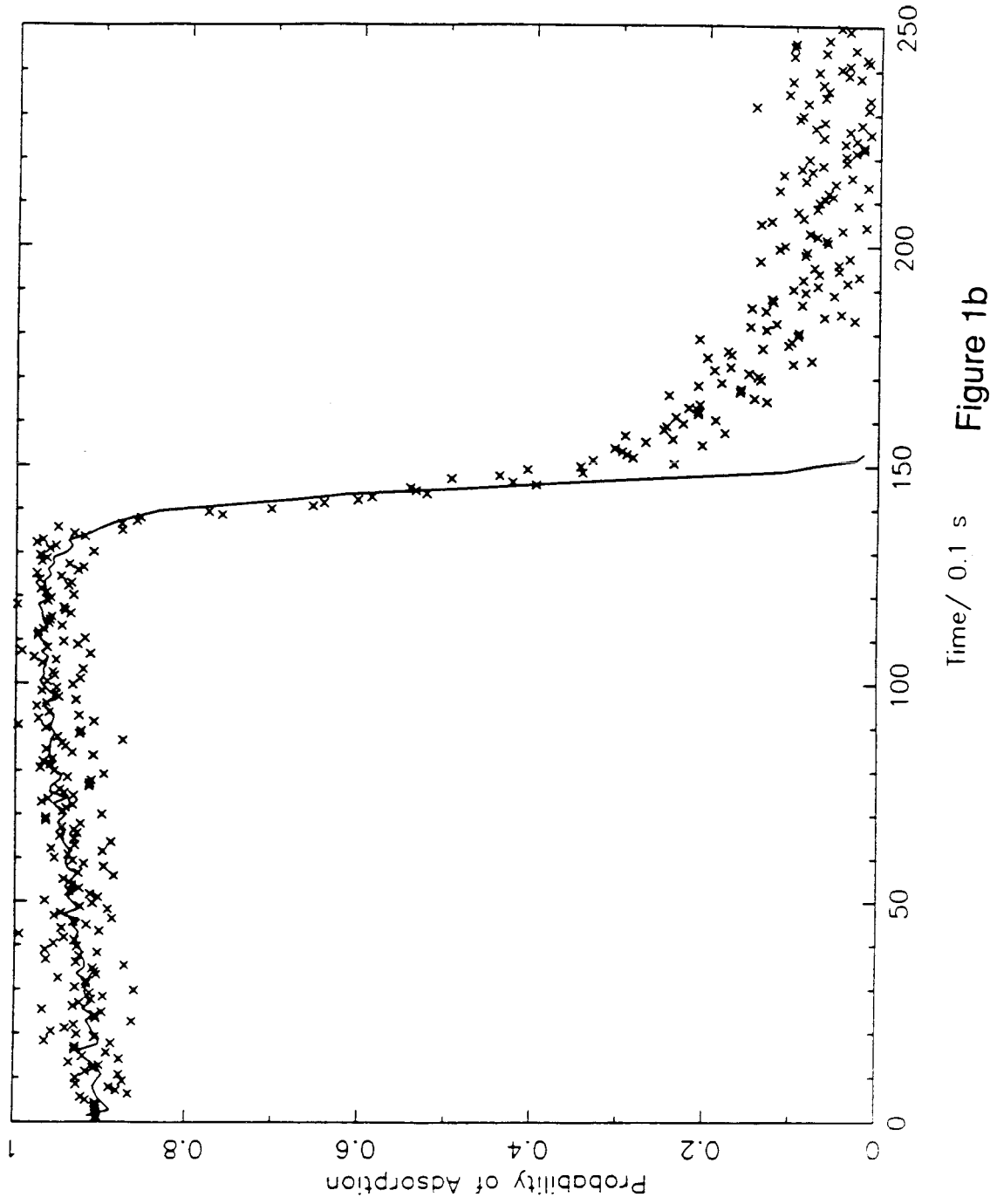


Figure 1b

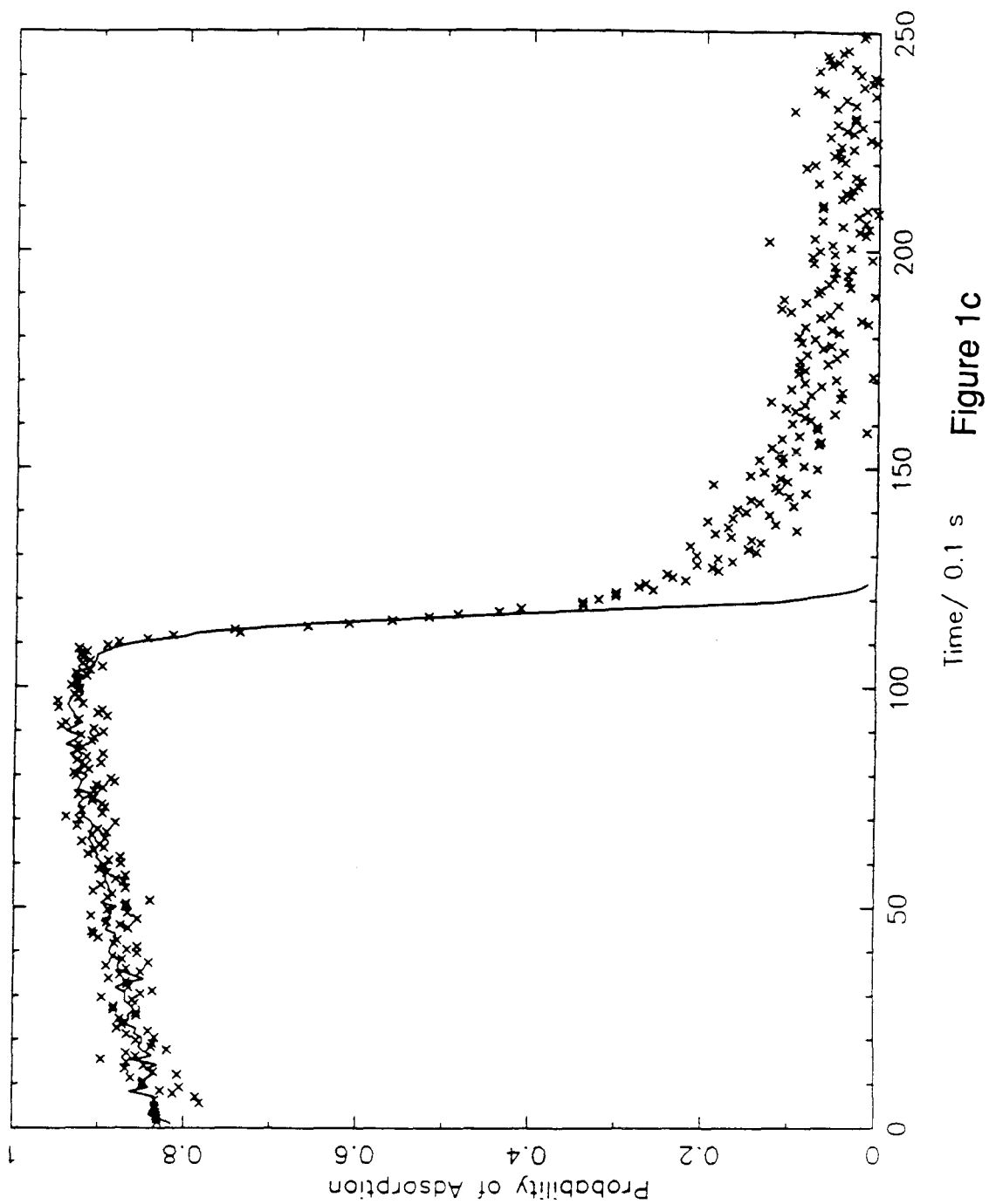


Figure 1c

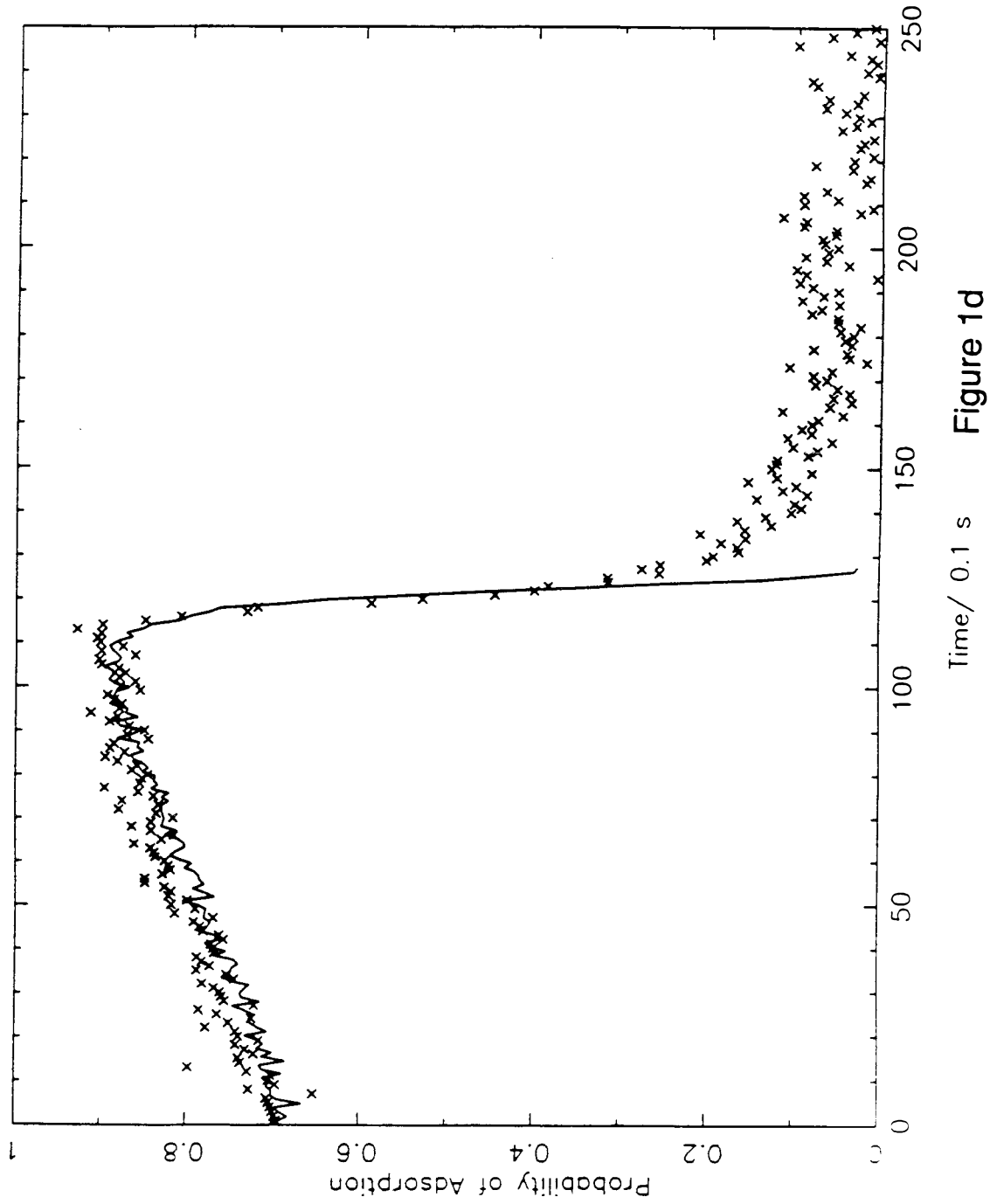


Figure 1d

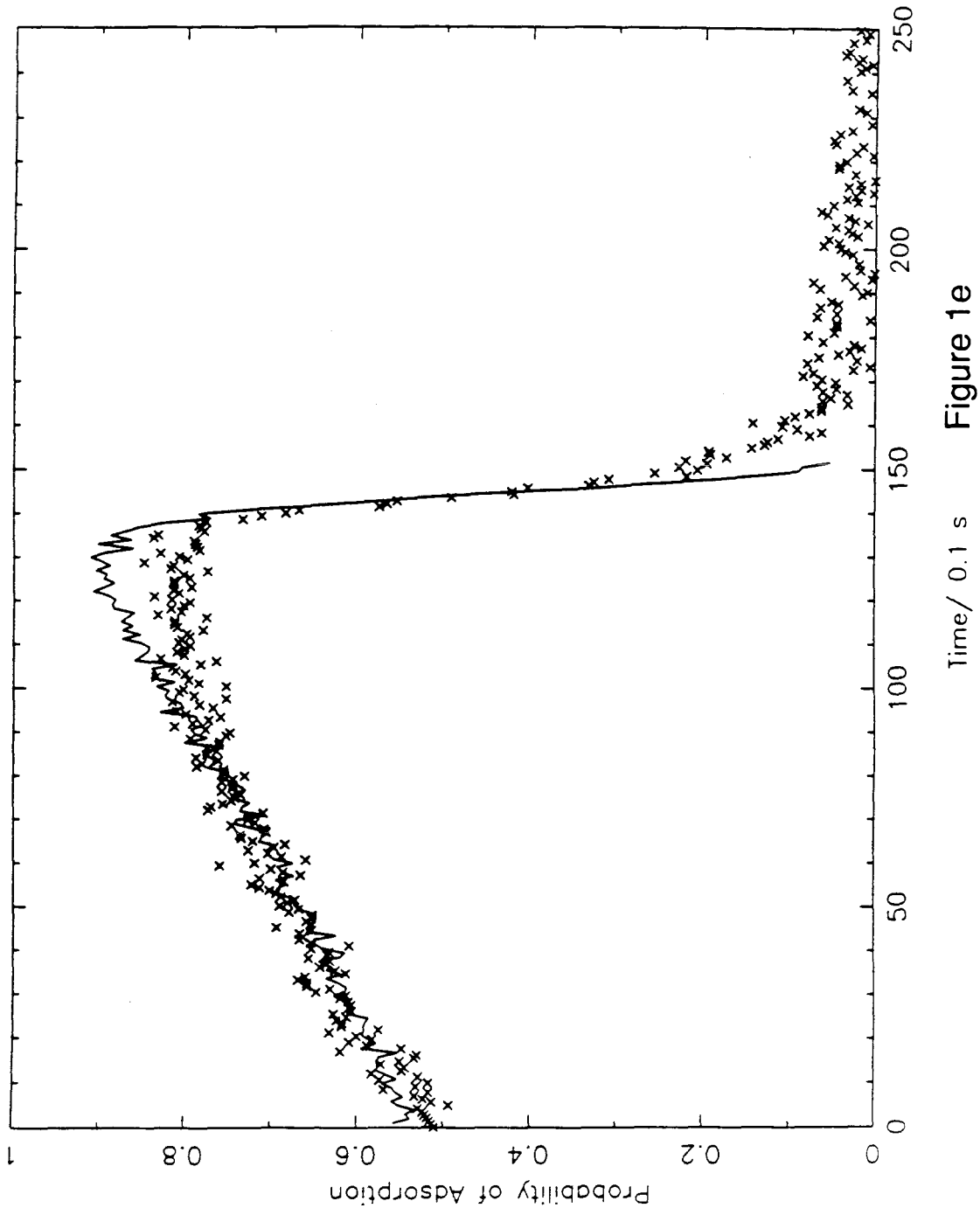


Figure 1e

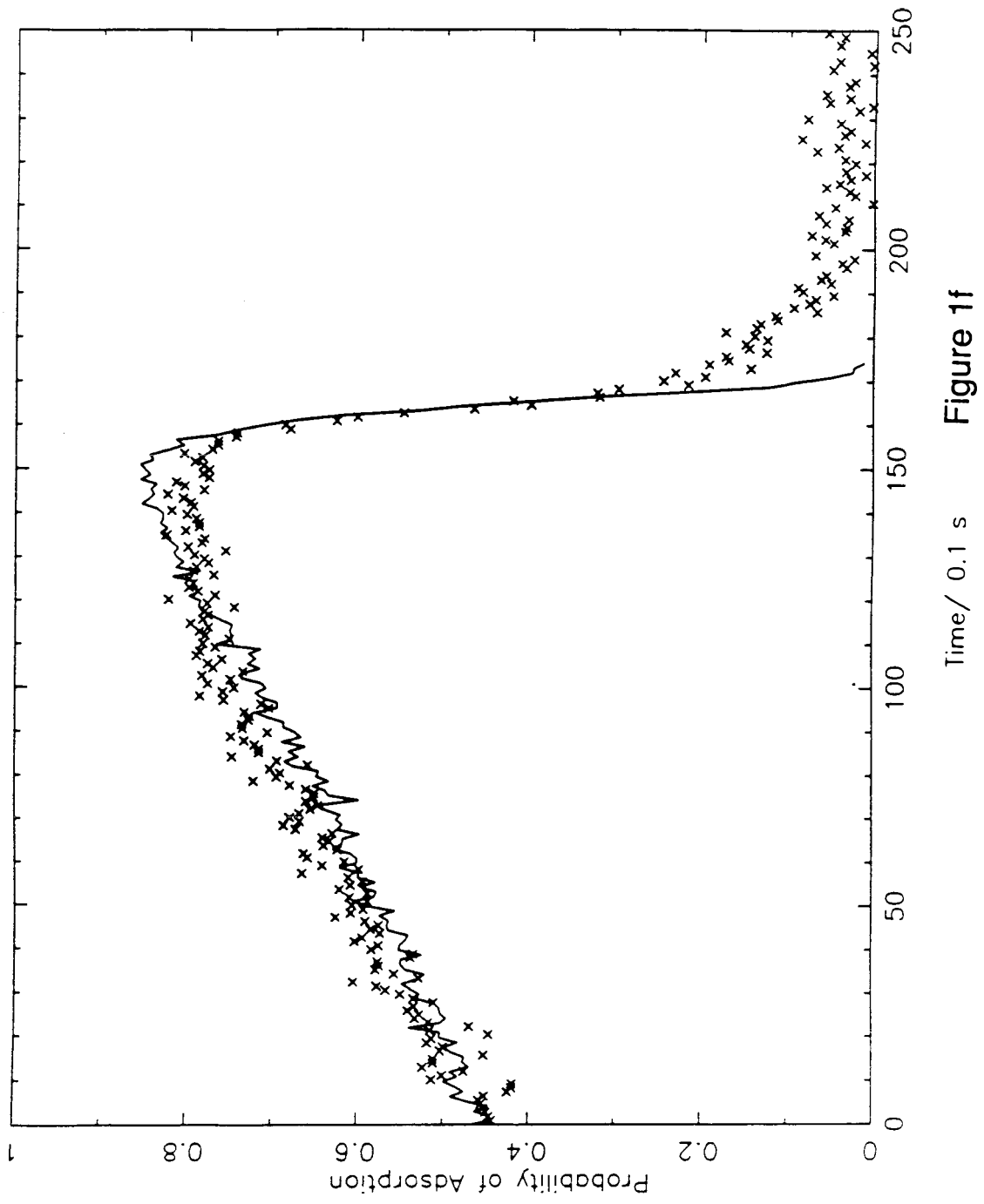
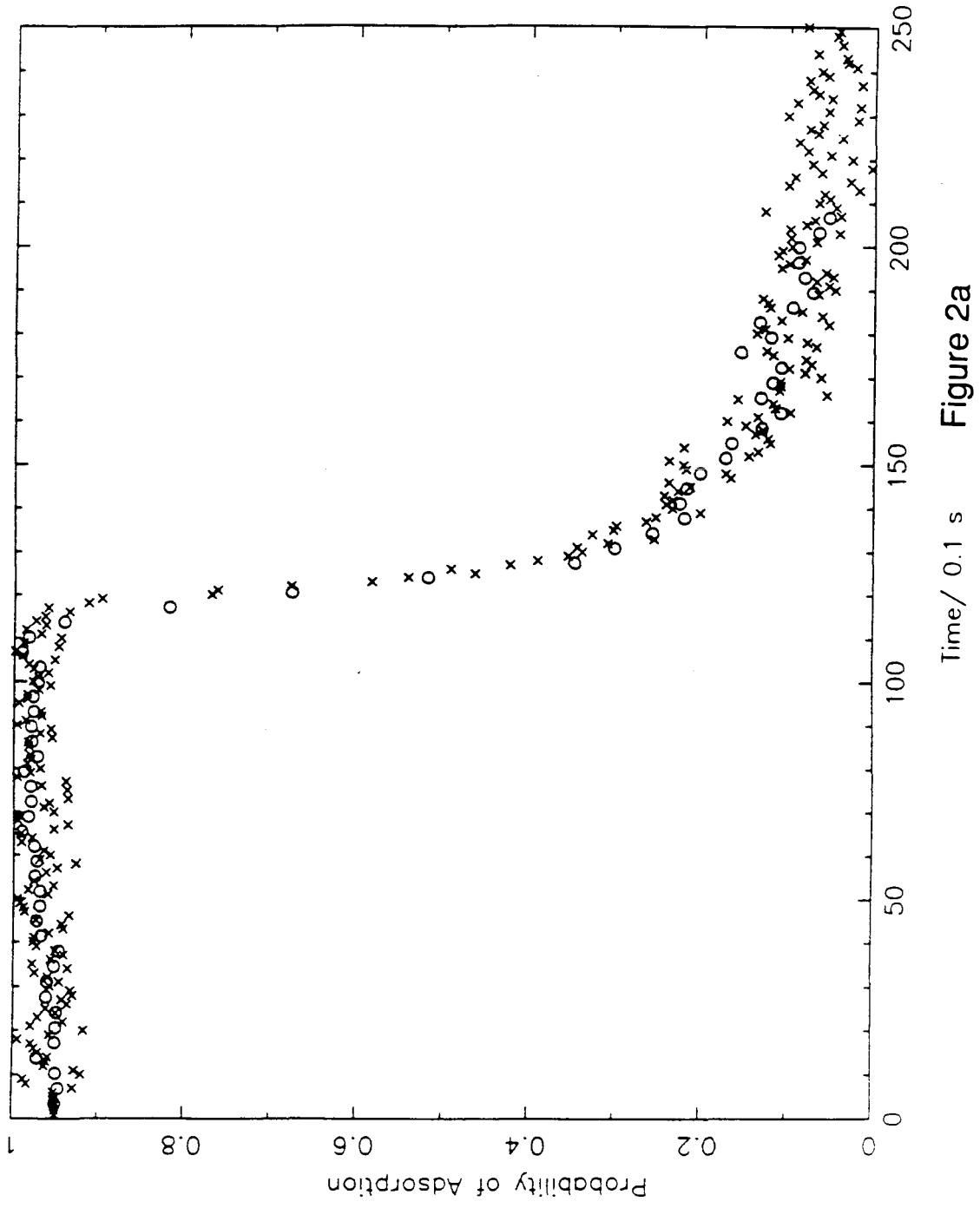


Figure 1f



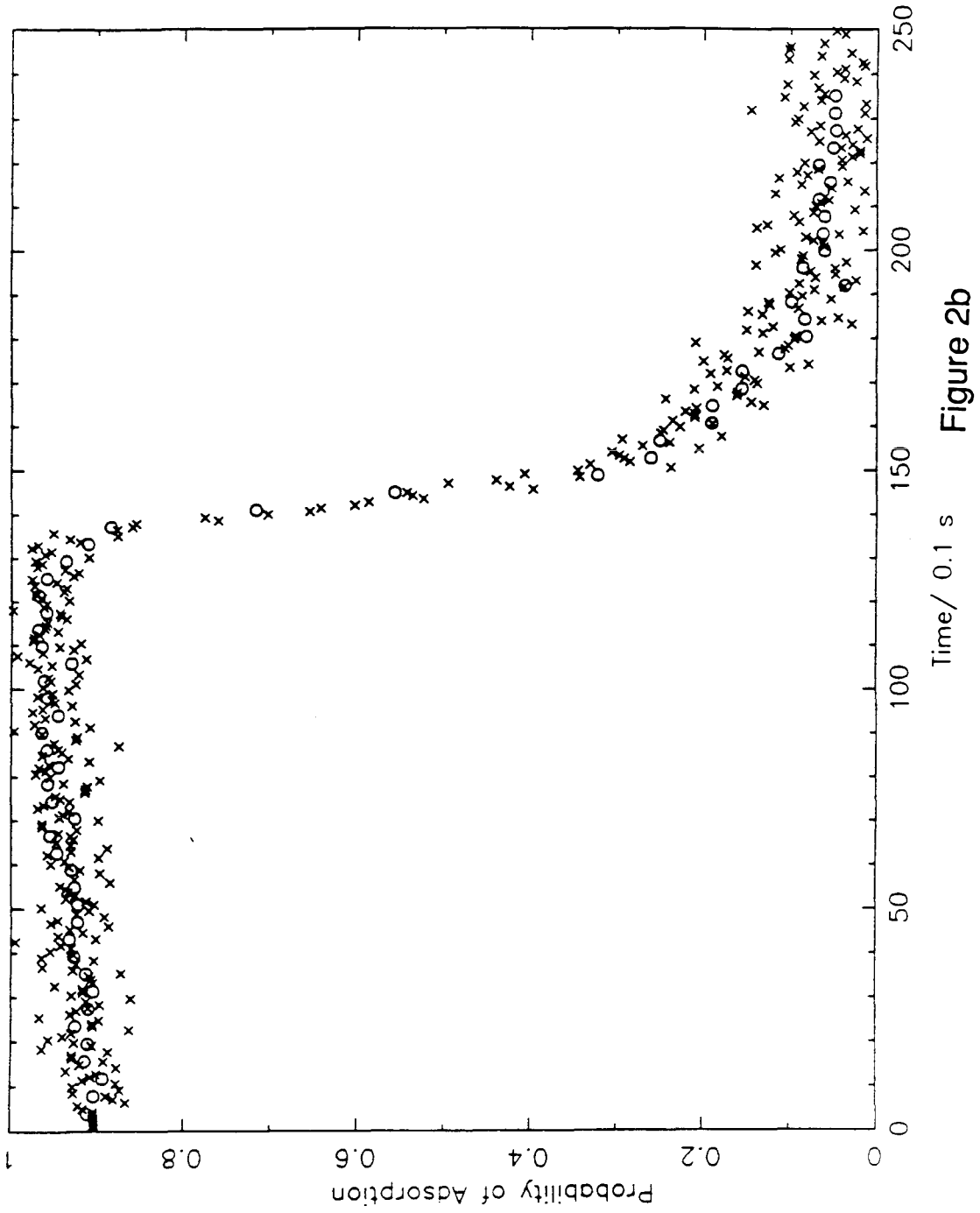


Figure 2b

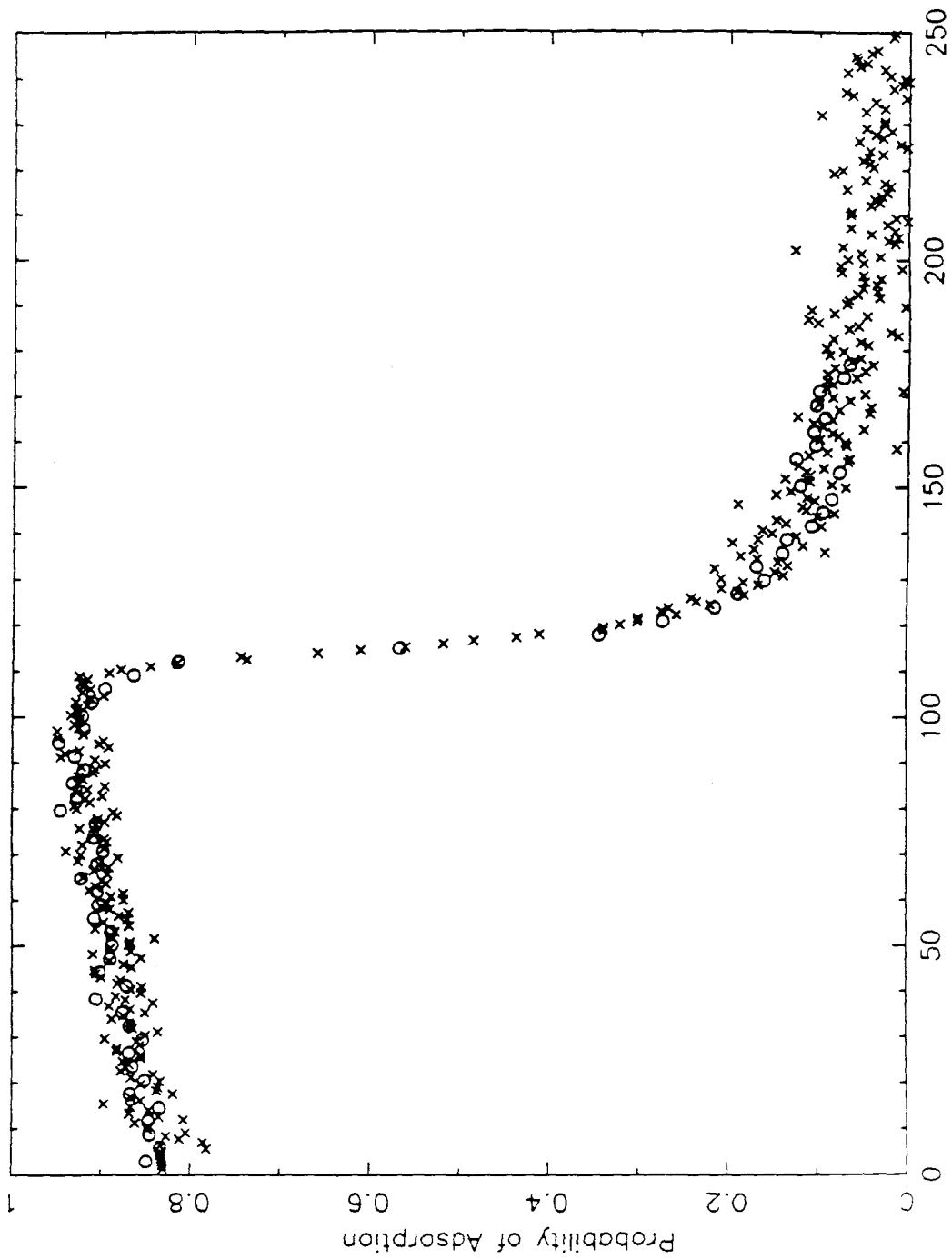


Figure 2c

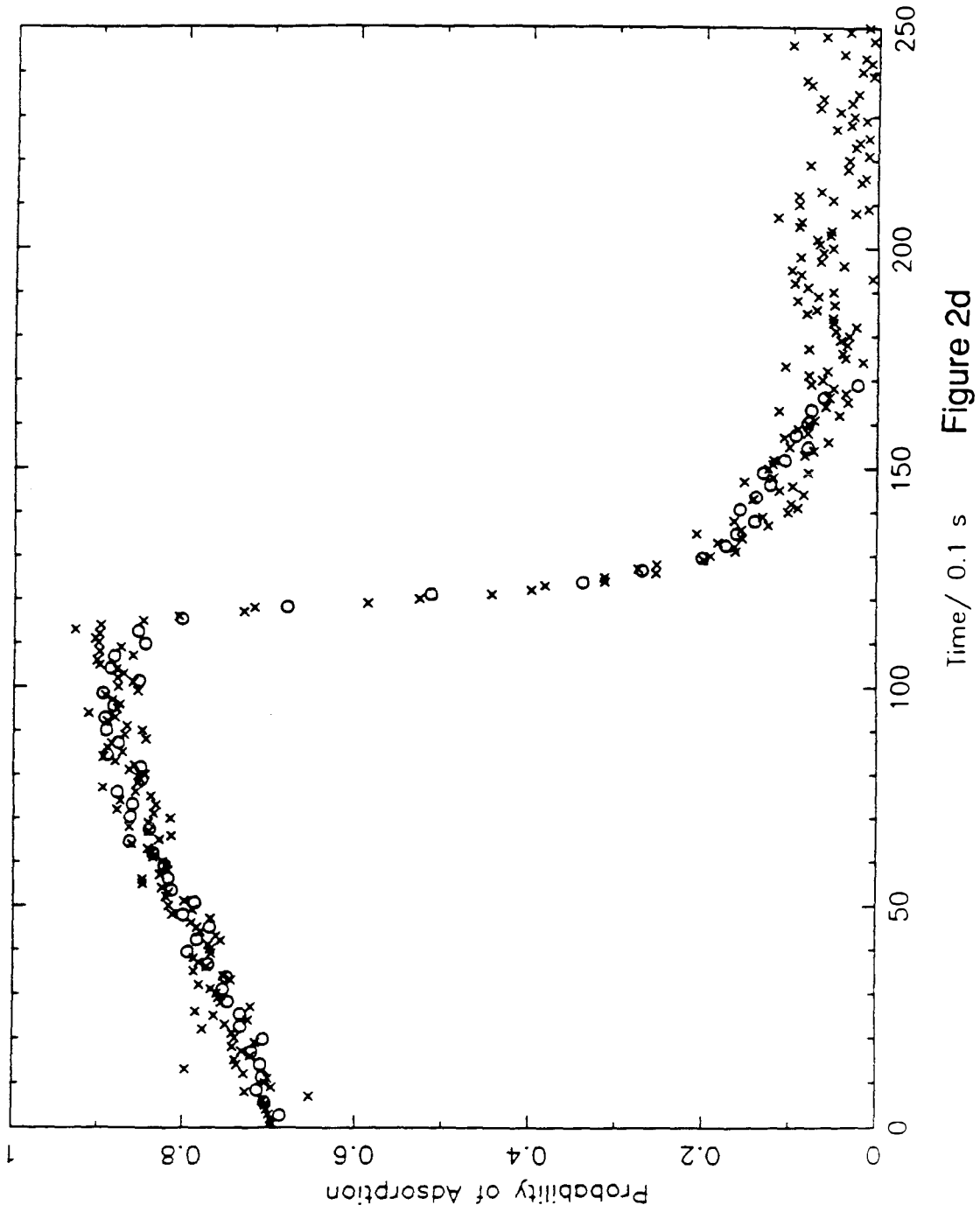


Figure 2d

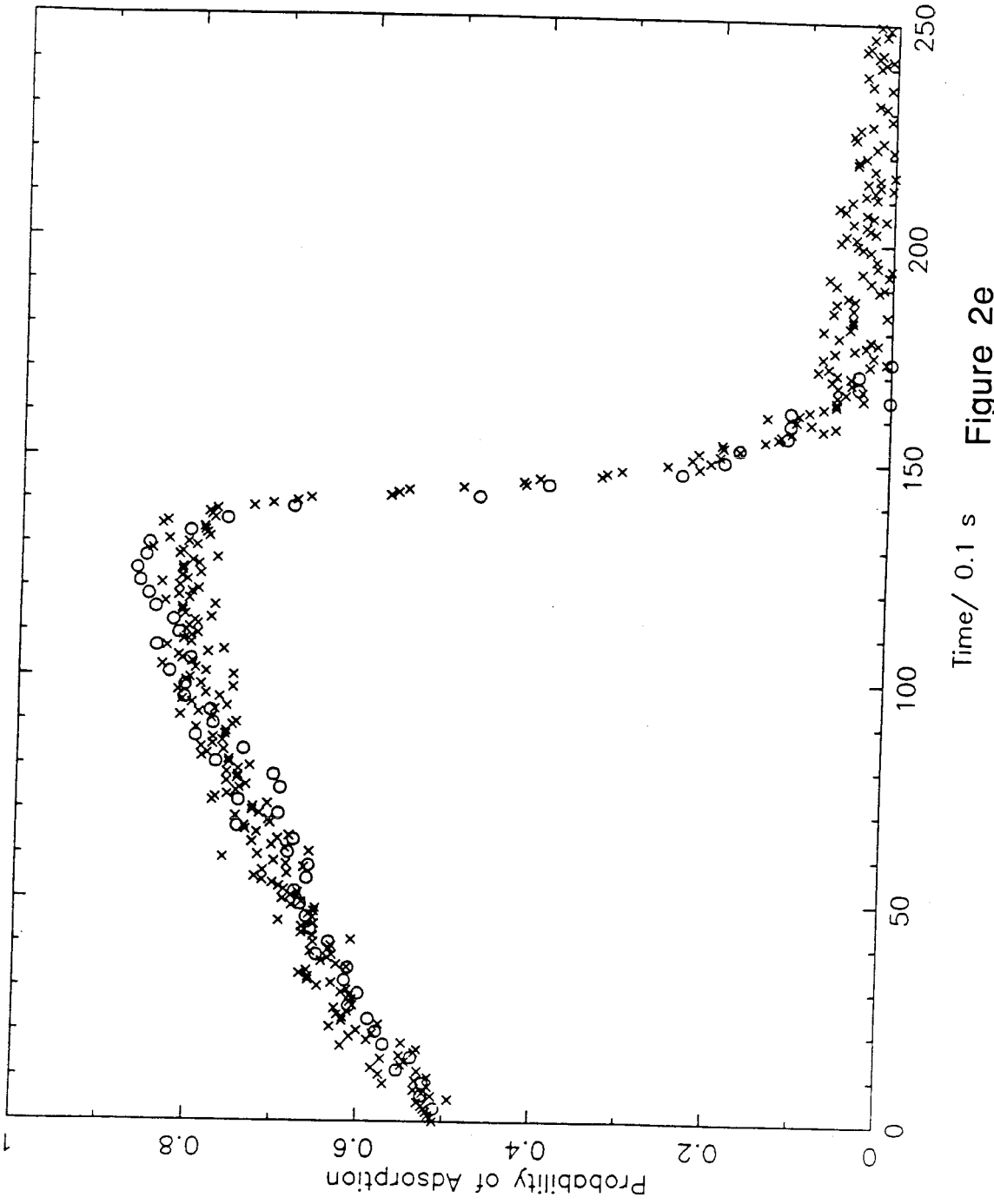


Figure 2e

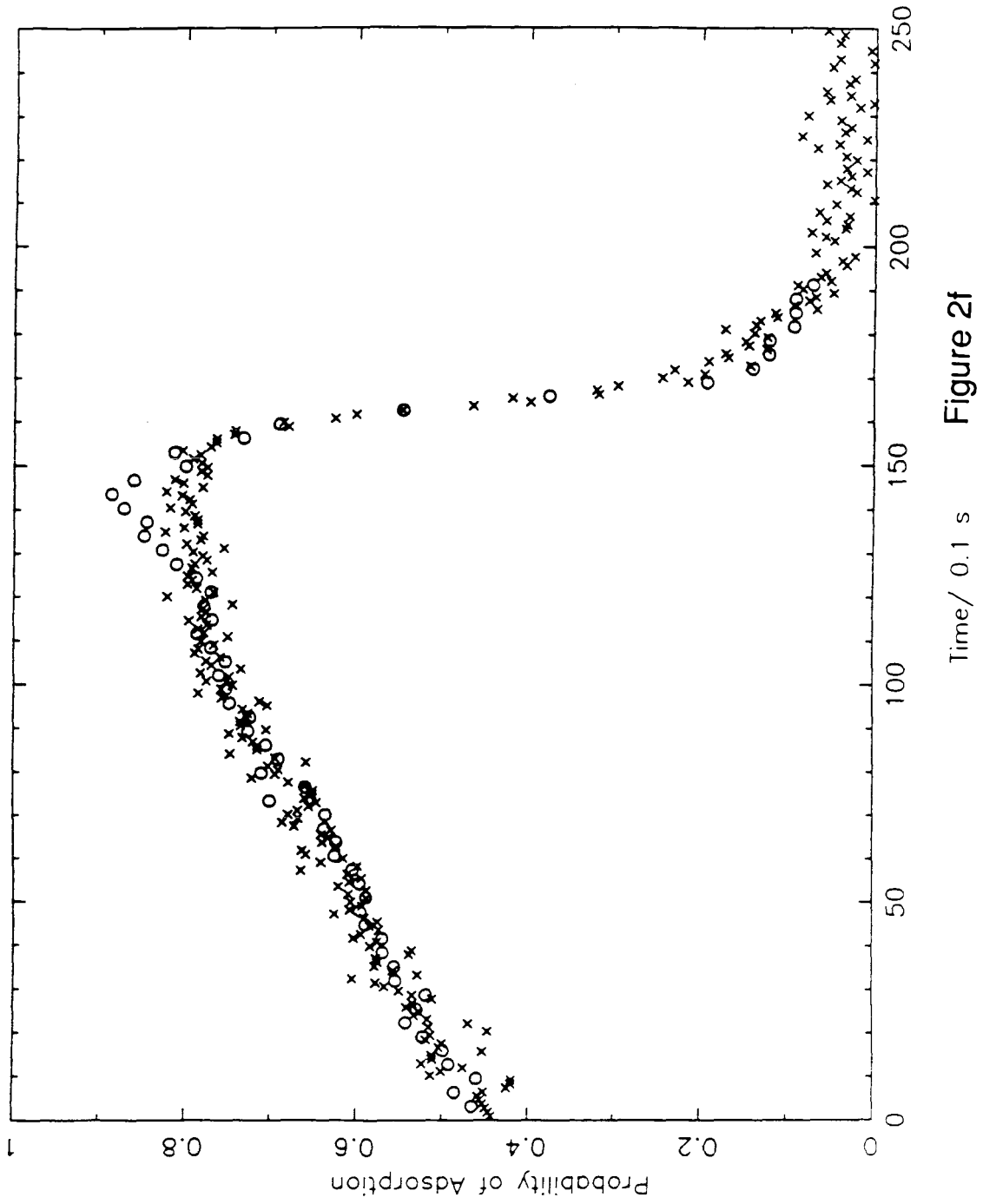


Figure 2f

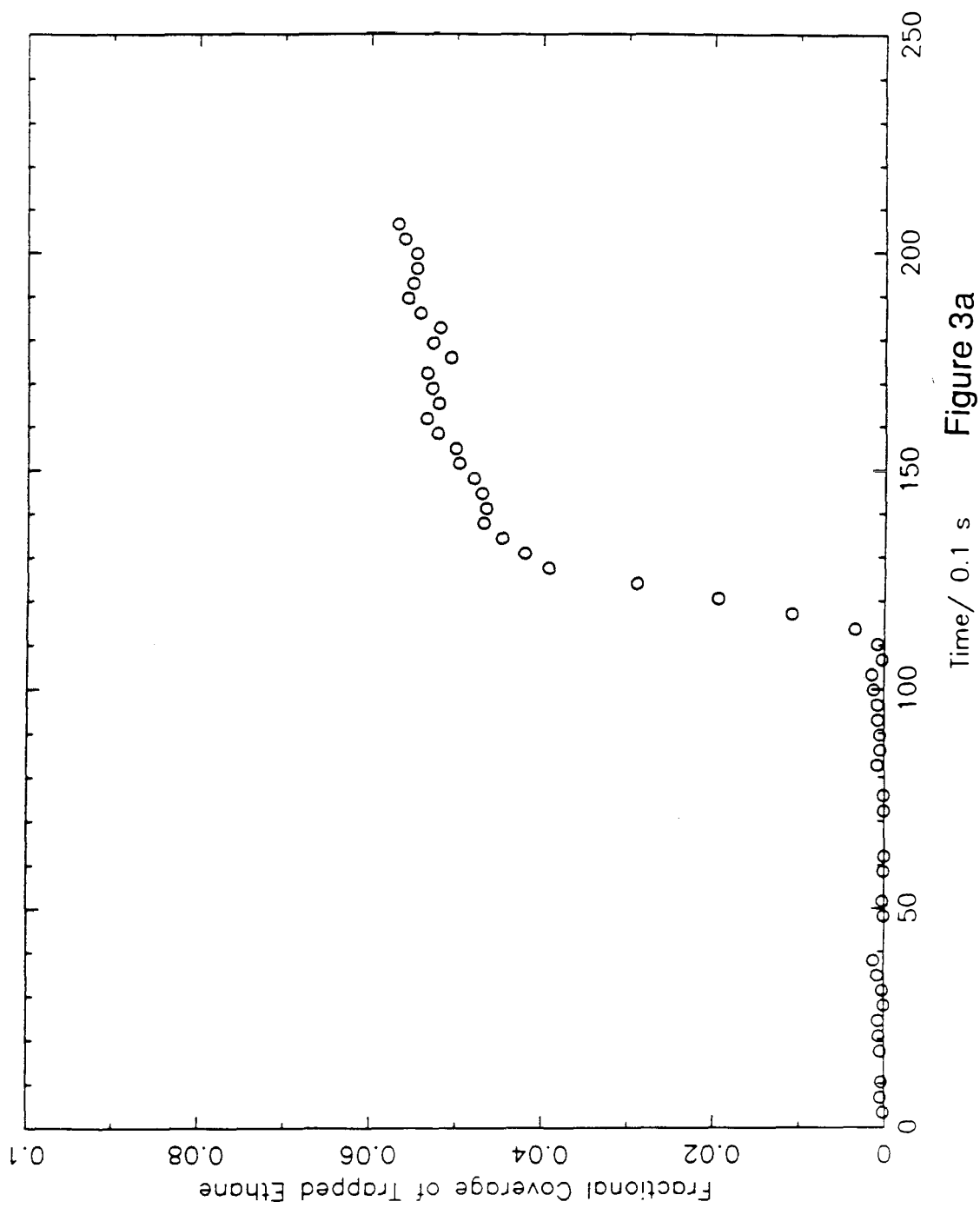


Figure 3a

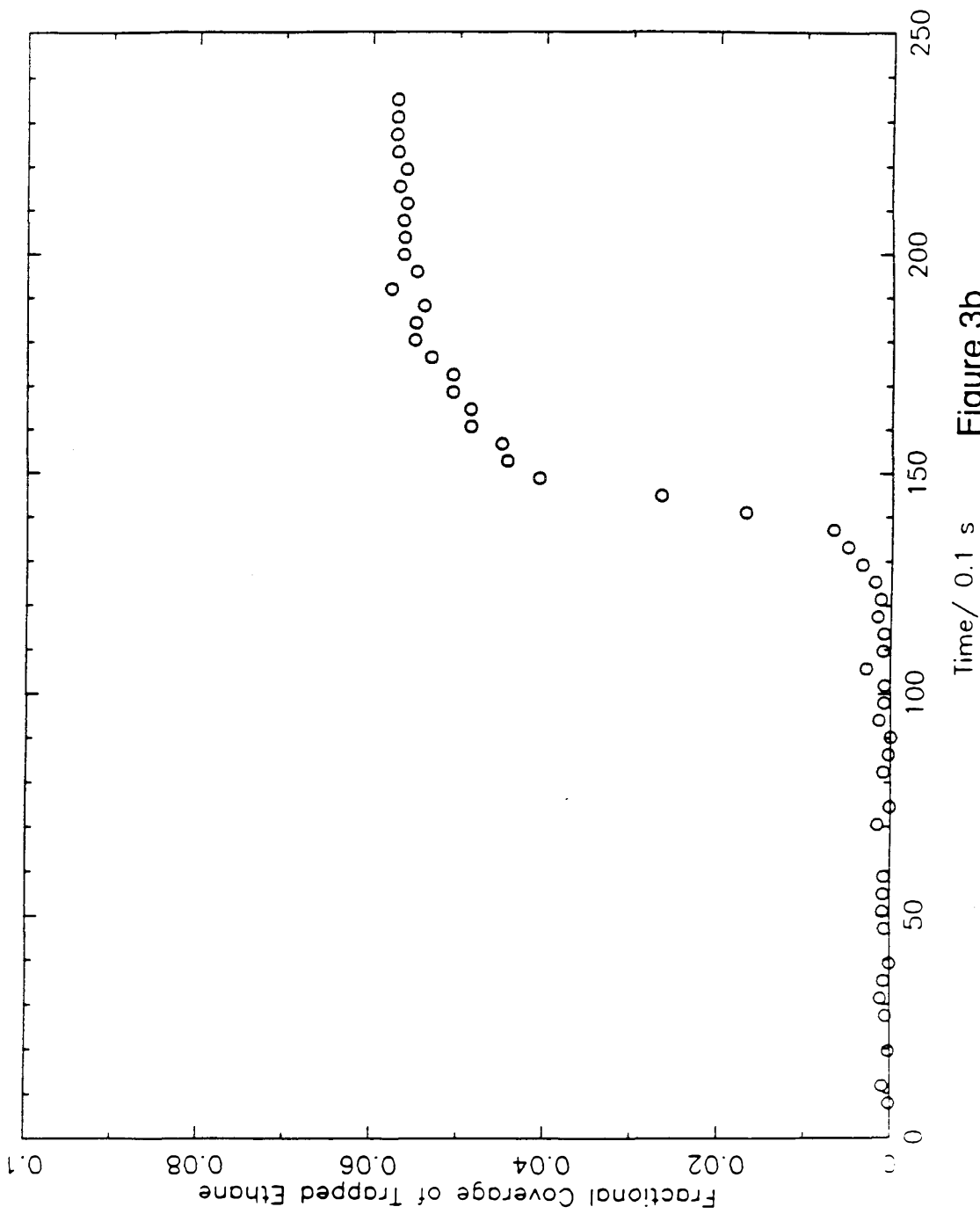


Figure 3b

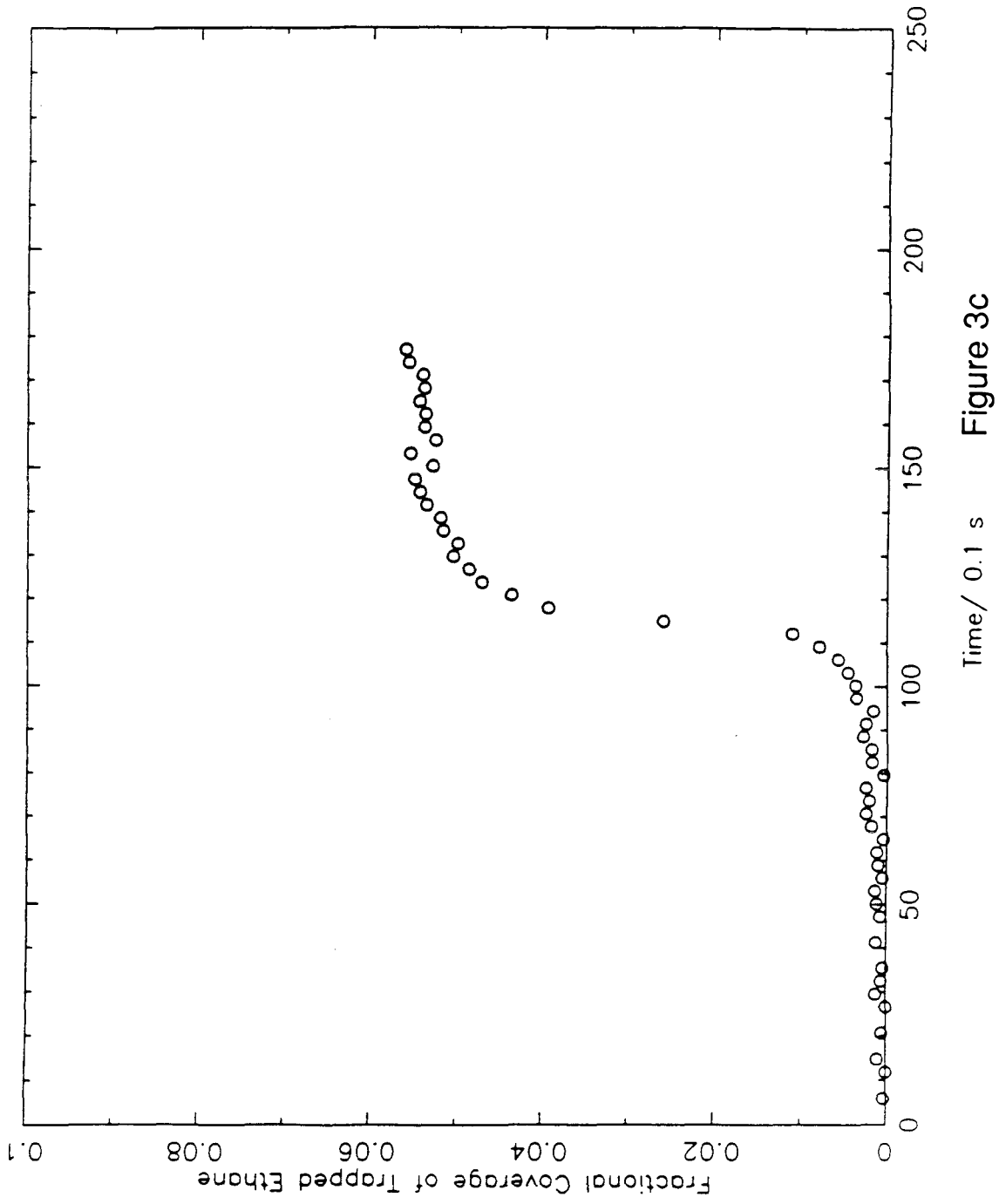


Figure 3c

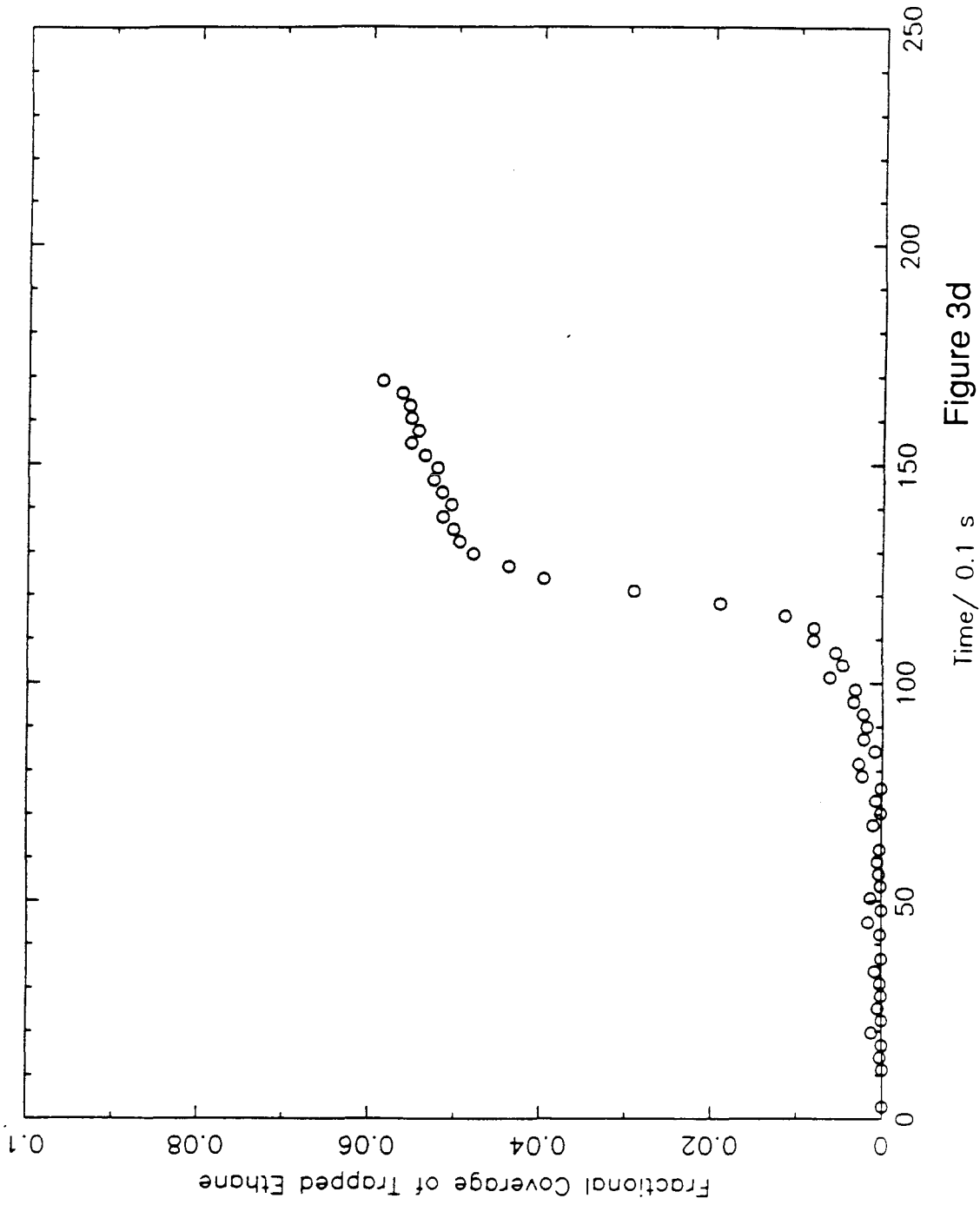


Figure 3d

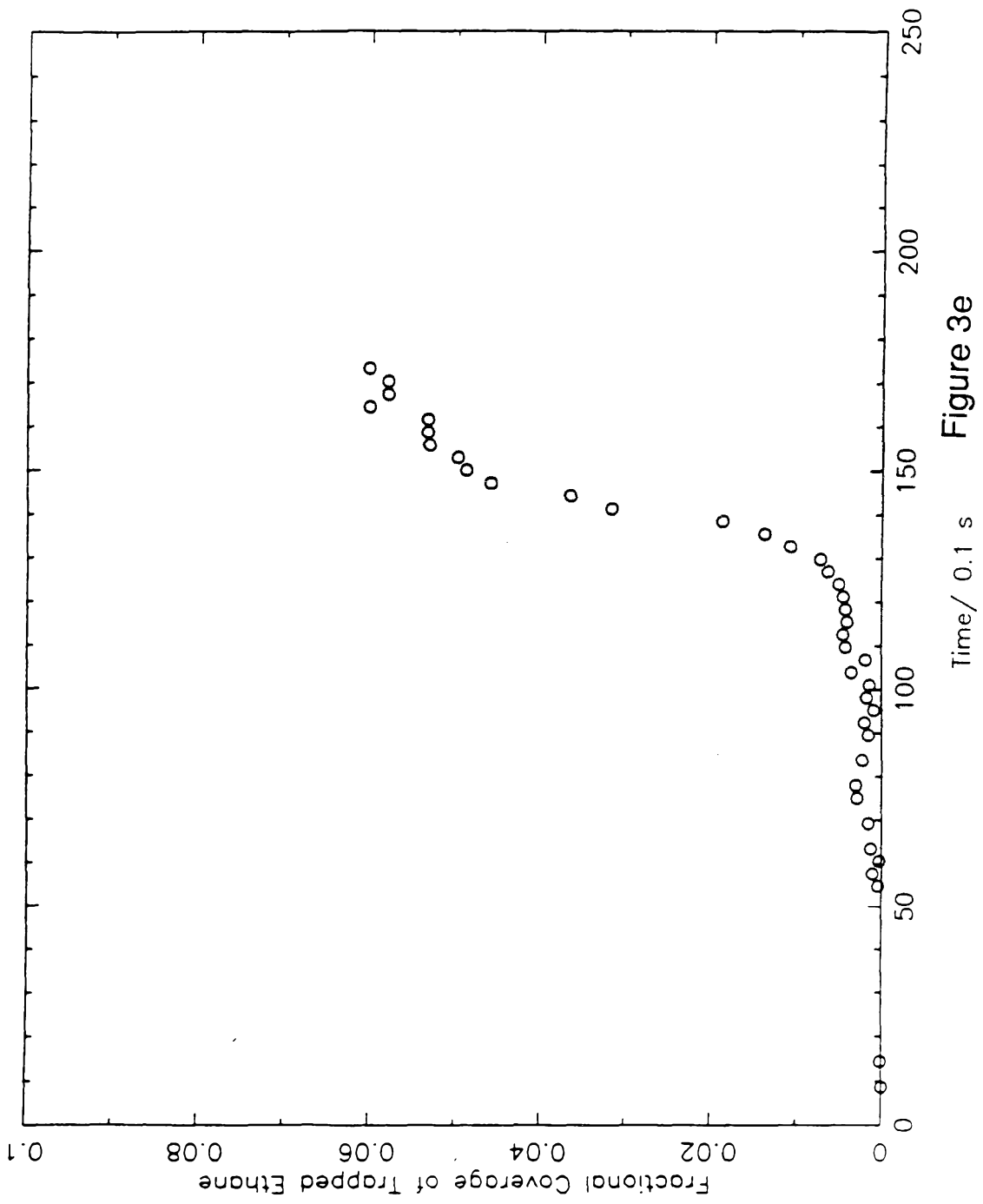


Figure 3e

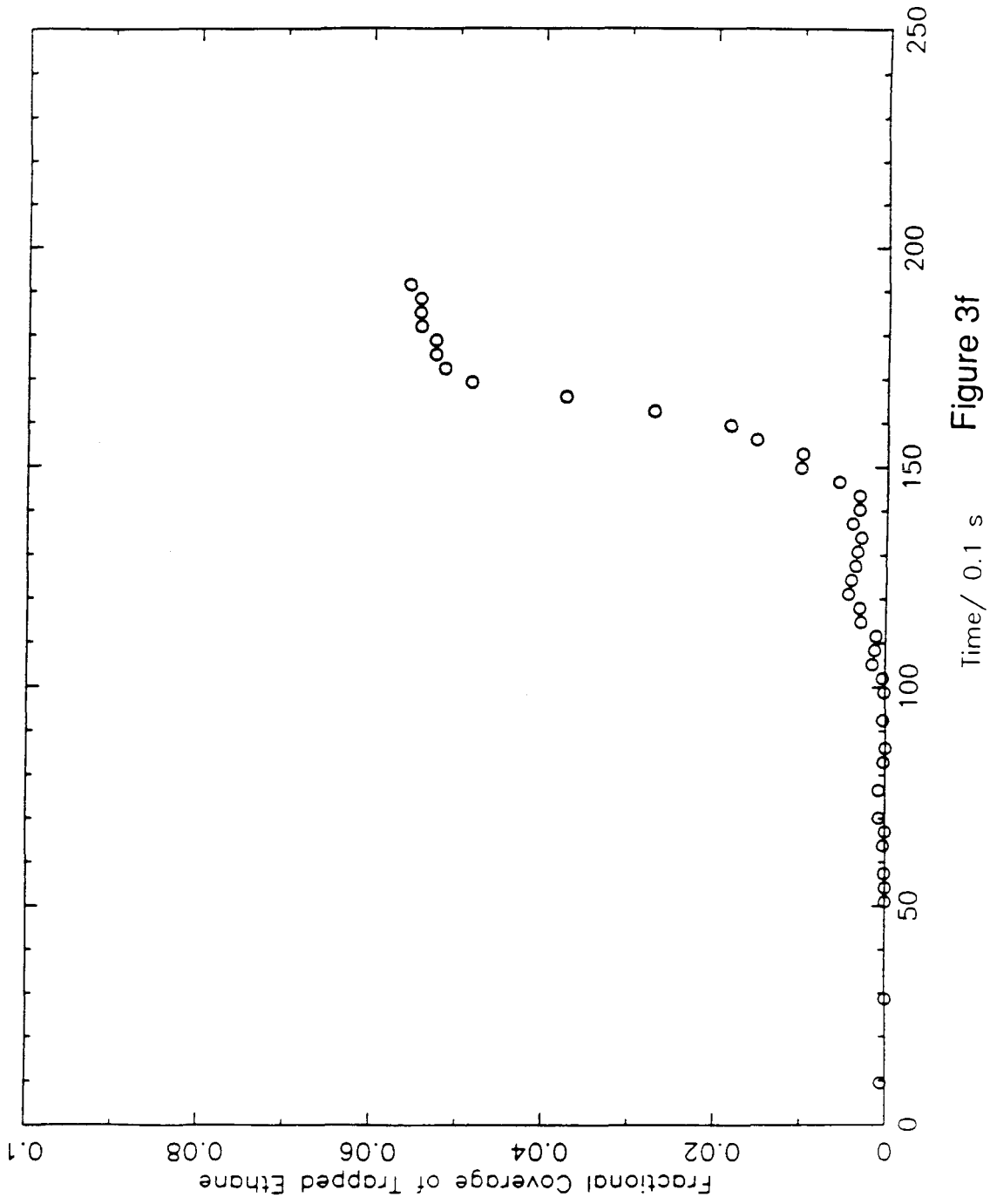


Figure 3f

APPENDIX B

DESORPTION AND TRAPPING OF ARGON AT A 2H-W(100) SURFACE
AND A TEST OF THE APPLICABILITY OF DETAILED BALANCE TO A
NONEQUILIBRIUM SYSTEM

[The text of Appendix B consists of an article coauthored with C. T. Rettner and E. K. Schweizer, which has appeared in *J. Chem. Phys.* **90**, 3800 (1989).]

Desorption and trapping of argon at a 2H-W(100) surface and a test of the applicability of detailed balance to a nonequilibrium system

C. T. Rettner, E. K. Schweizer, and C. B. Mullins^{a)}
IBM Almaden Research Center, K33/801, San Jose, California 95120-6099

(Received 3 October 1988; accepted 8 December 1988)

Molecular beam techniques have been used to probe the dynamics of the trapping and trapping-desorption of Ar at a hydrogen-saturated W(100) surface. Trapping probabilities have been measured as a function of incidence energy E_i , and angle θ_i for a surface temperature T_s of 85 K. We find that this probability scales approximately with $E_i \cos \theta_i$, rather than E_i or the so-called "normal energy" $E_i \cos^2 \theta_i$. Trapping probabilities approach unity for low energies, falling to 0.5 and 0.05 for $E_i \cos \theta_i \sim 30$ and 100 meV, respectively. The time-of-flight distributions of scattered Ar are clearly bimodal in many cases, having both direct-inelastic and trapping-desorption components. The latter component has been characterized over a wide range of conditions to provide information on the desorption of Ar from this surface. We find that desorbing species emerge with a near-cosine angular distribution for $T_s \approx 85$ K. However, these distributions become increasingly noncosine as T_s is raised, becoming substantially broader than cosine. In addition, at the lowest temperature employed (~ 85 K), the velocity distributions of the desorbing atoms are well described by Maxwell-Boltzmann distributions characteristic of the surface temperature. At higher temperatures, these distributions are still approximately Boltzmann, but the characteristic temperature falls below T_s . The "lag" between this effective temperature and T_s increases with T_s and is most pronounced for atoms desorbing at angles close to the normal. We show that the desorption results are very close to the predictions of a model in which angular and velocity distributions for desorption are synthesized by applying detailed balance arguments to the trapping data. Similarly the trapping results are close to trapping curves extracted from the desorption data.

I. INTRODUCTION

Trapping and desorption are two key steps in gas-surface chemistry and are arguably two of the most elementary.¹ The dynamics of the trapping process in particular would appear transparent. Here a species must simply lose sufficient energy in colliding with the surface to be unable to escape the gas-surface potential. Desorption is the reverse of this, occurring when the gas-surface coordinate accumulates energy in excess of the well depth. In reality, the dynamics of such systems is deceptively complex. Current descriptions of the trapping process are far from adequate, and "in spite of being investigated both experimentally and theoretically for almost a century, the mechanism of desorption is still not understood in detail."²

In the case of trapping, the dynamics are complicated by the fact that while the initial step requires only loss of momentum normal to the surface, parallel momentum must also be lost before trapping is assured. This is often a relatively slow process,³ so that the dependence of the trapping probability on incidence angle, for example, is difficult to predict.⁴ This is true even in the absence of appreciable chemical interactions, as for the adsorption of the rare gases on smooth metal surfaces. Again, modeling of the energy transfer dynamics strictly requires accurate knowledge of the full hyperpotential surface of the system. Approximate

methods can be of value but rely heavily on experimental input to set parameters. Thus cube models require knowledge of the effective cube mass, but since this mass may vary with collision energy, they provide little more than a consistency check for measurements. In fact there have been remarkably few detailed experimental studies to provide a basis for such modeling. Thus while some aspect of rare gas scattering has received considerable attention, yielding detailed knowledge of inelastic scattering dynamics,⁵⁻¹¹ the trapping process has rarely been addressed specifically. The few exceptions include the extraction of thermally averaged trapping probabilities from accommodation coefficients,¹² and a small number of measurements for Ar on Pt(111),¹³ and Ir(110).¹⁴ Relatively detailed measurements have been reported recently for the trapping of Ne on Ru(001).¹⁵ Although these results are of great fundamental interest, they may not be typical as the low mass and weak binding of Ne serve to restrict trapping to very low energies, where the dynamics are strongly affected by quantum effects.

The primary obstacle to developing a detailed theoretical treatment of thermal desorption is the rare nature of the relevant events. In principle, one would like to picture the entire process by which desorbing species acquire energies of many times kT before escaping into the vacuum. However, this may require, say, 10^{10} vibrations in the gas-surface well. If initial conditions are chosen such that desorption is relatively prompt, it is difficult to be sure that the chosen trajectories correspond to a representative sample. This makes

^{a)} Permanent address: Department of Chemical Engineering, California Institute of Technology, Pasadena, CA.

"brute force" computation impractical, requiring instead the application of special techniques for dealing with infrequent events.^{3,16} Again, comparison with experiment is vital. Of the detailed studies reported to date, the majority have concerned recombinative desorption, where the desorbing species is the product of a surface reaction.² Here the dynamics appear to be dominated by a potential barrier which serves, for example, to focus the desorbing flux close to the surface normal. In contrast, the desorption of Xe from Pt(111) is found to follow a cosine distribution,¹⁷ while Ar desorbs from this surface into a still broader distribution.¹³

Faced with the paucity of data and the difficulties in modeling these two processes, it is reasonable to exploit their complementary nature by correlating dynamical results for the two. At the most basic level, microscopic reversibility allows desorption to be studied computationally by following trajectories of species which trap,^{3,16} thereby circumventing the sampling problems encountered in the forward direction. More generally, for systems at equilibrium, the principles of detailed balance and/or reciprocity can be used to rigorously characterize the desorption process given knowledge of only the trapping dynamics, and vice versa.^{2,18-24} As will be discussed later, these principles are based on time-reversal invariance and serve to maintain the steady properties of equilibrated systems. However, it is not immediately obvious how to treat nonequilibrium systems. While it is reasonable to imagine that detailed balancing will not lead to useful predictions for highly nonequilibrium systems or systems that are incapable of reaching equilibrium, detailed balance *does* appear to hold, at least approximately, for many nonequilibrium systems of interest.^{13,18,19,22,24}

In this paper we present a study of the Ar/2H-W(100) system in which we have measured the dependence of the trapping probability on incidence kinetic energy E_i and angle θ , and have determined the velocity distributions of desorbing Ar under conditions that facilitate a direct comparison of the two processes. Specifically, trapping probabilities have been measured for a surface temperature T_s of 85, for E_i from ~ 29 to 250 meV and for $\theta = 30^\circ, 45^\circ,$ and 60° . Time-of-flight distributions have been obtained for angles θ , from -25° to 85° from the normal and for T_s from 85 to 275 K. (Here the minus sign indicates an angle on the opposite side of the normal to specular.) The 2H-W(100) surface is obtained by saturating a clean W(100) surface with H₂ and was chosen for study because, unlike clean W(100), it is possible to clearly resolve the direct-inelastic and trapping-desorption scattering components in the same manner as reported previously for the Xe/Pt(111) system.¹⁷ We find that trapping probabilities approach unity for low energies, falling to 0.5 and 0.05 for $E_i \cos \theta_i \sim 30$ and 100 meV, respectively. Desorbing species are found to emerge with a near-cosine angular distribution at $T_s = 85$ K. However, angular distributions are observed to become increasingly non-cosine as T_s is raised, becoming substantially broader than cosine. Similarly, at the lowest temperatures employed (~ 85 K), the velocity distributions of the desorbing atoms are well-described by Maxwell-Boltzmann distributions characteristic of the surface temperature. At higher temperatures, these distributions are still approximately Max-

wellian, but the characteristic temperature falls below T_s . It is shown that the desorption results are very close to the predictions of a model in which angular and velocity distributions are synthesized for desorption by applying detailed balance arguments to the trapping data. Similarly the trapping results are close to trapping curves extracted from the desorption data. This nonequilibrium system is thus found to behave in a manner similar to what would be predicted at equilibrium.

II. EXPERIMENTAL

A. General

The apparatus and techniques have been described in detail elsewhere,²⁵⁻²⁷ but will be summarized here for completeness. Supersonic beams of Ar are directed at a sample mounted in a UHV chamber on a manipulator which provides accurate control of the incidence angle and surface temperature in the range ~ 85 to 2500 K. The sample consists of a W(100) crystal that has been prepared and cleaned using standard techniques. Sharp LEED patterns are obtained and contamination levels are below 1% as determined by Auger electron spectroscopy. In addition, He scattering gives a specular peak with a width indistinguishable from the instrumental resolution of 1.6° and close to 100% of a 1.6 eV Ar beam can be accounted for within a 12° wide specular lobe. While the coherent He scattering indicates that the crystal has well-ordered regions, they do not readily provide an indication of the fraction of the surface area that might be "damaged" or rough. The Ar scattering data thus complements the He measurements by allowing us to account for the entire scattered flux. The clean crystal is saturated with hydrogen by dosing with ~ 1000 L provided over a 100 s period from an auxiliary beam. During the dosing period the sample typically cools from 275 to 150 K, after which it is annealed to 275 K.

Beam energies are varied by changing the temperature T_{noz} of a 75 μm nozzle and by seeding in He. For the lowest energies, the nozzle is cooled to ~ 100 K, for which the pressure of Ar behind the nozzle is held at about 500 Torr, to ensure against condensation. For $T_{\text{noz}} > 250$ K, Ar pressures of up to 1500 Torr are employed. The insensitivity of results to beam conditions suggests that the level of clusters in these beams is negligible. The beam energies are determined from flight times between a high-speed chopper and a differentially pumped rotatable mass spectrometer.²⁵⁻²⁷ This device is also used to record the time-of-flight and angular distributions of the scattered and desorbing species. Angular distributions are obtained in two basic modes. The distributions of the total scattered and desorbing flux can be recorded using phase sensitive detection referenced to the chopper and processed with a lock-in amplifier. Alternatively, distributions are constructed by analyzing time-of-flight spectra for specific scattering angles in such a way as to select out either the direct-inelastic or trapping-desorption scattering channel. This latter approach also permits velocities to be calculated so that *flux* distributions can be obtained, rather than the density distributions that result from the lock-in method. Details of the time-of-flight analysis are given below.

B. Time-of-flight analysis

Time-of-flight (TOF) distributions recorded at different scattering angles, can be analyzed to yield details of the velocity and angular distributions of both the scattered and desorbing Ar, as well as relative trapping probabilities for different incident beams.

The TOF spectra are treated in much the same manner as described previously by us,²⁷ using an approach which follows closely that described by Hurst *et al.*^{10,13,17} The basic strategy that we employ is as follows. First we prepare the data for fitting by subtracting the background level and the 23 μ s ion flight time, and then normalizing the largest channel to unity. The resulting array is then fed into a nonlinear least-squares fitting subroutine that fits a model function to the data by adjusting a number of carefully chosen fitting parameters.

Information on the velocity distributions of the scattered molecules is restricted to the determination of just two parameters: γ , which is a correlation parameter relating the incoming velocity v_i to the outgoing velocity v_f , and α_f

which is a width parameter, where our analysis and notation is the same as that of Ref. 10. The beam distribution is first fit to a flux-weighted velocity distribution formula of the form:

$$F(v_i)dv_i = C_i^{\text{norm}}v_i^3 \exp[-(v_i - v_i)^2/\alpha_i^2]dv_i, \quad (1)$$

to yield the stream velocity v_i and the width parameter α_i , via a nonlinear least squares fitting routine. Then each incident velocity v_i is assumed to yield a distribution of scattered velocities v_f of the form:

$$F(v_f, v_i)dv_f = C_f^{\text{norm}}v_f^3 \exp[-(v_f - v_0)^2/\alpha_f^2]dv_f, \quad (2)$$

where $v_0 = \gamma v_i$, and we are assuming zero surface residence time. We note that even at the lowest surface temperature of 85 K, the surface residence time is believed to be negligible. For example, assuming a binding energy of 0.1 eV²⁸ combined with a preexponential of, say, 10^{12} would give a residence time of only $\sim 2 \mu$ s at this temperature.

The normalization parameter in Eq. (2), C_f^{norm} , can be written as

$$C_f^{\text{norm}} = \frac{2N^{\text{norm}}}{\alpha_f^2(v_0^2 + \alpha_f^2)\exp(-v_0^2/\alpha_f^2) + (\pi^{1/2}/2)\alpha_f v_0(3\alpha_f^2 + 2v_0^2)[1 + \text{erf}(v_0/\alpha_f)]} \quad (3)$$

in order to uncouple the parameters α_f and γ from the overall normalization parameter N^{norm} . Thus [$N^{\text{norm}} = \int F(v_i)dv_i$]. Equation (3) can be approximated or set to a constant in many cases, providing a considerable decrease in running time without unduly hindering the fitting convergence. This is particularly true for cases where it is possible to provide the fitting routine with good initial guesses for the various parameters. The corresponding parameter in Eq. (1), C_i^{norm} , is given by a similar expression with v_i replacing v_0 and α_i in place of α_f .

It will be apparent from Eq. (2) that the scattered molecules are assumed to have velocities corresponding to a shifted Boltzmann distribution, of the same form as for a supersonic expansion, but shifted to a stream velocity of γv_i , and with a width related to an effective temperature by $\alpha_f = (2kT/m)^{1/2}$. Here perfect elastic scattering would yield $\gamma = 1.0$ and $\alpha_f = 0.0$, while complete accommodation at the surface temperature would yield $\gamma = 0.0$ and $\alpha_f = (2kT_s/m)^{1/2}$. The fitting procedure includes a convolution of $F(v_f, v_i)$ with the velocity distribution of the incident beam, $F(v_i)$ from Eq. (1), so that each incident velocity also has a different arrival time at the sample.

In practice, the fitting routine compares the intensity or signal in each TOF channel with that predicted by the model. The total TOF, t_{tot} is the sum of the flight time from the chopper to the surface, $t_{\text{cs}} = s_{\text{cs}}/v_i$, and from the surface to the detector $t_{\text{sd}} = s_{\text{sd}}/v_f = t_{\text{tot}} - t_{\text{cs}}$. Here s_{cs} and s_{sd} are the chopper-surface and surface-detector distances of 10.7 and 10.0 cm, respectively. For each data point, with a given t_{tot} , the model subroutine integrates over time t , setting $v_i = s_{\text{cs}}/t$, and $v_f = s_{\text{sd}}/(t_{\text{tot}} - t)$. The contribution for each

v_i is then weighted according to Eq. (1) with $v = v_i$, and for each v_f according to Eq. (2). The result is then compared to the intensity or signal associated with t_{tot} . After stepping through all data points, the fitting routine adjusts the various free parameters and repeats the whole process until a satisfactory fit is obtained to the TOF distribution.

Our analysis program also includes provision for a convolution over the shutter function of the chopper, but this was not found necessary here, as the ~ 5 - 10μ s FWHM chopper function is negligible compared to the $> 300 \mu$ s Ar flight times. In cases where it is needed, convolution over the chopper function is included by means of an "outer loop" over time, where weighting is set for each time step to match the measured chopper function, which is contained in an array in tabulated form.

As will be seen later, in most cases bimodal TOF distributions were obtained, corresponding to a combination of direct-inelastic and trapping-desorption channels. This required a modification of our model function to represent a sum of two components, i.e., to include a contribution from the trapping-desorption channel. Thus we assume that each v_i yields two contributions to the total flux F_{tot} :

$$F_{\text{tot}}(v_f, v_i)dv_f = [(1 - \sigma)F_{\text{di}}(v_f, v_i) + \sigma F_{\text{td}}(v_f)]dv_f, \quad (4)$$

where the direct-inelastic and trapping-desorption components, F_{di} and F_{td} , are given by Eq. (2), with relative contributions fit by σ . In order for the fitting to converge with the addition of these extra parameters, care must be taken to accurately represent the denominator of Eq. (3), and, if possible, to carry out preliminary fits to different sections of the

TOF distribution with reduced numbers of parameters, which are then fed in to the full fit as initial guesses.

III. RESULTS

Time-of-flight distributions have been recorded for Ar scattering from 2H-W(100) over a wide range of conditions. These are clearly bimodal in many cases, as is illustrated by Fig. 1. This shows spectra recorded for "scattering" in the direction of the surface normal, $\theta_f = 0^\circ$, for a surface temperature of 85 K for two different incident beams. The upper spectrum was obtained for $E_i = 0.085$ eV, $\theta_i = 60^\circ$, and the lower one for $E_i = 0.180$ eV, $\theta_i = 60^\circ$. It is apparent that they are composed of a relatively narrow fast peak that is superimposed on the leading edge of a much broader peak. It is also apparent from Fig. 1 that the TOF of the "fast" peak varies with incident energy. In addition, we also find that it depends slightly on θ_i and T_s and reaches a peak intensity close to the specular angle. We therefore assign this feature to direct-inelastic scattering. In contrast, the shape of the broad peak is independent of the incident beam energy and angles, being sensitive primarily to the surface temperature. This is illustrated in Fig. 2 where the two distributions given in Fig. 1 are scaled to show how the "slow" peaks can be superimposed. Consequently we assign this peak to a trapping-desorption component. Qualitatively similar distributions have been reported once previously in a study of Xe scattering from Pt(111),¹⁷ where the same assignments were made and supported by subsequent modeling.^{29,30}

From Figs. 1 and 2 it can be seen that the ratio of direct-inelastic to trapping-desorption peaks changes in favor of the direct-inelastic channel as the incident energy increases. In fact, the effect is even stronger than suggested by these figures, as the angular distribution of the direct-inelastic

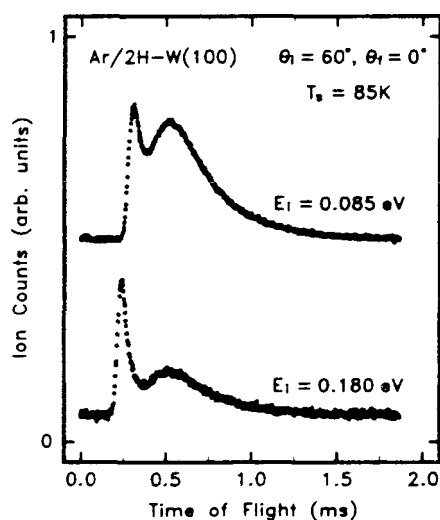


FIG. 1. Time-of-flight distributions for Ar scattering from 2H-W(100) in the direction of the surface normal for two different incident beam energies of 0.085 and 0.18 eV, with $\theta_i = 60^\circ$. The surface temperature in both cases was 85 K.

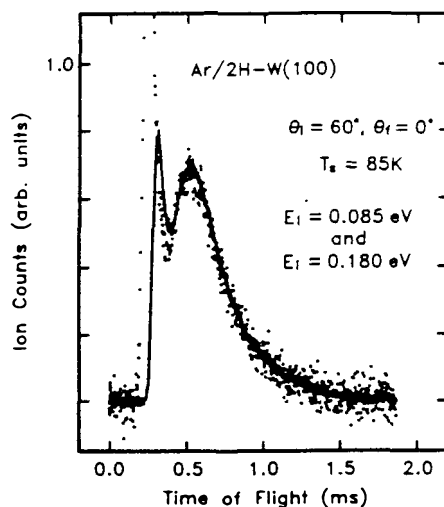


FIG. 2. Time-of-flight distributions for Ar scattering from 2H-W(100) in the direction of the surface normal for the two different incident beams shown in Fig. 1. The two spectra have been superimposed to demonstrate the insensitivity of the shape of the trapping-desorption component to E_i . The data points for the $E_i = 0.085$ eV case have been connected to distinguish them from the $E_i = 0.180$ eV data which has been rescaled to bring the two slow (trapping-desorption) components into coincidence. Note that the fast (direct-inelastic) peaks are quite different and that in the $E_i = 0.180$ eV case this feature is off-scale.

channel narrows with increasing E_i , so that the direct-inelastic flux scattered in the direction of $\theta_f = 0^\circ$ is reduced. This is a manifestation of a general trend; the trapping-desorption intensity falls quite sharply with increasing E_i , indicating that the trapping probability, $\beta(E_i, \theta_i, T_s)$, falls from values close to unity at the lowest energies employed to zero as E_i exceeds ~ 0.25 eV. We can in fact use the integrated signal in the trapping-desorption peak as a measure of the

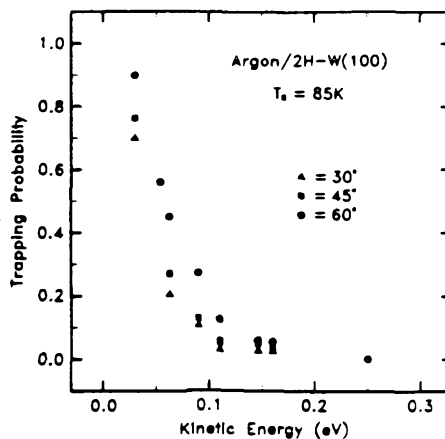


FIG. 3. Trapping probabilities of Ar on 2H-W(100) at $T_s = 85$ K for different incident energies and angles.

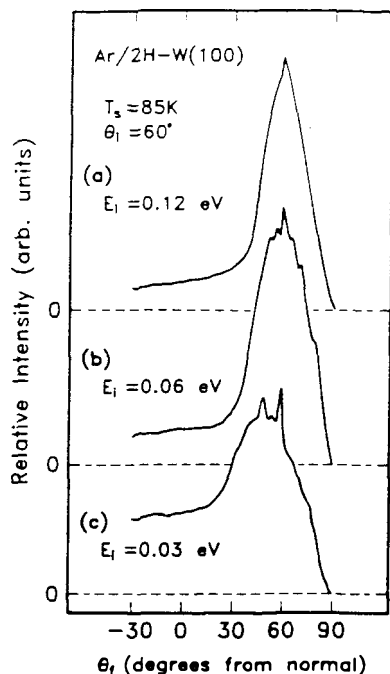


FIG. 4. Angular distributions for the scattering of Ar from 2H-W(100) at $T_s = 85$ K for an incident angle of 60° . These distributions have been taken directly from the mass spectrometer signal, and as such represent the measured density, rather than flux. The lobes close to specular belong to the direct-inelastic channel, while the "background" level at large angles from specular arise from trapping-desorption. Also apparent are sharp features on the direct-inelastic lobe due to Ar diffraction.

relative trapping probabilities for different incident beam conditions. This has been done for a range of conditions, and the results are displayed in Fig. 3 for $T_s = 85$ K.

Trapping probabilities can also be estimated from angular distributions, where this probability is taken as being the fraction of scattered species *not* contained in the direct-inelastic lobe, as described previously.³¹ Figure 4 displays some representative angular distributions recorded for $\theta_i = 60^\circ$ and $T_s = 85$ K. Here it is necessary to estimate the form of the out-of-plane distribution for the direct-inelastic lobe. We have not measured out-of-plane angular distributions, but comparison with the Ar/Pt(111)¹⁰ system suggests that the out-of-plane angular width for the Ar/2H-W(100) system should be between 1/2 to 1 times the in-plane width. In fact, the accuracy of this method increases rapidly as the trapping probability approaches unity, where the flux contained in the direct-inelastic lobe becomes negligible. The data of Fig. 3 have been normalized to a single point at $\beta(E_i = 29$ meV, $\theta_i = 60^\circ$, $T_s = 85$ K) = 0.90, obtained assuming that the out-of-plane width is half the in-plane value. Taking the two widths as equal, lowers this to 0.82, so that the scaling of Fig. 3 should be considered accurate to only $\sim \pm 10\%$. The resulting normalized data of Fig. 3 also agree within experimental uncertainties with absolute trapping estimation at $\beta(E_i = 63$ meV, $\theta_i = 60^\circ$, $T_s = 85$

K). This latter measurement in turn agrees with a separate method of estimation of absolute trapping probabilities based on comparing the absolute intensities in the desorption component with the diffuse scattering from a nominally flat part of the sample holder aligned at the crystal position. In this case we observe only a single scattering component that peaks at the surface normal, which we take to represent 100% trapping.³¹

Analysis of the TOF distributions can also provide information on the desorption dynamics. In principle, we can obtain the velocity distributions of species desorbing at each final angle and surface temperature. In practice it is not possible to separate the full trapping-desorption signal from the direct-inelastic component for angles close to specular, where the latter fraction dominates the TOF distributions. This is illustrated in Fig. 5 which shows TOF distributions at different θ_f angles for $T_s = 85$ K. However, it is possible to separate enough of the distributions to determine that at $T_s = 85$ K the shape of the trapping-desorption part of the observed TOF spectra is essentially independent of θ_f . Thus we find that the slow tails of these spectra ($t > 400$ μ s) are well described by the same functional form that fits the distributions in the region of the surface normal. This distribution in fact is very close to a Boltzmann at the surface temperature, i.e., to Eq. (2) with $\gamma = 0.0$ and $\alpha_f = (2kT_s/m)^{1/2}$. This is illustrated in Fig. 6(a) which shows a TOF distribution for $\theta_f = 60^\circ$ and $T_s = 85$ K. Also shown is a fit to the data, following the approach described in Sec.

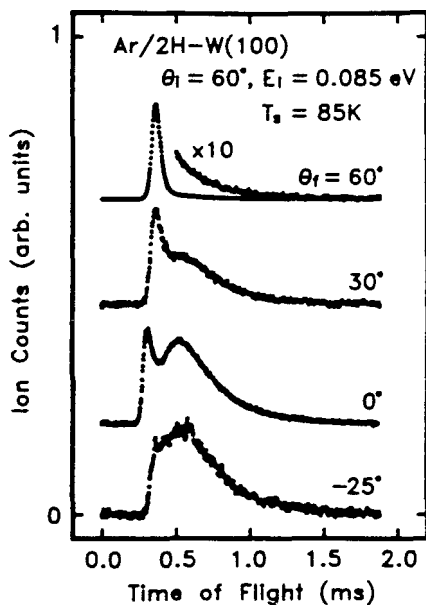


FIG. 5. Time-of-flight distributions for Ar scattering from 2H-W(100) at different scattering angles with respect to the surface normal. In each case $\theta_i = 60^\circ$ and $T_s = 85$ K. Also displayed for the 60° case is the tail of the distribution multiplied in intensity by a factor of 10. The data for -25° was taken with the detection axis on the opposite side of the normal to the specular.

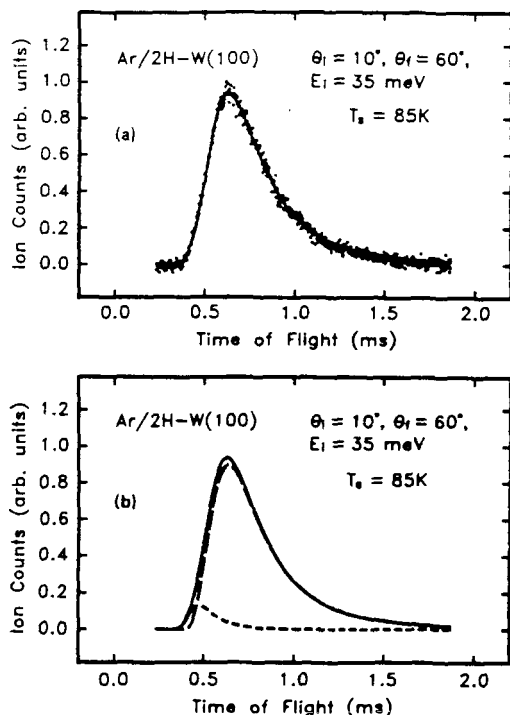


FIG. 6. (a) Time-of-flight distribution for Ar scattering from 2H-W(100) at $\theta_i = 60^\circ$ for $E_i = 35$ meV, $\theta_i = 10^\circ$ and $T_s = 85$ K. Also displayed is a fit to the data where the intensity is assumed to contain a trapping-desorption component corresponding to a Boltzmann distribution appropriate to the surface temperature of 85 K, together with an arbitrary direct-inelastic contribution. (b) Actual fitted form shown in (a), together with the fitted direct-inelastic and trapping-desorption contributions. Notice that the fit is dominated by the desorption component.

II, which, although not perfect, gives a fairly good representation of the behavior. This fit also contains a small direct-inelastic component, as can be seen in Fig. 6(b) which displays the fitted curve and its decomposition into trapping-desorption and direct-inelastic contributions. The fit can be slightly improved in this case by allowing the T_s to be a free parameter, but the improvement is almost certainly not statistically significant. Slightly different best-fit temperatures are obtained for different θ_f values. These range from ~ 75 K at the normal to almost 90 K at $\theta_f = 80^\circ$, but again it is not obvious that this variation is significant compared to estimated uncertainties of $\sim \pm 10$ K (due primarily to ambiguities in subtracting the direct-inelastic component, which varies drastically with θ_f).

The trapping-desorption components of the TOF distributions at different θ_f 's can be integrated to provide a measure of the total desorbing flux as a function of angle. Where overlap with the direct-inelastic intensity is severe this integral is estimated by fitting to the slow tails, away from the direct-inelastic contribution. Figure 7 displays the resulting angular distribution for Ar desorbing from 2H-W(100) at $T_s = 85$ K. The data have been fit to a form $F(\theta_f) \propto \cos^n \theta_f$, for which we obtain optimum agreement with $n \sim 0.6$. This

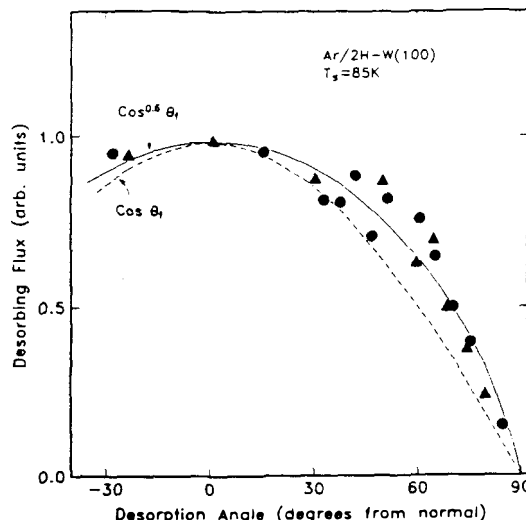


FIG. 7. Angular distributions for Ar atoms desorbing from 2H-W(100) at $T_s = 85$ K. The two sets of symbols refer to two different experiments with $E_i = 63$ meV and with an incidence angle of 60° , however, the sample was tilted out of plane by 15° in the case of the filled circles. The solid line represents the results of a best fit to a $\cos^n \theta_f$, yielding $n = 0.6$. The dashed curve shows a simple cosine distribution for comparison.

curve is given as the solid line in Fig. 7, while the dashed line displays a $\cos^{1.0} \theta_f$ curve for comparison. A qualitatively similar broader-than-cosine angular distribution has been reported previously by Hurst *et al.*¹³ for Ar desorbing from Pt(111) at 110 K.

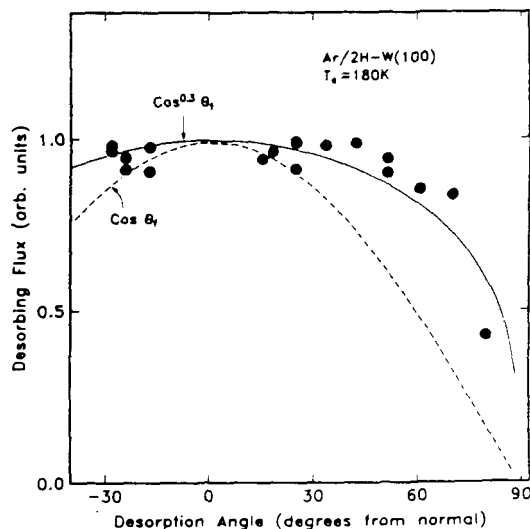


FIG. 8. Angular distributions for Ar atoms desorbing from 2H-W(100) at $T_s = 180$ K. Here $E_i = 90$ meV, the in-plane incidence angle was 60° , and the sample was tilted out of plane by 15° , giving an $\theta_i = 61^\circ$. The solid line represents the result of a best fit to a $\cos^n \theta_f$, yielding $n = 0.3$. The dashed curve shows a simple cosine distribution for comparison.

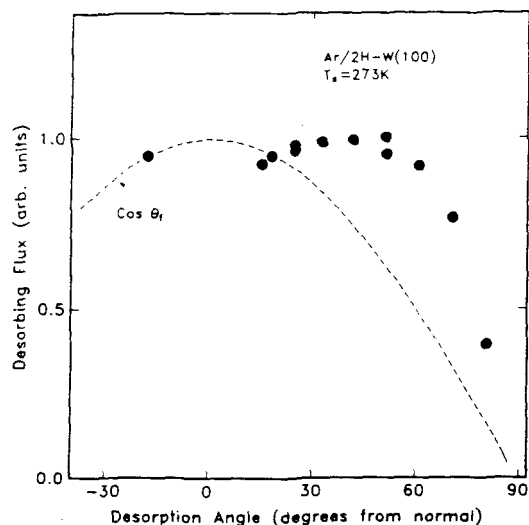


FIG. 9. Angular distributions for Ar atoms desorbing from 2H-W(100) at $T_s = 273$ K. Here $E_i = 90$ meV, the in-plane incidence angle was 60° , and the sample was tilted out of plane by 15° , giving an $\theta_f = 61^\circ$. The dashed curve shows a simple cosine distribution for comparison.

Figures 8 and 9 show corresponding plots for $T_s = 180$ and 273 K. It is apparent that the angular distributions of desorbing Ar deviate even more noticeably from a cosine at these higher temperatures. A best-fit of a $\cos^n \theta_f$ to the data for 180 K yields $n = 0.3$, but it is clearly questionable whether such a form is reasonable. No attempt was made to fit such a form in the 273 K case for which the distribution appears to peak at an angle other than zero. These distributions were obtained without allowing for possible variations in the velocity distributions of the desorbing species, which could serve to cause slight distortions in the forms.

At higher surface temperatures, the desorption TOF's become faster and are harder to distinguish from the direct-inelastic channel. Thus bimodal TOF's are no longer observed even at 180 K. While it is possible to clearly separate and unambiguously fit the TOF's obtained under such conditions for angles far from specular, fitting becomes increasingly difficult as the specular is approached. This so called "aliasing" has been encountered and described previously for the case of N_2 scattering from polycrystalline tungsten.³² Figure 10 displays TOF data for three surface temperatures for $\theta_f = -25^\circ$. Here $E_i = 35$ meV and $\theta_i = 60^\circ$, so that for these data θ_f is 85° from specular, minimizing the direct-inelastic component. While it is clear that the corresponding velocity distributions become substantially faster on raising T_s , they do not in fact "keep pace" with T_s . Although the data are well described by Boltzmann distributions, the effective temperatures T_{eff} obtained as a best fit fall further and further below T_s as this temperature is raised. Thus the results of Fig. 10 for $T_s = 85, 160,$ and 273 K, $T_{eff} = 90, 150,$ and 192 K, respectively. Again, there is a substantial and qualitatively similar "lag" between T_{eff} and T_s at higher temperatures.

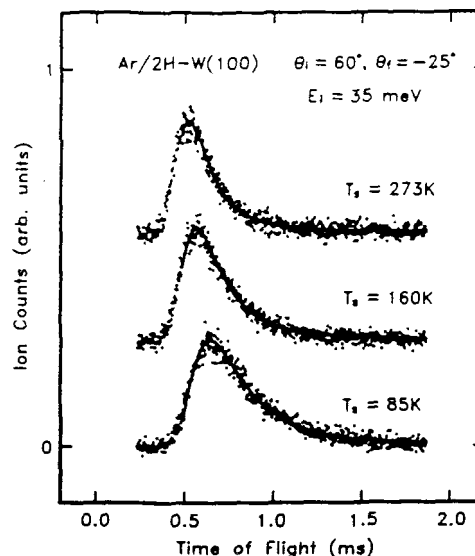


FIG. 10. Time-of-flight distributions for Ar scattering from 2H-W(100) at different surface temperatures, for $E_i = 35$ meV, $\theta_i = 60^\circ$ and $\theta_f = -25^\circ$, i.e., with the detection axis on the opposite side of the normal to the specular. The solid curves refer to a fit to a model based on detailed balancing, as presented in Sec. IV.

ance arguments presented in Sec. IV C 3. Similar results are obtained at other final angles. Thus for $\theta_f = 60^\circ$ we find for $T_s = 85, 200, 230,$ and 273 K, $T_{eff} = 90, 150, 170,$ and 192 K, respectively. Again, there is a substantial and qualitatively similar "lag" between T_{eff} and T_s at higher temperatures.

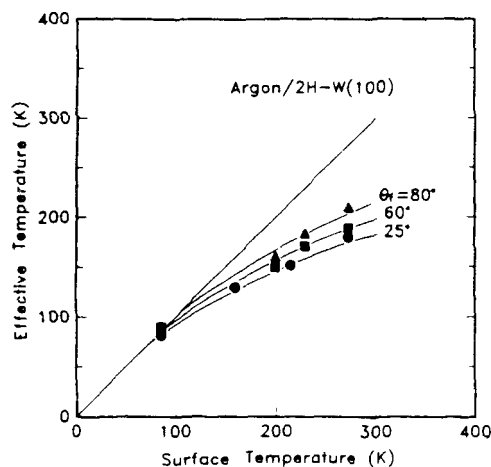


FIG. 11. Effective temperature of Ar desorbing from 2H-W(100) as a function of surface temperature. These temperatures are obtained by fitting a Boltzmann distribution to the time-of-flight distributions of the trapping-desorption component of Ar scattering from this surface. Results are displayed for three desorption, or final, angles of $80^\circ, 60^\circ,$ and 25° . Curves have been drawn through the data points as a guide to the eye. Also shown is a line indicating full accommodation where $T_{eff} = T_s$.

In this case $\theta_i = 10^\circ$, giving 50° between θ_f and the specular. These results are summarized in Fig. 11, together with data for $\theta_f = 80^\circ$. This figure also shows a line corresponding to full accommodation, with $T_{\text{eff}} = T_s$. It is clear that T_{eff} deviates less from T_s as θ_f increases.

IV. DISCUSSION

A. Trapping vs incidence energy and angle

There have been remarkably few reported measurements of $\beta(E_i, \theta_i, T_s)$. We recently reported such data for the $\text{N}_2/\text{W}(100)$ system, where a surprising insensitivity to θ_i was observed.²⁷ As with that system, we find that the trapping probability of Ar on the H-saturated $\text{W}(100)$ surface falls with increasing E_i (see Fig. 3). Such behavior is intuitively reasonable, since as E_i is raised a larger and larger fraction of the collision energy must be lost for trapping to occur. The actual form of this fall-off is less obvious. Let us first consider a highly simplified picture of the trapping dynamics, appropriate to a cube model.⁵ For trapping to occur, there must of course be a potential well, say of effective depth ϵ . Then we can say that trapping will occur when the fraction of the incidence energy that is lost to translation exceeds $E_i/(E_i + \epsilon)$. For a stationary cube (equivalent to a surface temperature = 0 K), we would then predict a trapping probability of unity for all energies up to some critical ("normal") energy E_c above which it will fall to zero, giving a step function form to $\beta(E_i, T_s = 0)$. For a hard cube model we obtain

$$E_c = \frac{4\epsilon(m/M)}{[1 - (m/M)]^2}, \quad (5)$$

where M and m are the cube and incident atom masses, respectively. Any thermal motion of the cube will serve to smooth this step function. This motion may be included in the modeling by adding a component to the collision energy consistent with a one-dimensional Maxwellian distribution of velocities, but weighted by the actual relative velocity.³³ Such a distribution has a most probable value close to zero velocity, with a roughly equal probability of finding faster and slower velocities. The result is that in this simple picture, we expect a trapping probability of about 0.5 at $E_i = E_c$, going smoothly to 1 at lower energies and to zero at higher energies. This behavior is reminiscent of the density of states form predicted by the Fermi function, where E_c is equivalent to the Fermi energy. In fact we find that $\beta(E_i, T_s)$ values obtained from cube models can be well described by an expression similar to a Fermi function, but with $T_s^{1/2}$ in place of T_s .³⁴ That is we suggest that it may be useful to describe $\beta(E_i, T_s)$ by the form

$$\beta(E_i, T_s) = \frac{1}{\exp[(E_i - E_c)/xT_s^{1/2}] + 1} \quad (6a)$$

or equivalently,

$$\beta(E_i, T_s) = \frac{1}{\exp(xE_i - E_c) + 1} \quad (6b)$$

treating E_c , x , and y as adjustable parameters. A rather similar form has been employed by Hurst *et al.*¹³ in modeling the trapping-desorption of Ar on Pt(111).

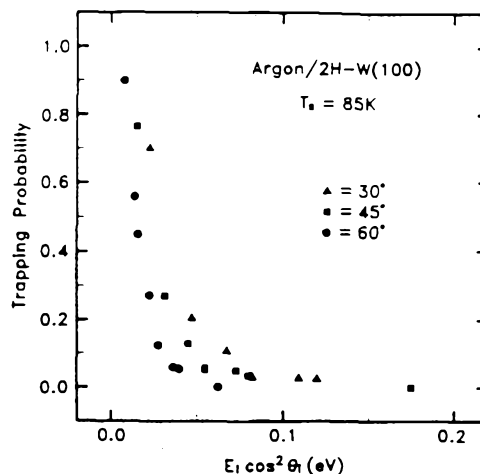


FIG. 12. Trapping probabilities of Ar on 2H-W(100) at $T_s = 85$ K for different incident energies and angles. The data are the same as in Fig. 3, but have been plotted as a function of the so-called "normal energy," $E_n = E_i \cos^2 \theta_i$.

It may be apparent that such a form can be used to describe the trapping vs energy curves of Fig. 3, for any fixed value of θ_i . However, the data clearly do not scale with E_n , so that different curves are required for each θ_i . In the limit where parallel momentum is conserved, we might reasonably expect results to scale as the so-called "normal energy," $E_n = E_i \cos^2 \theta_i$. This is not the case here, as is apparent in Fig. 12, which shows the data of Fig. 3 replotted against E_n . Comparison of Figs. 3 and 12 suggest that the true scaling parameter is somewhere between total and normal energy.

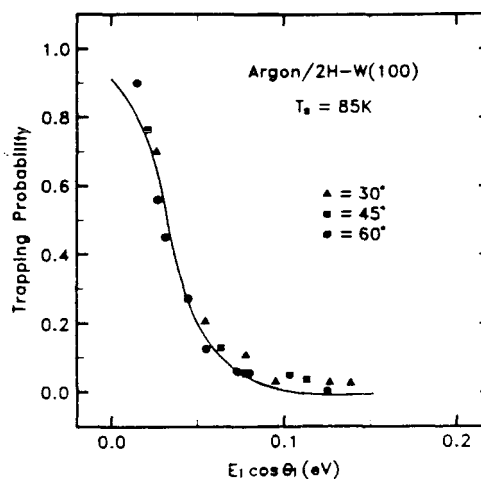


FIG. 13. Trapping probabilities of Ar on 2H-W(100) at $T_s = 85$ K for different incident energies and angles. The data are the same as in Fig. 3, but have been plotted as a function of the quantity $E_i \cos \theta_i$. The curve represents a fit to the data based on Eq. 6(b), as discussed in the text.

We find empirically that the data scale rather well with $E_i \cos \theta$, as is apparent from Fig. 13. This suggests a rather corrugated interaction, which is supported by our observations of scattering rainbows in this system for example for $E_i \sim 100$ meV and $\theta_i = 30^\circ$, as will be described elsewhere.³⁵

Also shown in Fig. 13 is the result of a best fit to the data using Eq. 6(b) with $E_i \cos \theta_i$, in place of E_i . Here we obtain $x = 78 \text{ eV}^{-1}$ and $y = 2.65$, giving $E_c = 34$ meV. This is consistent with Eq. 5 with M equal to about 2 W atoms, taking $\epsilon \sim 80$ meV.²⁸ We stress that the intention here is not to extract accurate dynamical parameters, so much as to gain a qualitative understanding of the trapping vs energy behavior.

B. Desorption

We have shown that the TOF distributions of Ar scattering from the hydrogen-saturated W(100) surface contain a clearly resolvable trapping-desorption component. As such, the form and spatial distribution of this component reflect the velocity and angular distributions of Ar desorbing from this surface. Analysis of data obtained over a wide range of conditions leads us to several important conclusions. At the lowest temperatures employed (~ 85 K), the velocity distributions of the desorbing atoms are well described by Maxwell-Boltzmann distributions characteristic of the surface temperature. Moreover, these species emerge with an angular distribution in quite close agreement with the Knudsen Cosine Law (see Fig. 7). At higher temperatures, velocity distributions are still approximately Maxwellian in form, but the characteristic temperature falls below T_s . The lag between T_{eff} and T_s increases with T_s and is most pronounced for desorbing angles close to the normal (Fig. 11). Similarly, angular distributions become increasingly noncosine as the surface temperature is raised.

Considering first the velocity distributions, we note that there have been surprisingly few previous studies of this kind. Although velocity distributions of desorbing species have been reported for a number of systems, going back to 1971,³⁶ these pertain mostly to the desorption of reaction products.^{2,36-39} In these cases strong deviations from Maxwell-Boltzmann distributions are observed, but in most cases in the opposite sense to that reported here. For example, the energy of D_2 desorbing from Cu(100), Cu(111), and Ni(111) surfaces following permeation through the bulk is found to be much higher than $2kT_s$.³⁷ The exception here is the desorption of the D_2O product of the oxidation of D_2 on Pt(111), where mean energies equivalent to only $T_s/2$ have been reported.³⁹ Energies in excess of $2kT_s$ are thought to arise due to the presence of a potential barrier which rises above the large-separation asymptote, or zero level, and provides the departing species with energy comparable to the barrier height.² Conversely, systems with $\langle E_i \rangle$ less than $2kT_s$ are unlikely to be associated with such a barrier.

The closest previous studies to the present work involved the scattering of Xe¹⁷ and Ar¹³ from Pt(111). Here Hurst *et al.* were able to identify trapping-desorption components in the TOF distributions of Xe and Ar scattering from Pt(111). In the former case, the velocity distribution of

Xe desorbing from a 185 K surface was found to fit a Maxwell-Boltzmann with $T_{\text{eff}} = 185 \pm 3$ K.¹⁷ In the Ar study, data were obtained for several desorption angles with $T_s \sim 100$ K. Mean energies of between 70% and 90% of $2kT_s$ were observed, increasing with increasing angle from the normal. A casual comparison with the present study suggests that the Ar/2H-W(100) and Ar/Pt(111) systems behave similarly.

Shortly after the Xe study, Tully reported the results of stochastic trajectory calculations for the desorption of Xe and Ar from Pt(111),³ which are in fairly good agreement with the limited measurements available. Of particular interest here is that Tully was able to examine the effect of T_s on the desorption energies. He found that at temperatures somewhat above those employed by Hurst *et al.*, these energies lag behind $2kT_s$, in a qualitatively similar manner to the results reported here (Fig. 11). This behavior was again observed in calculations by Muhlhausen, Williams, and Tully⁴⁰ for the case of NO desorbing from Ag(111).

The dynamical origin for this effect is not immediately obvious. There are at least two distinct ways in which a subthermal velocity distribution could result. If we consider those atoms destined to desorb after one further collision with the surface, which we will term "protodesorbers," we expect that the velocity distribution of these species after desorption will reflect both the dynamics of the last collision and their energy distribution prior to this collision. Thus translational cooling might arise if: (i) the energy distribution of the protodesorbers is out of equilibrium with T_s , decaying faster than $\exp(-E/kT_s)$, or (ii) the final collision does not just add a fixed amount of normal momentum to the desorbing species, but a variable amount with a probability that falls off with increasing energy transfer. Effects due to (i) must certainly exist, as the constant loss of energetic species has to preferentially deplete the high energy tail of the distribution of protodesorbers. However, as we will see below, our results are in good agreement with detailed balance, which strictly applies to a system at equilibrium. Under such conditions, the protodesorbers should indeed be equilibrated to T_s , since "evaporative cooling" is perfectly matched by "condensation." This suggests that the velocity distributions of desorbing atoms rather reflects (ii), the dynamics of the last collision. Here the idea is simply that the Boltzmann term, $P(E) = \exp(-E/kT_s)$, appropriate to the surface temperature will be replaced by a function based on the product of $P(E)$ with a transition probability function²³ that decays with increasing energy gain. The resulting function will then fall off with increasing E faster than $P(E)$, and therefore will correspond to a subthermal velocity distribution. At the lowest temperatures, the fall off associated with $P(E)$ must dominate the dynamical term, so that the effective translational temperature approaches T_s . Finally we note that the extra normal momentum needed for desorption may be acquired either by the redirection of parallel momentum by surface corrugation or by energy transfer from the substrate. Since the effective surface mass is considerably higher than the departing atoms, direction changing collisions may be more important.

There have been more studies of the angular distribu-

tions of desorbing species.³ Here the situation is rather similar to the case of velocity distributions, in that most work applies to reaction products.^{2,13,22,24,41-43} In this case, angular distributions are found to deviate from a cosine by being sharper, rather than broader than this function. Steinrück *et al.* found that H₂ desorbs from Ni(111) with a cos⁵ θ_f distribution,⁴¹ while the CO₂ product of the oxidation of CO on Pt(111) emerges with a remarkably peaked cos¹⁶ θ_f distribution.⁴² Again the presence of a potential barrier is inferred, which serves to "focus" the emerging species along the surface normal, by increasing their normal energy.

The desorption of Ar from Pt(111), by contrast, was found to yield a broader-than-cosine distribution,¹³ consistent with trajectory studies for this system. This behavior is consistent with the "translational cooling" effects discussed above. The rate of desorption in a given direction must contain a factor corresponding to the rate of leaving the surface, i.e., a velocity factor. Lower velocities along the surface normal then lead to smaller fluxes. This effect must, of course, "compete" with the phase-space weighting factor of cos θ_f which dominates to give a cosine distribution at low T_f, where the perpendicular momentum approaches that of the parallel, at which point the mean energy is close to 2kT_f.

C. Test of detailed balance

1. General

A valuable aspect of the current study is that results have been obtained simultaneously for the complementary processes of trapping and desorption. These data can therefore provide the basis for a test of the extent to which detailed balancing arguments can be applied to relate such processes for a system that is not in strict equilibrium. Before proceeding, it is useful to review the thinking in this area.

The principle of detailed balance rigorously applies to systems at equilibrium, for which it relates the (transition) probabilities or rates for all distinguishable processes in such a way that the steady properties of the system are maintained. It may be expressed as²⁰

$$T(A \rightarrow B, C \rightarrow D) = T(B \rightarrow A, D \rightarrow C), \quad (7)$$

where $T(A \rightarrow B, C \rightarrow D)$ is the probability per unit time that a state A of the system will make a transition to state B, while at the same time C goes to D (in order to conserve energy and momentum). Averaging over an equilibrium distribution of initial states C, and summing over final states D, leads to the simpler relationship²⁰

$$N(A \rightarrow B) = N(B \rightarrow A), \quad (8)$$

where $N(A \rightarrow B)$ is the number of particles in state A making transitions to state B per second.

These expressions are based on time-reversal invariance and invariance under reflection of spatial coordinates.⁴⁴ As a result, they do not strictly apply to the gas-surface interface, as the collision represented by the right-hand side of Eq. (7) does not exist at a surface where the collision represented by the left side exists.²⁰ Thus if A is a momentum state of an atom moving towards the surface, the collision might cause a surface atom to move in towards the bulk in a manner given by state D. (Alternatively we may view this as creating a

phonon with momentum directed away from the surface.) The incoming atom will change to a state B, having momentum directed away from the surface, so that B and D are both moving away from the interface (and each other). In order to collide, B would need to strike a surface that has been reflected about the surface plane, where D (or the phonon) would be moving towards the surface. In more general terms, detailed balance cannot be applied here as the gas-surface interface is not invariant under reflection of spatial coordinates.

Instead it is reciprocity, which is expressed as

$$T(A \rightarrow B, C \rightarrow D) = T(B_R \rightarrow A_R, D_R \rightarrow C_R) \quad (9a)$$

$$N(A \rightarrow B) = N(B_R \rightarrow A_R) \quad (9b)$$

which may be used to derive the relationships relevant to the gas-surface interface. Here A_R is in every way identical to state A, except for a reversal of its momentum, i.e., it is travelling in the opposite direction. Actually two extra key assumptions are needed to permit these relationships to be applied to the gas-surface interface. First we must assume that the surface is capable of maintaining a canonical distribution appropriate to T_f, i.e., that the impinging flux of gas does not disturb this distribution. In addition, we must specifically preclude any sorting of trajectories by a Maxwell's demon-type entity.²⁰

2. Relationship between trapping and desorption

Equation 9(b) then expresses a rather basic idea that we might have about a gas-surface system at equilibrium: *at equilibrium the flux of each distinguishable incident state is matched by an equal but opposite flux of that state leaving the surface.* Thus it can be shown that the cosine distribution of incident species that must apply at equilibrium gives rise to a cosine distribution of particles leaving the surface.²⁰ Similarly, a Maxwell-Boltzmann distribution of velocities is demanded for species leaving the surface under these conditions. However, note that these constraints apply only to the sum of the scattering channels, so that *the individual channels of inelastic scattering and (trapping-)desorption may deviate arbitrarily from cosine and Maxwell-Boltzmann distributions, provided the other channels behave in a complementary manner.* Only if one channel dominates the scattering does it become constrained. For example, the angular distribution for desorption at T_f must approach a cosine as the trapping probability for all species in the Boltzmann distribution at this temperature approaches unity.

We might consider at this point that it is possible to equate the individual channels of adsorption and desorption, arguing that whatever species are lost to the scattering channel in trapping, have to be made up for in desorption, in order to preserve the detailed sums. Then we would write²⁴

$$f_{des}(v_f, \theta_f, T_f, \dots) = f_{ads}(v_i = v_f, \theta_i = \theta_f, T_f, \dots), \quad (10)$$

where f_{des} and f_{ads} are the differential flux for desorption and adsorption, respectively, which may depend in addition on, say, surface coverage, etc. However, acceptance of such an expression requires a further assumption that the differential fluxes for the scattering channel must be the same before and after encountering the surface, i.e., the scattering must be

have on average in a manner that is indistinguishable from elastic scattering at the specular. Thus it *could* be that inelastic scattering somehow, on average, slows down or speeds up the scattered species, or focuses them towards or away from the normal. If this occurred, the desorption distributions would need to "compensate" by assuming the complementary behavior. In fact Eq. (10) is likely to be rigorously true, due to the fact that reciprocity may be applied to the scattering channel alone,²³ permitting Leuthäusser to arrive at an expression equivalent to Eq. (10).²³

Equation (10) can thus be written as

$$f_{des}(v, \theta_f, T_s) \propto \cos \theta_f v^3 \exp(-mv^2/2kT_s) \beta(v = v_i, \theta_f = \theta_i, T_s), \quad (11)$$

where the $\cos \theta_f$ and $v^3 \exp(-mv^2/2kT_s)$ terms correspond to the incident cosine and (flux-weighted) Boltzmann distribution, respectively. Angular distributions can be obtained simply by integrating over velocities, giving

$$\langle f_{des}(\theta_f, T_s) \rangle \propto \cos \theta_f \int v_i^3 \exp(-mv_i^2/2kT_s) \beta(v_i, \theta_i, T_s) dv_i, \quad (12)$$

where the angle brackets signify an average over all desorbing velocities. Thus, for a system at equilibrium we are able to synthesize desorption properties from a knowledge of the trapping probability as a function of angle and energy, and *vice versa*. We will now test the extent to which these expressions hold for the Ar/2H-W(100) system under molecular beam conditions.

Finally, we should make a semantic point. We have stated that detailed balance as such does not strictly apply to the gas-surface interface and that Eqs. (10)–(12) are based on the related principle of reciprocity.²⁰ However, the practical application of these equations to the gas-surface interface involves an *exercise in detailed balancing*, where the differential fluxes associated with adsorption and desorption are compared or balanced. This may account for the adoption of this term in many previous studies.^{13,18,19,22,24} We will therefore sacrifice rigor in favor of consistency and refer to the process of comparing our results with the predictions of Eqs. (10)–(12) as one of testing the applicability of detailed balance, in the sense accepted by the surface science community.

3. Application to Ar/2H-W(100)

While Eqs. (10)–(12) are valid for a system at equilibrium, there is no *a priori* reason why they should hold for systems even slightly out of equilibrium. However, "detailed balance" constructions based on these relationships do seem to work, at least approximately, for many systems of interest under conditions comparable to the present study.^{13,18,19,22,24} We are thus encouraged to apply them here.

Equations (11) and (12) can be used to predict both the velocity and angular distributions of Ar desorbing from this surface, provided that the trapping function $\beta(v, \theta, T_s)$ is known. We are indeed able to estimate this function based on

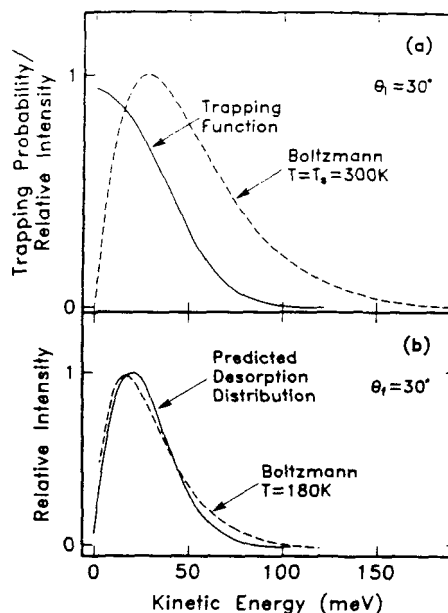


FIG. 14. Construction illustrating the prediction of the energy distribution of desorbing species based on detailed balance. (a) Boltzmann distribution corresponding to a (surface) temperature of 300 K, together with the trapping vs energy function estimated to apply to the case of Ar trapping on 2H-W(100) for $E_i = 30^\circ$. (b) The result of multiplying the two curves in (a) to obtain the velocity distribution predicted for desorption at θ_f , assuming detailed balance holds for this system (solid curve). Also shown in (b) is a Boltzmann distribution obtained as a best fit to the actual desorbing distribution, yielding an effective temperature of 180 K.

fits to our discrete observations, as discussed in Sec. IV A above. The process by which Eq. (11) is used to predict velocity distributions is illustrated in Fig. 14. The top panel displays a Boltzmann at 300 K, corresponding to the $v^3 \exp(-mv^2/2kT_s)$ term of Eq. (11), and a curve of the trapping function $\beta(v, \theta = 30^\circ)$. The distribution function for the velocities of those particles that trap for $\theta_f = 30^\circ$ and $T_s = 300$ K is given by the product of these two curves, which is then the distribution function for desorption, as predicted by Eq. (11). For the purposes of this example, we have taken the function

$$\beta(E_i, \theta_i) = \frac{1}{\exp(78E_i \cos \theta_i - 2.65) + 1} \quad (13)$$

as discussed in Sec. IV A, where E_i is in eV. Actually this applies to trapping data obtained at $T_s = 85$ K, rather than 300 K, but for now we will neglect this difference. The lower panel of Fig. 14 shows the resulting velocity distribution, which would be predicted for Ar desorbing at $\theta_f = 30^\circ$. Also displayed is a curve corresponding to a Maxwell-Boltzmann at 180 K, the "best fit" temperature for this case.

This construction has been incorporated into the TOF analysis procedure described in Sec. II, so that the trapping-desorption components can be fit not to a simple Maxwell-Boltzmann, but to the product of this function and the trapping function for the particular value of θ_f , generated using

Eq. (13) with $\theta_i = \theta_f$. The Maxwell-Boltzmann temperature is left as a free parameter that is optimized by the nonlinear least-squares fitting program. We find that for $\theta_f = 25^\circ$, (i.e., the data of Fig. 10) the fitted temperature is virtually identical to T_s . In fact the solid curves in Fig. 10 show the resulting fits obtained for data recorded at $T_s = 273, 160,$ and 85 K. We obtain best-fits values of $T_{fit} = 267, 153,$ and 84 K, which are in remarkably good agreement with the actual surface temperatures. It is also possible to take the opposite approach here: to deduce the trapping function from desorption spectra. In this case our analysis program again fits TOF spectra to a product of a Maxwell-Boltzmann distribution and a trapping function, but fixes the Boltzmann temperature at T_s , and fits the data by optimizing the parameters of the trapping function. This function is assumed to be of the form given in Eq. 6(b), with x and y as fitting parameters. With this approach, however, there is a substantial uncertainty in the absolute trapping values, as the TOF fitting program also fits a normalization constant, which is coupled to the absolute scaling of the trapping function. Figure 15(a) displays the result of one such fit, to the 273 K data of Fig. 10, compared to the results of a fit of Eq. 6(b) directly to the trapping data of Fig. 2 for $\theta_i = 30^\circ$. Consistent with the above, the fit only yields the shape of the

desorption function, while the overall normalization has been adjusted here for the purposes of presentation. Only the shape of the curve is actually fit. Again we note that this comparison is not quite perfect, as the trapping data refer to $T_s = 85$ K, while the desorption temperature is 273 K. Nevertheless, the agreement is within experimental uncertainties.

Carrying out similar analysis at other angles leads to qualitatively similar results, but with less satisfactory agreement at larger $\theta_f(\theta_i)$ values. Thus for $\theta_f = 60^\circ$, the fitting procedure described above with T_s as a free parameter gives for $T_s = 273, 200,$ and 85 K, best fits of $T_{fit} = 220, 185,$ and 91 K. Similarly, the trapping function obtained from the 273 trapping-desorption TOF spectrum is in only modest agreement with the measured function, as shown in Fig. 15(b). It may be that variation of β with temperature is greater at grazing angles. It is clear that a precise test of detailed balance requires trapping data over a range of temperatures to match desorption data.

As a final comment on the form of the observed TOF distributions, we have noted that these can always be well described by a Maxwell-Boltzmann distribution, albeit at a temperature other than the surface temperature. This implies that the trapping function must be close to exponential. Thus if $\beta(E) = A \exp(-E/T_w)$ is substituted in Eq. (11), we will obtain $f_{des}(E) \propto E \exp(-E/T_{eff})$ where $1/T_{eff} = 1/T_s + 1/T_w$, as was recognized by Hurst *et al.*¹³ It should also be apparent from Fig. 13, for example that the actual trapping function is indeed likely to be close to exponential. In our opinion, the TOF data are not precise enough to distinguish between Eq. 6(b) and an exponential.

Continuing this line of reasoning, we may also use the trapping results to predict angular distributions assuming detailed balance to apply. Here we can build up distributions by use of Eq. 12 to give the desorbing flux at each value of θ_f . Figure 16 displays predicted distributions for $T_s = 100, 200,$ and 300 K, based on Eq. 12 with $\beta(v, \theta_i)$ as given by Eq.

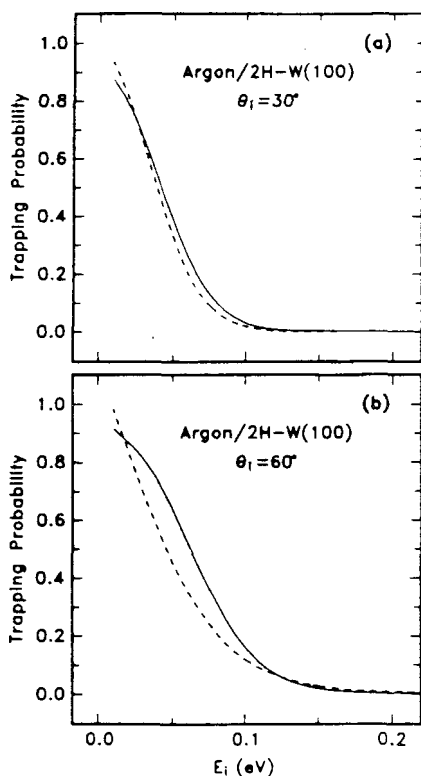


FIG. 15. Trapping vs energy curves obtained from a fit to actual trapping vs energy data (solid line) and from an analysis of the trapping-desorption component of TOF spectra (dashed line), as discussed in text. (a) $\theta_i = 30^\circ$ (derived using desorption data for $\theta_f = 25^\circ$). (b) $\theta_i = 60^\circ$.

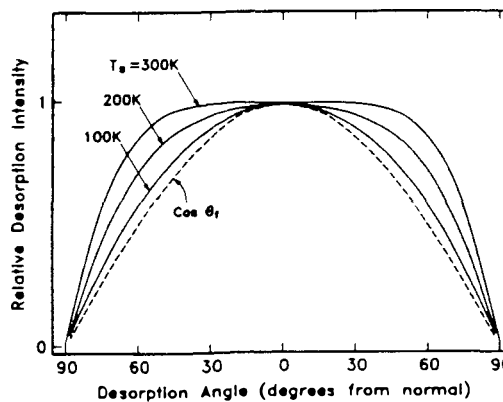


FIG. 16. Angular distributions predicted for Ar desorbing from 2H-W(100) at $T_s = 100, 200,$ and 300 K, assuming detailed balance holds for this system (solid curves). The curves are based on the trapping function described in the text. Also shown for reference is a simple cosine distribution (dashed curve).

(13). It is seen that these distributions become increasingly noncosine as T_s is increased, in good qualitative agreement with direct observations for $T_s = 85, 180,$ and 273 K, shown in Figs. 7-9, respectively. Here we have not attempted to best-fit the detailed balance synthesis to the data, feeling that the added complexity of the modeling is not merited at this point. We do note, however, that both the synthesized and measured angular distributions for $T_s \sim 300$ K peak at angles away from the normal.

Several further observations are apparent here. We note that it is the θ , dependence of the $\beta(v, \theta)$ term in Eq. (14) which is responsible for deviations from a cosine angular distribution. Thus systems for which trapping is a function of the total incidence energy, such as $N_2/W(100)$ ²⁷ would be predicted to always desorb with cosine angular distributions. At the other extreme, systems in which trapping scales with $E, \cos^2 \theta$, would display even more pronounced deviations than observed here for the Ar/2H-W(100) system, and would be expected to show clear minima at the surface normal. Further, distributions will be broader than cosine where the trapping function falls with increasing energy, but will be narrower for systems involving activated sticking, where adsorption increases with E .^{22,24} It would appear that the trapping and desorption results obtained here are indeed consistent with detailed balance. That is to say the individual adsorption and desorption processes behave as if the system were at equilibrium. This may not be too surprising when it is appreciated that the surface conditions of the present study may well be indistinguishable from those attainable at equilibrium. In both cases the incident flux is likely to be too small to perturb the canonical distribution of states at the surface or to produce significant Ar coverage. Thus detailed balance is seen here to be more than a simple consequence of the need to maintain the steady properties of a system at equilibrium. That is to say the differential fluxes of desorbing species (i.e., into each velocity, angular element, etc.) at equilibrium are not driven by any buildup of particles, energy, momentum, etc. Only the total yield of desorbing atoms is controlled by the incident flux. *The relative differential fluxes in desorption must rather be governed by intrinsic properties of the adsorbate-surface system.* These properties also independently govern the trapping dynamics. The connection between adsorption and desorption may therefore be understandable, as the two processes share a common potential and are intimately related by the fact that the equations of motion are invariant to time reversal. Thus any given trajectory can equally apply to either adsorption or desorption. It is only the relative occurrence of each element of differential flux that is, in principle, free to vary for a nonequilibrium system. The actual differential fluxes in each direction may be thought of as arising from a combination of dynamical and statistical factors. For example in Eq. (11) we might identify the $\beta(v, \theta, T_s)$ term as "dynamical," and the cosine and Maxwell-Boltzmann terms as "statistical." The fact that we find that this equation seems to be approximately true even in the absence of the incident Maxwell-Boltzmann suggests that this factor arises naturally at the surface. Indeed, this is again reasonable, since, as discussed in Sec. IV B, protodesorbers most likely have a Boltzmann distribu-

tion of energies (shifted by the well depth, which simply introduces an $\exp(-\epsilon/kT_s)$ normalizing factor) prior to their final collision with the surface.

V. SUMMARY AND CONCLUSIONS

We have shown that Ar traps on a hydrogen-saturated W(100) surface with a probability that scales roughly with $E, \cos \theta$, and which falls from values close to 1 at the lowest energies to zero as $E, \cos \theta$, approaches about 0.2 eV. This scaling law suggests that the interaction potential is quite corrugated. The falloff with increasing energy was shown to be consistent with a simple cube model for a cube mass of close to 2 surface atoms. Time-of-flight distributions of scattered Ar are found to be clearly bimodal in many cases, having both direct-inelastic and trapping-desorption components; the latter of which has been characterized over a wide range of conditions to provide information on the desorption of Ar from this surface. We have found that desorbing species emerge with a near-cosine angular distribution at $T_s = 85$ K, but that these distributions become increasingly noncosine as T_s is raised, becoming substantially broader than cosine. Similarly, velocity distributions of the desorbing atoms are well described by Maxwell-Boltzmann distributions at $T_s = 85$ K. At higher temperatures, these distributions are still approximately Boltzmann, but the characteristic temperature falls below T_s . The lag between this effective temperature and T_s increases with T_s , and is most pronounced for desorbing angles close to the normal. Analysis of these results has revealed that the desorption data are very close to the predictions of a model in which angular and velocity distributions are synthesized for desorption by applying detailed balance arguments to the trapping data. Similarly the trapping results are close to trapping curves extracted from the desorption data. Thus we have learned that detailed balance can be used quite reliably to extend trapping and desorption data by permitting one to be derived from the other. Finally, we have speculated that detailed balance is applicable to a nonequilibrium system in this case because desorption and trapping produce complementary differential flux distributions at equilibrium [Eq. (10)] rather than being driven to do this by any feedback from one process to the other.

ACKNOWLEDGMENTS

We are indebted to J. E. Schlaegel for assistance in the maintenance and upkeep of the apparatus and to D. S. Bethune, D. J. Auerbach, G. M. McClelland, and J. A. Barker for useful discussions. C. B. M. would also like to thank IBM for a Predoctoral Fellowship and the NSF for partial support under Grant No. CHE8617826.

¹J. A. Barker and D. J. Auerbach, Surf. Sci. Rep. 4, 1 (1984).

²G. Comsa and R. David, Surf. Sci. Rep. 5, 145 (1985).

³J. C. Tully, Surf. Sci. 111, 461 (1981).

⁴M. Persson and J. Harris, Surf. Sci. 187, 67 (1987).

⁵F. O. Goodman and H. Y. Wachmann, *Dynamics of Gas-Surface Scattering* (Academic, New York, 1976).

⁶D. R. Miller and R. B. Subbarao, J. Chem. Phys. 52, 425 (1970).

⁷S. M. Lui, W. E. Rodgers, and E. L. Knuth, *Proceedings of the Ninth Inter-*

- national Symposium on Rarefied Gas Dynamics* (DFVLR, Porz-Wahn, Germany, 1974), Vol. II, p. E. 8-1.
- ⁸C. W. Muhlhäuser, J. A. Serri, J. C. Tully, G. E. Becker, and M. J. Cardillo, *Isr. J. Chem.* **22**, 315 (1982).
- ⁹K. C. Janda, J. E. Hurst, J. Cowin, L. Wharton, and D. J. Auerbach, *Surf. Sci.* **130**, 395 (1983).
- ¹⁰J. E. Hurst, L. Wharton, K. C. Janda, and D. J. Auerbach, *J. Chem. Phys.* **78**, 1559 (1983).
- ¹¹A. Amirav, M. J. Cardillo, P. L. Trevor, C. Lim, and J. C. Tully, *J. Chem. Phys.* **87**, 1796 (1987).
- ¹²W. H. Weinberg and R. P. Merrill, *J. Vac. Sci. Technol.* **8**, 718 (1971).
- ¹³J. E. Hurst, L. Wharton, K. C. Janda, and D. J. Auerbach, *J. Chem. Phys.* **83**, 1376 (1985).
- ¹⁴H. P. Steinrück and R. J. Madix, *Surf. Sci.* **185**, 36 (1987).
- ¹⁵H. Schlichting, D. Menzel, T. Brunner, W. Brenig, and J. C. Tully, *Phys. Rev. Lett.* **60**, 2515 (1988).
- ¹⁶E. K. Grimmelmann, J. C. Tully, and E. Helfand, *J. Chem. Phys.* **74**, 5300 (1981).
- ¹⁷J. E. Hurst, C. A. Becker, J. P. Cowin, K. C. Janda, L. Wharton, and D. J. Auerbach, *Phys. Rev. Lett.* **43**, 1175 (1979).
- ¹⁸R. L. Palmer, J. N. Smith, Jr., H. Saltburg, and D. R. O'Keefe, *J. Chem. Phys.* **53**, 1666 (1970).
- ¹⁹R. L. Palmer and D. R. O'Keefe, *Appl. Phys. Lett.* **16**, 529 (1970).
- ²⁰E. P. Wenaas, *J. Chem. Phys.* **54**, 376 (1971).
- ²¹I. Kuscer, *Surf. Sci.* **25**, 225 (1971).
- ²²M. J. Cardillo, M. Balooch, and R. E. Stickney, *Surf. Sci.* **50**, 263 (1975).
- ²³U. Leuthäusser, *Z. Phys. B* **50**, 65 (1983).
- ²⁴H. P. Steinrück, K. D. Rendulic, and A. Winkler, *Surf. Sci.* **154**, 99 (1985).
- ²⁵H. E. Pfnür, C. T. Rettner, J. Lee, R. J. Madix, and D. J. Auerbach, *J. Chem. Phys.* **85**, 7452 (1986).
- ²⁶C. T. Rettner, L. A. DeLouise, and D. J. Auerbach, *J. Chem. Phys.* **85**, 1131 (1986).
- ²⁷C. T. Rettner, H. Stein, and E. K. Schweizer, *J. Chem. Phys.* **89**, 3337 (1988).
- ²⁸We are not aware of measurements of the binding energy of Ar on this 2H-W(100) surface, but expect it to be smaller than for the clean surface, for which a value of 0.08 eV has been estimated for example in Ref. 12 and by T. Engel and R. Gomer, *J. Chem. Phys.* **52**, 5572 (1970).
- ²⁹J. A. Barker and D. J. Auerbach, *Faraday Discuss. Chem. Soc.* **80**, 277 (1985).
- ³⁰J. C. Tully, *Faraday Discuss. Chem. Soc.* **80**, 291 (1985).
- ³¹C. T. Rettner, E. K. Schweizer, H. Stein, and D. J. Auerbach, *Phys. Rev. Lett.* **61**, 986 (1988).
- ³²K. C. Janda, J. E. Hurst, C. A. Becker, J. Cowin, L. Wharton, and D. J. Auerbach, *Surf. Sci.* **93**, 270 (1980).
- ³³E. K. Grimmelmann, J. C. Tully, and M. J. Cardillo, *J. Chem. Phys.* **72**, 1039 (1980).
- ³⁴C. T. Rettner and J. A. Barker (to be published).
- ³⁵E. K. Schweizer and C. T. Rettner (to be published).
- ³⁶A. E. Dabiri, T. J. Lee, and R. E. Stickney, *Surf. Sci.* **26**, 522 (1971).
- ³⁷G. Comsa, R. David, and B. J. Schumacher, *Surf. Sci.* **85**, 45 (1979); G. Comsa and R. David, *ibid.* **117**, 77 (1982).
- ³⁸C. A. Becker, J. P. Cowin, L. Wharton, and D. J. Auerbach, *J. Chem. Phys.* **67**, 3394 (1977).
- ³⁹S. T. Ceyer, W. L. Guthrie, T.-H. Lin, and G. A. Somorjai, *J. Chem. Phys.* **78**, 6982 (1983); T.-H. Lin and G. A. Somorjai, *ibid.* **81**, 704 (1984).
- ⁴⁰C. W. Muhlhäuser, L. R. Williams, and J. C. Tully, *J. Chem. Phys.* **83**, 2594 (1985).
- ⁴¹H. P. Steinrück, A. Winkler, and K. D. Rendulic, *J. Phys. C* **17**, L311 (1984).
- ⁴²T. Matsushima, *Surf. Sci.* **123**, L663 (1983); *J. Catalysis* **83**, 446 (1983); *Surf. Sci.* **127**, 403 (1983).
- ⁴³R. C. Cossier, S. R. Bare, S. M. Francis, and D. A. King, *Vacuum* **31**, 503 (1981).
- ⁴⁴See for example: W. Heitler, *The Quantum Theory of Radiation* (Oxford University, Oxford, England, 1954), p. 412.

C-1

APPENDIX C

ELECTRON ENERGY LOSS SPECTROSCOPY OF AMMONIA ON Ru(001)

[The text of Appendix C consists of an article coauthored with J. E. Parmeter, Y. Wang and W. H. Weinberg, which has appeared in *J. Chem. Phys.* **88**, 5225 (1988).]

Electron energy loss spectroscopy of ammonia on Ru(001)

J. E. Parmeter,^{a)} Y. Wang, C. B. Mullins,^{b)} and W. H. Weinberg

Division of Chemistry and Chemical Engineering, California Institute of Technology, Pasadena, California 91125

(Received 23 October 1987; accepted 13 January 1988)

The adsorption of ammonia on Ru(001) has been studied using high-resolution electron energy loss spectroscopy. Multilayer, second-layer, and monolayer ammonia have been characterized vibrationally. These three states desorb near 115, 130 and between approximately 150 and 350 K, respectively. The symmetric deformation mode of chemisorbed ammonia shifts down in frequency continuously with increasing coverage from approximately 1160 cm^{-1} in the low-coverage limit to approximately 1070 cm^{-1} at (monolayer) saturation. The frequency of this mode in coordination compounds of ammonia is sensitive to the charge on the metal atom (increasing with increasing positive charge), and the frequency shift of this mode on the Ru(001) surface can be correlated with the work function decrease that this surface undergoes as the ammonia coverage increases. Off-specular EEL spectra allow the weak NH_3 rocking mode and the frustrated translation of the ammonia perpendicular to the surface (i.e., the metal–nitrogen stretch) of chemisorbed ammonia to be resolved near 625 and 340 cm^{-1} , respectively. These modes have not been identified in previous EELS studies of chemisorbed ammonia on hexagonally close-packed metal surfaces. Second-layer and multilayer ammonia yield EEL spectra similar to those observed on other metal surfaces. In agreement with previous results, the adsorption of ammonia on Ru(001) at 80 K, followed by annealing, leads only to reversible desorption.

I. INTRODUCTION

The adsorption of ammonia on well-defined single-crystalline metal surfaces under ultrahigh vacuum (UHV) conditions has received considerable attention in recent years.^{1–31} This subject is of interest both because it relates to industrial catalytic processes such as ammonia synthesis,³² and because ammonia is a prototypical example of a weak donor ligand that bonds to metal atoms both in organometallic compounds^{33–42} and on surfaces via the electron lone pair on the nitrogen atom. As part of a continuing study of the chemistry of nitrogen-containing molecules on the hexagonally close-packed Ru(001) surface,^{43–44} we report here the results of a high-resolution electron energy loss spectroscopic (EELS) investigation of ammonia adsorption on this surface.

The interaction of ammonia with Ru(001) has been the focus of several previous studies.^{18–23} Danielson *et al.*¹⁸ employed thermal desorption mass spectrometry (TDMS), Auger electron spectroscopy, and low-energy electron diffraction (LEED) to study this system, and concluded that for adsorption temperatures below 300 K the chemisorbed ammonia desorbed completely reversibly, with negligible dissociation occurring upon annealing. Dissociation could be induced only by electron beam bombardment of the adsorbed ammonia, or by exposing the surface to large fluences of ammonia with the surface temperature maintained above 300 K. Bennndorf and Madey²¹ used LEED, TDMS, electron stimulated desorption ion angular distribution (ESDIAD)

measurements, and work function change ($\Delta\phi$) measurements to study ammonia adsorption on Ru(001), and also concluded that for low adsorption temperatures (approximately 80 K) ammonia adsorption is completely reversible. They showed that large ammonia exposures at 80 K lead to ammonia desorption over a broad temperature range, with monolayer desorption between approximately 150 and 350 K (and displaying weak maxima near 180 and 270 K), desorption of second-layer ammonia at 140 K, and multilayer desorption in a sharp peak at 115 K. Both ESDIAD and $\Delta\phi$ measurements supported the expected model of bonding for monolayer ammonia, namely via the lone pair of electrons on the nitrogen atom. The saturation monolayer coverage of chemisorbed ammonia was estimated to be approximately 0.25 monolayer (or 3.9×10^{14} molecule cm^{-2}) based primarily on LEED data and in analogy to previous studies of ammonia adsorption on Pt(111)⁵ and Ni(110).¹¹ It was also suggested that ammonia adsorbs in threefold hollow sites on this surface.

Electron energy loss spectroscopy has been used previously to study ammonia adsorption on Pt(111),³ Ni(111),⁹ Ni(110),⁹ Ag(110),¹ Ag(311),² and Fe(110).²⁴ In all cases, ammonia adsorbs molecularly at low temperatures (approximately 80–120 K) and only on Fe(110)²⁴ and Ni(110)¹¹ does significant dissociation occur as the surface is annealed. The EEL spectra of ammonia adsorbed in the monolayer are dominated in most cases by a strong loss feature occurring between approximately 1050 and 1170 cm^{-1} , which is due to the NH_3 symmetric deformation mode. Considerably weaker loss features occur in the frequency ranges of 1580 – 1650 , 3200 – 3320 , and 3340 – 3400 cm^{-1} , which are due, respectively, to the NH_3 asymmetric (degenerate) deformation, symmetric stretch, and asymmetric (degenerate)

^{a)} AT&T Bell Laboratories Predoctoral Fellow.

^{b)} Link Predoctoral Fellow 1985–86, IBM Predoctoral Fellow 1986–87.

ate) stretch. The characteristic frequency ranges for an NH_3 rocking mode and the frustrated translation of the ammonia perpendicular to the surface [i.e., the metal–nitrogen stretch, $\nu(\text{M}-\text{NH}_3) \equiv T_z$] are much less certain, however. The NH_3 rocking mode has not been identified previously for chemisorbed ammonia on any metal surface, although a frequency of 720 cm^{-1} has been reported for second-layer ammonia on Pt(111).³ The $\nu(\text{M}-\text{NH}_3)$ mode has been identified on only three of the metal surfaces studied, and there is a large variation in the reported values: 340 cm^{-1} on Fe(110),²⁸ 470 cm^{-1} on Ag(311),² and 570 cm^{-1} on Ni(110).⁹ It was partly in the hope of identifying these latter two modes clearly that we undertook this study of ammonia on Ru(001). As in several of the previous studies, we have measured EEL spectra of both NH_3 and ND_3 in order to confirm our mode assignments. Several of the earlier studies have also characterized second-layer and multilayer ammonia vibrationally. As might be expected, the formation of a second-layer, molecularly adsorbed state (desorbing between 120 and 160 K) and of a multilayer state (desorbing between 110 and 120 K) appears to be a general feature of ammonia adsorption on these metal surfaces, and both the second layers and the multilayers show some common EEL features on all surfaces on which they have been studied.

II. EXPERIMENTAL DETAILS

The EEL spectrometer used in this study, and the UHV chamber housing it, have been described in detail elsewhere.⁴⁹ The spectrometer employs 180° hemispheres as the energy dispersing elements in both the monochromator and the analyzer. The analyzer is rotatable within the scattering plane to allow off-specular EEL spectra to be measured. Typical parameters used in obtaining the EEL spectra presented here were the following: energy of the electron beam incident on the surface, 4 eV; resolution (full width at half-maximum of the elastically scattered beam), $50\text{--}85 \text{ cm}^{-1}$; count rate in the elastic peak, $1\text{--}3 \times 10^5$ counts per second; and (fixed) angle of incidence of the electron beam, approximately 60° with respect to the surface normal. All EEL spectra were collected in the specular direction, except as noted. All EEL spectra were recorded with the surface at a temperature of 80–100 K, after annealing to indicated temperatures.

The stainless steel UHV chamber was pumped by a 220 l/s^{-1} Varian noble vacuum pump and a titanium sublimation pump. Typical working pressures during experiments were in the range of $1\text{--}3 \times 10^{-10}$ Torr. The Ru(001) crystal could be cooled to 80 K using liquid nitrogen, and could be heated resistively to temperatures exceeding 1600 K. After each experiment, the surface was heated to 1000 K prior to the next exposure in order to desorb any trace amounts of atomic nitrogen⁵⁰ that might be formed as the result of ammonia decomposition at defects or the cracking of ammonia on hot filaments, as well as any residual hydrogen⁵¹ and carbon monoxide⁵² adsorbed from the chamber background. Periodic, extensive cleaning of the surface was accomplished both by argon ion sputtering and annealing the crystal in a background of oxygen. Surface cleanliness was verified by EELS, and by H_2 ⁵¹ and CO ⁵² thermal desorption spectra

that are characteristic of the clean surface.

The UHV chamber also contains a quadrupole mass spectrometer for performing TDMS experiments, and for the analysis both of background gases and of the purity of the ammonia that was admitted into the chamber. The thermal desorption measurements performed in connection with this work were obtained with a heating rate of approximately 8 K s^{-1} . The NH_3 used in these studies was obtained from Matheson (99.99% reported purity) and was purified by several freeze–pump–thaw cycles. The NH_3 exposures were performed by backfilling the UHV chamber through a leak valve, and the purity of the NH_3 was verified in situ using mass spectrometry. The ND_3 was obtained from MSD isotopes (99 at. % D). Due to H/D exchange of the deuterated ammonia either on the walls of the UHV chamber or in the stainless steel leak lines, ND_3 could not be admitted into the chamber cleanly through a leak valve and was therefore admitted into the chamber via a directional beam doser consisting of a microcapillary array. The purity of the ND_3 adsorbed on the surface was best monitored by comparing the integrated intensities of the ND and NH stretching vibrations measured in subsequent EEL spectra. All exposures were effected at a surface temperature of 80 K, except as noted.

III. RESULTS

A. Thermal desorption mass spectrometry

Since a detailed study of the thermal desorption of ammonia from Ru(001) has already been carried out,²¹ this subject was investigated only briefly, primarily to determine the appropriate ammonia exposures and annealing temperatures to obtain EEL spectra characteristic of multilayer, second-layer, and (various coverages of) monolayer ammonia. In reasonable agreement with the previous results, we detect the desorption of second-layer ammonia at 130 K for exposures in excess of approximately 1 L (1 L \equiv 1 Langmuir $\equiv 10^{-6}$ Torr s), and the desorption of multilayer ammonia at 115 K for exposures exceeding approximately 2 L. While the two monolayer desorption maxima were not well resolved using our apparatus, our EELS results (cf. Sec. III B) indicated that monolayer ammonia desorbed between approximately 150 and 350 K. This is also in good agreement with the previous results.

The possibility that some of the ammonia dissociates rather than desorbs as the surface is annealed was investigated briefly using H_2 thermal desorption. The H_2 thermal desorption spectra that were measured following saturation ammonia exposures were compared to those obtained following saturation hydrogen exposures on Ru(001). This allowed the maximum possible amount of ammonia that dissociates to be estimated by using the known saturation coverage of hydrogen adatoms (approximately 0.85 monolayer) on Ru(001).⁵¹ The amount of hydrogen adatoms that desorbed was never greater than 0.03 monolayer, which corresponds at most to 0.01 monolayer of NH_3 . This could correspond to the decomposition of a small amount of ammonia at defect sites. However, such a small amount of hydrogen desorption could also result from the adsorption of hydrogen from the residual gas or from a small hydrogen impurity in

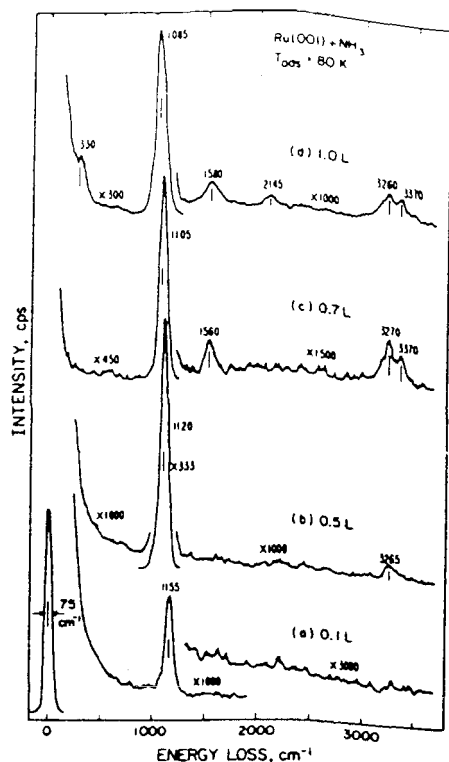


FIG. 1. The EEL spectra that result following several exposures of NH_3 to the Ru(001) surface at 80 K. (In the case of the 0.7 L exposure, the surface temperature was closer to 90 K, and the elastic peak count rate was only 2×10^6 .)

the ammonia sample. Thus, we are in complete agreement with the previous conclusion^{18,21} that ammonia decomposition is negligible on Ru(001) following ammonia adsorption at 80–100 K.

B. Electron energy loss spectroscopy

Electron energy loss spectra for several coverages of ammonia on Ru(001) at 80–90 K are shown in Fig. 1. The exposures involved correspond to submonolayer coverages; no second-layer or multilayer ammonia is present in any of these spectra with the exception of spectrum (d), where a very small amount of second-layer ammonia is probably present. Following a 0.1 L ammonia exposure, only a single loss feature is resolved at 1155 cm^{-1} . For larger ammonia exposures, this loss feature shifts downward in frequency, reaching approximately 1085 cm^{-1} following a 1 L exposure. It is by far the most intense loss feature for all submonolayer coverages, and is identified easily as being due to $\delta_s(\text{NH}_3)$, the symmetric deformation mode of molecularly adsorbed ammonia. At all coverages, it is strongly upshifted in frequency from its gas phase value of 950 cm^{-1} .⁵³ Following a 0.5 L exposure, a second loss feature is observed at 3265 cm^{-1} due to the (unresolved) symmetric and asymmetric NH_3 stretching modes. Increasing the exposure to 0.7 L allows these two modes to be resolved at 3270 and 3370 cm^{-1} , respectively, and another loss feature becomes apparent at 1560 cm^{-1} which is assigned as the asymmetric deformation mode of ammonia, $\delta_a(\text{NH}_3)$. Following a 1 L exposure all of these loss features are again resolved, and a very weak loss feature appears at 2145 cm^{-1} which is assigned as the overtone of the NH_3 symmetric deformation. Another loss feature appears at 330 cm^{-1} . While this feature may derive some intensity from the very weak frustrated translational

TABLE I. Vibrational frequencies (in cm^{-1}) and mode assignments for gas phase ammonia, and for chemisorbed ammonia on several metal surfaces.

Mode	Ru(001)									
	$\text{NH}_3(\text{g})$ (Ref. 53)	$\text{ND}_3(\text{g})$ (Ref. 53)	NH_3 (This work)	ND_3 (This work)	Pt(111) (Ref. 3)	Ni(111) (Ref. 9)	Ni(110) (Ref. 9)	Fe(110) (Ref. 28)	Ag(110) (Ref. 1)	Ag(311) (Ref. 2)
$\nu_s(\text{NH}_3)$	3414	2556	3370	2515	3340	3360	3350	3370	3390	
$\nu_a(\text{NH}_3)$	3337	2420	3260	2335	3240	3270	3200	3290		3410
$\delta_s(\text{NH}_3)$	1628	1191	1580	1165	1600	1580	1580	1640	3320	
$\delta_a(\text{NH}_3)$	950	747	1070–	835–	1140	1140	1120	1105–	1640	1648
			1160	910				1170	1050	1100
$\rho(\text{NH}_3)$	625 ^a	480 ^a	n.o. ^b	n.o.	n.o.	n.o.	n.o.	n.o.
$\nu(\text{M-NH}_3)$	340 ^a	350 ^a	n.o.	n.o.	570	340	n.o.	470

^a Generally observed only in off-specular EEL spectra.

^b s = symmetric; a = asymmetric; n.o. = not observed.

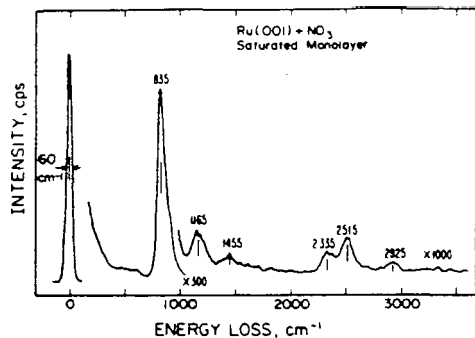


FIG. 2. The EEL spectrum that results after a Ru(001) surface with condensed multilayers of ND₃ is annealed to 150 K. This spectrum is characteristic of monolayer ND₃.

mode (normal to the surface) of the chemisorbed ammonia (cf. Fig. 3), it is most likely due primarily to the presence of a very small amount of second-layer ammonia, which exhibits an intense loss feature due to a librational mode at 360 cm^{-1} (cf. Fig. 6 and Table II). The vibrational frequencies of chemisorbed ammonia on Ru(001) are summarized in Table I, and compared to those of gas phase ammonia,⁵³ and of ammonia chemisorbed on several other single crystalline metal surfaces. (Information is also included in this table that is derived from off-specular data, cf. Fig. 3.) It should be noted that while the weak loss features due to $\delta_s(\text{NH}_3)$, $\nu_s(\text{NH}_3)$, and $\nu_a(\text{NH}_3)$ occasionally were found to have frequencies differing by as much as $\pm 40\text{ cm}^{-1}$ from the average values listed in Table I, they showed no consistent frequency shifts as a function of coverage. Although such shifts would be difficult to detect due to the low intensities of these loss features, all of these features could usually be detected in off-specular spectra following exposures as low as 0.5 L.

A typical EEL spectrum of a saturated monolayer of ND₃ on Ru(001) is shown in Fig. 2. The surface was prepared by exposing the Ru(001) crystal at 100 K to approximately 30 L ND₃, followed by annealing to 150 K to remove multilayer and second-layer ND₃. The intense $\delta_s(\text{ND}_3)$ mode occurs at 835 cm^{-1} . As in the case of $\delta_s(\text{NH}_3)$, the frequency of this mode was found to shift up with decreasing coverage, and it occurred near 910 cm^{-1} in the low coverage limit. The $\delta_a(\text{ND}_3)$, $\nu_s(\text{ND}_3)$, and $\nu_a(\text{ND}_3)$ modes occur at frequencies of 1165, 2335, and 2515 cm^{-1} , respectively. The frequencies of these modes are also listed in Table I, and the observed frequency shifts upon deuteration clearly support the assignments. A very weak loss feature is observed at 1455 cm^{-1} in Fig. 2. A similar loss feature was observed in the EEL spectrum of second-layer ND₃ on Pt(111) and was attributed to $\delta_s(\text{ND}_2\text{H})$ of a small ND₂H impurity.³ The slight asymmetry on the high energy side of the $\delta_s(\text{ND}_3)$ loss feature could also be due to the presence of a small amount of ND₂H. The weak loss feature at 2930 cm^{-1} is most likely due to $\nu(\text{CH})$ of a small hydrocarbon impurity.⁵⁴

Off-specular EEL spectra of both NH₃ and ND₃ al-

lowed two additional loss features to be resolved clearly in the low-frequency region. Figure 3 shows EEL spectra of nearly saturated monolayers of (a) NH₃ and (b) ND₃ obtained with the analyzer rotated approximately 5° off-specular (towards the surface normal). In addition to the loss features observed in specular EEL spectra, Fig. 3(a) shows features at 625 and 340 cm^{-1} , and Fig. 3(b) shows features at 480 and 350 cm^{-1} . Based on the observed frequency shifts and a comparison to vibrational data for metal-amine compounds (see Sec. IV A), the loss feature at 625 (480 cm^{-1}) is assigned to the NH₃ (ND₃) rocking mode $\rho(\text{NH}_3)$ and the loss feature at 340 (350 cm^{-1}) is assigned to the frustrated translation of the ammonia perpendicular to the surface $\nu(\text{Ru-NH}_3)$. Both of these modes are absent in gas phase ammonia, where the "rock" corresponds to a free rotation and the "frustrated translation" to a free translation of the molecule. The low intensity of the $\nu(\text{Ru-NH}_3)$ mode is consistent with previous results for ammonia adsorption on hexagonally close-packed metal surfaces, in which no metal-nitrogen stretching mode was resolved.^{3,9} Due to the low intensities of the $\rho(\text{NH}_3)$ and $\nu(\text{Ru-NH}_3)$ loss features, it is impossible to say whether or not these modes undergo frequency shifts as a function of coverage. Note that in the off-specular EEL spectra presented here the $\delta_s(\text{NH}_3)$ [$\delta_s(\text{ND}_3)$] loss feature has decreased greatly in intensity relative to the other loss features of chemisorbed ammonia. This indicates that this mode is strongly dipole enhanced in specular EEL spectra, while the remaining modes of chemisorbed ammonia are primarily impact excited.⁵⁵ It should be noted that the $\rho(\text{NH}_3)$ mode was occasionally observed as a very weak shoulder in specular EEL spectra, near 650 cm^{-1} for NH₃ and near 500 cm^{-1} for ND₃. Indeed, such shoulders are barely visible in Figs. 1(d) and 2, but the frequency cannot be assigned accurately based on these spectra.

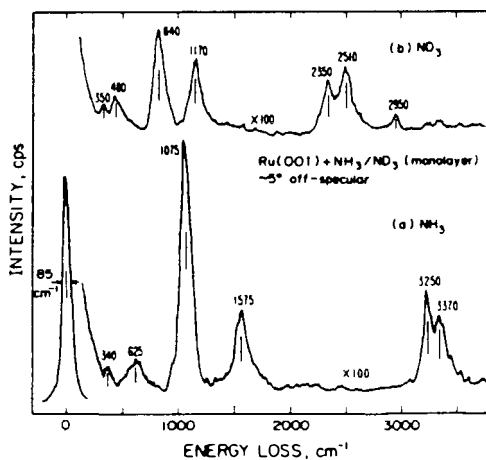


FIG. 3. Off-specular EEL spectra of monolayer (a) NH₃ and (b) ND₃ on Ru(001). Prior to spectral collection, the surface was annealed to 150 K to remove any second-layer ammonia.

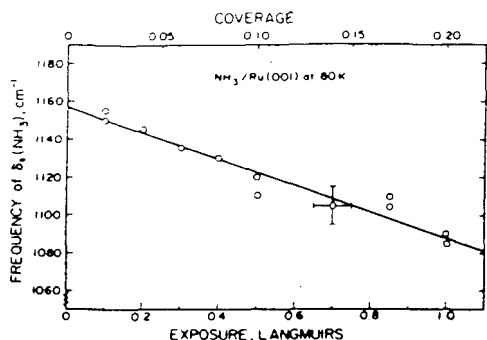


FIG. 4. The frequency of the $\delta_s(\text{NH}_3)$ mode of chemisorbed ammonia on Ru(001) as a function of ammonia coverage. The approximate coverages given are relative to the surface concentration of ruthenium atoms, which is $1.57 \times 10^{13} \text{ cm}^{-2}$, and they are based on the assumption that the saturation (monolayer) ammonia coverage is 0.25.

Figure 4 shows the variation in the frequency of the symmetric deformation mode of ammonia adsorbed on Ru(001) at 80 K as a function of the ammonia exposure. The exposure of 1 L corresponds to the coverage where the second-layer thermal desorption feature just begins to appear. However, this coverage does not correspond to monolayer saturation because the second layer begins to form before the monolayer is saturated²¹; it is estimated that this exposure corresponds to approximately 80% of monolayer saturation or an absolute coverage of approximately 0.2.²⁴ Note that the assumption of a constant probability of adsorption, in agreement with the results of Benndorf and Madey²¹ and as expected for NH_3 at 80 K given that ammonia multilayers condense at this temperature, means that the coverages are directly proportional to the ammonia exposure. The frequency of the $\delta_s(\text{NH}_3)$ mode decreases monotonically with increasing coverage, from approximately 1155 cm^{-1} following a 0.1 L NH_3 exposure. The frequency decrease is very nearly linear with coverage, although there may be a slight decrease in the absolute value of the slope at high coverages. A linear least-squares fit to the data yields

$$\delta_s(\text{NH}_3) = -69.6\epsilon + 1157, \quad (1)$$

where $\delta_s(\text{NH}_3)$ is the frequency of the NH_3 symmetric deformation mode in cm^{-1} , and ϵ is the exposure in Langmuirs.

Figure 5 shows the variation with annealing temperature of the frequency of the symmetric deformation mode of ammonia adsorbed on Ru(001) for a number of different ammonia exposures at 80 K. Following all exposures, the surface was annealed first to 150 K to be certain that only monolayer ammonia was present. It may be seen by comparison to Fig. 4 that annealing from 80 to 150 K generally did not change the frequency of $\delta_s(\text{NH}_3)$ by more than 10 cm^{-1} for exposures of 1 L or less. Following a 0.1 L ammonia exposure, the frequency of $\delta_s(\text{NH}_3)$ is nearly constant at $1150\text{--}1160 \text{ cm}^{-1}$ regardless of annealing temperature. This is consistent with the fact that the coverage is not

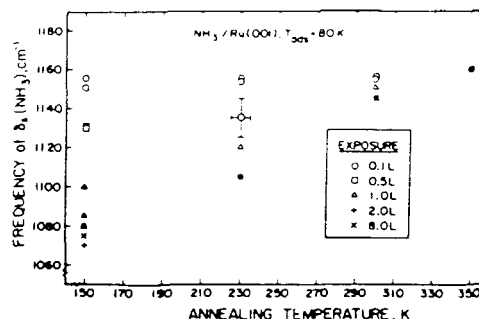


FIG. 5. The frequency of the $\delta_s(\text{NH}_3)$ mode of chemisorbed ammonia on Ru(001) as a function of annealing temperature for several initial exposures.

changing for annealing temperatures between 80 and 300 K: for such a low exposure (i.e., coverage) the ammonia desorbs only in a single peak near 315 K.²¹ On the other hand, the exposures of 2.0 and 8.0 L correspond to exposures well in excess of monolayer saturation, and annealing the surface to 150 K in each case produces a saturated monolayer of ammonia. Thus, the measured frequencies in these two cases should be the same for annealing temperatures of 150 K and greater, and this is found to be true within experimental error ($\pm 10 \text{ cm}^{-1}$). The measured frequencies increase markedly as the surface is annealed from 150 to 230 and 300 K, because for a saturated monolayer of ammonia, significant molecular desorption occurs in these temperature ranges.²¹ This results in a decrease in the coverage and thus an increase in the symmetric deformation frequency, as would be expected from an inspection of Fig. 4. For initial exposures of 0.5 and 1.0 L, the measured frequencies for any given annealing temperature fall between those obtained following 0.1 L or saturation exposures, and also increase (though less dramatically than for saturation exposures) with increasing annealing temperature. These results are all consistent with the $\delta_s(\text{NH}_3)$ frequency being a function of ammonia coverage only; the annealing temperature appears to have no effect other than to change the coverage. It should be noted that the two data points obtained following annealing to 350 K correspond to trivial amounts (≤ 0.01 monolayer) of ammonia readsorbed from the chamber background, since the thermal desorption of ammonia from Ru(001) is complete between 300 and 350 K. The $\delta_s(\text{NH}_3)$ frequency of 1160 cm^{-1} thus corresponds to the zero-coverage limit for ammonia on Ru(001), in agreement with the data of Fig. 4 and Eq. (1).

Electron energy loss spectra of second-layer NH_3 and ND_3 on Ru(001) are shown in Fig. 6, and the observed frequencies are compared to those of second-layer ammonia on other metal surfaces in Table II. The EEL spectra were obtained after the Ru(001) surface at 85 K was exposed to large fluences of NH_3 and ND_3 , followed by annealing to 120 K to remove multilayer ammonia. The loss features due to $\delta_s(\text{NH}_3)$, $\delta_a(\text{NH}_3)$, $\nu_s(\text{NH}_3)$, and $\nu_a(\text{NH}_3)$ are assigned easily as for monolayer ammonia. The $\delta_s(\text{NH}_3)$ loss feature

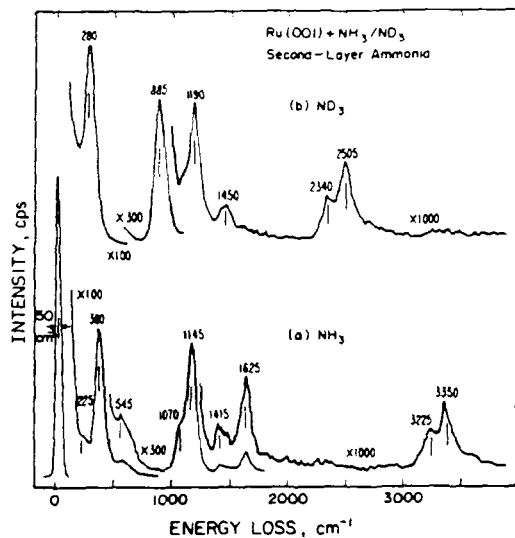


FIG. 6. The EEL spectra that result when a Ru(001) surface with condensed multilayers of (a) NH_3 and (b) ND_3 is annealed to 120 K. These spectra are characteristic of second-layer ammonia.

of second-layer NH_3 at 1145 cm^{-1} shows a pronounced shoulder at 1070 cm^{-1} , which is due to the partially screened $\delta_s(\text{NH}_3)$ loss feature of monolayer NH_3 . The corresponding shoulder in the case of ND_3 is not so well resolved because the peak frequencies are closer together (i.e., approximately 50 rather than 75 cm^{-1} splitting). The spectrum of NH_3 (ND_3) contains an intense mode at 360 (280) cm^{-1} assigned to the NH_3 twisting mode $\tau(\text{NH}_3)$ (equivalent to the frustrated librational mode R_{τ}). Note that this mode is not

observed for monolayer ammonia because in that case it corresponds to a free rotation about the ruthenium–nitrogen bond. Evidence for this free rotation in the monolayer has been obtained from ESDIAD data.²¹ This rotation is hindered in the second layer due to hydrogen bonding of the second-layer ammonia molecules to the monolayer ammonia. The EEL spectrum of Fig. 6(a) also shows loss features at 545 and 225 cm^{-1} which we tentatively assign, respectively, to an NH_3 rocking mode and the frustrated translation (perpendicular to the surface) T_z of the second-layer ammonia. The corresponding loss features are not well resolved in the case of ND_3 due to overlap with the $\tau(\text{ND}_3)$ loss feature at 280 cm^{-1} . Both spectra of Fig. 6 show a weak loss feature near 1400 cm^{-1} , the identity of which is uncertain. As stated previously, a similar loss feature has been attributed to $\delta_s(\text{ND}_2\text{H})$ of an ND_2H impurity in the case of second-layer ND_3 on $\text{Pt}(111)$.³ In the case of NH_3 , the 1415 cm^{-1} loss feature is probably a combination band (i.e., $360 + 1070$ and/or 1145).^{1,3,24} We can think of no likely impurity that would give rise to a loss feature in this frequency range; $\delta(\text{H}_2\text{O})$ of water occurs at the considerably higher frequency of 1560 cm^{-1} .²⁷

Figure 7 shows EEL spectra of (a) NH_3 and (b) ND_3 multilayers on Ru(001), and the vibrational frequencies and their assignments are listed in Table III along with data for solid ammonia and for NH_3 multilayers on other metal surfaces. Both of the EEL spectra in Fig. 7 were measured following ammonia exposures of approximately 30 L. The loss features due to the $\nu_s(\text{NH}_3)$, $\nu_a(\text{NH}_3)$, $\delta_s(\text{NH}_3)$, and $\delta_a(\text{NH}_3)$ modes are again assigned in a straightforward manner. Both spectra also show a weak loss feature due to the $\delta_s(\text{NH}_3)$ overtone/double loss. A strong loss feature at 200 cm^{-1} in both cases corresponds to an ammonia lattice mode (i.e., a frustrated translation of the ammonia molecules within the multilayers). Two strong librational modes are observed, one at 540 (420) cm^{-1} and the other a shoul-

TABLE II. Vibrational frequencies (in cm^{-1}) and mode assignments for second-layer NH_3 and ND_3 on Ru(001), and for second-layer NH_3 on several other metal surfaces.

Mode	Ru(001)					
	NH_3 (This work)	ND_3	Pt(111) (Ref. 3)	Ag(110) (Ref. 1)	Ni(110) (Ref. 9)	Ag(311) (Ref. 2)
$\tau(\text{NH}_3)^a$	360	280	350	340	360	260
$\rho(\text{NH}_3)$	545	n.o. ^b	720	n.o. ^c	n.o.	n.o.
$\delta_s(\text{NH}_3)$	1145	885	1190	1100	1110	1100
$\delta_a(\text{NH}_3)$	1625	1190	1630	1630	1630	1650
$\nu_s(\text{NH}_3)$	3225	2340	3150	3320	3200	
$\nu_a(\text{NH}_3)$						3410
T_z	225	n.o.	n.o.	n.o.	n.o.	n.o.

^a This mode is also referred to in the literature as R_{τ} (= rotation about an axis normal to the surface), or simply as ν_s (a "frustrated libration"), although the latter designation alone is ambiguous.

^b In some EEL spectra, a shoulder was present at approximately 450 cm^{-1} that might be assigned to $\rho(\text{ND}_3)$.

^c s = symmetric; a = asymmetric; n.o. = not observed.

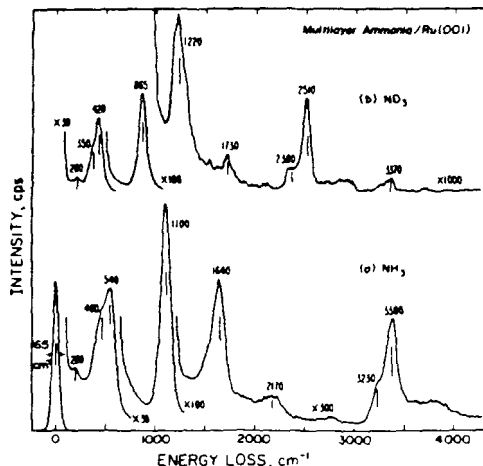


FIG. 7. The EEL spectra of condensed multilayers of (a) NH_3 and (b) ND_3 on Ru(001). The exposures were approximately 30 L at a surface temperature of 85 K.

TABLE III. Vibrational frequencies (in cm^{-1}) and mode assignments for solid ammonia, and for ammonia multilayers on several metal surfaces.

Mode	Solid ammonia		Ru(001)		Pt(111)	Ag(110)	Ag(311)
	NH_3 (Ref. 58) ^a	ND_3 (Ref. 58) ^a	NH_3 (This work)	ND_3	NH_3 (Ref. 3)	NH_3 (Ref. 1)	NH_3 (Ref. 2)
ν_s^b	138-184	132-174	200	200	n.o.	140	n.o.
ν_s^c	325-386	242-312	460	350			
ν_s^e	412-462	315-406	540	420	410	400	430
$\delta_s(\text{NH}_3)$	1057-1080	815-836	1100	865	1120	1070	1150
$\delta_a(\text{NH}_3)$	1630-1679	1183-1217	1640	1220	1640	1630	1570
$\nu_a(\text{NH}_3)$	3160-3330	2318-2336	3230	2380	n.o. ^d	3320	n.o.
$\nu_a(\text{NH}_3)$	3370-3378	2505-2511	3380	2520	3320	3380	n.o.

^a A range of values is given for each frequency of solid NH_3 and ND_3 , based on several IR and Raman studies at temperatures ranging from 18 to 151 K. In some studies, more than one frequency was observed due to crystal splitting.

^b ν_s = frustrated translation or lattice mode.

^c ν_s = frustrated libration. Since there is some confusion over the assignments of these modes in the literature, we do not attempt to assign them to specific librations.

^d s = symmetric; a = asymmetric; n.o. = not observed.

der at 460 (350) cm^{-1} . These frequencies are somewhat higher than those reported previously for both ammonia multilayers and solid ammonia,⁵⁸ although we note that the frequencies were lower if only a few layers of ammonia were present (e.g., approximately 370 and 450 cm^{-1} following an 8 L NH_3 exposure). Both spectra show low intensity tails on the high energy side of the $\nu_a(\text{NH}_3)$ loss features, the origins of which are not entirely clear, although they may be due to combination bands of $\nu_a(\text{NH}_3)$ [$\nu_a(\text{ND}_3)$] and the librational and/or frustrated translational modes. The peak at 3370 cm^{-1} in the ND_3 multilayer spectrum is due primarily to the combination band $\delta_s(\text{ND}_3) + \nu_a(\text{ND}_3)$, although $\nu(\text{NH})$ modes due to contamination of the ND_3 sample may also contribute to its intensity. A loss feature of similar intensity was observed at 4480 cm^{-1} in NH_3 multilayer spectra that were scanned to higher loss energy, and this peak is assigned as $\delta_s(\text{NH}_3) + \nu_a(\text{NH}_3)$.

IV. DISCUSSION

A. Comparison to ammonia on other metal surfaces and in coordination compounds

The EEL spectra that have been obtained for ammonia adsorbed on Ru(001) show strong similarities to those obtained when ammonia is adsorbed on other hexagonally close-packed metal surfaces [i.e., Pt(111)³ and Ni(111)⁹], and on the pseudo-close-packed Fe(110) surface.²⁴ On the more highly corrugated surfaces, the EELS data currently available do not provide a consistent picture. On Ag(110),¹ the EEL spectra of adsorbed ammonia are very similar to the spectra obtained for ammonia on the more densely packed surfaces, with the $\delta_s(\text{NH}_3)$ loss feature at 1050 cm^{-1} being by far the most intense feature in the entire spectrum. The EEL spectra of ammonia adsorbed on Ag(311) are also similar, although in this case a mode of moderate intensity was

observed at 470 cm^{-1} that was assigned as $\nu(\text{Ag-NH}_3)$.² The EEL spectra of ammonia on Ni(110) are surprisingly different, with $\delta_s(\text{NH}_3)$, $\delta_a(\text{NH}_3)$, and $\nu_a(\text{NH}_3)$ loss features of comparable intensity and an additional strong mode at 570 cm^{-1} that was assigned as $\nu(\text{Ni-NH}_3)$.⁹ However, this mode assignment does not appear to have been verified by obtaining EEL spectra of chemisorbed ND_3 on this surface. Despite the lack of a consistent pattern of mode intensities on the highly corrugated surfaces, the mode frequencies of $\delta_s(\text{NH}_3)$, $\delta_a(\text{NH}_3)$, $\nu_a(\text{NH}_3)$, and $\nu_s(\text{NH}_3)$ are quite similar on all of the metal surfaces where ammonia chemisorption has been studied by EELS. This fact, along with the consistent pattern of mode intensities on Ru(001), Pt(111), Ni(111), Fe(110), and Ag(110), suggests some useful comparisons to infrared data for metal compounds containing ammonia ligands.

Table IV provides a compilation of vibrational data for ammonia adsorbed on metal surfaces and in four different classes of metal-ammonia compounds. The data for the metal compounds show some interesting trends with regard to the charge (both formal and actual) on the metal atom. Note that the "electron richness" of the metal atoms in these compounds is expected to follow the order



The frequency of the $\delta_s(\text{NH}_3)$ mode is very charge sensitive and shifts upward with increasing charge on the metal atom, having average values of 1158 cm^{-1} in the $\text{M}(\text{NH}_3)_6^{2+}$ compounds, 1333 cm^{-1} in the $\text{M}(\text{NH}_3)_6^{3+}$ compounds, and intermediate average values in the case of the $\text{M}(\text{NH}_3)_4^{2+}$ compounds. The changes observed in the frequency of this mode when the metal atom is changed and the charge held constant are minor compared to those resulting from charge changes.³⁹ The $\rho(\text{NH}_3)$ and $\nu(\text{M-NH}_3)$ modes are also charge sensitive and show marked upshifts in frequency in

TABLE IV. Vibrational frequencies (in cm^{-1}) for various modes of ammonia adsorbed on Ru(001) and other metal surfaces (Refs. 1-3, 9, and 28), and in various types of inorganic compounds (Ref. 64). The first number given in each case is the average frequency for the specific mode in a certain type of compound, and is followed in parentheses by the number of compounds that was used in calculating the average. Below this, the range (low and high extremes) is listed for the same mode.

Mode	Ru(001) (This work)	Other metal surfaces ^a	$M(\text{NH}_3)_6^{2+}$ (Ref. 64) ^b	$M(\text{NH}_3)_4^{2+}$ (Ref. 64) ^c	$M(\text{NH}_3)_4^{2+}$ tetrahedral (Ref. 64) ^d	$M(\text{NH}_3)_4^{2+}$ square planar (Ref. 64) ^e
$\nu_s(\text{NH}_3)^f$	3370	3363(5) 3340- 3400	3269(3) 3240- 3310	3336(7) 3300- 3353	3316(3) 3233- 3354	3272(3) 3236- 3327
$\nu_t(\text{NH}_3)$	3260	3264(5) 3200- 3320	3183(3) 3130- 3250	3200(7) 3160- 3250	3226(3) 3150- 3267	3165(3) 3156- 3170
$\delta_s(\text{NH}_3)$	1580	1615(6) 1580- 1648	1616(6) 1587- 1630	1601(8) 1585- 1610	1608(3) 1596- 1617	1612(3) 1563- 1669
$\delta_t(\text{NH}_3)$	1115	1119(6) ^g 1070- 1160	1333(6) 1290- 1368	1158(8) 1091- 1220	1227(3) 1176- 1253	1298(3) 1279- 1325
$\rho(\text{NH}_3)$	625	Not observed previously	806(6) 748- 857	656(8) 592- 769	683(3) 670- 693	807(3) 735- 849
$\nu(\text{M-NH}_3)$ (A_1)	340	Reported values of 340, 470, 570	488(6) 462- 527	332(6) 298- 370	409(3) 370- 432	481(3) 420- 524

^a Data are for Ag(110), Ag(311), Pt(111), Ni(111), Ni(110), and Fe(110).

^b Data are for M = Cr, Ru, Os, Co, Rh, and Ir.

^c Data are for M = Mg, Mn, Fe, Ru, Co, Ni, Zn, and Cd.

^d Data are for M = Co, Zn, and Cd.

^e Data are for M = Pd, Pt, and Cu.

^f In the case of Fe(110), where $\delta_t(\text{NH}_3)$ was reported to shift in frequency as a function of coverage (Ref. 28), an average value was used as the characteristic frequency of chemisorbed ammonia.

^g s = symmetric; a = asymmetric; n.o. = not observed.

going from the $M(\text{NH}_3)_6^{2+}$ to the $M(\text{NH}_3)_4^{2+}$ metal compounds, although in these cases there is somewhat larger overlap between the frequency ranges for these compounds and the $M(\text{NH}_3)_6^{2+}$ compounds. The $\nu_s(\text{NH}_3)$ mode is slightly charge sensitive, and shifts upward in frequency with decreasing charge on the metal atom. The $\nu_t(\text{NH}_3)$ and $\delta_s(\text{NH}_3)$ modes are not sensitive to the oxidation state of the metal atom and show no consistent frequency shifts.

Comparing the EELS data for ammonia on metal surfaces to the data for coordination compounds reveals immediately that the $\delta_t(\text{NH}_3)$ frequencies observed on surfaces are very similar to those observed in the $M(\text{NH}_3)_6^{2+}$ compounds, although the average frequency of 1119 cm^{-1} and the high and low extremes are all 40-50 cm^{-1} lower for the adsorbed ammonia. It is expected that the $\delta_t(\text{NH}_3)$ frequencies would be somewhat lower on metal surfaces, since the formal oxidation state of the surface metal atoms is zero. Thus, the observed frequencies of this mode for ammonia adsorbed on a number of metal surfaces appear to correlate well with the IR data for coordination compounds. The same is true in the case of the $\nu_s(\text{NH}_3)$ mode, the average frequency of which is higher on surfaces than in the coordination compounds. However, this is of only minor significance because this mode is only slightly charge sensitive, and due to its low intensity and overlap with the $\nu_t(\text{NH}_3)$ loss

feature, its frequency on any given surface cannot be determined as accurately as that of $\delta_t(\text{NH}_3)$.

The fact that the $\delta_t(\text{NH}_3)$ frequencies of chemisorbed ammonia are similar to those of $M(\text{NH}_3)_6^{2+}$ compounds suggest that the frequencies of the other two vibrational modes that are strongly charge sensitive, $\rho(\text{NH}_3)$ and $\nu(\text{M-NH}_3)$, might also be similar in these two cases. While very few data for these two vibrational modes of chemisorbed ammonia are available, our results provide strong support for this proposition. The measured $\rho(\text{NH}_3)$ frequency of 625 cm^{-1} is well within the range of $592-769 \text{ cm}^{-1}$ reported for the $M(\text{NH}_3)_6^{2+}$ compounds, and is slightly lower than the average value of 656 cm^{-1} , just as our measured average $\delta_t(\text{NH}_3)$ frequency of 1115 cm^{-1} is slightly lower than the average value of 1158 cm^{-1} in these compounds. The $\rho(\text{NH}_3)$ frequencies of the $M(\text{NH}_3)_6^{2+}$ compounds are considerably higher, ranging from 748 to 857 cm^{-1} .

In the case of $\nu(\text{M-NH}_3)$, the available data for ammonia on metal surfaces present a more complex picture, but our measured frequency of 340 cm^{-1} is in good agreement with data for the $M(\text{NH}_3)_6^{2+}$ compounds and identical to the value reported for ammonia on the pseudo-close-packed Fe(110) surface.²⁸ The reported values of $\nu(\text{M-NH}_3)$ for Ag(311)² and Ni(110)⁹ of 470 and 570 cm^{-1} , respectively, are considerably higher and similar to those observed in the

$M(\text{NH}_3)_6^{+}$ compounds (462 to 527 cm^{-1}), even though the observed $\delta_1(\text{NH}_3)$ frequencies on both surfaces are very similar to those observed on close-packed and pseudo-close-packed surfaces and in the $M(\text{NH}_3)_6^{+}$ compounds. While this difference is no doubt related in some way to the highly corrugated structures of the Ag(311) and Ni(110) surfaces, its exact explanation is unclear. In general, however, the comparison of the vibrational spectra of chemisorbed and coordinated ammonia appears promising, and also serves to point out the importance of obtaining off-specular spectra when EELS is used to study ammonia chemisorption.

B. Origins of the frequency shift of $\delta_1(\text{NH}_3)$: Correlation with work function data

The pronounced charge sensitivity of the $\delta_1(\text{NH}_3)$ frequency in coordination compounds also provides an explanation for the observed shift in the frequency of this mode as a function of coverage for ammonia chemisorbed on Ru(001). The work function change of Ru(001) as a function of ammonia coverage at 80 K has been studied by Benndorf and Madey,²¹ and the work function was found to decrease monotonically by approximately 1.8 eV as the coverage is increased from 0 to 0.25 monolayer. The work function change is saturated only after a total ammonia coverage of approximately 0.6 monolayer, and the work function is then approximately 2.3 eV less than on the clean surface. The decrease in the work function is initially linear with coverage, but it increases slightly less rapidly with coverage above a coverage of approximately 0.15 to 0.20 monolayer, and much less rapidly above 0.25 monolayer. The work function decrease results from a net transfer of electrons from the ammonia to the ruthenium surface atoms, so that the electron richness of these surface atoms is increased as the coverage increases. The decreased "charge" on the metal atoms then leads to a lower $\delta_1(\text{NH}_3)$ frequency, just as in the coordination compounds of Table IV.

The magnitude of this charge, or the number of electrons donated to each surface metal atom by the ammonia adlayer for a given ammonia coverage, can be estimated approximately using the surface-ammonia dipole moment of 1.9 D calculated by Benndorf and Madey,²¹ and assuming a surface-nitrogen bond distance of 2.15 Å.⁶⁰ This suggests that approximately 0.18 electron is transferred to the surface per adsorbed ammonia molecule. While the dipole moment of 1.9 D was based on the slope of the work function vs ammonia coverage curve in the limit of zero coverage, the curve is only slightly nonlinear below a coverage of 0.25, and a large part of this nonlinearity is probably due to the fact that some adsorption into the second layer occurs before the monolayer is completely saturated.²¹ Our results showing that the frequency of $\delta_1(\text{NH}_3)$ decreases nearly linearly with coverage up to at least a coverage of approximately 80% of monolayer saturation supports this point of view, and it is therefore reasonable to assume this same dipole moment for each adsorbed ammonia molecule up to monolayer saturation. Thus, for a saturation monolayer ammonia coverage of 0.25, an average of approximately 0.045 electron is transferred to each surface ruthenium atom from the ammonia adlayer.

This interpretation of the frequency shift of $\delta_1(\text{NH}_3)$ has several important implications regarding ammonia chemisorption on Ru(001) and other metal surfaces. First, it suggests that this downshift should occur as the ammonia coverage is increased on all metal surfaces, and that the magnitude of the shift should scale approximately with the amount of charge transfer characteristic of ammonia adsorption. This hypothesis cannot yet be tested fully due to a lack of experimental data, but it is interesting to note that on Fe(110) a comparable work function decrease (approximately 2 eV)²⁶ and frequency shift (from 1170 to 1105 cm^{-1})²⁸ have been found. The Pt(111) surface exhibits a work function decrease of approximately 2.7 eV when a monolayer saturation coverage of ammonia is adsorbed.⁵ While the published EEL spectra for monolayer ammonia on this surface show $\delta_1(\text{NH}_3)$ frequencies varying from at least 1170 to 1090 cm^{-1} ,³ it is not clear whether there is a monotonic shift as a function of coverage. It must also be pointed out that a series of EEL spectra for various ammonia coverages on Ag(311) show no apparent shift in the frequency of this mode.² Work function data are not available for this surface. This interpretation suggests also that the $\delta_1(\text{NH}_3)$ frequency of ammonia chemisorbed on Ru(001) should be increased by the presence of electronegative adatoms such as oxygen, and decreased by the presence of electropositive adatoms such as alkali metals. In the case of oxygen, however, the effects of hydrogen bonding will complicate the analysis.²³

Finally, we note that frequency shifts as a function of ammonia coverage might also be expected for the $\rho(\text{NH}_3)$ and $\nu(\text{Ru-NH}_3)$ modes of ammonia chemisorbed on Ru(001), since these modes are also charge sensitive for ammonia in coordination compounds. We cannot address this question unambiguously because the loss features due to these modes are below our limit of detectability for ammonia coverages less than approximately half of monolayer saturation. In addition, these low frequency modes are likely to be more affected than the $\delta_1(\text{NH}_3)$ mode by such effects as tilting of the ammonia at high coverages, a phenomenon which has been proposed to occur based on ESDIAD results.²¹

C. Adsorption site of NH_3 on Ru(001)

The adsorption site(s) of ammonia on metal surfaces has been the subject of some disagreement in the literature. Based on indirect evidence obtained using a variety of experimental techniques, it has been suggested that ammonia adsorbs with the nitrogen atom in threefold hollow sites on Ru(001),²¹ Pt(111),³ Ir(111),^{17(a)} and Ni(111),⁹ and with the nitrogen atom in the long bridging sites on the pseudo-close-packed Fe(110) surface.²⁶ On the other hand, the on-top site was favored for ammonia adsorption on Al(111),³¹ and calculations for ammonia adsorption on Al(111)⁶¹ and Cu(111)⁶² support this model, showing the interaction between the nitrogen lone pair and the threefold hollow sites to be repulsive. The great similarities among the EEL spectra of ammonia chemisorbed on Ru(001), Pt(111),³ Ni(111),⁹ Fe(110),²⁸ and Ag(110)¹ suggest (but do not prove) that a common adsorption site is occupied on all of these surfaces.

For several reasons, we prefer the on-top site as the bonding site of chemisorbed ammonia on Ru(001). The primary reason is that the vibrational frequencies of adsorbed ammonia agree so well with those of ammonia ligands in hexamine compounds, which are "on-top" by definition. We would expect that the frequencies of $\rho(\text{NH}_3)$ and especially $\nu(\text{Ru-NH}_3)$ would be substantially different if bonding occurred in threefold hollow or twofold bridge sites. This hypothesis cannot be tested because *there is no example known to us in metal cluster chemistry of an ammonia ligand that occupies a threefold hollow or twofold bridging site, or any site other than an on-top site.*⁶³ The same is true of the closely related phosphine (PR_3) ligands. In fact, to our knowledge, NH_3 , $\text{NH}_2(\text{NR}_2)$, and $\text{NH}(\text{NR})$ ligands occupy only on-top, twofold bridging and threefold hollow sites, respectively, in metal cluster compounds.⁶³

We note also that the Fe(110) surface contains no true threefold hollow sites, although it is possible that the pseudo-threefold sites on this surface might be sufficiently similar to true threefold sites to give rise to virtually identical EEL spectra for an adsorbed species. All of these arguments support the intuitive expectation that a strong σ -electron donor such as ammonia should adsorb on the most electron deficient site on these surfaces, namely, the on-top site.⁶² While none of these points taken alone is compelling, we believe that together they provide considerable support for on-top bonding. Hopefully, additional data for ammonia adsorption on surfaces and (especially) in metal clusters will clarify this issue.

D. Second-layer and multilayer ammonia

As pointed out in Sec. III B, the EELS spectra of second-layer ammonia on Ru(001) show strong similarities to those obtained on other metal surfaces. Most notably, the strong $\tau(\text{NH}_3)$ loss feature at 350 cm^{-1} is very similar both in frequency and intensity to the corresponding loss features on Pt(111),³ Ag(110),¹ and Ni(110).⁹ Surprisingly, the corresponding loss feature on Ag(311)² was observed at the substantially lower frequency of 260 cm^{-1} . Nevertheless, it appears that a strong $\tau(\text{NH}_3)$ loss feature near 350 cm^{-1} is characteristic of second-layer ammonia on most surfaces and may be used as a vibrational fingerprint for the second layer. Note that the librational modes reported to date for multilayer ammonia (*cf.* Table III) occur at frequencies greater than 400 cm^{-1} . The intensity of the $\tau(\text{NH}_3)$ loss feature, and the fact that it is strongly attenuated in off-specular EEL spectra indicate that it is dipole enhanced and thus belongs to the totally symmetric representation of the surface/second-layer ammonia complex. This suggests that at least some of the second-layer ammonia is adsorbed with the molecular axis tilted significantly with respect to the surface normal. This is in agreement with the ESDIAD results of Benndorf and Madey,²¹ who observed normal emission of H^+ for second-layer but not monolayer ammonia, and interpreted this in terms of tilting of the molecules within the second layer.

We note also that our $\rho(\text{NH}_3)$ frequency of second-layer ammonia of 545 cm^{-1} is substantially lower in frequency than that of 720 cm^{-1} reported for second-layer ammonia

on Pt(111).³ The corresponding loss feature in the case of second-layer ND_3 on Pt(111) occurred at 570 cm^{-1} .³ In our study, the corresponding mode in the case of ND_3 was not resolved unambiguously, although in some EEL spectra of second-layer ND_3 a shoulder was observed at approximately 450 cm^{-1} . For both of these reasons, and because this mode has not been identified in EEL spectra of second-layer ammonia on other metal surfaces, our assignment should be regarded as tentative.

The vibrational frequencies of multilayer NH_3 and ND_3 on Ru(001) are in reasonably good agreement with those of solid ammonia, although the frustrated translational and librational modes occur at slightly higher frequencies. We emphasize that even though all ammonia layers above the second are indistinguishable in thermal desorption spectra, quite large ammonia exposures were necessary in order to obtain an EEL spectrum of true ammonia multilayers, *i.e.*, a spectrum that showed no changes in the frequencies of the various vibrational modes with increasing exposure of the surface to ammonia at 85 K. The main changes for lower exposures were in the frequencies of the librational modes, which shifted upward with increasing exposure until a total exposure of 15–20 L was reached. This would correspond, very approximately, to 15 "layers" of ammonia. It is possible that some of the previously reported librational frequencies of ammonia multilayers on metal surfaces would have been upshifted further if the exposures had been increased, and the fact that the observed librational frequencies of multilayer ammonia are in all cases higher than those of the strong librational mode of second-layer ammonia is consistent with our results.

V. CONCLUSIONS

High-resolution electron energy loss spectroscopy has been used to study the interaction of ammonia with the Ru(001) surface. The results are generally in agreement with those of previous studies of the ammonia/Ru(001) system utilizing other experimental techniques. In particular, we find no significant decomposition of ammonia following exposures to the Ru(001) surface at 80–100 K, and our EEL spectra support the desorption temperatures for multilayer, second-layer, and monolayer ammonia that have been reported previously. The principal new conclusions that may be drawn from the EELS results are the following:

(1) Monolayer ammonia on Ru(001) exhibits EEL spectra with $\delta_s(\text{NH}_3)$, $\delta_a(\text{NH}_3)$, $\nu_s(\text{NH}_3)$, and $\nu_a(\text{NH}_3)$ frequencies very similar to those of ammonia chemisorbed on other close-packed and pseudo-close-packed metal surfaces. In addition, the NH_3 rocking mode and the frustrated translational mode of the ammonia perpendicular to the surface are observed in off-specular EEL spectra and occur at frequencies of approximately 625 and 340 cm^{-1} , respectively. The $\rho(\text{NH}_3)$ mode has not been identified previously for chemisorbed ammonia, and the $\nu(\text{metal-NH}_3)$ mode has been identified only rarely. These results indicate the importance of obtaining off-specular spectra in EELS studies of chemisorbed ammonia.

(2) The vibrational spectra of ammonia chemisorbed on Ru(001) and other metal surfaces of similar geometry

are very similar to those of hexamine 2+ compounds, $M(NH_3)_6^{2+}$, and agree much less well with those of $M(NH_3)_8^{2+}$ and $M(NH_3)_4^{2+}$ compounds, regardless of the type of metal atom and counter ions in the complexes. Thus, both on surfaces and in coordination compounds, the real (not formal) "oxidation state" of the metal is of paramount importance in determining the vibrational frequencies of coordinated ammonia.

(3) The intense $\delta_1(NH_3)$ mode of chemisorbed NH_3 on Ru(001) shifts down continuously and essentially linearly with increasing coverage, from 1160 cm^{-1} in the low coverage limit to 1070 cm^{-1} at monolayer saturation. This parallels the downshift of the frequency of this mode in coordination compounds as the charge on the metal atom decreases. This change can be correlated with the large decrease ($\sim 2\text{ eV}$) in the work function of the Ru(001) surface that occurs as ammonia is adsorbed,²¹ making the surface atoms, in effect, more "negatively charged."

(4) The EELS results, and the organometallic literature concerning NH_3 ligands, are more consistent with chemisorbed NH_3 bonding in on-top sites, rather than in threefold sites.

(5) The vibrational characteristics of second-layer and multilayer ammonia on Ru(001) are generally quite similar to those of second-layer and multilayer ammonia on other metal surfaces. The intense $\tau(NH_3)$ loss feature near 350 cm^{-1} appears to be a general feature of second-layer ammonia on most metal surfaces. The fact that this mode is dipolar in nature suggests a tilting of the molecular axis of the second-layer ammonia away from the surface normal, consistent with previous ESDIAD results.²¹ While all layers above the second are indistinguishable in thermal desorption spectra, substantially larger coverages (i.e., approximately 15 layers) of condensed ammonia are necessary to obtain a multilayer EEL spectrum which shows no further changes in the vibrational frequencies of the various modes when additional exposures are made.

ACKNOWLEDGMENTS

We are indebted to Dr. Udo Schwalke for assistance in the early stages of this work. Helpful discussions with Professor J. E. Bercaw, Dr. T. E. Madey, and Professor W. A. Goddard are gratefully acknowledged. This work was supported by the National Science Foundation under Grant No. CHE-8617826.

- ¹J. L. Gland, B. A. Sexton, and G. E. Mitchell, *Surf. Sci.* **115**, 623 (1982).
²S. T. Ceyer and J. T. Yates, Jr., *Surf. Sci.* **155**, 584 (1985).
³B. A. Sexton and G. E. Mitchell, *Surf. Sci.* **99**, 523 (1980).
⁴B. A. Sexton and G. E. Mitchell, *Surf. Sci.* **99**, 539 (1980).
⁵G. B. Fisher, *Chem. Phys. Lett.* **44**, 683 (1981).
⁶J. L. Gland, *Surf. Sci.* **71**, 327 (1978).
⁷J. L. Gland and V. N. Korechak, *J. Catal.* **53**, 9 (1978).
⁸J. L. Gland and E. B. Kollin, *Surf. Sci.* **104**, 478 (1981).
⁹G. B. Fisher and G. E. Mitchell, *J. Electron Spectrosc. Relat. Phenom.* **29**, 253 (1983).
¹⁰C. W. Seabury, T. N. Rhodin, R. J. Purtell, and R. P. Merrill, *Surf. Sci.* **93**, 117 (1980).
¹¹M. Grunze, M. Golze, R. K. Driscoll, and P. A. Dowber, *J. Vac. Sci. Technol.* **18**, 611 (1981).

- ¹²K. Jacobi, E. S. Jensen, T. N. Rhodin, and R. P. Merrill, *Surf. Sci.* **108**, 397 (1981).
¹³T. E. Madey, J. E. Houston, C. W. Seabury, and T. N. Rhodin, *J. Vac. Sci. Technol.* **18**, 476 (1981).
¹⁴F. P. Netzer and T. E. Madey, *Phys. Rev. Lett.* **47**, 928 (1981).
¹⁵F. P. Netzer and T. E. Madey, *Surf. Sci.* **119**, 422 (1982).
¹⁶M. Grunze, P. A. Dowber, and C. R. Brundle, *Surf. Sci.* **128**, 311 (1983).
¹⁷(a) R. J. Purtell, R. P. Merrill, C. W. Seabury, and T. N. Rhodin, *Phys. Rev. Lett.* **44**, 1279 (1980); (b) W. M. Kang, C. H. Li, S. Y. Tang, C. W. Seabury, K. Jacobi, T. N. Rhodin, R. J. Purtell, and R. P. Merrill, *ibid.* **47**, 931 (1981).
¹⁸L. R. Danielson, M. J. Dresser, E. E. Donaldson, and J. T. Dickinson, *Surf. Sci.* **71**, 599 (1978).
¹⁹L. R. Danielson, M. J. Dresser, E. E. Donaldson, and D. R. Sandstrom, *Surf. Sci.* **71**, 615 (1978).
²⁰T. E. Madey and J. T. Yates, Jr., in *Proceedings of the 7th International Vacuum Congr. and 3rd International Conference on Solid Surfaces*, edited by R. Dobrozemsky, F. Rüdener, F. P. Viehbock, and A. Breth (Vienna, 1977), p. 1183.
²¹C. Benndorf and T. E. Madey, *Surf. Sci.* **135**, 164 (1983).
²²C. Benndorf and T. E. Madey, *Chem. Phys. Lett.* **101**, 59 (1983).
²³T. E. Madey, C. Benndorf, D. L. Doering, and S. Semancik, *Proc. 8th Int. Congr. Catal.* **4**, 51 (1984).
²⁴M. Grunze, F. Bozso, G. Ertl, and M. Weiss, *Appl. Surf. Sci.* **1**, 241 (1978).
²⁵M. Drechsler, H. Hoinkes, H. Kaarmann, H. Wilsch, G. Ertl, and M. Weiss, *Appl. Surf. Sci.* **3**, 217 (1979).
²⁶M. Weiss, G. Ertl, and F. Nitschke, *Appl. Surf. Sci.* **3**, 614 (1979).
²⁷M. Grunze and G. Ertl, in *Ref. 20*, p. 1137.
²⁸W. Erley and H. Ibach, *Surf. Sci.* **119**, L357 (1982).
²⁹K. Kishi and M. W. Roberts, *Surf. Sci.* **62**, 252 (1977).
³⁰J. D. Gay, M. Textor, R. Mason, and Y. Iwasawa, *Proc. R. Soc. London Ser. A* **356**, 25 (1977).
³¹F. P. Netzer and T. E. Madey, *Chem. Phys. Lett.* **88**, 315 (1982).
³²See, for example, G. C. Bond, *Catalysis by Metals* (Academic, New York, 1962).
³³J. R. Hall and G. A. Swile, *J. Organomet. Chem.* **42**, 479 (1972).
³⁴R. P. Shibaeva, L. P. Rozenberg, R. M. Lobkovskaya, A. E. Shilov, and G. B. Shulpin, *J. Organomet. Chem.* **220**, 271 (1981).
³⁵L. M. Vallano and S. W. Shearfold, *Inorg. Chim. Acta* **36**, 243 (1979).
³⁶W. Rigby, J. A. McCleverty, and P. M. Maitlis, *J. Chem. Soc. Dalton Trans.* **1979**, 382.
³⁷B. P. Sullivan, J. A. Baumann, T. J. Meyer, D. J. Salmon, H. Lehmann, and A. Ludi, *J. Am. Chem. Soc.* **99**, 7368 (1977).
³⁸H. Lehmann, K. J. Schenk, G. Chapuis, and A. Ludi, *J. Am. Chem. Soc.* **101**, 6197 (1979).
³⁹D. Rehder, *J. Organomet. Chem.* **37**, 303 (1972).
⁴⁰J. E. Ellis and K. L. Fjare, *Organomet.* **1**, 898 (1982).
⁴¹D. Sellmann, A. Brandl, and R. Endell, *J. Organomet. Chem.* **111**, 303 (1976).
⁴²M. Herberhold, F. Wehrmann, D. Neugebauer, and G. Huttner, *J. Organomet. Chem.* **152**, 329 (1978).
⁴³A. B. Anton, N. R. Avery, B. H. Toby, and W. H. Weinberg, *J. Electron. Spectrosc.* **29**, 181 (1983).
⁴⁴A. B. Anton, N. R. Avery, T. E. Madey, and W. H. Weinberg, *J. Chem. Phys.* **85**, 507 (1986).
⁴⁵U. Schwalke, J. E. Parmeter, and W. H. Weinberg, *J. Chem. Phys.* **84**, 4036 (1985).
⁴⁶U. Schwalke, J. E. Parmeter, and W. H. Weinberg, *Surf. Sci.* **178**, 625 (1986).
⁴⁷J. E. Parmeter, U. Schwalke, and W. H. Weinberg, *J. Am. Chem. Soc.* **109**, 1876 (1987).
⁴⁸R. P. Parmeter, U. Schwalke, and W. H. Weinberg, *J. Am. Chem. Soc.* **109**, 5083 (1987).
⁴⁹G. E. Thomas and W. H. Weinberg, *Rev. Sci. Instrum.* **50**, 497 (1979).
⁵⁰The recombinative desorption of nitrogen adatoms from Ru(001) occurs near 800–850 K (Ref. 21).
⁵¹The recombinative desorption of hydrogen adatoms from Ru(001) occurs below 450 K; H. Shimizu, K. Christmann, and G. Ertl, *J. Catal.* **61**, 412 (1980).
⁵²The desorption of molecularly chemisorbed CO from Ru(001) occurs below 500 K. (a) T. E. Madey and D. Menzel, *J. Appl. Phys. Suppl.* **2**, Part 2, 229 (1974); (b) H. Pfnür, P. Feulner, H. A. Engelhardt, and D. Menzel, *Chem. Phys. Lett.* **59**, 481 (1978); (c) H. Pfnür, P. Feulner, and D. Menzel, *J. Chem. Phys.* **79**, 4613 (1983).

- ¹³H. Ibach and D. L. Mills, *Electron Energy Loss Spectroscopy and Surface Vibrations* (Academic, New York, 1982), p. 348.
- ¹⁴While it is unclear exactly what this impurity might be, this loss feature is quite clear in off-specular spectra, consistent with its assignment as a $\nu(\text{CH})$ mode. It seems too low in frequency to be due to a $\nu(\text{NH})$ mode.
- ¹⁵For a discussion of dipole and impact scattering, see Ref. 53, Chaps. 1 and 3.
- ¹⁶The estimate of 80% of monolayer saturation is arrived at from both the thermal desorption spectra of Ref. 21, and by noting in Fig. 5 that the minimum $\delta_1(\text{NH}_3)$ frequency for monolayer ammonia on Ru(001) is approximately 1070 cm^{-1} , and assuming the frequency decrease to be linear up to saturation.
- ¹⁷P. A. Thiel, F. M. Hoffmann, and W. H. Weinberg, *J. Chem. Phys.* **75**, 5556 (1981).
- ¹⁸O. S. Binbrek and A. Anderson, *Chem. Phys. Lett.* **15**, 421 (1972), and references therein.
- ¹⁹For example, consider the $\delta_1(\text{NH}_3)$ frequencies (in cm^{-1}) of the following series of $\text{M}(\text{NH}_3)_6^{2+}$ compounds: Mn, 1146; Fe, 1156; Co, 1163; Ni, 1176; Zn, 1145. On the other hand, there is a large frequency difference between $\text{Co}(\text{NH}_3)_6^{2+}$ (1163) and $\text{Co}(\text{NH}_3)_5^{2+}$ (1329).
- ²⁰This distance appears to be typical of metal-nitrogen bond distances in organometallic compounds of ammonia. See, for example, Ref. 38.
- ²¹K. Hermann, P. S. Bagus, and C. W. Bauschlicher, *Phys. Rev. B* **31**, 6371 (1985).
- ²²C. W. Bauschlicher, *J. Chem. Phys.* **83**, 2619 (1985).
- ²³These statements are based on a thorough search of the *Dictionary of Organometallic Compounds* (Chapman and Hall, London, 1984). While data for ammonia are not very extensive, the data for PR₃ ligands are, and they indicate that only on-top sites are occupied.
- ²⁴K. Nakamoto, *Infrared and Raman Spectra of Inorganic and Coordination Compounds*, 3rd ed. (Wiley, New York, 1978), pp. 197-202.

D-1

APPENDIX D

INTERACTION OF ETHYLENE WITH THE Ru(001) SURFACE

[The text of Appendix D consists of an article coauthored with M. M. Hills, J. E. Parmeter and W. H. Weinberg, which has appeared in *J.A.C.S.* **108**, 3554 (1986).]

Reprinted from the *Journal of the American Chemical Society*, 1986, 108, 3554.
 Copyright © 1986 by the American Chemical Society and reprinted by permission of the copyright owner.

Interaction of Ethylene with the Ru(001) Surface[†]

M. M. Hills, J. E. Parmeter,[‡] C. B. Mullins,[‡] and W. H. Weinberg*

Contribution from the Division of Chemistry and Chemical Engineering, California Institute of Technology, Pasadena, California 91125. Received October 8, 1985

Abstract: The interaction of ethylene with the Ru(001) surface has been investigated via high-resolution electron energy loss spectroscopy and thermal desorption mass spectrometry. Following desorption of an ethylene multilayer at 110 K, di- σ -bonded molecular ethylene is present on the surface. Competing desorption of molecular ethylene and dehydrogenation to form adsorbed ethylidyne (CCH₃) and acetylide (CCH) as well as hydrogen adatoms occur between approximately 150 and 260 K. The ethylidyne is stable to approximately 330 K, whereupon it begins to decompose to carbon and hydrogen adatoms. The desorption of hydrogen occurs in a sharp peak centered at 355 K, resulting from simultaneous ethylidyne decomposition and desorption of surface hydrogen. Further annealing of the overlayer to 380 K causes cleavage of the carbon-carbon bond of the acetylide, creating carbon adatoms and adsorbed methylidyne (CH). The methylidyne decomposes above 500 K with accompanying hydrogen desorption, leaving only carbon adatoms on the surface at 700 K.

Introduction

The adsorption and reaction of ethylene on single crystalline surfaces of the groups 8–10 transition metals^{1–17} have been the subject of intense study both as a prototype for olefin hydrogenation and dehydrogenation reactions^{18–21} and to provide a basis for comparing the bonding of olefins to surfaces with the bonding that has been observed to occur in multinuclear organometallic cluster compounds. Spectroscopic studies of ethylene adsorbed on these surfaces have shown that both the nature of the bonding of molecular ethylene to the substrate as well as the thermal decomposition pathway of the adsorbed ethylene vary widely. For example, ethylene rehybridizes to a di- σ -bonded molecular species when adsorbed on Fe(110), Fe(111), Ni(110), Ni(111), Ni(5(111)(110)), Pt(111), and Pt(100),^{1–7} whereas molecularly adsorbed ethylene on Co(001) at 115 K is π -bonded,⁸ as is ethylene adsorbed on Pd(111) at 150 K and on Pd(110) at 110 K.^{4,9–13,17} A mixed

overlayer of π - and di- σ -bonded ethylene forms on Pd(100) at 150 K.^{14,15} Ethylene adsorption on the Ru(001) surface has been

- (1) Eley, W.; Baro, A. M.; McBreen, P.; Ibach, H. *Surf. Sci.* **1982**, *120*, 273.
- (2) Seip, U.; Tsai, M.-C.; Küppers, J.; Ertl, G. *Surf. Sci.* **1984**, *147*, 65.
- (3) Strocio, J. A.; Bare, S. R.; Ho, W. *Surf. Sci.* **1984**, *148*, 499.
- (4) Lehwald, S.; Ibach, H. *Surf. Sci.* **1979**, *89*, 425.
- (5) Carr, R. G.; Sham, T. K.; Eberhardt, W. E. *Chem. Phys. Lett.* **1985**, *113*, 63.
- (6) Demuth, J. E. *Surf. Sci.* **1979**, *84*, 315.
- (7) Steininger, H.; Ibach, H.; Lehwald, S. *Surf. Sci.* **1982**, *117*, 685.
- (8) Albert, M. R.; Snoddon, L. G.; Plummer, E. W. *Surf. Sci.* **1984**, *147*, 127.
- (9) Gates, J. A.; Keamodell, L. L. *Surf. Sci.* **1982**, *120*, L461.
- (10) Gates, J. A.; Keamodell, L. L. *Surf. Sci.* **1983**, *124*, 68.
- (11) Tysoc, W. T.; Nyberg, G. L.; Lambert, R. M. *J. Phys. Chem.* **1984**, *88*, 1960.
- (12) Ratajczykowa, I.; Szymerka, I. *Chem. Phys. Lett.* **1983**, *96*, 243.
- (13) Keamodell, L. L.; Gates, J. A. *Surf. Sci.* **1981**, *111*, L747.
- (14) Stuve, E. M.; Madix, R. J. *J. Phys. Chem.* **1985**, *89*, 105.
- (15) Stuve, E. M.; Madix, R. J.; Brundell, C. R. *Surf. Sci.* **1985**, *152/153*, 532.
- (16) Dubois, L. H.; Castner, D. G.; Somorjai, G. A. *J. Chem. Phys.* **1980**, *72*, 5234.
- (17) Gupta, N. M.; Kamble, V. S.; Iyer, R. M. *J. Catal.* **1984**, *88*, 457.
- (18) Chesters, M. A.; McDougall, G. S.; Pemble, M. E.; Sheppard, N. *Appl. Surf. Sci.* **1985**, *22/23*, 369.
- (19) Boudart, M.; McDonald, M. A. *J. Phys. Chem.* **1984**, *88*, 2185.
- (20) Henrici-Olivé, G.; Olivé, S. *Angew. Chem., Int. Ed. Engl.* **1976**, *15*, 136.

[†]In this paper the periodic group notation in parentheses is in accord with recommendations by IUPAC and ACS nomenclature committees. A and B notation is eliminated because of wide confusion. Groups IA and IIA become groups 1 and 2. The d-transition elements comprise groups 3 through 10, and p-block elements comprise groups 13 through 18. (Note that the former nomenclature designation is preserved in the last digit of the numbering: III → 3 and 13.)

*AT&T Bell Laboratories predoctoral fellow.
[‡]Link Foundation predoctoral fellow.

studied recently by Barreau and co-workers.²² A detailed comparison between our more complete study and the preliminary results of Barreau et al.²² is presented in section IV.

The thermal decomposition of ethylene (ultimately to hydrogen and surface carbon) on the surfaces mentioned above has been investigated by vibrational electron energy loss spectroscopy (EELS), thermal desorption mass spectrometry (TDMS), and UV photoelectron spectroscopy. The thermal decomposition intermediates in ethylene dehydrogenation on Fe(110), Ni(111), Ni[5(111) × (110)], and Ni(110) are acetylene and acetylide (CCH).^{1,3,4} Madix and Stuve have postulated the formation of a vinyl group from ethylene adsorbed on Pd(100).^{14,15} On Co(001) and Fe(111) no stable surface intermediates were observed; chemisorbed ethylene evidently dehydrogenates completely just below room temperature to carbon and hydrogen.²⁴ On Pt(111), Rh(111), Pd(111), and Pt(100), chemisorbed ethylene dehydrogenates to form ethylidyne below 300 K.^{7,9-13,16,23} Thus, ethylene adsorbed on the close-packed surfaces of each of the 4d and 5d groups 8-10 metals studied previously forms ethylidyne.²⁴ On the other hand, ethylene adsorbed on all of the surfaces of the 3d groups 8-10 metals studied to date, including the close-packed surfaces, dehydrogenates more completely to acetylene, acetylide, or directly to carbon. Hence it is of fundamental interest to determine whether ethylene adsorbed on the Ru(001) surface behaves as it does on the other hexagonal 4d and 5d transition-metal surfaces studied previously [Rh(111), Pd(111), Pt(100), and Pt(111)] or whether it dehydrogenates more completely, as it does on the hexagonal Ni(111) and Co(001) surfaces.

II. Experimental Procedures

The experimental measurements were conducted in two different ultrahigh-vacuum (UHV) chambers, each with base pressures below 1×10^{-10} torr. The first UHV chamber is equipped with a quadrupole mass spectrometer, a single pass cylindrical mirror electron energy analyzer with an integral electron gun for Auger electron spectroscopy, and LEED optics. All thermal desorption measurements were carried out in this chamber; data were collected by using an LSI-11 DEC laboratory computer, and linear heating rates of 5-15 K/s were employed. A glass enclosure is placed around the ionizer of the mass spectrometer, and a small aperture in the front of the glass envelope permits sampling of gas that is desorbed only from the well-oriented front of the single crystal. Thus the effects of desorption from the edge of the crystal, the support leads, and the manipulator are excluded from the thermal desorption spectra.²⁴

The second UHV chamber contains both a quadrupole mass spectrometer and a home-built EELS spectrometer of the Kuyatt-Simpson type.^{27,28} The energy dispersing elements in the EELS monochromator and rotatable analyzer are 180° hemispherical deflectors. The "off-specular" EEL spectra were measured with the analyzer rotated 7-10° from the specular direction, toward the surface normal. All EEL spectra were measured using a beam energy of 4 eV and with the incident beam approximately 60° from the surface normal. The instrumental resolution (full-width at half-maximum of the elastically scattered peak) varied between 60 and 80 cm^{-1} , while maintaining a count rate of approximately 3×10^5 cps in the elastic peak. A more extensive description of these UHV chambers as well as the procedures followed for cutting, polishing, mounting, and cleaning the Ru(001) crystals has been discussed in detail previously.²⁷⁻³⁰ The cleanliness of the surfaces was monitored with Auger spectroscopy in the first chamber and with EELS in the second.

Research purity hydrogen (99.9995%) and C.P. grade deuterium and ethylene (99.5%) were purchased from Matheson. Research purity tetradeuterated ethylene (99.99%) was obtained from Merck. The H_2 , D_2 , and C_2D_4 were used without further purification, whereas the C_2H_4 was subjected to freeze-thaw-pump cycles prior to use. The purity of

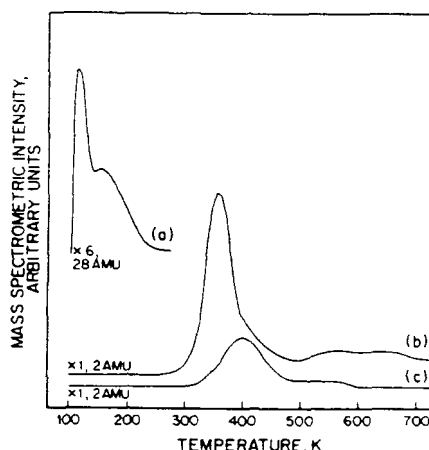


Figure 1. Thermal desorption spectra after C_2H_4 adsorption on Ru(001) at 90 K: (a) C_2H_4 and (b) H_2 desorption following a 1-langmuir exposure and (c) H_2 desorption following a 0.2-langmuir exposure.

all gases was verified in situ with mass spectrometry.

III. Results

Typical thermal desorption spectra following exposure of the Ru(001) surface to 1 langmuir ($1 \text{ langmuir} = 1 \times 10^{-6}$ torr s) or more of C_2H_4 at 90 K are shown in Figure 1a and 1b.³¹ Only hydrogen and ethylene are observed to desorb from the surface. In particular, no ethane, methane, or acetylene is detected as judged by the absence of 30 and 16 amu peaks and by comparison of the 28, 27, and 26 amu peaks to the cracking pattern of ethylene.

Figure 1b establishes that most of the hydrogen, after an ethylene exposure exceeding 0.6 langmuir, desorbs in a sharp peak centered at 355 K (independent of coverage), with a small high-temperature shoulder above 400 K and a broad tail extending from 500 to 700 K of which the latter represents 10-15% of the desorbing hydrogen. It will be shown below that the major peak corresponds to the desorption of hydrogen enhanced by the decomposition of ethylidyne (one of the decomposition products of ethylene), the shoulder corresponds to desorption-limited hydrogen from the surface, and the high-temperature tail corresponds to the dehydrogenation of surface methylidyne (another decomposition product). The thermal desorption spectrum of molecular ethylene (cf. Figure 1a) shows that ethylene desorbs in a sharp peak centered near 110 K, followed by a broad peak of which the tail extends to approximately 250 K. As discussed below, EEL spectra of the surface on which ethylene is adsorbed and which is annealed to various temperatures show that the higher-temperature peak corresponds to the desorption of di- σ -bonded ethylene, while multilayer ethylene desorbs in the lower-temperature peak. The "multilayer" peak shown in Figure 1a actually corresponds to only desorption from a second layer. This multilayer peak does not saturate with increasing ethylene exposure, however, and is sufficiently intense following a 15-langmuir exposure of ethylene that it obscures the desorption peak due to chemisorbed ethylene.

For lower exposures of ethylene, below 0.6 langmuir, the hydrogen thermal desorption spectra are quite different. The thermal desorption spectrum of H_2 after an ethylene exposure of 0.2 langmuir, shown in Figure 1c, contains a high-temperature tail terminating below 600 K that is due to methylidyne decomposition and a rather broad peak centered at 420 K that shifts to lower temperature as the initial surface coverage of chemisorbed ethylene increases. The latter is essentially identical with that which is observed after adsorption of hydrogen on the clean Ru(001) surface.³² The maximum rate of H_2 desorption shifts from 420

(21) Dixit, R. S.; Tavlirides, L. L. *Ind. Eng. Chem. Process Des. Dev.* **1983**, *22*, 1.

(22) Barreau, M. A.; Broughton, J. Q.; Menzel, D. *Appl. Surf. Sci.* **1984**, *19*, 92.

(23) Ibach, H. Presented at the Proceedings of the International Conference on Vibrations in Adsorbed Layers, Jülich, 1978; paper 64.

(24) The Pt(100) surface reconstructs to a slightly buckled, close-packed (5×20) superstructure.²⁵

(25) Heilmann, P.; Heinz, K.; Müller, K. *Surf. Sci.* **1979**, *83*, 487.

(26) Feulner, P.; Menzel, D. *J. Vac. Sci. Technol.* **1980**, *17*, 662.

(27) Thomas, G. E.; Weinberg, W. H. *Phys. Rev. Lett.* **1978**, *418*, 1181.

(28) Thomas, G. E.; Weinberg, W. H. *Rev. Sci. Instrum.* **1979**, *50*, 497.

(29) Williams, E. D.; Weinberg, W. H. *Surf. Sci.* **1979**, *82*, 93.

(30) Williams, E. D.; Weinberg, W. H. *J. Vac. Sci. Technol.* **1982**, *20*, 534.

(31) All exposures reported are uncorrected for the sensitivity of the ion gauge to the various gases.

(32) Shimizu, H.; Christmann, K.; Ertl, G. *J. Catal.* **1980**, *61*, 412.

Table I. Comparison of Vibration Frequencies of Multilayer C₂H₄ Adsorbed on Ru(001) at 80 K with C₂H₄(g), C₂H₄(l), and C₂H₄(s)^a

no./repr.	mode	C ₂ H ₄ (g) ³³		C ₂ H ₄ (l) ³⁴		C ₂ H ₄ (s) ³⁴ IR	multilayer C ₂ H ₄ on Ru(001)
		Raman	IR	Raman	IR		
$\nu_1 A_g$	$\nu_s(\text{CH}_2)$	3026	f	3019	3016	2973	3000
$\nu_{11} B_{2g}$		f	2989		2983		
$\nu_5 B_{1g}$	$\nu_s(\text{CH}_2)$	3103	f	3075		3075	3095
$\nu_9 B_{2g}$		f	3105		3085		
$\nu_2 A_g$	$\nu(\text{CC})$	1623	f	1621	1620	1616	1630
$\nu_3 A_g$	CH ₂ scis.	1342	f	1340	1339	1336	1350
$\nu_{12} B_{3g}$		f	1444		1437	1438	1460
$\nu_4 A_g$	CH ₂ twist	f	f		~1010		n.r.
$\nu_6 B_{1g}$	CH ₂ rock	f	f	1236	1239		
$\nu_{10} B_{2g}$		f	810		828	827	860
$\nu_7 B_{1g}$	CH ₂ wag	f	949		960	970	970
$\nu_8 B_{2g}$		950	f	943			
	$\nu_s(\text{RuC})$						440

no./repr.	mode	C ₂ D ₄ (g) ³³		multilayer C ₂ D ₄ on Ru(001)	
		Raman	IR	Raman	IR
$\nu_1 A_g$	$\nu_s(\text{CD}_2)$	2251			2310
$\nu_{11} B_{2g}$		2200			
$\nu_5 B_{1g}$	$\nu_s(\text{CD}_2)$	2304			n.r.
$\nu_9 B_{2g}$		2345			
$\nu_2 A_g$	$\nu(\text{CC})$	1515			1550
$\nu_3 A_g$	CD ₂ scis.	981			1015
$\nu_{12} B_{3g}$		1078			1175
$\nu_4 A_g$	CD ₂ twist	728			n.r.
$\nu_6 B_{1g}$	CD ₂ rock	1009			n.r.
$\nu_{10} B_{2g}$		586			
$\nu_7 B_{1g}$	CD ₂ wag	720			735
$\nu_8 B_{2g}$		780			
	$\nu_s(\text{RuC})$				425

^an.r. = not resolved. f = forbidden.

K for an ethylene exposure of 0.2 langmuir to 395 K for a 0.4-langmuir exposure and then drops to 355 K for all ethylene exposures exceeding 0.6 langmuir. The decrease in peak temperature for exposures of ethylene below 0.6 langmuir is indicative of second-order desorption kinetics of surface hydrogen. For these lower exposures of ethylene, below 0.6 langmuir, no desorption of molecular ethylene is observed.

Figure 2a and 2b shows the EEL spectra of 4 langmuir of C₂H₄ and 3 langmuir of C₂D₄, respectively, adsorbed at 80 K on the Ru(001) surface. Consistent with the thermal desorption spectra, a comparison of the observed energy loss features to IR and Raman spectra of gaseous, liquid, and solid ethylene (cf. Table I^{33,34}) demonstrates that the overlayers of Figure 2 correspond to molecular multilayers. Note the intense CH₂ wagging mode at 970 cm⁻¹, which is the best fingerprint of molecular ethylene multilayers, and also the carbon-hydrogen stretching mode at 3000 cm⁻¹. The frequencies of both these modes are characteristic of an sp³-hybridized carbon atom. Table I also shows that the isotopic shifts for multilayer C₂D₄ on Ru(001) are in good agreement with those of C₂D₄(g).

Annealing these overlayers to 110 K desorbs the multilayer, as shown in the thermal desorption spectra (cf. Figure 1a), leaving di-σ-bonded ethylene which is stable to 150 K. The EEL spectra of this chemisorbed species are exhibited in Figure 3a for C₂H₄ and Figure 3b for C₂D₄. The rehybridization of the carbon atoms to nearly sp² is reflected in the shifts of the CH₂ wagging mode and the carbon-hydrogen stretching mode to 1145 and 2985 cm⁻¹, respectively. The shoulder at 1040 cm⁻¹ is probably due to the carbon-carbon stretching mode, but it is poorly resolved from the CH₂ twisting mode in C₂H₄ and the CD₂ wagging mode in C₂D₄ both of which are at 900 cm⁻¹. A carbon-carbon stretching frequency of 1040 cm⁻¹ is consistent with the rehybridization of the carbon atoms of ethylene to sp². Other modes of di-σ-bonded

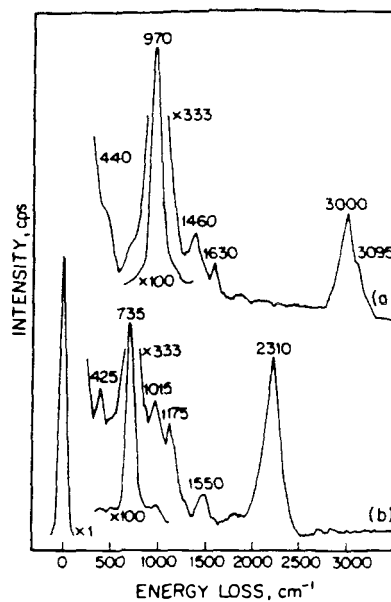


Figure 2. EEL spectra of molecular multilayers of ethylene on Ru(001): (a) 4 langmuir of C₂H₄ at 80 K and (b) 3 langmuir of C₂D₄ at 80 K.

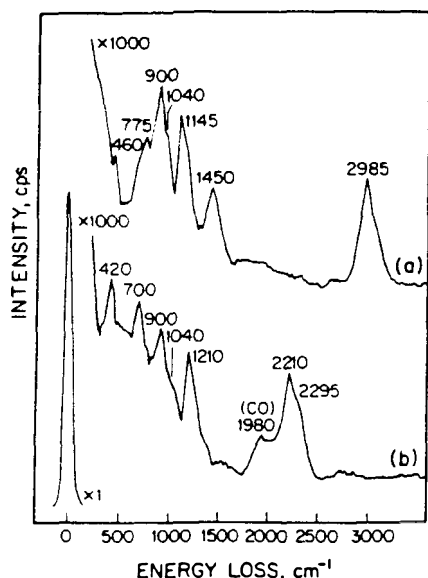
ethylene are the symmetric ruthenium-carbon stretching mode at 460 cm⁻¹ (420 cm⁻¹ for C₂D₄), the CH₂ rocking mode at 775 cm⁻¹, the CH₂ twisting mode at 900 cm⁻¹ (700 cm⁻¹ for C₂D₄), and the CH₂ scissoring mode at 1450 cm⁻¹ (1210 cm⁻¹ for C₂D₄). The CD₂ rocking mode of di-σ-bonded C₂D₄ was not resolved in Figure 3b due to the poorer cutoff in the elastic peak. The symmetric ruthenium-carbon stretching mode of di-σ-bonded

(33) Shimanouchi, T. *NSRDS-NBS* 1972, 39, 74.

(34) Brecher, C.; Halford, R. S. *J. Chem. Phys.* 1961, 35, 1109.

Table II. Comparison of Vibrational Frequencies of Di- σ -bonded C_2H_4 on Ru(001) at 130 K with Other Chemisorbed Ethylene Species, Gaseous Ethylene Compounds, Organometallic Ethylene Compounds, and a Surface Methylene Species^a

	di- σ - C_2H_4 on						gauche $C_2H_4Br_2(g)^{33}$	K[PtCl ₃ - (C ₂ H ₄)]H ₂ O ³⁵	Ni ₂ - (C ₂ H ₄) ³⁶	CH ₂ on Ru(001) ³⁴
	Ru(001)	Ni(110) ³	Ni(111) ⁴	Fe(110) ¹	Fe(111) ²	Pt(111) ⁷				
mode C_2H_4 (or CH_2)										
$\nu_s(CM)$	460	420	450	480	580	470			376	n.r.
$\nu_a(CM)$	n.r.	n.r.	610	410	450	560				n.r.
CH ₂ rock	775	715	720	720	n.r.	660	826	848	841	910
CH ₂ twist	900	850	880	915	870	790	f	1104		785
CH ₂ wag	1145	1145	1110	1105	n.r.	980	949	1278	975	1180
CH ₂ scissors	1450	1435	1430	1410	1385	1430	1444	1420	1515	1208
$\nu_s(CH_2)$	2940	2970	2930	2960	2980	2980	2989	2953	3013	2880
$\nu_a(CH_2)$	3050	n.r.	n.r.	n.r.	n.r.	3000	3096	3005	3075	2908
$\nu(C-C)$	1040	n.r.	1200	1250	1115	1060	1623	1019	1243	1488
mode C_2D_4										
$\nu_s(CM)$	420	390	420	440		450				
$\nu_a(CM)$	n.r.	n.r.	590	n.r.		n.r.				
CD ₂ rock	n.r.	615	650	635/540		n.r.	586	712		
CD ₂ twist	700	725	740	700		600	f	791		
CD ₂ wag	900	925	870	850		740	720	947		
CD ₂ scissors	1210	1235	1200	1040		1150	1078	1141		
$\nu_s(CD_2)$	2210	2170	2170	2175		2150	2251	2174		
$\nu_a(CD_2)$	2295	2290	2270	n.r.		2250	2304	2271		
$\nu(C-C)$	n.r.	n.r.	n.r.	1160		900	1515	1014		

^af = forbidden. n.r. = not resolved.**Figure 3.** EEL spectra of di- σ -bonded ethylene on Ru(001): (a) 4 langmuir of C_2H_4 annealed to 139 K and (b) 3 langmuir of C_2D_4 annealed to 123 K.

C_2D_4 also contains a small contribution from $\nu(Ru-CO)$. The symmetric and asymmetric carbon-hydrogen stretching modes of C_2H_4 at 2940 and 3050 cm^{-1} were resolved in spectra similar to Figure 3a.

Peak assignments for di- σ -bonded ethylene (both C_2H_4 and C_2D_4) on Ru(001) are compared in Table II with those of other chemisorbed ethylene species as well as IR data for $C_2H_4Br_2(g)$, $C_2H_4(g)$, Zeise's salt, and a low-valent nickel complex $[Ni(C_2H_4)_4]^{1-7,33,35,36}$. A comparison of the frequencies of the modes of di- σ -bonded C_2H_4 on Ru(001) to these data shows that ethylene undergoes rehybridization on the Ru(001) surfaces as on Ni(110), Ni(111), and Fe(110).^{1,3-5} The existence of a π -bonded ethylene ad-molecule can be excluded by a comparison to the IR data for

Zeise's salt and Ozin's nickel complexes, which have, among other differences, higher frequency CH_2 rocking modes and carbon-carbon stretching modes.

A comparison of EEL spectra of di- σ -bonded ethylene with spectra of diazomethane led to an original assignment of the spectrum of Figure 3a as a bridging methylene species.³⁷ However, a subsequent review of these and other spectra has shown that the reaction of CH_3N_2 to form C_2H_4 and N_2 may occur in the gas dosing lines prior to introduction into the UHV chamber. An assignment of EEL spectra of uncontaminated diazomethane, which produces μ_2-CH_2 groups on Ru(001), is listed in the last column in Table II. Additional vibrational data concerning bridging methylene may be found elsewhere.³⁹⁻⁴³ The adsorption of C_2H_4 on Ru(001) with annealing to 110 K produces di- σ -bonded molecular ethylene, which can be distinguished from μ_2-CH_2 by the intense CH_2 twisting mode at 900 cm^{-1} . In agreement with this conclusion, the thermal desorption spectra of ethylene on Ru(001) show desorption of molecular ethylene up to 250 K.

In an effort to describe further the character of the di- σ -bonded ethylene on Ru(001), isotopic exchange, thermal desorption experiments of coadsorbed C_2H_4 and C_2D_4 were carried out. In all cases, only C_2H_4 and C_2D_4 desorbed from the multilayer. However, all five isotopically labeled species (C_2H_4 , C_2H_3D , $C_2H_2D_2$, C_2HD_3 , and C_2D_4) appeared in the di- σ -bonded ethylene that desorbs molecularly. Figure 4 shows the relative ratios of these five species that desorb molecularly above 150 K. These ratios were obtained by correcting the areas under the thermal desorption peaks of the 26-32-amu spectra, both for the cracking patterns of the five species and for the relative sensitivity of the mass spectrometer to each species. (These ratios exclude multilayer C_2H_4 and C_2D_4 .) Figure 4 shows that isotopic exchange is limited, and no mixed species (C_2H_3D , $C_2H_2D_2$, or C_2HD_3) is favored over the other two. On the other hand, the corresponding $H_2/HD/D_2$ thermal desorption spectra exhibited complete isotopic exchange. The above results suggest that the isotopic mixing observed for

(37) George, P. M.; Avery, N. R.; Weinberg, W. H.; Tebbe, F. N. *J. Am. Chem. Soc.* **1983**, *105*, 1393.(38) EEL spectra of 2.5 langmuir of H_2CN_2 dosed at 80 K, annealed to 192-316 K, and cooled to 80 K prior to measurement.(39) Fox, D. J.; Schaefer, H. F. *J. Chem. Phys.* **1983**, *78*, 328.(40) Theopold, K. H.; Bergman, R. G. *J. Am. Chem. Soc.* **1981**, *103*, 2489.(41) Oxtun, I. A.; Powell, D. B.; Sheppard, N.; Burgess, K.; Johnson, B. F. G.; Lewis, J. *J. Chem. Soc., Chem. Commun.* **1982**, 719.(42) McBroen, P. H.; Erley, W.; Ibach, H. *Surf. Sci.* **1984**, *148*, 292.(43) Chang, S.-C.; Kafafi, Z. H.; Hauge, R. H.; Billups, W. E.; Margrave, J. L. *J. Am. Chem. Soc.* **1985**, *107*, 1447.(35) Hiraishi, J. *Spectrochim. Acta, Part A* **1969**, *25A*, 749.(36) Ozin, G. A. *J. Am. Chem. Soc.* **1978**, *100*, 4750.

Table III. Comparison of Vibrational Frequencies of Ethylidyne

mode	CCH ₃ on Ru(001) at 280 K	CCH ₃ on Pd(111) at 300 K ^a	CCH ₃ on Pt(111) at 300 K ⁷	CCH ₃ on Rh(111) at 300 K ¹⁶	(CO) ₃ Co ₃ (μ ₃ -CCH ₃) ⁴⁵
$\nu_s(\text{CM}) A_1$	480 ^b	409	435 vs	450	401
$\nu_a(\text{CM}) E$	n.r. ^a	n.r.	600 w	n.r.	555
$\rho(\text{CH}_3) E$	1000	n.r.	980 sh	n.r.	1004
$\nu(\text{CC}) A_1$	1140	1080 s	1130 vs	1130	1163
$\delta_s(\text{CH}_3) A_1$	1370	1334 vs	1355 vs	1350	1356
$\delta_a(\text{CH}_3) E$	1450	1400	1420 sh	n.r.	1420
$\nu_s(\text{CH}_3) A_1$	2945	2900 m	2920	2900	2888
$\nu_a(\text{CH}_3) E$	3045	n.r.	3050	3000	2930
Deuterated Species					
$\nu_s(\text{CM}) A_1$	480	n.r.	410		393
$\nu_a(\text{CM}) E$	n.r.	n.r.	~600		536
$\rho(\text{CD}_3) E$	800	n.r.	790		828
$\nu(\text{CC}) A_1$	1150	1120	1160		1182
$\delta_s(\text{CD}_3) A_1$	1000	n.r.	990		1002
$\delta_a(\text{CD}_3) E$	n.r.	n.r.	1030		1031
$\nu_s(\text{CD}_3) A_1$	2190	2181	2080		n.r.
$\nu_a(\text{CD}_3) E$	2280	n.r.	2220		2192

^an.r. = not resolved. ^bIdentified from spectra similar to that of Figure 5a but without CO contamination.

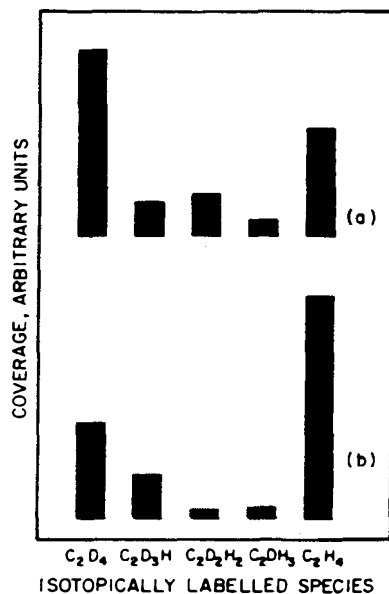


Figure 4. Coadsorption of C₂H₄ and C₂D₄. Relative coverages of C₂H₄, C₂H₃D, C₂H₂D₂, C₂HD₃, and C₂D₄ from thermal desorption spectra: (a) 0.6-langmuir exposure of C₂H₄ followed by 3 langmuir of C₂D₄ at 110 K and (b) 1-langmuir exposure of C₂H₄ followed by 3 langmuir of C₂D₄ at 110 K.

chemisorbed ethylene that desorbs molecularly results from exchange between an ethylene ad molecule and a hydrogen (or deuterium) adatom, since the onset of desorption of the mixed molecular ethylene species (C₂H₂D_{4-x}, 1 ≤ x ≤ 3) coincides with the initial decomposition of ethylene to ethylidyne, acetylide, and surface hydrogen via carbon-hydrogen bond cleavage.

Annealing di-σ-bonded ethylene to 250 K produces two new carbon-containing surface species as well as hydrogen adatoms. The modes due to surface hydrogen were not resolved in the corresponding EEL spectrum shown in Figure 5a. The weak losses of hydrogen adatoms, which occur at 845 and 1115 cm⁻¹,⁴⁴ were obscured by various carbon-hydrogen and carbon-carbon modes. However, the presence of hydrogen adatoms was confirmed by stoichiometric considerations and hydrogen postadsorption experiments which will be discussed later. The two hydrocarbon fragments present on the surface have been identified

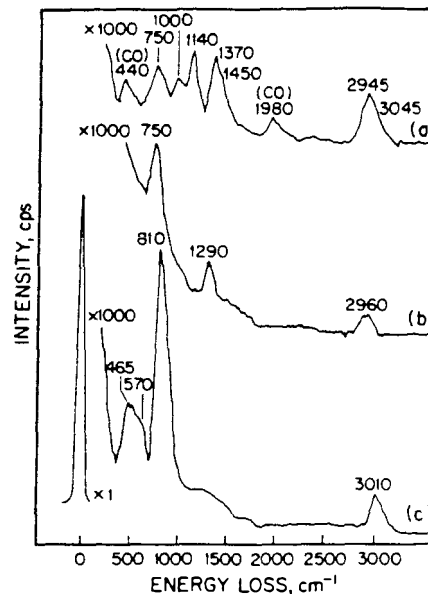


Figure 5. EEL spectra of 4 langmuir of C₂H₄ adsorbed on Ru(001) at 80 K and annealed to (a) 280, (b) 360, and (c) 500 K. Spectrum a exhibits the modes of both ethylidyne and acetylide. Spectrum b is characteristic of acetylide. Spectrum c corresponds to methylidyne.

as ethylidyne and acetylide from the EEL spectrum of Figure 5a, the corresponding EEL spectrum of the deuterated species, off-specular EELS measurements, and EEL spectra measured following annealing to various temperatures.

Peak assignments for CCH₃ and CCD₃ are compared in Table III to IR data for a tricobalt ethylidyne complex as well as EELS results for ethylidyne adsorbed on various close-packed groups 8-10 metal surfaces.^{4,7,16,45} A triruthenium ethylidyne complex has also been synthesized, but no relevant IR data have been published.⁴⁶ For all of the ethylidyne adspecies listed in Table III, the carbon-carbon stretching mode produces a strong, dipolar enhanced peak. By analogy to the structure of the triruthenium and tricobalt organometallic compounds, and considering the relative intensities of the (dipolar-enhanced) carbon-carbon stretching modes, the carbon-carbon bond axis of each of the

(45) Skinner, P.; Howard, M. W.; Oxton, I. A.; Kettle, S. F. A.; Powell, D. B.; Sheppard, N. *J. Chem. Soc., Faraday Trans 2* 1981, 77, 1203.

(46) Sheldrick, G. M.; Yesinowski, J. P. *J. Chem. Soc., Dalton Trans* 1975, 873.

(44) Barbeau, M. A.; Broughton, J. Q.; Menzel, D. *Surf. Sci.* 1983, 133, 443.

Table IV. Comparison of Vibrational Frequencies of Acetylide^a

mode	CCH on Ru(001) at 360 K	CCH on Pd(100) at 400 K ^{44,49}
ν_1 (CM)	435	n.r.
ν_2 (CM)	n.r.	n.r.
δ (CH)	750	750
ν (CH)	2960	3000
ν (CC)	1290	1340

mode	CCD	CCD
ν_1 (CM)	n.r.	n.r.
ν_2 (CM)	n.r.	n.r.
δ (CD)	550	540
ν (CD)	2210	2220
ν (CC)	1260	1340

^an.r. = not resolved.

ethylidyne adspecies is nearly perpendicular to the surface plane. A comparison of the EELS losses for CCH₃ and CCD₃ on Ru(001) with IR data for (CO)₉Co₃(μ_3 -CCH₃) and (CO)₉Co₃(μ_3 -CCD₃) (cf. Table III) shows that the structure and bonding of the ethylidyne in the two cases are quite similar.

The acetylide species is characterized by a carbon-hydrogen bending mode at 750 cm⁻¹, a carbon-hydrogen stretching mode at 2960 cm⁻¹, and a carbon-carbon stretching mode at 1290 cm⁻¹. The vibrational modes of acetylide are partially obscured by the ethylidyne modes because the ratio of ethylidyne to acetylide present in Figure 4a is approximately 3:2, on the basis of hydrogen thermal desorption measurements. Annealing this overlayer to 360 K decomposes the ethylidyne, leaving acetylide, carbon, and a small concentration of hydrogen adatoms on the surface. Thus the modes of the acetylide are completely resolved in spectra measured after annealing the overlayer to 360 K (cf. Figure 5b). This acetylide also forms from the thermal decomposition of acetylene and is discussed in greater detail in the following paper.⁴⁷ We merely note here that these assignments agree quite well with those of Kesmodel et al. for acetylide on Pd(100) for which δ (CH) is 750 cm⁻¹, ν (CC) is 1340 cm⁻¹, and ν (CH) is 3000 cm⁻¹.^{44,49}

The EEL spectra of the deuterated acetylide show that the carbon-deuterium bending mode of CCD downshifts to 550 cm⁻¹ from 750 cm⁻¹ for CCH (cf. Table IV), which compares well with the value of δ (CD) of 540 cm⁻¹ for CCD on Pd(100).^{44,49} We also observe a slight shift in ν (CC) from 1290 cm⁻¹ in CCH to 1260 cm⁻¹ in CCD and the expected shift in ν (CD) from 2960 cm⁻¹ in CCH to approximately 2210 cm⁻¹ in CCD. These losses persist up to 380 K where cleavage of the carbon-carbon bond of the acetylide occurs, forming surface carbon and methylidyne.

The adsorbed methylidyne is identified from the EEL spectrum of Figure 5c with ν (RuC) at 465 cm⁻¹, δ (RuCH) at 810 cm⁻¹, and ν (CH) at 3010 cm⁻¹ of which the latter two are significantly higher than the corresponding modes of the acetylide. The disappearance of the 1290-cm⁻¹ carbon-carbon stretching mode of acetylide upon annealing to 500 K also assists us in distinguishing acetylide and methylidyne. The mode at 570 cm⁻¹ in Figure 5c is the carbon-metal stretching mode of carbon adatoms and/or carbon dimers. The broad feature at 1100-1600 cm⁻¹ may be attributed to the carbon-carbon stretching mode of these dimers. The vibrational modes of the methylidyne are compared in Table V to those of high-temperature ($T > 400$ K) methylidyne on various transition-metal surfaces, as well as tricobalt and triruthenium μ_3 -CH complexes.^{12,49,10,50-53} Our assignments agree quite well with those of methylidyne adsorbed on the Fe(111), Ni(111), and Pd(111) surfaces and are consistent with those of the organometallic complexes. The isotopic shifts of the vibrational

modes of methylidyne adsorbed on Ru(001) are also in agreement with those of (CO)₄Co₃(μ_3 -CD).

All of the methylidyne modes are eliminated by annealing the Ru(001) surface above 700 K. After this annealing, weak modes near 600 and 1100-1600 cm⁻¹ are observed which are attributed to ν (RuC) of carbon adatoms and dimers and ν (CC) of carbon dimers. These modes are present in the EEL spectra of both C₂H₄ and C₂D₄. No other features are present in the high-temperature EEL spectra, supporting the thermal desorption results which show complete desorption of hydrogen (and ethylene) below 700 K.

Bearing in mind what we have learned from EELS concerning the decomposition of ethylene on Ru(001), we now return to a more detailed analysis of the thermal desorption spectra. In the case of ethylene adsorbed on the Ru(001) surface, three reactions generate surface hydrogen below 400 K, namely, (1) C₂H₄ dehydrogenation to CCH(a) and 3H(a), beginning at 150 K; (2) C₂H₄ dehydrogenation to CCH₃(a) and H(a), also beginning at 150 K; and (3) CCH₃ decomposition to 2C(a) or C₂(a) and 3H(a), beginning at 330 K. As shown in Figure 1b, a large ethylene exposure produces a sharp peak at 355 K with a shoulder near 400 K in the hydrogen thermal desorption spectrum, followed by a long, high-temperature tail. Since the high-temperature tail corresponds exclusively to methylidyne decomposition and represents a small fraction of the total hydrogen that is desorbed (approximately 10%), a hydrogen mass balance requires that the desorption which occurs below 500 K corresponds to surface hydrogen from acetylide and ethylidyne formation as well as from ethylidyne decomposition.

For rather low exposures of ethylene, below 0.6 langmuir, the hydrogen thermal desorption spectra are quite different, although the EEL spectra of all coverages of ethylene adsorbed on Ru(001) are qualitatively the same. The thermal desorption spectrum of hydrogen following a low ethylene exposure contains a prominent peak (which shifts as a function of coverage) and also a high-temperature tail (cf. Figure 1c). As shown by the EELS results, the tail corresponds to hydrogen desorption that is limited by methylidyne decomposition. The hydrogen desorbing in the major peak is due to surface hydrogen from ethylene decomposition to ethylidyne and acetylide and ethylidyne decomposition to surface carbon, as is the hydrogen desorbing in the 355 K peak following higher ethylene exposures. The shift in this peak as a function of ethylene coverage indicates that the desorption of this hydrogen is desorption-limited. This is confirmed by experiments conducted on the carbonaceous residue that remains after annealing to 700 K the ruthenium surface which had been exposed to 0.4 langmuir of C₂H₄ at 100 K. Hydrogen was adsorbed on this carbonaceous residue at 90 K, and then a thermal desorption measurement was carried out. The thermal desorption spectra showed that the major hydrogen thermal desorption peak was repopulated, confirming that this peak is due to desorption of surface hydrogen.

The sharp peak at 355 K in the thermal desorption spectra of hydrogen following an exposure of ethylene *exceeding* 0.6 langmuir consists of surface hydrogen formed from ethylene decomposition at lower temperatures (150-280 K) and driven by the presence of that hydrogen from ethylidyne decomposition. The maximum rate of the latter occurs at 355 K. The high-temperature shoulder on this peak (near 400 K) corresponds to desorption of residual surface hydrogen. That the sharp peak at 355 K and its high-temperature shoulder are derived from surface hydrogen has been confirmed by hydrogen postadsorption experiments. First, the Ru(001) surface was exposed to 5 langmuir of C₂H₄ at 90 K, annealed to 800 K, cooled to 90 K, and exposed to 30 langmuir of hydrogen. A subsequent thermal desorption spectrum (Figure 6b) shows a peak at 355 K with a high-temperature shoulder.⁵⁴ A comparison with the hydrogen thermal desorption spectrum after an exposure to 5 langmuir of C₂H₄ (Figure 6a) shows that less hydrogen is present in the 355 K peak of Figure 6b and that the leading edge of the peak in this spectrum is not so sharp. These differences are due solely to the presence of ethylidyne decom-

(47) Parmeter, J. E.; Hills, M. M.; Weinberg, W. H. *J. Am. Chem. Soc.*, following paper in this issue.

(48) Kesmodel, L. L. *Vac. Sci. Technol. A* 1984, 2, 1083.

(49) Kesmodel, L. L.; Wadill, G. D.; Gates, J. A. *Surf. Sci.* 1984, 138, 464.

(50) Demuth, J. E.; Ibach, H. *Surf. Sci.* 1978, 78, L238.

(51) Erley, W.; McBreen, P. H.; Ibach, H. *J. Catal.* 1983, 84, 229.

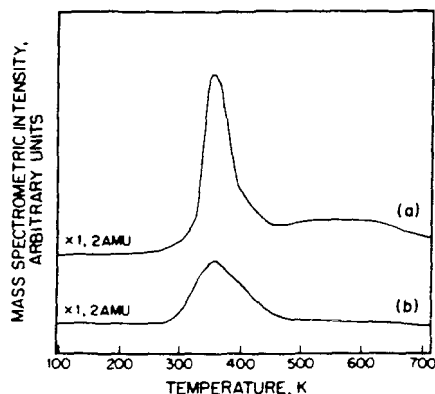
(52) Oxtou, I. A. *Spectrochim. Acta, Part A* 1982, 38, 181.

(53) Howard, M. W.; Kettle, S. F.; Oxtou, I. A.; Powell, D. B.; Sheppard, N.; Skinner, P. *J. Chem. Soc., Faraday Trans 2* 1981, 77, 397.

(54) EEL spectra of this adlayer support the presence of only carbon and hydrogen adatoms; in particular, no modes of methylidyne are observed.

Table V. Comparison of Vibrational Frequencies of Surface Methylidyne Species to Those of $(\text{CO})_4\text{Co}_3(\mu_3\text{-CH})$ and $(\text{CO})_9\text{H}_3\text{Ru}_3(\mu_3\text{-CH})$

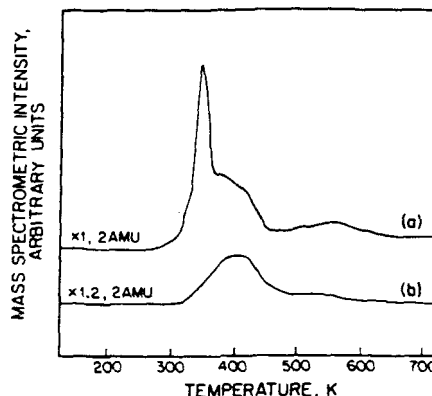
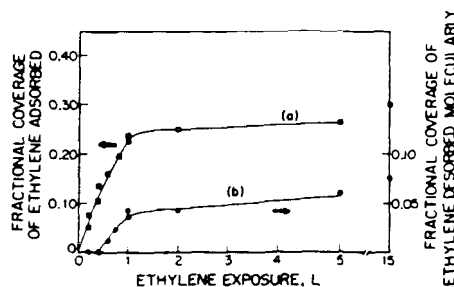
mode	CH on Ru(001)	CH on Fe(111) ²	CH on Fe(110) ^{1,50}	CH on Ni(111) ^{4,51}	CH on Pd(111) ^{9,10}	$(\text{CO})_9\text{H}_3\text{Ru}_3(\mu_3\text{-CH})$ ⁵²	$(\text{CO})_4\text{Co}_3(\mu_3\text{-CH})$ ⁵³
$\nu(\text{CH})$	3010	3015	3050	2980	3002	2988	3041
$\delta(\text{MCH})$	810	795	880	790	762	894	850
(c)							
$\nu_s(\text{MC})$	465					670	715
(a ₁)							
$\nu_s(\text{MC})$	n.r.					424	417
(e)							
$\nu(\text{CD})$	2250						2268
$\delta(\text{MCD})$	615						680
(c)							
$\nu_s(\text{MC})$	415						696
(a ₁)							
$\nu_s(\text{MC})$	n.r.						410
(e)							

Figure 6. Hydrogen thermal desorption following (a) exposure of 5 langmuir of C_2H_4 and (b) exposure of 5 langmuir of C_2H_4 followed by annealing to 800 K, cooling to 90 K, and exposure to 30 langmuir of H_2 .

position in Figure 6a and its absence in Figure 6b.

In a second experiment, the ruthenium surface was exposed to 0.4 langmuir of C_2H_4 , followed by 1 langmuir of H_2 at 90 K. A subsequently measured hydrogen thermal desorption spectrum (Figure 7a) was unlike that following an exposure of 0.4 langmuir of C_2H_4 (Figure 7b). Rather, it appears qualitatively similar to that observed after an exposure of 1 langmuir of C_2H_4 (cf. Figure 1b) in that both spectra contain sharp peaks at 355 K. The major difference between the two spectra of Figure 7 is that more hydrogen adatoms are present in spectrum a, and this is reflected in the much more prominent high-temperature shoulder. Furthermore, more ethylidyne is formed relative to acetylide following the postadsorption of hydrogen, suggesting that this branching ratio is a function of hydrogen coverage. This will be discussed in greater detail in section IV.

To summarize, at all coverages ethylene adsorbs in a di- σ -bonded configuration that decomposes to ethylidyne, acetylide, and surface hydrogen above 150 K. The ethylidyne dehydrogenates above 330 K, generating additional surface hydrogen. The surface hydrogen desorbs at a temperature which decreases with increasing coverage following ethylene exposures below 0.6 langmuir and at 355 K following higher exposures of ethylene. The acetylide decomposes to carbon adatoms and methylidyne near 380 K. Finally, methylidyne decomposes, evolving hydrogen, after annealing above 500 K. For exposures of ethylene below 0.6 langmuir, complete decomposition of methylidyne occurs below 600 K. For higher ethylene exposures, the carbon adatoms (which are present in a higher concentration on the surface) stabilize the methylidyne, such that methylidyne decomposition extends up to 700 K. A plot of ethylene coverage as a function of ethylene exposure as well as a plot of the fractional coverage of ethylene which desorbs molecularly as a function of ethylene exposure is presented in Figure 8.

Figure 7. Hydrogen thermal desorption following exposures of (a) 0.4 langmuir of C_2H_4 followed by 2 langmuir of H_2 and (b) 0.4 langmuir of C_2H_4 at 100 K.Figure 8. (a) Fractional coverage of chemisorbed C_2H_4 as a function of exposure and (b) fractional coverage of chemisorbed C_2H_4 that desorbs molecularly as a function of exposure. The temperature of adsorption is 80 K.

IV. Discussion

As described in section III, ethylene chemisorbs on the Ru(001) surface in a di- σ -bonded configuration (at a surface temperature below 150 K) and at 80 K condenses into a molecular multilayer that resembles the free ethylene molecule (cf. Table I). As may be seen in Figure 2, all five IR-active modes of ethylene appear in the EEL spectra of the molecular multilayer. In addition, the carbon-carbon stretching mode, the CH_2 rocking mode, and the asymmetric CH_2 scissoring mode were resolved in some spectra. These modes are excited via an impact scattering mechanism.

Chemisorbed ethylene, which is stable below 150 K, is di- σ -bonded to the Ru(001) surface, and assignments of the observed vibrational modes are listed in Table II. This molecularly chemisorbed ethylene on the Ru(001) surface appears to undergo a somewhat greater degree of rehybridization than it does on the

Ni(110), Ni(111), and Fe(110) surfaces.^{1,3-5} The differences in frequency between the CH₂ twisting and scissoring modes of C₂H₄ on Ru(001) and on Fe(111) are not unexpected since ethylene on Fe(111) is severely tilted with respect to the surface plane such that two hydrogens are subject to multicenter interactions, which are manifested by a softened $\nu(\text{CH})$ mode at 2725 cm⁻¹.² This distorted geometry downshifts both the CH₂ wagging and scissoring modes.

Rather little can be said conclusively concerning the symmetry of the di- σ -bonded ethylene on Ru(001). Application of the dipolar selection rule would imply that the symmetry of the adsorbate-substrate complex is C₁, since both the CH₂ rocking and twisting modes appear in Figure 3a. However, EEL spectra measured off-specular show that these modes are largely impact excited, and therefore, the dipolar selection rule does not apply. Hence, the symmetry of di- σ -bonded ethylene on Ru(001) remains indeterminate. A near-edge X-ray absorption fine structure (NEXAFS) study of ethylene adsorbed on Pt(111) at 90 K by Horsley and co-workers⁵⁵ has shown that ethylene is symmetrically di- σ -bonded to two platinum atoms with the carbon-carbon bond axis parallel to the surface and a carbon-carbon bond length of 1.49 \pm 0.03 Å. We expect that di- σ -bonded ethylene would be adsorbed similarly on the Ru(001) surface.

Barreau et al.²² have reported a di- σ -bonded ethylene species on Ru(001) with a carbon-carbon stretching mode at 1330 cm⁻¹. Our results indicate that their assignments are incorrect, however, for the following reasons. First, they adsorbed ethylene at 170 K, a temperature at which we have shown that di- σ -bonded C₂H₄ has begun to decompose forming a mixed overlayer of C₂H₄(a), CCH₃(a), CCH(a), and H(a). Thus the modes they identify as resulting from di- σ -bonded C₂H₄ are in fact a combination of di- σ -bonded C₂H₄, CCH₃, and CCH modes. The 1330-cm⁻¹ loss which they assign to $\nu(\text{CC})$ is actually the $\delta_s(\text{CH}_3)$ mode of ethylidyne. This feature becomes more intense with further annealing which decomposes the C₂H₄(a) and produces more ethylidyne. Second, our EEL spectra of C₂D₄ on Ru(001) annealed at 170 K show clearly that the previous assignment²² is incorrect, because the 1330-cm⁻¹ loss downshifts to 1000 cm⁻¹ in the deuterated spectra, and there are no modes of comparable intensity to the 1300-cm⁻¹ mode between 1150 and 2190 cm⁻¹ in the deuterated spectra. Barreau and co-workers²² did not measure any EEL spectra of deuterated ethylene and thus could not distinguish carbon-carbon vibrational modes from hydrogen modes. A comparison of the EEL spectra of C₂H₄ and C₂D₄ is essential to the correct identification of these vibrational modes. As shown in Tables II-IV, EEL spectra of C₂D₄ on Ru(001) annealed between 110 and 400 K confirm our mode assignments for the three adspecies, di- σ -bonded ethylene, ethylidyne, and acetylide. Finally, we note that a carbon-carbon stretching frequency of 1040 cm⁻¹ is more reasonable than one of 1330 cm⁻¹ for an sp³-hybridized hydrocarbon species, and it is consistent with the carbon-carbon stretching mode observed at 1135 cm⁻¹ for acetylene chemisorbed on Ru(001).⁴⁷ It would be expected that $\nu(\text{CC})$ of chemisorbed ethylene on Ru(001) would be lower than this value, ruling out the assignment of the 1145-cm⁻¹ mode to $\nu(\text{CC})$ of C₂H₄. Furthermore, the 1145-cm⁻¹ mode shifts considerably (to 900 cm⁻¹) in the spectra of C₂D₄ and certainly cannot be due to $\nu(\text{CC})$.

No LEED patterns other than the (1 \times 1) of the substrate were observed for the ethylene overlayer between 90 and 300 K. Hence LEED measurements cannot aid in a determination of the ethylene surface structure or absolute coverages. However, thermal desorption results for C₂H₄ and H₂ have been used to estimate the ethylene coverage using the known saturation fractional coverage of hydrogen (0.85).³² The ethylene coverage (excluding the multilayer) is presented as a function of ethylene exposure in Figure 8a. From this figure, we see that the saturation (fractional) coverage of chemisorbed ethylene is approximately 0.30. Figure 8a was used also to obtain the initial probability of adsorption

of ethylene at 100 K, which was found to be unity within the limits of experimental uncertainty. The activation energy of desorption (equal to the heat of adsorption) of di- σ -bonded C₂H₄ was estimated from the thermal desorption measurements. When the method of Redhead⁵⁶ is used and a preexponential factor of 10¹³-10¹⁴ s⁻¹ is assumed, a value of approximately 11.6 \pm 1 kcal/mol is obtained. Considering the changes in bond strengths due to rehybridization of the carbon atoms, we have also estimated that the binding energy of di- σ -bonded ethylene is between 105 and 135 kcal/mol. Thus the observation of a low heat of adsorption for chemisorbed ethylene on Ru(001) does not imply that the ruthenium-carbon bond is weak.

When the saturated overlayer of chemisorbed ethylene is annealed to 250 K, approximately 20% of the ethylene desorbs, while the remainder dehydrogenates to ethylidyne, acetylide, and surface hydrogen. The stoichiometry of the ethylidyne formed by ethylene decomposition on Pt(111) was confirmed by hydrogen thermal desorption spectra in which approximately 25% of the total hydrogen desorbed from the surface at 300 K, the same temperature at which ethylidyne was shown to form via EELS.⁵⁷ Unfortunately, the hydrogen from ethylidyne formation remains adsorbed on the Ru(001) surface, ultimately desorbing with hydrogen from ethylidyne decomposition. Hence we are unable to confirm directly the stoichiometry of the ethylene decomposition products from hydrogen thermal desorption spectra. The ethylidyne on Ru(001) begins to decompose at approximately 330 K, whereas the ethylidyne formed on Pt(111) is stable to 400 K.⁷ The reduced stability of ethylidyne on Ru(001) is undoubtedly due to the stronger metal-hydrogen and metal-carbon bonds formed on the ruthenium surface, which makes the decomposition of ethylidyne via metal-hydrogen and metal-carbon bond formation more favorable both thermodynamically and kinetically.

The identification of ethylidyne and acetylide as the decomposition products of di- σ -bonded ethylene on Ru(001) can be contrasted to the results of Barreau et al.²² who only identified ethylidyne. We also note that Barreau assigned the $\rho(\text{CH}_3)$ mode of ethylidyne to a loss at 870 cm⁻¹. We observed no such mode in our EEL spectra and cannot account for this discrepancy but merely mention that our assignment of the 1000-cm⁻¹ loss to $\rho(\text{CH}_3)$ and the observed isotopic shift to 800 cm⁻¹ for $\rho(\text{CD}_3)$ are in agreement with the frequencies observed for other ethylidyne species.

Our EEL spectra of the thermal evolution of ethylidyne and acetylide on Ru(001) and complementary thermal desorption spectra show that virtually all of the ethylidyne dehydrogenates to surface carbon below 360 K, leaving only CCH(a) and H(a) on the surface. Thus an EEL spectrum measured after annealing to 360 K (Figure 5b) contains only the loss features of acetylide, permitting unambiguous identification of this intermediate. The observation of the carbon-hydrogen bending mode of acetylide at 280 K, prior to the onset of ethylidyne dehydrogenation, implies that acetylide is not a decomposition product of ethylidyne. Further proof of this assertion comes from CO and C₂H₄ coadsorption experiments.⁵⁸

By analogy to all relevant organometallic ethylidyne complexes synthesized to date, it is almost certain that the carbon-carbon bond axis of ethylidyne on Ru(001) is very nearly perpendicular to the surface. This configuration is also supported by the strong intensity of the $\nu(\text{CC})$ mode of ethylidyne at 1140 cm⁻¹ in the EEL spectrum of Figure 5a and its predominantly dipolar character. Furthermore it is very probable that ethylidyne is bonded to the Ru(001) surface in a threefold hollow site both by analogy to the trimetal $\mu_3\text{-CCH}_3$ complexes^{45,46} and because ethylidyne has been observed only on hexagonal surfaces.^{4,7,16} A further indication of this bonding of ethylidyne on Ru(001) is provided by NEXAFS results of ethylidyne on Pt(111),⁵⁵ which showed that the ethylidyne is symmetrically bonded to three

(56) Redhead, P. A. *Vacuum* 1962, 203.

(57) Ibach, H.; Mills, D. L. *Electron Energy Loss Spectroscopy and Surface Vibrations*; Academic: New York, 1982.

(58) Hills, M. M.; Parmeter, J. E.; Weinberg, W. H., unpublished results.

(55) Horsley, J. A.; Stöhr, J.; Koestner, R. J. *J. Chem. Phys.* 1985, 83, 3146.

platinum atoms with the carbon-carbon bond axis essentially perpendicular to the surface.

Next, we consider the effects of simultaneous ethylidyne decomposition and hydrogen desorption on the observed shape of the hydrogen thermal desorption peak. When the Ru(001) surface on which ethylene is adsorbed (exposures above 0.6 langmuir) is annealed to 300 K, hydrogen desorption is observed. In these measurements, hydrogen desorbs at this low temperature due to its higher surface coverage. As the overlayer is annealed to 330 K, additional hydrogen desorbs, and ethylidyne begins to dehydrogenate, replenishing the supply of surface hydrogen. Thus adjacent to the decomposing ethylidyne, an area of high local density of hydrogen adatoms is formed, which accelerates the rate of desorption of hydrogen and gives the hydrogen thermal desorption peak a sharp leading edge. Comparing Figure 6a and 6b, it is clear that the high-temperature shoulder on the 355 K hydrogen thermal desorption peak results from residual surface hydrogen.

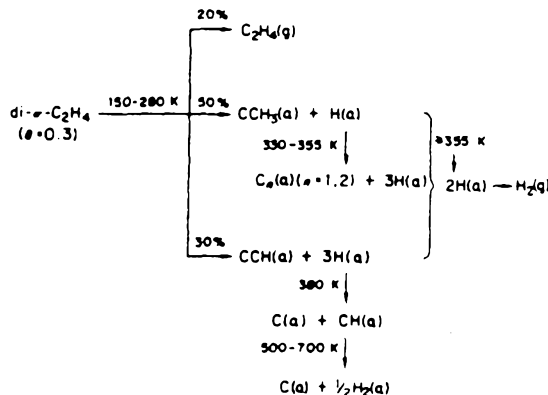
For these higher exposures of ethylene, the temperature of the hydrogen thermal desorption peak remains at 355 K independent of coverage. Ethylidyne decomposition dictates this hydrogen desorption since the desorption of hydrogen occurs at a lower temperature in a broader peak at higher hydrogen adatom coverages (from the adsorption of hydrogen). The adsorption and decomposition of ethylene at high coverages is otherwise identical with that for lower coverages with three exceptions. First, a multilayer of ethylene forms which desorbs at 110 K. Second, some of the di- σ -bonded ethylene desorbs (cf. Figure 8b). Finally, the ratio of ethylidyne to acetylide that is formed is increased. Recall that annealing to 400 K the Ru(001) surface on which ethylene is adsorbed not only decomposes the ethylidyne but also causes cleavage of the carbon-carbon bond of the acetylide, leaving methylidyne and carbon adatoms. The high-temperature tail of the hydrogen thermal desorption peak after ethylene adsorption corresponds to dehydrogenation of methylidyne. Consequently, the ratio of ethylidyne to acetylide that is formed from ethylene can be obtained from the relative areas of the 355 K peak and the tail. The acetylide coverage is equal to the coverage of the hydrogen desorbing in the high-temperature tail. The ethylidyne coverage is obtained by subtracting 3 times the acetylide coverage from the coverage of hydrogen desorbing in the 355 K hydrogen thermal desorption peak and its high-temperature shoulder and dividing this number by four. We find that a saturation exposure of ethylene decomposes to ethylidyne and acetylide in the approximate ratio of 60:40, whereas a lower exposure, 0.4 langmuir of C_2H_4 , yields a ratio of 50:50. Consequently ethylidyne formation is favored at higher surface coverages. This result may be interpreted in terms of the number of hydrogen adatoms generated by ethylene decomposition to ethylidyne (one per C_2H_4) vs. acetylide (three per C_2H_4). At higher surface coverages, more threefold sites, required for hydrogen adatoms, will be either occupied or blocked. Also, the coverage of hydrogen will be greater as ethylene dehydrogenation proceeds. Thus, the decomposition product that requires fewer vacant surface sites for formation and is composed of more hydrogen atoms, ethylidyne, is favored. The dependence of the ratio of ethylidyne to acetylide formed upon the hydrogen coverage has also been confirmed by hydrogen thermal desorption experiments measured following a saturation ethylene exposure at 350 K. At this temperature, the hydrogen adatom concentration on the surface is reduced. This lower hydrogen coverage caused the acetylide coverage to increase by approximately 50% compared to the coverage of acetylide formed following a saturation ethylene exposure at 80 K, and annealing to 350 K, as judged by the relative intensities of the high-temperature tails in the hydrogen thermal desorption spectra.

Finally, we discuss briefly the mechanism of dehydrogenation of ethylidyne. The EEL spectra measured immediately following the decomposition of ethylidyne show no enhancement of the carbon-hydrogen bending mode of acetylide and provide no evidence for methylidyne formation. Thus, we can rule out both

acetylide and methylidyne formation from ethylidyne decomposition and conclude that ethylidyne must dehydrogenate completely to either carbon-carbon dimers [with $\nu(CC)$ at 1100-1600 cm^{-1} in the EEL spectra of Figure 5b and 5c] and hydrogen or carbon adatoms and hydrogen. The observed complete dehydrogenation of ethylidyne at a temperature at which acetylide is stable on the surface is quite important. It implies that the reaction coordinate that results in the loss of the first hydrogen atom from ethylidyne is not the one which would lead to the stable surface acetylide. A plausible but most certainly speculative scenario for the dehydrogenation of ethylidyne would involve interaction with an adjacent threefold hollow site, whereas the stable acetylide (almost certainly not oriented parallel to the surface plane) has a structure that is rotated 60° with respect to this reaction coordinate.

V. Conclusions

Ethylene chemisorbs on Ru(001) in a di- σ -bonded configuration at temperatures below approximately 150 K. When heated, competing molecular desorption, dehydrogenation to acetylide, and dehydrogenation to ethylidyne occur. The resulting thermal decomposition scheme for a saturation coverage of chemisorbed ethylene ($\theta = 0.30$) may be depicted as



The ethylidyne formed on Ru(001) is less stable than on other groups 8-10 metal surfaces; e.g., it begins to decompose to carbon and hydrogen adatoms near 330 K compared to the decomposition temperature of approximately 400 K observed on Pt(111) and Rh(111). Carbon-carbon bond cleavage of the acetylide occurs at 380 K, producing surface carbon and methylidyne of which the latter dehydrogenates between 500 and 700 K. Following ethylene exposures exceeding 0.6 langmuir, desorption of hydrogen occurs in a sharp peak with a maximum rate of desorption at 355 K, which is limited by ethylidyne decomposition, in a shoulder at approximately 400 K on this peak due to desorption-limited hydrogen and also in a high-temperature tail due to methylidyne decomposition. Hydrogen desorption following lower ethylene exposures becomes desorption-limited, except for the hydrogen that is evolved from the decomposition of methylidyne.

To summarize, ethylene adsorbed on Ru(001) produces both ethylidyne and the more extensively dehydrogenated acetylide. Thus, the behavior of ethylene adsorbed on Ru(001) appears to be intermediate between the more complete dehydrogenation observed on Ni(111) and Co(001) and the exclusive formation of the less dehydrogenated stable ethylidyne species found on the hexagonal surfaces of rhodium, palladium, and platinum.

Acknowledgment. This work was supported by the National Science Foundation under Grant CHE-8516615. Acknowledgment is also made to the donors of the Petroleum Research Fund, administered by the American Chemical Society, for the partial support of this research.

Registry No. C_2H_4 , 74-85-1; Ru, 7440-18-8; CCH₃, 67624-57-1; CCH, 29075-95-4; CH, 3315-37-5.